Mesoscale ionospheric plasma irregularities and scintillation over Svalbard

Christer van der Meeren

Dissertation for the degree of Philosophiae Doctor (PhD)

Department of Physics and Technology
University of Bergen

June 2016

Disstertation date: October 21st

Acknowledgements

This thesis is funded by the Research Council of Norway. My PhD project has been carried out over three years in one of the research groups at the Birkeland Centre for Space Science (BCSS) at the Department of Physics and Technology, University of Bergen, Norway. At BCSS I have been lucky to be part of a team of accomplished and inquisitive researchers and students. They have all played a role in making my research what it is, and making me who I am. Fruitful discussions and much needed coffee breaks were never more than a knock away, and I am highly grateful to the fellow students I had the pleasure of working, talking, and laughing with.

I have been lucky to have Kjellmar Oksavik as my supervisor. I truly appreciate your robust knowledge of ionospheric physics, your candid feedback, and your ability to spot potential. Your advice has been invaluable, and I have enjoyed working with you since I started my Master's degree in 2011. I am also very grateful to my co-supervisor, Dag Lorentzen. We have not had the opportunity to sit down and discuss our research face-to-face on a daily basis, but when we did, the research and my understanding always seemed to skip ahead by two steps. My thesis would not have been the same without you.

The studies conducted in this thesis would not have been possible without using the network of all-sky imagers in Svalbard operated by the University of Oslo, Norway. My thanks go out to Jøran Moen and Bjørn Lybekk for fruitful discussions. In particular I would like to thank Lasse Clausen for valuable contributions to several of the papers in this thesis, and for creating an excellent and easy-to-use database of all-sky imager data. Without this database, the studies would have been significantly more cumbersome to carry out; indeed, some might not have happened at all.

Last, but not least, I would like to thank my family: My parents, for always encouraging my curiosity throughout my childhood, for believing in me, and for providing comforting words in times of need; my siblings, for all the laughs and much-needed wind-down time; my grandparents, for enthusiastically cheering from the sidelines; and Aina, my dear Aina, for all of the above, for all your love, and for being just the way you are.

Bergen, June 2016
Christer van der Meeren

Abstract

This thesis investigates how navigation signals are compromised by ionospheric plasma irregularities in the auroral and polar ionosphere over Svalbard. In 2013, four multi-constellation global navigation satellite system (GNSS) receivers were installed in Ny-Ålesund, Longyearbyen, Hopen, and Bjørnøya. These receivers provide unprecedented coverage of scintillation and plasma density (total electron content) in the region. The four research papers in this thesis are detailed case studies investigating mesoscale irregularities and scintillation. We use data from these GNSS receivers, all-sky imagers, coherent and incoherent scatter radars, ionosondes, and in-situ satellite measurements.

Paper I [*van der Meeren et al.*, 2014] investigates scintillation and irregularities on the front of a tongue of ionization (TOI) in the polar cap. Moderate scintillation and structuring is observed on the leading edge of the TOI. We employ a novel method where we use spectrograms of the phase of raw GNSS signals to show that the structuring is real and not due to erroneous data detrending of the σ_ϕ phase scintillation index.

Paper II [*Oksavik et al.*, 2015] investigates irregularities in the dayside auroral region, specifically in relation to poleward-moving auroral forms (PMAFs). Scintillation is strongly localized to these intense and transient features, even in the presence of polar cap patches.

Paper III [*van der Meeren et al.*, 2015] investigates scintillation from substorm auroral emissions as polar cap patches enter the nightside auroral oval. The most severe scintillation is found when the auroral precipitation coincides with polar cap patches. The scintillation is strongly localized to signals intersecting intense auroral emissions.

Paper IV [*van der Meeren et al.*, 2016] investigates irregularities during quiet geomagnetic conditions. We find weak irregularities in relation to a stable and intense transpolar arc, but no scintillation is seen.

The main results in this thesis are:

- Scintillation-producing irregularities can exist on the leading edge of TOIs, in PMAFs, and in substorm auroral precipitation when patches enter the nightside auroral oval. Of these, auroral precipitation on top of pre-existing plasma patches seems to produce the strongest scintillation.

- The scintillation generally shows a high degree of localization, varying significantly over distances of $\sim 100\,\mathrm{km}$. This clearly indicates the need for a dense network of scintillation receivers in the polar ionosphere to fully resolve this spatial variation. It also shows that detailed case studies are important to complement the averaged, static, large-scale picture common in statistical studies.
- We have developed a novel method of using spectrograms of the phase of raw GNSS signals to get a more complete view of irregularities than aggregate scintillation indices like σ_ϕ. Furthermore, our method does not require data detrending, and it is therefore more robust than traditional scintillation indices that are frequently used by the community.
- The observed irregularities cover a wide range of spatial scale sizes, from decameters to several kilometers. Irregularities at these spatial scale sizes can affect radio wave propagation from HF to GNSS frequencies.

Contents

List of Abbreviations

ASI	all-sky imager
GDI	gradient drift instability
GNSS	global navigation satellite system
GPS	Global Positioning System
HF	high frequency
IMF	interplanetary magnetic field
KHI	Kelvin-Helmholtz instability
MSP	meridian-scanning photometer
PMAF	poleward-moving auroral form
SED	storm enhanced density
STEC	slant total electron content
SuperDARN	Super Dual Auroral Radar Network
TEC	total electron content
TECU	TEC units, $1\,\mathrm{TECU} = 10^{16}\,\mathrm{m}^{-2}$
TOI	tongue of ionization
VTEC	vertical total electron content

Chapter 1

Introduction

Satellite navigation is becoming an increasingly important part of modern society. Global navigation satellite systems (GNSS) receivers are prevalent in consumer devices such as smartphones and watches, as well as integrated into cars and other vehicles. The aviation and oil industries are examples where satellite navigation has become increasingly critical to life and safety of operations. As the polar ice is disappearing, the polar areas might see more travel and industrial activity. Therefore, it is important to explore problems with satellite navigation in polar areas. This can lead to more accurate prediction and better mitigation of adverse ionospheric effects on GNSS signals.

In addition to the well-known Global Positioning System (GPS), several countries and intergovernmental entities have launched or are launching their own satellite navigation systems, such as the Russian GLONASS, the European Galileo, and the Chinese BeiDou. The availability of several GNSS constellations increases the coverage for multi-constellation GNSS receivers. This benefits commercial GNSS usage as well as scientific receivers used for monitoring the ionosphere, allowing better spatial resolution measurements. The desire to have these systems work reliably across the globe, including in the polar areas, also increases the interest in predicting and mitigating adverse effects on GNSS signals.

In 2013, several multi-constellation GNSS receivers were installed in Svalbard, providing unprecedented coverage in the region for monitoring of ionospheric plasma density and irregularities that cause disturbances on GNSS signals. The Svalbard region is well suited for studying the high-latitude and polar ionosphere. Firstly, it is inside the polar cap most of the time, allowing for the observation of complex polar cap dynamics, yet it is far enough south that auroral dynamics can be studied too, as well as the interplay between the polar cap and auroral regions. Secondly, a wide variety of instruments is operating in the region, allowing for detailed multi-instrument studies. The instruments in the region include high-resolution GNSS receivers, an all-sky imager network (co-located with the GNSS receivers, which allows for direct line of sight comparisons), meridian-scanning photometers, incoherent and coherent scatter radars, ionosondes, and several magnetometers. Additionally, several satellites in polar or near-polar orbits provide valuable data.

Motivation

The overall objective of this thesis is to advance our understanding of mesoscale plasma irregularities in the polar ionosphere and their impact on L band (1–2 GHz) GNSS signals. The primary question behind these studies is:

> **How are dynamic phenomena in the polar cap and auroral ionosphere causing disturbances (scintillation) on transionospheric radio signals at GNSS frequencies?**

In pursuing this question, we will shed light on more specific topics, such as:

- Which features in the polar ionosphere produce the strongest irregularities and scintillation?
- How severe is the GNSS scintillation during active and quiet conditions?
- What are the spatial scales of the irregularities?

Our pre-existing knowledge (which is outlined in Chapter 2) is primarily based on statistical studies, potentially averaging out important effects due to temporal and spatial variability in the system. The excellent instrumentation in Svalbard allows for detailed investigations of when and where scintillation and irregularities occur in relation to polar cap and auroral phenomena. This thesis consists of four case studies:

- Paper I: GPS scintillation and irregularities at the front of an ionization tongue in the nightside polar ionosphere
- Paper II: Scintillation and loss of signal lock from poleward moving auroral forms in the cusp ionosphere
- Paper III: Severe and localized GNSS scintillation at the poleward edge of the nightside auroral oval during intense substorm aurora
- Paper IV: Scintillation and irregularities from the nightside part of a sun-aligned polar cap arc

We start by explaining the theoretical background in Chapter 2. The open questions that triggered our four studies are summarized in Section 2.4. In Chapter 3, we provide a quick overview of the instruments we have used. Chapter 4 provides a brief summary of the papers. A more detailed discussion of the results is given in Chapter 5. Finally, Chapter 6 concludes and provides open questions for future studies.

Chapter 2

Theoretical background

This section provides a brief theoretical background to the research field of this thesis. We start by providing some fundamentals on the terrestrial ionosphere in Section 2.1. Section 2.2 covers relevant phenomena such as polar cap patches and auroral blobs, and Section 2.3 briefly presents and plasma instability mechanisms that can produce small-scale irregularities. Finally, Section 2.4 briefly presents the current state of knowledge and key questions in this thesis.

2.1 Ionospheric structure, production, and loss

This section provides a brief overview of the terrestrial ionosphere based on *Kelley* [2009] and *Hunsucker and Hargreaves* [2002]. Solar radiation in the extreme ultraviolet range partly ionizes the Earth's upper atmosphere. The ionosphere is the part of the terrestrial atmosphere that is significantly ionized. A key parameter of the ionosphere is the plasma density, often referred to as the electron density N_e due to the charge neutrality of the plasma. This parameter governs or influences several ionospheric processes and effects. It can also be represented by the plasma frequency ω_p, which is a simple function of the plasma density ($\omega_p = \sqrt{N_e e^2/m_e \varepsilon_0}$ where e is the electron charge, m_e is the electron mass, and ε_0 is the permittivity of free space).

The ionosphere is divided vertically into different regions according to its plasma density profile, shown in Figure 2.1. The density profile is to first order caused by the increasing absorption of solar radiation at lower altitudes [*Chapman*, 1931]. This means that at nighttime, when the Sun is below the horizon, the rate of ionization is significantly reduced. Loss processes (to be detailed below) then reduce the plasma density. The difference between nighttime and daytime densities can be more than one order of magnitude, as seen in Figure 2.1.

Additionally, the rate of ionization is significantly influenced by solar activity. The dashed lines in Figure 2.1 shows typical density profiles for day/night during periods of low solar activity, whereas the solid lines indicate the density profiles for high solar activity. The difference is a factor of $\sim$ 2–10, depending on the altitude and day-

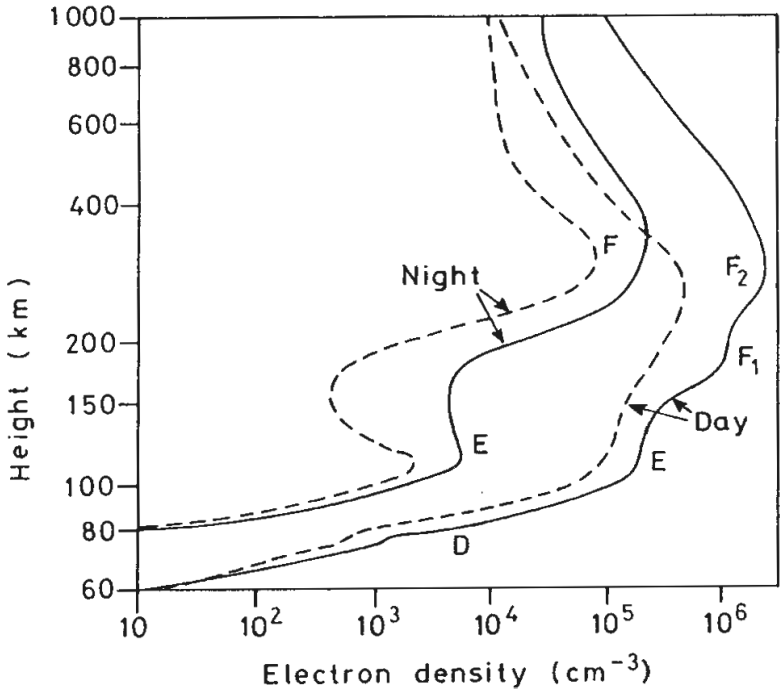

Figure 2.1: Typical daytime/nighttime electron density profiles in the ionosphere for solar minimum (dashed lines) and solar maximum (solid lines). [From *Hunsucker and Hargreaves*, 2002]

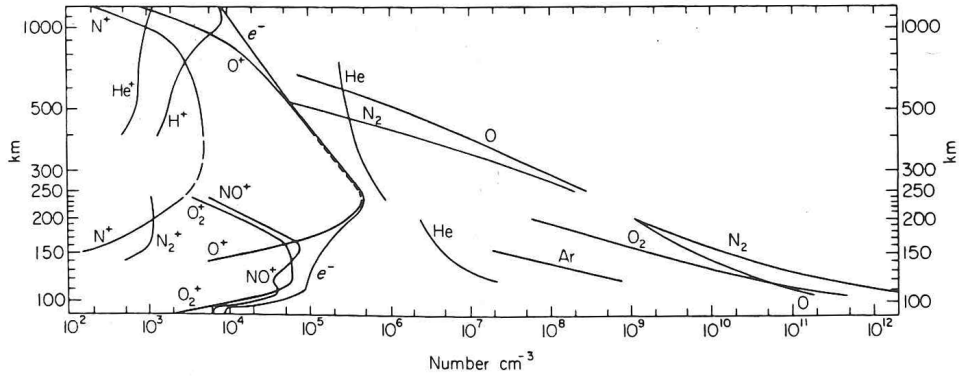

Figure 2.2: Daytime ionospheric ion composition altitude profile during the International Quiet Solar Years (1964–1965) based on mass spectrometer measurements. Retrieved from *Kelley* [2009], originally from *Johnson* [1969].

time/nighttime.

While solar ionization is the dominant production mechanism in the sunlit ionosphere, ionization by energetic particle precipitation can significantly influence the density profile at nighttime auroral latitudes during active geomagnetic conditions.

The production of ionization is balanced by loss processes. The most common loss process is dissociative recombination, in which a molecular ion and an electron combine to produce two neutral atoms. It can be generally written as

$$\mathrm{XY}^+ + \mathrm{e}^- \longrightarrow \mathrm{X} + \mathrm{Y}, \tag{2.1}$$

where X and Y are placeholders for atoms such as N and O. The reaction rate is proportional to the density of the reactants, and an equilibrium is thus reached between production and loss of ionization.

Since the loss of ionization through dissociative recombination is governed by the density of particular ions, we have shown a daytime ionospheric ion composition altitude profile in Figure 2.2. Below 150 km, O_2^+ and NO^+ are by far the dominating ion species, with similar concentrations around half the plasma density (the line labeled e^-). Around 150 km, O^+ becomes important, with concentrations similar to the two molecular ions. From $\sim$ 200 km upwards, O^+ is completely dominant, with concentrations essentially equal to the plasma density.

In this thesis only the *E* region ($\sim$ 90–150 km) and *F* region ($\sim$ 150–500 km) are relevant. In the following, we will briefly describe production and loss in these two regions.

E region production and loss

In the dayside sunlit *E* region, production is dominated by absorption of 80–102.7 nm radiation by O_2. The dominant ion species are NO^+ and $O_2{}^+$ (see Figure 2.2), and ionization loss mainly occurs through the following dissociative recombinations:

$$NO^+ + e^- \longrightarrow N + O \tag{2.2}$$

$$O_2{}^+ + e^- \longrightarrow O + O \tag{2.3}$$

Typical daytime *E* region densities are several times $10^{11}\,m^{-3}$. At nighttime, without solar ionization, a weakly ionized layer remains with densities of around $5 \times 10^9\,m^{-3}$. If there is ongoing particle precipitation, the *E* region will be enhanced.

F region production and loss

The *F* region usually contains the peak plasma density in the ionosphere, and is divided into the $F1$ and $F2$ layers. The $F1$ layer exists only at daytime (as shown in Figure 2.1) and is created by the absorption of 20–90 nm radiation by atomic oxygen at 140–170 km altitude. $F2$ is the topmost layer and typically contains the maximum ionospheric density. In the $F2$ layer, O^+ is the dominating ion species (see Figure 2.2). While ionization may be lost by the recombination reaction

$$O^+ + e^- \longrightarrow O + \text{photon}, \tag{2.4}$$

the reaction rate is slow, and ionization in the $F2$ layer is mainly lost through a two-step process. First, a charge exchange occurs between O^+ and molecular oxygen or nitrogen:

$$O^+ + O_2 \longrightarrow O_2{}^+ + O \tag{2.5}$$

$$O^+ + N_2 \longrightarrow NO^+ + N \tag{2.6}$$

Then, ionization is lost through dissociative recombination similar to the *E* region (Equations 2.2 and 2.3). Around the $F1$ layer, $O_2{}^+$ and NO^+ are abundant even without charge exchange. This quickly reduces the daytime densities of 10^{11}–$10^{12}\,m^{-3}$ when the Sun disappears, effectively removing the $F1$ layer at night. In the $F2$ layer, the slow charge exchange limits the overall reaction rate. This means that the daytime densities of several times $10^{12}\,m^{-3}$ have a lifetime of many hours and are only weakly reduced at night, typically to 10^{10}–$10^{11}\,m^{-3}$.

Type	$\boldsymbol{v}$ [km s^{-1}]	B [nT]	N_p [m^{-3}]	Proton E_K [keV]
Slow	300–500	5	8×10^6	1
Fast	600–800	4	3×10^6	4

Table 2.1: Typical solar wind parameters for slow and fast solar wind: Velocity v, magnetic field strength B, proton number density N_p and proton kinetic energy E_K [*Axford*, 1985; *Balogh et al.*, 1999; *Ebert et al.*, 2009].

2.2 Relevant phenomena in the high-latitude ionosphere

The polar cap and auroral ionosphere is highly dynamic, and different phenomena may be observed for different geomagnetic conditions. In this section we briefly define the various ionospheric phenomena that have been studied in this thesis. For more details we refer the reader to the scientific papers and references therein. First we describe the interplanetary magnetic field, which significantly influences the processes taking place in the magnetosphere-ionosphere system.

2.2.1 The interplanetary magnetic field

The solar wind is a continuous stream of particles, mainly electrons and protons, being emitted from the Sun. The solar wind is divided into two categories: The fast solar wind flows from coronal holes, while the slow solar wind is an extension of the solar corona into interplanetary space [*Axford*, 1985; *Breen et al.*, 1997; *Balogh et al.*, 1999; *Tsurutani et al.*, 2006]. Table 2.1 gives typical solar wind parameters.

The interplanetary magnetic field (IMF) is frozen into the solar wind [e.g., *Nicholson*, 1983]. When the IMF approaches the Earth, it interacts with the terrestrial magnetic field [*Dungey*, 1961]. The north/south component of the IMF, or B_z, governs the strength of plasma circulation in the polar cap [e.g., *Cousins and Shepherd*, 2010]. When the solar wind has a southward pointing component, i.e., when $B_z < 0$, the IMF and the terrestrial magnetic field reconnect [e.g., *Hones*, 1984]. During this process, magnetospheric field lines are opened, or "peeled off", at the magnetopause and carried antisunward [e.g., *Baumjohann and Treumann*, 1996]. The ionospheric footprints of the field lines move correspondingly, and the high-density dayside plasma gets drawn into and across the polar cap [*Dungey*, 1961; *Foster and Doupnik*, 1984; *Foster*, 1993].

When the IMF has a northward pointing component, the field lines do not reconnect at the magnetopause, and there is generally no strong plasma circulation [e.g., *Cousins and Shepherd*, 2010]. The polar ionosphere may still exhibit interesting phenomena; most notably, auroral arcs may appear inside the polar cap [e.g., *Newell et al.*, 2009].

Figure 2.3 illustrates the polar cap during northward and southward IMF conditions. For northward IMF, polar cap arcs appear. For southward IMF, the polar cap is filled with plasma in the form of polar cap patches. Polar cap arcs and patches will be described below.

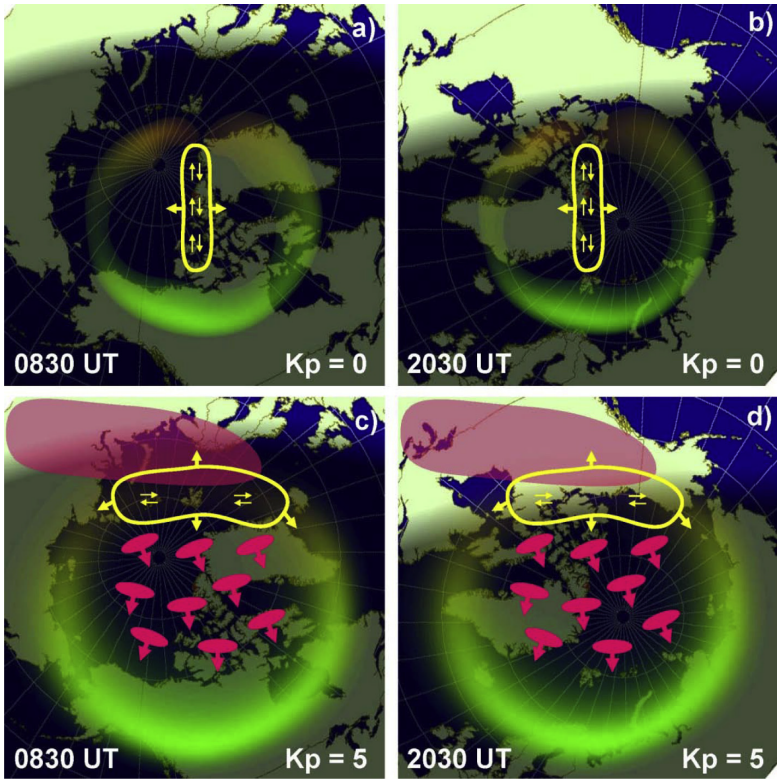

Figure 2.3: A schematic illustration of irregularities in the polar cap. (a–b) Polar cap arcs in the central polar cap during northward IMF. (c–d) Polar cap patches originating from the dayside tongue of ionization transit the polar cap during southward IMF. Due to the offset of the magnetic pole from the rotational axis, more of the northern winter high-latitude ionosphere is sunlit at UTs around 20:30 (panels (b) and (d)), corresponding to Svalbard being located on the nightside. [From *Moen et al.*, 2013]

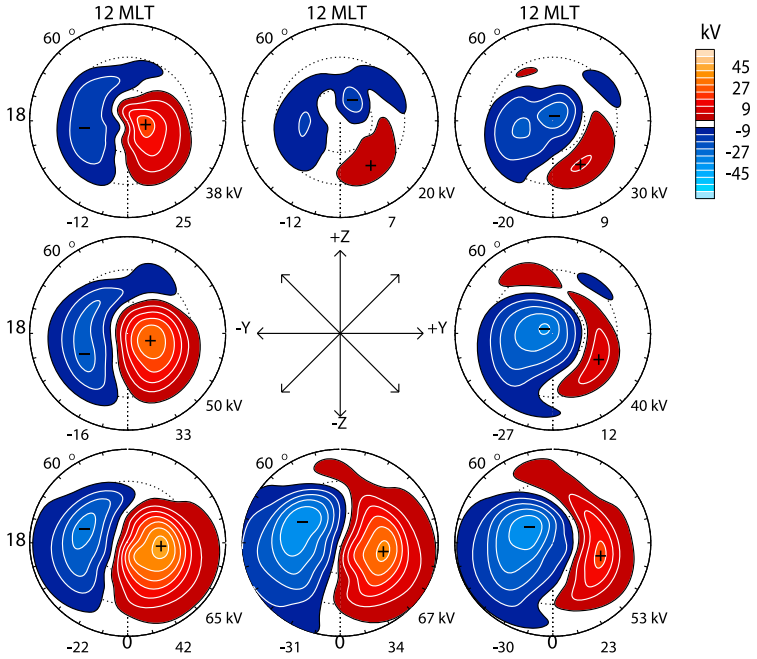

Figure 2.4: The influence of different combinations of B_y and B_z on electrostatic potentials in the northern hemisphere. [From *Cousins and Shepherd*, 2010]

Another important IMF component is the dawn-dusk component, or B_y. This parameter shifts the dayside plasma intake region. For positive B_y, the plasma intake region is shifted post-noon, and the plasma is drawn northeast into the polar cap. For negative B_y the opposite is true [e.g., *Cousins and Shepherd*, 2010].

Figure 2.4 shows the statistical ionospheric convection pattern binned by IMF B_y and B_z. The effect of B_z on the large-scale circulation is evident, as is the movement of the dayside plasma intake region depending on B_y during southward IMF. The plasma is convected along the white isopotential contours.

2.2.2 The auroral oval and substorms

Auroral emissions are perhaps the most visible effect of the active magnetosphere-ionosphere system. Energetic particle precipitation close to the polar cap boundary is manifested as emissions at several wavelengths, primarily 557.7 nm emissions from O(^1S) at $\sim$ 120 km altitude and 630.0 nm emissions from O(^1D) at $\sim$ 220–250 km altitude [e.g., *Solomon et al.*, 1988].

The auroral oval is significantly influenced by the geomagnetic activity, in particular magnetospheric substorms. A magnetospheric substorm is defined as *a transient process initiated on the nightside of the Earth, in which a significant amount of energy derived from the solar wind-magnetosphere interaction is deposited in the auroral*

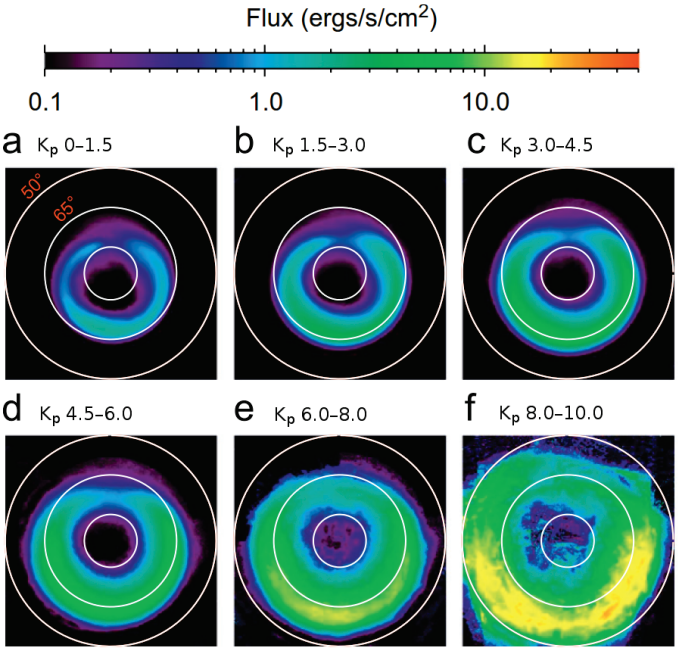

Figure 2.5: Global distributions of mean electron energy flux for six levels of geomagnetic activity (as determined by the K_p index) obtained from 4 years of GUVI data from both hemispheres. Magnetic noon/midnight is at the top/bottom, and magnetic dawn/dusk is to the right/left. [Adapted from *Zhang and Paxton*, 2008]

ionosphere and in the magnetosphere [*Rostoker et al.*, 1980]. A substorm normally consists of the growth, expansion, and recovery phases [e.g., *McPherron*, 1979, 1970; *Akasofu*, 1964]. A review of the substorm is provided by *Elphinstone et al.* [1996]. A brief overview follows. In the growth phase, a southward oriented IMF loads energy into the magnetosphere by dayside reconnection. The added open flux makes the polar cap and the auroral oval expands equatorward. In the expansion phase, the energy stored in the magnetotail is explosively released into the ionosphere. This is manifested as a sudden brightening and poleward expansion of the aurora as the magnetotail becomes more dipolar. In the recovery phase, the auroral emission intensity is reduced. A substorm typically lasts 2–3 hours [e.g., *Akasofu*, 1964].

Figure 2.5 provides a statistical view of the auroral oval through the mean electron energy flux for six different geomagnetic activity levels (K_p intervals 0–1.5, 1.5–3.0, 3.0–4.5, 4.5–6.0, 6.0–8.0 and 8.0–10.0). The effect of increased geomagnetic activity on the auroral oval is clearly visible. For increased geomagnetic activity, the oval is significantly expanded and located further equatorward, and more energy is dumped into the ionosphere through precipitating particles.

2.2.3 Poleward-moving auroral forms

The dayside aurora contains several types of auroral features, such the cusp aurora, poleward-moving auroral forms (PMAFs), diffuse arcs south of the cusp, and discrete arcs toward the dawn and dusk sectors [*Sandholt et al.*, 1998]. A schematic overview of these features are provided in Figure 2.6. The only dayside auroral feature studied in this thesis is the PMAF.

PMAFs are auroral signatures that detach from the dayside auroral oval and drift into the polar cap [*Feldstein and Starkov*, 1967; *Vorobjev et al.*, 1975; *Fasel et al.*, 1993; *Fasel*, 1995]. They move northwest when IMF B_y is positive, and northeast when B_y is negative [e.g., *Sandholt et al.*, 1998]. PMAFs are interpreted as ionospheric signatures of flux transfer events, with similar repetition rates [e.g., *Sandholt et al.*, 1990, 1993; *Milan et al.*, 1999; *Thorolfsson et al.*, 2000]. The poleward motion and repetition of PMAFs can be seen in Figure 2.7.

2.2.4 Polar cap patches

F region polar cap patches, often referred to simply as patches, are discrete 100–1000 km islands of high-density plasma in the *F* region polar cap. The plasma is drawn into the polar cap and segmented in the cusp region. The dominant segmentation mechanism is believed to be transient magnetopause reconnection [*Lockwood and Carlson*, 1992; *Carlson et al.*, 2002, 2004, 2006; *Lockwood et al.*, 2005; *Moen et al.*, 2006; *Lorentzen et al.*, 2010; *Zhang et al.*, 2013], but other mechanisms have been proposed [e.g., *Carlson*, 2012, and references therein]. The transient reconnection mechanism is

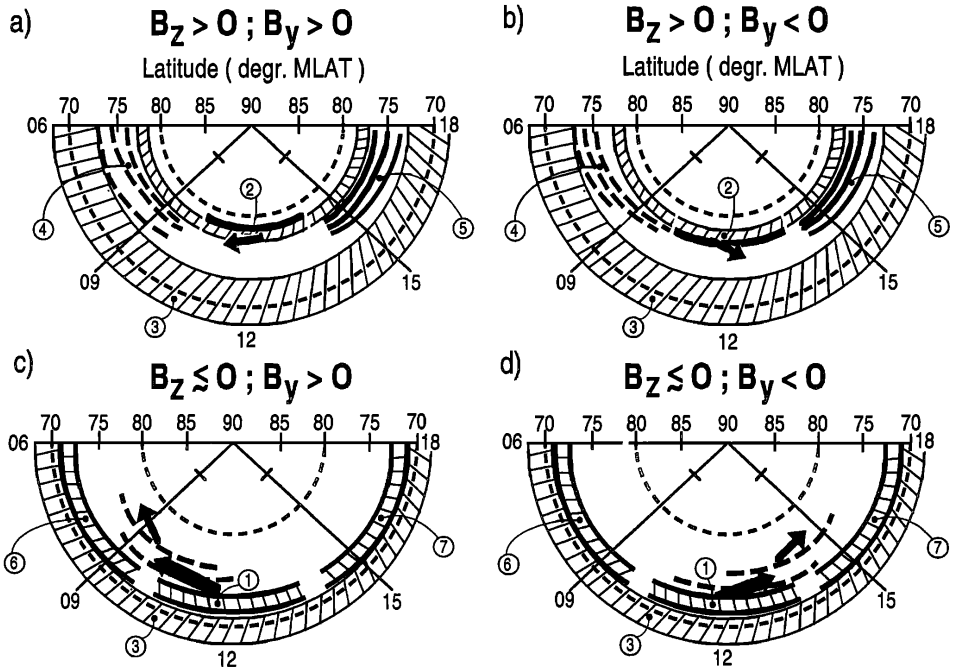

Figure 2.6: A classification of dayside auroral forms from *Sandholt et al.* [1998], to which we refer the reader for details. PMAFs occur for southward IMF (panels (c) and (d)) and are labeled ①. The black arrows shown in relation to the PMAFs show the direction of movement as determined by IMF B_y.

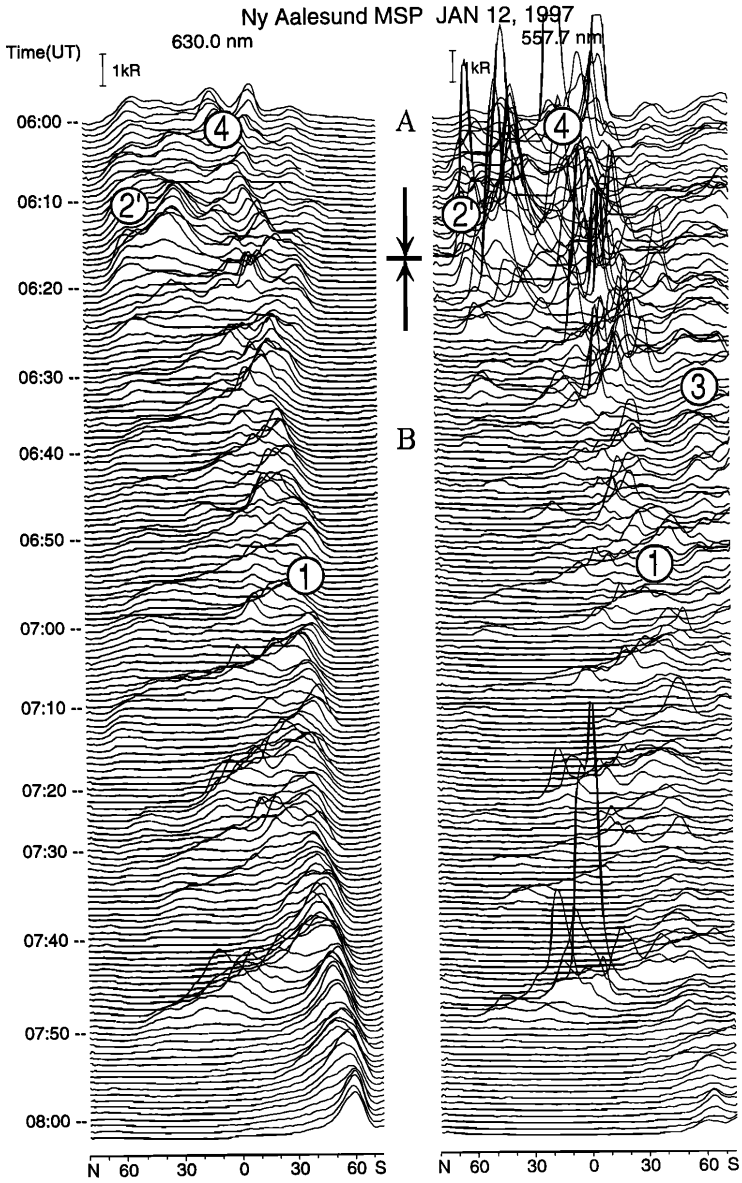

Figure 2.7: Poleward-moving auroral forms (labeled ①) as seen in meridian-scanning photometer measurements. The primary axis shows the zenith angle of the intensity measurements. The data clearly show the poleward motion and repetition of the PMAFs in both 630.0 nm and 557.7 nm emissions. [From *Sandholt et al.*, 1998]

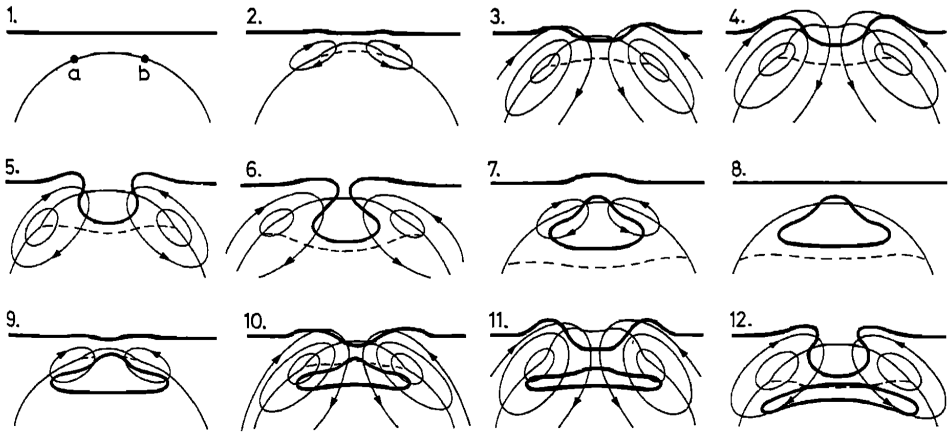

Figure 2.8: An illustration showing how plasma is drawn into the polar cap and segmented into discrete patches due to transient magnetopause reconnection. [From *Lockwood and Carlson*, 1992]

illustrated in Figure 2.8. Patches usually have densities of 2–10 times the background density, and drift across the polar cap with speeds of 250–1000 $\mathrm{m\,s^{-1}}$ [*Buchau et al.*, 1983; *Anderson et al.*, 1988; *De Franceschi et al.*, 2008], largely consistent with the general convection velocity [*Knudsen*, 1974]. The flow speeds can be highly dynamic and pulsed, and patches can also rotate during their transit of the polar cap [*Barth*, 2009; *Oksavik et al.*, 2010]. Patches exit the polar cap by entering the auroral oval, as seen in Figure 2.9. Due to dissociative recombination within the patch, they are visible as regions of enhanced airglow at 630.0 nm [*Weber et al.*, 1986; *Lorentzen et al.*, 2004; *Hosokawa et al.*, 2011].

2.2.5 Tongues of ionization

If high-density plasma is drawn into the polar cap but segmentation does not happen, a continuous tongue of ionization (TOI) is created rather than discrete patches. A TOI is an elongated area of high-density F region plasma stretching across the polar cap from the dayside cusp region toward the nightside auroral oval. The source of TOIs is the same as that of polar cap patches, possibly enhanced by the storm enhanced density (SED), which is a plume of ionization stretching from the sub-auroral dusk sector toward noon during major geomagnetic disturbances [e.g., *Sato*, 1959; *Knudsen*, 1974; *Foster et al.*, 2005; *Thomas et al.*, 2013; *David et al.*, 2016]. Figure 2.10 shows a TOI stretching across the polar cap.

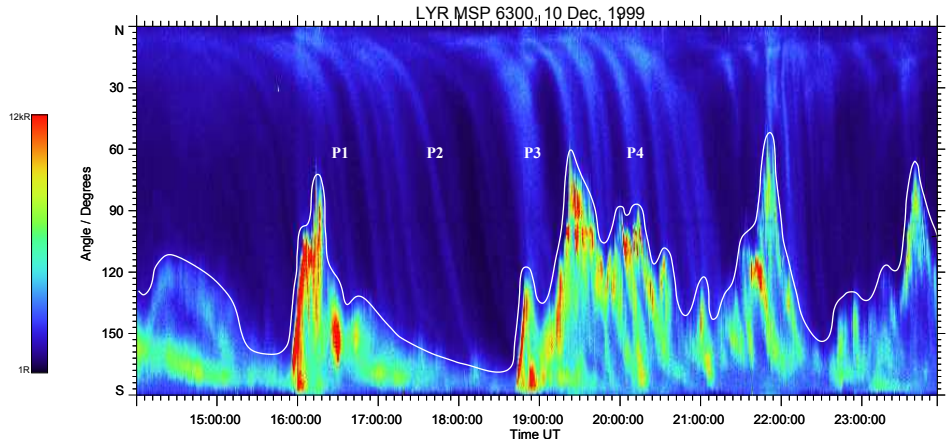

Figure 2.9: Meridian-scanning photometer data showing several polar cap patches (the waterfall-like features, like those labeled P1 through P4) drifting southwards from the polar cap into the auroral oval. [From *Lorentzen et al.*, 2004]

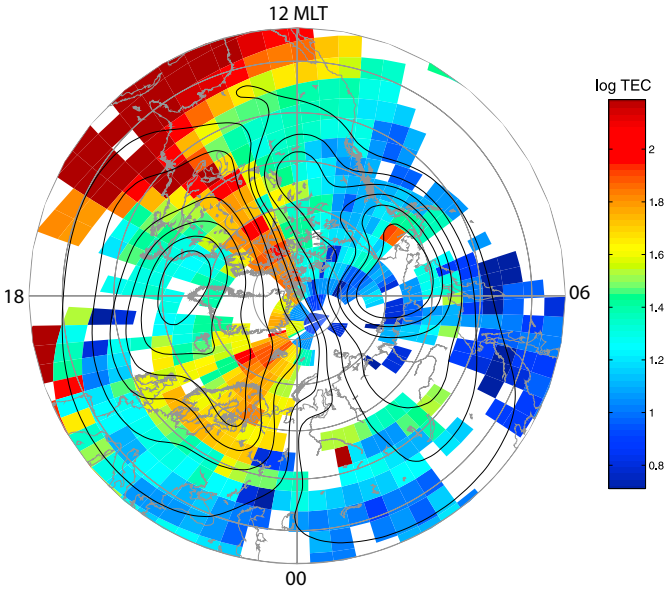

Figure 2.10: A TOI extending from the postnoon sunlit ionosphere and across the polar cap. [Adapted from *Foster et al.*, 2005]

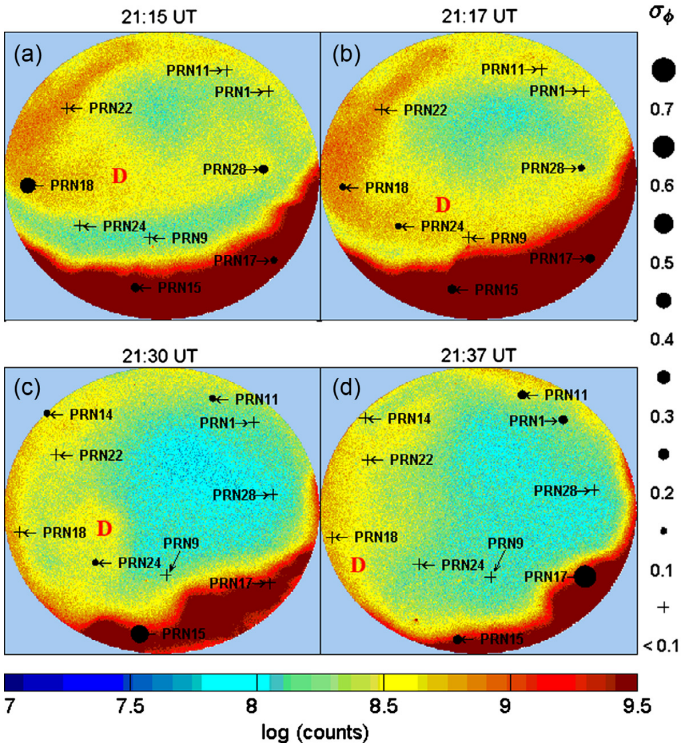

Figure 2.11: A sequence of all-sky images showing a polar cap patch (upper, orange part of panels (a) and (b)) drifting southward (downwards) and entering the active nightside aurora (lower, red part of the images) to become an auroral blob (not directly visible in the images due to the aurora). [Adapted from *Jin et al.*, 2014]

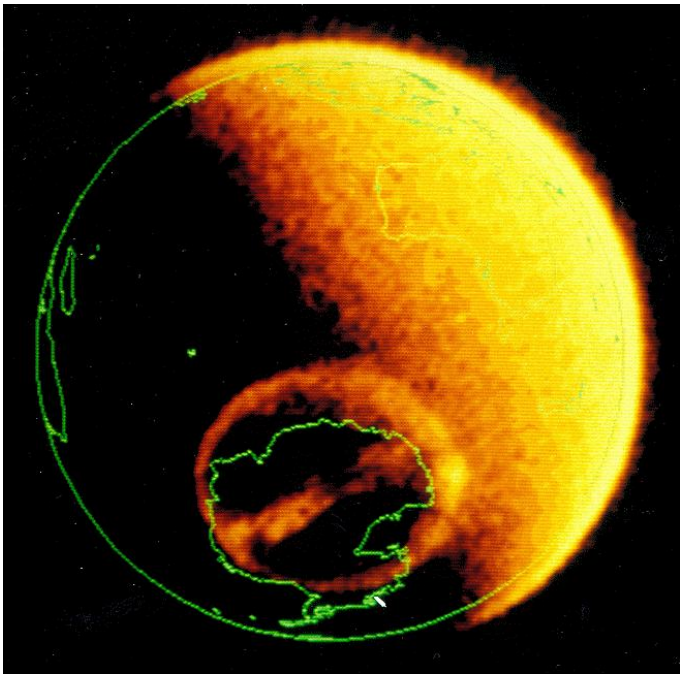

Figure 2.12: Theta aurora over Antarctica on 11 May 1983. Image credit: Dynamics Explorer-1 / University of Iowa

2.2.6 Auroral blobs

When polar cap patches enter the auroral oval, they become auroral blobs [*Tsunoda*, 1988; *Robinson et al.*, 1985; *Crowley et al.*, 2000; *Lorentzen et al.*, 2004; *Pryse et al.*, 2006; *Moen et al.*, 2007; *Jin et al.*, 2014, 2016]. Early literature refers to several types of auroral blobs, namely, boundary blobs, subauroral blobs, and auroral blobs [e.g., *Tsunoda*, 1988; *Crowley et al.*, 2000]. Recent studies have been focused on finding the effects of auroral blobs on transionospheric signal links, and use the term auroral blobs to refer to polar cap patches that have entered the auroral oval [*Jin et al.*, 2014, 2016; *van der Meeren et al.*, 2015; *Clausen et al.*, 2016]. An example of a patch entering the nightside auroral oval to become an auroral blob is shown in Figure 2.11.

2.2.7 Polar cap arcs

During quiet geomagnetic conditions and northward IMF, optical arcs may appear poleward of the auroral oval [*Mawson*, 1916; *Davis*, 1963; *Berkey et al.*, 1976; *Gussenhoven*, 1982; *Cumnock et al.*, 1995, 1997, 2002; *Cumnock and Blomberg*, 2004; *Kullen*, 2012]. There are several names for different types of polar cap arcs, although the naming is not entirely consistent in literature. The term “polar cap arc” and “high-latitude arc” usually refers to any type of aurora inside the polar cap [*Fear and Milan*, 2012a, b; *Carlson*,

1994; *Newell et al.*, 2009]. Such auroral features may be sun-aligned and stretch across most of the polar cap, and can in these cases be called "sun-aligned arcs" or "transpolar arcs". If they connect the dayside and nightside auroral oval, they are often called "theta aurora" due to the similarity of the entire auroral oval to the Greek letter Θ. Figure 2.12 shows an early example of theta aurora. In this thesis we will use the term "polar cap arc".

2.3 Plasma instability mechanisms

The high-density plasma associated with large-scale ionospheric features such as patches may be further structured on scale sizes down to tens of meters [*Buchau et al.*, 1985; *Basu et al.*, 1998; *Carlson et al.*, 2008; *Oksavik et al.*, 2011, 2012; *Moen et al.*, 2012]. Several mechanisms exist for structuring the plasma at smaller scale sizes [e.g., *Keskinen and Ossakow*, 1983; *Tsunoda*, 1988, and references therein]. In particular, two different mechanisms are believed to dominate F region irregularity production [*Oksavik et al.*, 2012; *Carlson et al.*, 2007]: The gradient drift instability (or $\mathbf{E} \times \mathbf{B}$ instability) and the Kelvin-Helmholtz instability.

2.3.1 The gradient drift instability

The gradient drift instability (GDI) [e.g., *Linson and Workman*, 1970, and references therein] occurs when the plasma drift and the plasma density gradient have parallel components. Under some approximations [*Huba et al.*, 1983; *Keskinen*, 1984; *Tsunoda*, 1988], the growth rate γ_{GDI} for the strong collisional limit (which suffices for this discussion) is

$$\gamma_{\mathrm{GDI}} = \frac{k_y}{k} \frac{\mathbf{k} \cdot \mathbf{V}_0}{kL}, \qquad \omega \ll \nu_{in}, \tag{2.7}$$

where k_y is the wave number of the perturbed quantities along the y direction, $\mathbf{k}$ is the gradient wave vector, $\mathbf{V}_0$ is the slip velocity (the plasma drift relative to the neutral wind), L is the gradient scale length, ω is the plasma frequency, and ν_{in} is the ion-neutral collision frequency. The instability occurs for positive growth rates, i.e., when the plasma drift and density gradient have parallel components. It is most effective on the trailing edge of plasma structures where the components are, ideally, exactly parallel. On leading edges, irregularity formation is hindered by stabilizing polarization electric fields. Figure 2.13 shows how a drifting high-density plasma structure is structured only from the trailing edge, with the leading edge being stable until the structuring has propagated throughout the high-density region.

The gradient drift instability is considered to be the dominant instability mode in the polar cap [e.g., *Ossakow and Chaturvedi*, 1979; *Keskinen and Ossakow*, 1983; *Buchau et al.*, 1985; *Tsunoda*, 1988; *Basu et al.*, 1990, 1998; *Coker et al.*, 2004; *Prikryl et al.*,

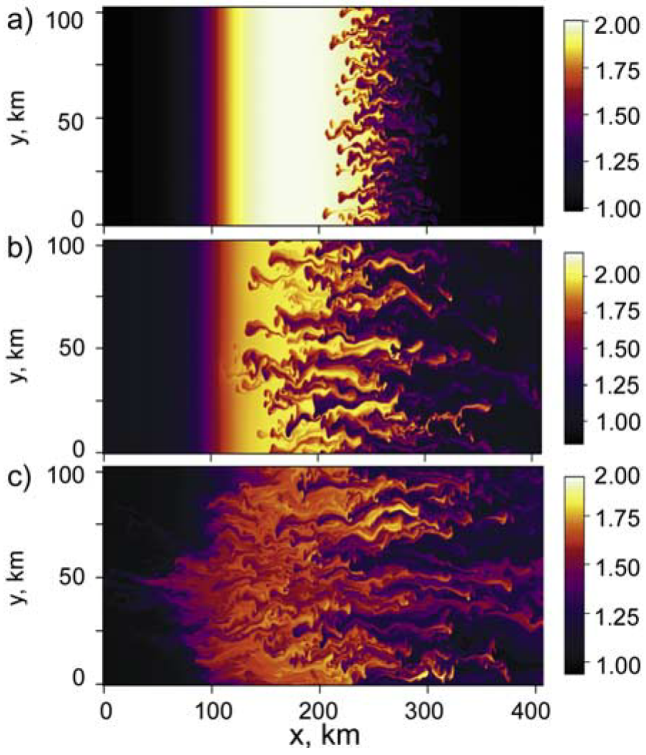

Figure 2.13: A simulation showing how the GDI can structure a polar cap patch starting at the trailing edge. [From *Gondarenko and Guzdar*, 2004b]

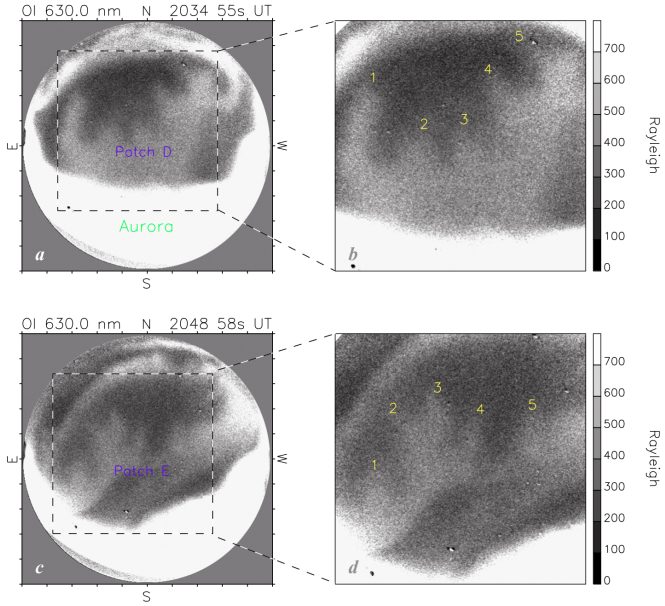

Figure 2.14: The first ever direct optical observations of the finger-like structures at the trailing edges of polar cap patches associated with structuring by the GDI (c.f. Figure 2.13). [From *Hosokawa et al.*, 2016]

2011a; *Basu et al.*, 1994; *Gondarenko and Guzdar*, 2004a]. In particular, polar cap patches may be structured by the gradient drift instability, with the instability starting at the trailing edge of the patch and potentially structuring the whole patch [*Gondarenko and Guzdar*, 2004b; *Hosokawa et al.*, 2016]. Figure 2.14 shows the first ever direct optical observations of the finger-like structures associated with GDI structuring at the trailing edges of patches.

2.3.2 The Kelvin-Helmholtz instability

The Kelvin-Helmholtz instability (KHI) [e.g., *Keskinen et al.*, 1988; *Basu et al.*, 1988b, 1990; *Carlson et al.*, 2007, 2008] is driven by velocity shears transverse to the magnetic field. The KHI is believed to dominate the structuring in the polar cap during northward IMF conditions [*Carlson et al.*, 2008]. The KHI growth rate can be estimated by [*Carlson et al.*, 2008; *Keskinen et al.*, 1988]

$$\gamma_{\mathrm{KHI}} = \frac{0.2\Delta V}{L}, \tag{2.8}$$

where ΔV is the velocity difference and L is the scale length of that difference. Figure 2.15 shows hos a plasma gradient is structured by a velocity shear due to the KHI.

The KHI is believed to be important for the initial structuring of patches. *Moen et al.*

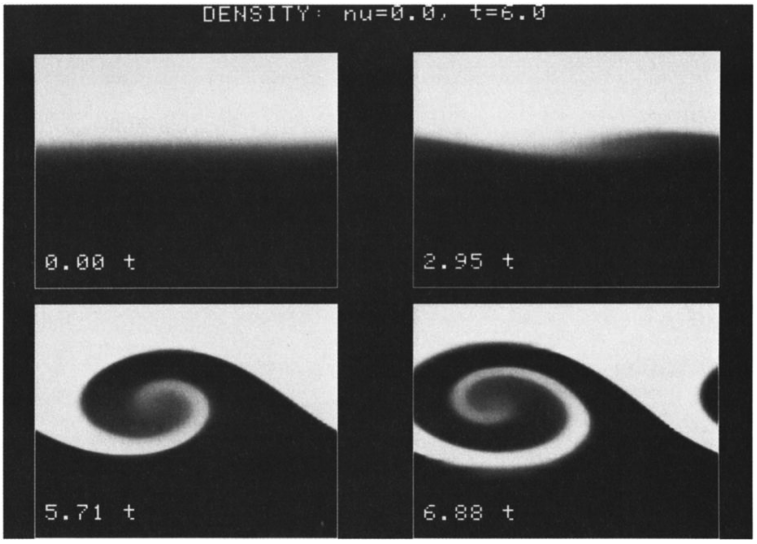

Figure 2.15: Simulation showing how a velocity shear creates structuring on a density gradient due to the KHI. [From *Keskinen et al.*, 1988]

[2002] found that the estimated GDI growth rates were too slow to explain the observed irregularity growth. *Carlson et al.* [2007, 2008] arrived at a new mechanism: Polar cap patches are initially structured in the cusp intake region by strong velocity shears and the KHI, which provides the GDI with a rich spectrum of existing structure on which to work as the patch transits the polar cap.

2.4 Open questions

We have now explained the different phenomena we study in this thesis. We refer to the individual papers for the state of knowledge relevant to each study. In this section we highlight the most relevant open questions driving the studies.

Are continuous TOIs in the nightside polar cap structured? Polar cap patches are structured down to scale sizes of tens of meters [*Buchau et al.*, 1985; *Basu et al.*, 1998; *Carlson et al.*, 2008; *Oksavik et al.*, 2011, 2012; *Moen et al.*, 2012]. In particular, there is evidence that patches are segmented and structured by the KHI in the cusp region, and are further structured by the GDI in the polar cap [*Carlson et al.*, 2006, 2007]. But what happens for continuous TOIs? Even though the plasma source and density is similar to that of polar cap patches, it is not segmented in the cusp region, meaning that the KHI, which is due to velocity shears associated with the patch segmentation, may not perform a similar initial structuring of a TOI. A possible lack of significant internal structure also means that the GDI may not have any trailing edges from which

to effectively develop smaller-scale irregularities. On the other hand, TOIs are regions of steep density gradients where strong irregularities generally may be present.

Which specific phenomena are associated with plasma structuring in the dayside auroral region? Several statistical studies have investigated structuring in the dayside region [e.g., *Spogli et al.*, 2009; *Li et al.*, 2010; *Alfonsi et al.*, 2011; *Prikryl et al.*, 2011b; *Tiwari et al.*, 2012; *Jin et al.*, 2015]. A few case studies have investigated the larger spatial scales and the stable cusp aurora [*Basu et al.*, 1998; *Prikryl et al.*, 2011c]. However, the dayside aurora is associated with intense and highly transient phenomena like PMAFs. No studies have investigated plasma structuring in relation to specific dayside auroral phenomena.

What causes the most severe structuring in the nightside auroral ionosphere? Several studies have shown a link between disturbances on transionospheric signal links (from ionospheric plasma structuring) and auroral emissions [e.g., *Aarons et al.*, 2000; *Spogli et al.*, 2009; *Kinrade et al.*, 2013; *Hosokawa et al.*, 2014]. However, the nightside ionosphere is associated with other features like polar cap patches, which exit the polar cap to become auroral blobs. The first study that specifically set out to shed light on which features caused the most significant structuring in the nightside auroral ionosphere was *Jin et al.* [2014]. That was a case study of a single night, and more studies were needed to further investigate the topic.

Are polar cap arcs regions of irregularity development in the quiet-time polar cap? Quiet, northward IMF conditions are much less studied than active, southward IMF conditions. Polar cap arcs are a prominent feature of the quiet-time polar cap [e.g., *Carlson*, 1994, and references therein], known to be associated with flow shears [e.g., *Carlson and Cowley*, 2005; *Eriksson et al.*, 2006; *Zou et al.*, 2015]. Since the KHI is driven by flow shears, it is possible that polar cap arcs in the quiet-time polar cap are associated with plasma structuring, as suggested by *Moen et al.* [2013].

These topics will be investigated in Papers I–IV in this thesis. First we will describe the instruments used to carry out the research.

Chapter 3

Instrumentation

In this chapter we briefly present the instruments used in this thesis. For more details, we refer to the individual studies. In addition to the instruments themselves, Section 3.9 covers how global navigation satellite system (GNSS) receivers are used for detecting ionospheric irregularities.

3.1 Ground-based optics

All four papers make extensive use of ground-based optical data from all-sky imagers (ASI) in Svalbard operated by the University of Oslo. The ASIs are located in Ny-Ålesund and in Longyearbyen. Both imagers use interference filters to measure ionospheric emissions at 557.7 nm (green) and 630.0 nm (red) at a cadence of 15 s and 30 s, respectively. While the imager locations are the same across all four studies, the imagers themselves were upgraded during the periods studied. This is the reason that the ASI data are sometimes calibrated (given in kR), and sometimes not (given in raw sensor counts).

After Paper III was published, the University of Oslo announced a calibration error for the Longyearbyen ASI used in that study. Specifically, the green channel values should be twice as high as they were in that study. This does not impact the conclusions of Paper III.

In addition to ASIs, Papers II and III use meridian-scanning photometer (MSP) data. The MSP is located in Longyearbyen and is operated by the University Centre in Svalbard. It uses a rotating mirror to scan from horizon to horizon along the magnetic meridian, measuring a full scan of 557.7 nm and 630.0 nm emissions at a 16 s cadence.

3.2 Coherent scatter radars

The Super Dual Auroral Radar Network (SuperDARN) is a network of coherent scatter radars in both hemispheres. The radars transmit and receive high-frequency (HF) sig-

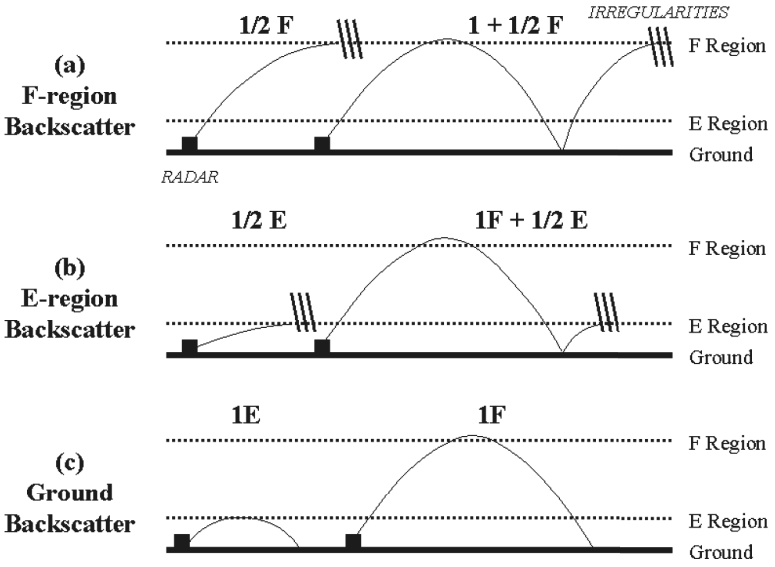

Figure 3.1: Illustration of the different types of SuperDARN signals propagation. Irregularities are marked by field-aligned slashes. (a) *F* region direct (half-jump) and indirect (1.5-jump) backscatter. (b) *E* region backscatter. (c) Ground backscatter. [*Chisham and Pinnock*, 2002]

nals, which refract in the ionosphere and experience Bragg scattering from field-aligned decameter-scale irregularities, causing the signals to be reflected (backscattered) back along the same raypath [*Greenwald et al.*, 1995]. The refraction needed for the signals to become field-orthogonal in order to backscatter normally occurs in the *F* region, although during periods of intense auroral precipitation, densities may also become sufficiently high to make the signal backscatter in the *E* region as well [*Greenwald et al.*, 1995; *Chisham et al.*, 2007, and references therein]. The different kinds of signal propagation are illustrated in Figure 3.1. The network was designed primarily to study the convection of ionospheric plasma, but has been very successful in studying a wider range of ionospheric and magnetospheric phenomena [*Chisham et al.*, 2007].

The radars have 16 or more antennae transmitting and receiving signals in the 8–20 MHz range. The field of view of each radar typically covers $\sim 52°$ in azimuth and extends from ~ 200 km to over 3000 km in range, jumping between the ionosphere and the ground multiple times. The range gate separation is typically 45 km and the time to complete a full scan is typically 1–2 min [*Chisham et al.*, 2008].

The studies in this thesis use the SuperDARN radars to study both the ionospheric convection pattern and detailed line of sight parameters from single radars. Ground backscatter is flagged by the raw data processing based on low line of sight Doppler velocity and spectral width [*Chisham and Pinnock*, 2002] and is omitted from our studies. Note that weak or absent backscatter may be due to noise, absorption, or unfavorable

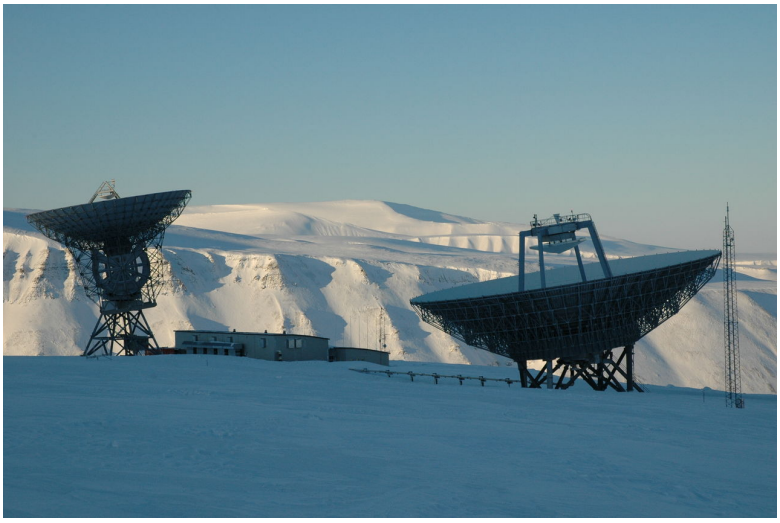

Figure 3.2: The steerable (left) and fixed (right) antennae of the EISCAT Svalbard Radar. (Photo: Tom Grydeland)

raypath geometry for the region in question. Thus, lack of backscatter is not an unambiguous indicator of lack of decameter-scale field-aligned irregularities.

3.3 Incoherent scatter radars

In Paper I we use data from the EISCAT Svalbard Radar (Figure 3.2), which is an incoherent scatter radar located in Longyearbyen. The radar consists of a 32 m fully steerable antenna and a 42 m fixed, field-aligned antenna (81.6° elevation, 182.1° azimuth).

Incoherent scatter radars measure weak scattering of radio signals due to density fluctuations from ion-acoustic and Langmuir waves the ionosphere. From parameters such as the Doppler shift, Doppler broadening, and dampening of the scattered signal, it is possible to extract information on e.g. electron density, ion and electron temperature, and line of sight ion drift velocity. Data from this radar is only briefly used in Paper I, and a thorough description of how coherent scatter radars work will not be provided here; we refer the reader instead to the literature [*Alcaydé*, 1995; *Nygrén*, 1996; *Lehtinen and Huuskonen*, 1996; *Wannberg et al.*, 1997].

3.4 Satellite measurements of the solar wind

All four studies use solar wind and IMF data. The data come from the Wind spacecraft located upstream in the solar wind. The specific location varies across the studies, and we refer the reader to the respective instrumentation sections for details. The IMF data

(the B_x, B_y, and B_z components) come from the Magnetic Field Investigation instrument [*Lepping et al.*, 1995], and the solar wind parameters (speed, density, etc.) come from the Solar Wind Experiment instrument [*Ogilvie et al.*, 1995]. The solar wind and IMF data in all four studies are provided by the NASA OmniWeb service, which automatically timeshifts the data from its upstream location to the magnetospheric bow shock. This timeshift is suffucient for our purposes, since the data are only used as a indicator of the solar wind conditions around the intervals under study.

3.5 Ionosonde

Papers III and IV make use of data from an ionosonde located in Longyearbyen (similar to the Tromsø dynasonde detailed in *Rietveld et al.* [2008]). The ionosonde works by transmitting signals at various frequencies into the ionosphere. When the signals reaches a region of the ionosphere where the plasma frequency is equal to the signal frequency, the signal reflects back to the ionosonde. Since the plasma density is a simple function of the plasma frequency (see Section 2.1), combining the time-of-flight information from several signals at different frequencies allows the determination of the altitude profile of the ionospheric plasma density above the ionosonde, up to the altitude of peak ionospheric density.

3.6 Magnetometer

In the Supporting Information of Paper III we use magnetometer data to indicate the development of the substorm. We show the horizontal component of the magnetic field, which during substorm activity is enhanced by the auroral electrojets. The magnetometer we use is located on Bjørnøya and is operated by Tromsø Geophysical Observatory, UiT The Arctic University of Norway.[1]

3.7 DMSP UV and particle data

Paper IV makes use of in situ particle and remote sensing optical data from several Defense Meteorological Satellite Program (DMSP) satellites. These satellites are in polar, sun-synchronous orbits at a nominal altitude of 840 km. The particle data come from the SSJ/4 detectors, which point toward zenith and measure precipitating electrons and ions between 30 eV and 30 keV [*Hardy et al.*, 1984]. The optical data come from the SSUSI instrument, which observes UV emissions at several wavelengths [*Paxton et al.*, 1992]. In our study we use 140–150 nm (Lyman-Birge-Hopfield short).

[1] `http://www.tgo.uit.no`

3.8 GNSS receivers

The GNSS receivers used in Papers II, III, and IV were installed in the Svalbard region in 2013 and are operated by the University of Bergen. The receivers are located in Ny-Ålesund, Longyearbyen, Hopen, and Bjørnøya. All are NovAtel GPStation-6 receivers running the same software. The receivers track GPS, GLONASS, and Galileo on multiple frequencies.

Below we provide the orbits and frequencies of GPS, GLONASS, and Galileo. While the signal plans are more complicated than reflected below, we have only included information that is relevant for the thesis. For details on the specific frequencies used in each study we refer to the respective instrumentation sections in each paper.

GPS

GPS transmits on 1575.42 MHz (L1) and 1227.6 MHz (L2).[2] The satellites orbit at an altitude of 20 200 km with an orbital period of 11 h 58 m. The orbits have an inclination of 55°.[3]

GLONASS

Each GLONASS satellite transmit on a different frequency around common center frequencies. The center frequencies are 1602 MHz (L1) and 1246 MHz (L2).[4] The satellites orbit at an altitude of 19 100 km with an orbital period of 11 h 15 m. The orbits have an inclination of 64.8°.[5]

Galileo

The Galileo satellites transmit on 1575.42 MHz (L1, also called E1) and 1191.795 MHz (E5).[6] The satellites orbit at an altitude of 23 222 km with an orbital period of 14 h 7 m. The orbits have an inclination of 56°.[7]

[2]ESA Navipedia: *GPS Signal Plan*, retrieved 2016-04-07. `http://navipedia.net/index.php/GPS_Signal_Plan`

[3]ESA Navipedia: *GPS Space Segment*, retrieved 2016-04-07. `http://navipedia.net/index.php/GPS_Space_Segment`

[4]ESA Navipedia: *GLONASS Signal Plan*, retrieved 2016-04-07. `http://navipedia.net/index.php/GLONASS_Signal_Plan`

[5]ESA Navipedia: *GLONASS Space Segment*, retrieved 2016-04-07. `http://navipedia.net/index.php/GLONASS_Space_Segment`

[6]ESA Navipedia: *Galileo Signal Plan*, retrieved 2016-04-07. `http://navipedia.net/index.php/Galileo_Signal_Plan`

[7]ESA Navipedia: *Galileo Space Segment*, retrieved 2016-04-07. `http://navipedia.net/index.php/Galileo_Space_Segment`

3.9 GNSS for ionospheric research

In this section we detail how GNSS systems are used for ionospheric research as a remote sensing technique.

GNSS data are increasingly fused with other data products to get data on ionospheric, magnetospheric, and other space weather phenomena with enhanced fidelity [e.g., *Morley et al.*, 2016; *Semeter et al.*, 2016]. However, the prevalent usage of GNSS data has long been centered around using dual frequency receivers to get a measure of the total plasma density along the signal path (called the total electron content) and using variations in the signal amplitude and phase (called scintillations) to get information on irregularities in the plasma density along the signal path. We will now briefly explain the basis for these two techniques.

3.9.1 Total electron content

Background

For a full mathematical derivation of radio wave propagation through plasma, we refer to *Kintner and Ledvina* [2005]. Salient points are highlighted below.

When a signal propagates through a plasma, the group velocity is reduced. The delay δt due to the ionosphere can be expressed in SI units as

$$\delta t = \frac{40.3}{cf^2} \int_{\rho^*} N_e \, \mathrm{d}\rho, \tag{3.1}$$

where c is the speed of light, f is the signal frequency, ρ^* is the signal path through the ionosphere, and N_e is the electron density. The integral is defined as the total electron content (TEC):

$$\mathrm{TEC} := \int_{\rho^*} N_e \, \mathrm{d}\rho \tag{3.2}$$

This is the number of electrons found in a $1\,\mathrm{m}^2$ column along the signal path from the receiver to the satellite, usually expressed in TEC units (TECU) where $1\,\mathrm{TECU} = 10^{16}\,\mathrm{electrons}/\mathrm{m}^2$.

Since the delay depends on the signal frequency, dual-frequency receivers can compare the delay of the two signals to compute the TEC.

Calibration of TEC

The delay of the signal from which TEC is calculated is influenced by a combination of factors such as the TEC along the signal path and biases intrinsic to the satellites and receivers. Satellite biases are available online and are fairly constant from day to day. However, receiver biases can vary significantly over intervals down to hours due to various factors like indoor/outdoor temperature and solar radio flux [*Coster et al.*, 2013],

making such estimations highly non-trivial [e.g., *Montenbruck et al.*, 2014; *Themens et al.*, 2015; *Xue et al.*, 2016].

In our studies the TEC has been calibrated in a simpler fashion. Based on one week of data, the following procedure is used:

1. Any data points where S_4 or σ_ϕ (see definition in Section 3.9.2) exceeds 0.2 are removed.

2. Any data points from problematic lines of sight (elevation and azimuth) are removed. Problematic lines of sight have been separately identified by analyzing more than one year of data for each receiver and identifying which elevation/azimuth combinations give consistently high levels of amplitude scintillation independent of geomagnetic activity (which is an indication of multipath, to be detailed later).

3. We use vertical TEC (detailed below) from a properly calibrated receiver located in Ny-Ålesund, operated by the University of Oslo. For each satellite/signal combination in our own receivers, we identify piercing points that are closely located (within 200 km) to piercing points in the calibrated receiver. The piercing points are mapped to an altitude of 300 km.

4. We compute the average and standard deviation of the correction for the whole week that is needed to be applied to each uncalibrated receiver-satellite pair. The average correction is then applied to the raw TEC data before being used in the analysis.

This simple method has proven to yield usable results. For example, most satellites show the same vertical TEC across a homogeneous region of the sky (as determined from radar data or all-sky images). The results are sufficiently accurate when we are concerned primarily with the relative TEC differences between satellites or the development of TEC over time for a single satellite, rather than the absolute magnitude of TEC.

Slant and vertical TEC

The signal path is generally not vertical, and will thus measure a slant section of the ionosphere. This is especially pronounced at low elevation angles. Normally, the slant TEC (STEC) is mapped to vertical TEC (VTEC) such that signals from different elevation angles can be directly compared. If we assume that the ionosphere is located in a thin layer at an altitude h, we can use geometrical considerations to obtain a mapping formula. According to Figure 3.3 we have

$$\frac{\text{VTEC}}{\text{STEC}} = \cos z', \tag{3.3}$$

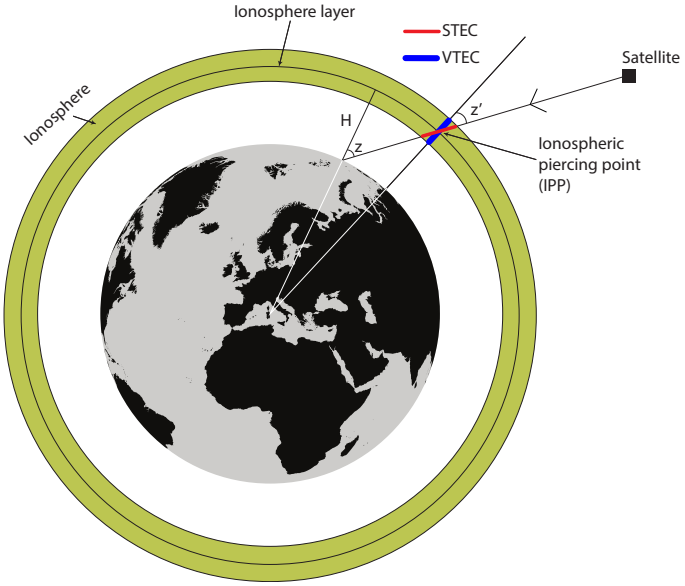

Figure 3.3: Illustration of STEC to VTEC mapping. The receiver measures STEC (red, thick line segment), but in many applications, we are interested in VTEC (blue, thick line segment).

where z' is the satellite's zenith angle observed from the ionospheric layer. This is related to the receiver-based zenith angle z by the equation

$$\sin z' = \frac{R_E}{R_E + H} \sin z. \tag{3.4}$$

Inserting Equation 3.4 into Equation 3.3 and using $\cos(\sin^{-1} x) = \sqrt{1 - x^2}$, we get

$$\text{VTEC} = \text{STEC} \times \sqrt{1 - \left(\frac{R_E}{R_E + H} \sin z \right)^2}. \tag{3.5}$$

Since the real ionosphere is not a thin layer, the projected VTEC may not give an accurate picture of the actual vertical electron content at the ionospheric piercing point. This is illustrated in Figure 3.4.

3.9.2 Scintillation

Scintillations are rapid variations in the amplitude or phase of a radio signal (called amplitude and phase scintillations, respectively) and are one of the first known effects of space weather [*Hey et al.*, 1946]. Below we will give a brief overview of how ionospheric scintillation occurs. For a detailed review, the reader is referred to *Bhattacharyya et al.* [1992] or *Kintner et al.* [2007].

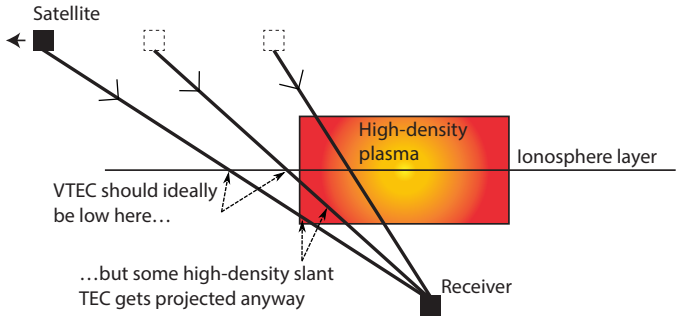

Figure 3.4: Illustration of a problem with VTEC mapping. Since the ionosphere has a nonzero thickness, the mapping may not accurately reflect the actual VTEC at the projected location. As seen on this illustration, VTEC may show a much more gradual change even when the plasma density changes suddenly.

Scintillation may occur due to diffraction or refraction. In the diffractive case, a wave passes through an irregular medium with many small changes in the index of refraction, and an incoming plane wave will exit the medium with irregular phase and interfere in the receiver. In the refractive case, the phase velocity is increased or decreased in the medium, and a plane wave will remain plane, but the phase observed by the receiver will change.

The phase screen approximation

The phase screen approximation was an early model used to study the effects of the ionosphere on radio waves [*Booker et al.*, 1950; *Hewish*, 1951; *Beach*, 1998]. The ionosphere is essentially treated as an infinitely thin layer, so that all its effects on the waves are modeled as abrupt phase changes in this layer, and the rest of the propagation to the receiver is through a homogeneous medium. For a more thorough mathematical description, we refer to *Kintner et al.* [2007] and references therein. Key points are summarized below. Also note that this is not the only scintillation model; for a comparison between different models, we refer to *Strangeways et al.* [2014].

Under the assumption of single, forward scattering and irregularity scale sizes larger than the wavelength of the radio wave, the wave propagation in the irregular medium is represented by the scalar Helmholtz equation.

$$\nabla^2 A + k^2[1 + \varepsilon_1(\mathbf{r}')]A = 0 \tag{3.6}$$

Here A is the complex amplitude of the electric field, ε_1 is the deviation from free-space permittivity, k is the wave number of the signal, and $\mathbf{r}'$ describes the location of the irregularities. Assuming small permittivity fluctuations, a plane wave, and irregularity

scales much larger than the Fresnel radius[8], one solution is [*Beach*, 1998, Equation (4.26)]

$$A(r) = -\frac{e^{ik(r+R)}}{4\pi(r+R)}\left(1+\frac{ik}{2}\int_{-L/2}^{L/2}\varepsilon_1(0,0,z')\,dz'\right), \tag{3.7}$$

where R is the distance between the transmitter and the irregularities, r is the distance between the receiver and the irregularities, k is the signal wave number, the z' direction is along the ray path, and L is the thickness of the irregularity layer. Thus, the effect of irregularities on radio waves is a function of the integral of the permittivity fluctuations along the ray path. By performing the phase screen approximation $L = 0$, wherein we assume that the irregular medium's effects on the radio wave is limited to an infinitely thin layer (the phase screen), the integral vanishes and we are left only with the first term. In the model's simplest form [e.g., *Beach*, 1998; *Wernik et al.*, 2003], the phase screen induces only phase perturbations on the incident radio wave, and as the wave propagates these perturbations evolve to produce amplitude and phase scintillations.

Note that the solution is dependent on the wave number, i.e. the signal frequency. Thus two signals with different frequencies will be affected differently by the same irregularities.

Amplitude scintillations and the S_4 index

Amplitude scintillations at L band frequencies are caused by irregularities with scale sizes from tens of meters to hundreds of meters, at and below the Fresnel radius [e.g., *Basu et al.*, 1998; *Kintner et al.*, 2007]. They are commonly quantified by the S_4 index, which is the standard deviation of the signal intensity normalized by its mean value [*Briggs and Parkin*, 1963]:

$$\mathrm{S}_4 = \sqrt{\frac{\langle I^2\rangle - \langle I\rangle^2}{\langle I\rangle^2}}, \tag{3.8}$$

Here $I = A^*A$ (where A is the complex amplitude of the electric field), and the brackets indicate ensemble averaging, in practice approximated by temporal averaging (normally over 60 s). In the phase screen model, S_4 is zero immediately after the phase screen, and as the wave front propagates toward ground the signal interferes, causing amplitude scintillation.

Phase scintillations and the σ_ϕ index

Phase scintillations at L band frequencies are caused by irregularities of scale size hundreds of meters to a few kilometers, above the Fresnel radius [e.g., *Basu et al.*, 1998; *Kintner et al.*, 2007]. The GPS signal phase deviation produced during transit of the

[8]The Fresnel radius is ~ 365 m for L1 signals assuming an irregularity layer mean altitude of 350 km and a signal path elevation of 90° [*Kintner et al.*, 2007].

ionosphere in SI units is [*Kintner et al.*, 2007, Equation (7)]

$$\phi = \frac{40.3}{cf}\text{TEC}, \tag{3.9}$$

where TEC is given as in Equation 3.2. This may also be written as $\phi = f\delta t$ where δt is the ionospheric delay given by Equation 3.1. The most common phase scintillation index is called σ_ϕ and is the standard deviation of the detrended phase ϕ in radians,

$$\sigma_\phi = \langle \phi^2 \rangle - \langle \phi \rangle^2, \tag{3.10}$$

normally computed over a period of 60 s after detrending the phase using a sixth-order Butterworth filter with a cutoff frequency of 0.1 Hz [e.g., *Mitchell et al.*, 2005; *Béniguel et al.*, 2009; *Li et al.*, 2010; *Alfonsi et al.*, 2011; *Forte et al.*, 2011; *Garner et al.*, 2011; *Gwal and Jain*, 2011; *Kinrade et al.*, 2012; *Jiao et al.*, 2013; *Jin et al.*, 2014].

Sensitivity to cutoff frequency The σ_ϕ index has been shown to be problematic. Specifically, σ_ϕ is highly sensitive to larger-scale (lower-frequency) phase variations not pertaining to scintillations, such as TEC gradients on the edges of large-scale plasma structures [e.g., *Basu et al.*, 1991; *Mushini et al.*, 2012], leading to an overestimation of σ_ϕ at high latitudes due to true scintillations being mixed with such TEC gradients [*Forte*, 2005]. The sensitivity of σ_ϕ to larger-scale phase variations means that it is highly sensitive to the cutoff frequency of the detrending filter [e.g., *Forte and Radicella*, 2002].

Geometric effects on scintillation

Scintillation is influenced by factors involving the receiver-satellite geometry relative to the ionosphere and local features around the receiver. The effects are described in the following paragraphs.

Irregularity anisotropy Due to ionospheric irregularities predominantly being field-aligned, scintillation peaks on signals that are close to field-aligned [e.g., *Kersley et al.*, 1988]. At high latitudes however, this is mainly a problem for satellites in polar orbits. *Forte and Radicella* [2004] studied geometrical control of scintillation on GPS satellites and found that this was not a significant issue at high latitudes. It is conceivable that the effect is more pronounced on GLONASS satellites due to the higher inclination of their orbits, but this has not been studied. In our case studies the increases in scintillation corresponds to observed features in other data such as patches and aurora in all-sky images. Furthermore, there is no significant difference in scintillation across the different constellations. Thus the geometrical effect is most likely irrelevant in our studies.

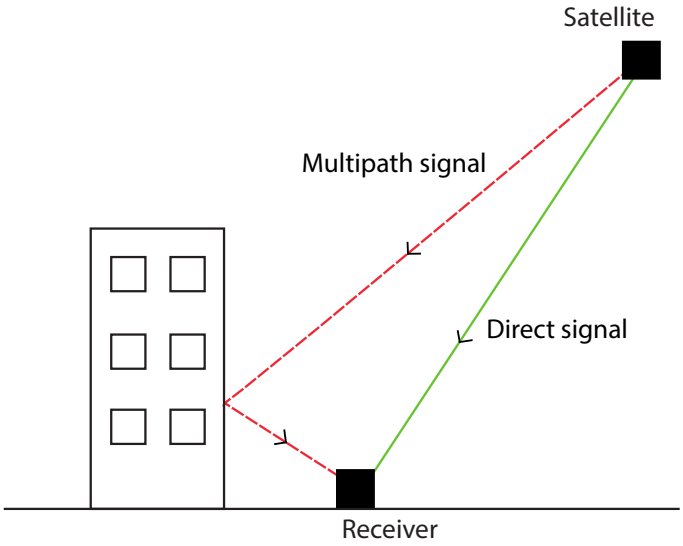

Figure 3.5: Illustration of multipath. A reflected signal combines with the direct signal in the receiver. This creates interference, resulting in variations in the observed amplitude.

Multipath GNSS signals may be disturbed by mountains or buildings around the receiver, as illustrated in Figure 3.5. Signals may be reflected off a surface toward the receiver and interfere with the direct line of sight signal. This is called multipath. Multipath-induced scintillation due to stationary objects will repeat at set intervals based on the orbit of the satellite. In our studies, our data has been filtered to avoid multipath. For each of the receivers used in the studies, we have identified which elevation and azimuth angles give consistently high levels of scintillation regardless of magnetic activity. Signals from these areas have been discarded.

Chapter 4

Description of papers

To address the overarching question of how various high-latitude ionospheric phenomena are related to scintillation-inducing irregularities, we have performed four multi-instrument case studies. They investigate scintillation and irregularities in relation to four different ionospheric phenomena in unprecedented detail and have provided new insights into which phenomena cause irregularities and scintillation, and where in relation to these phenomena the irregularities and structures are present. We will now provide a brief description of each of the four studies. Further results are presented and discussed in Chapter 5. For details we refer to the individual papers.

Paper I: GPS scintillation and irregularities at the front of an ionization tongue in the nightside polar ionosphere

In Paper I we study scintillation and irregularities on the front of a TOI in the polar cap, which has not previously been done in the literature. We employ a novel technique where spectrograms of the raw phase are used to obtain information on irregularity scale sizes and the relative strength between different irregularity events and between different irregularity scales. We found moderate scintillation on the leading edge of the TOI.

Paper II: Scintillation and loss of signal lock from poleward moving auroral forms in the cusp ionosphere

Paper II focuses on PMAFs. We used optical and GNSS data (including spectrograms of raw phase as well as high-resolution scintillation indices) to show that two PMAFs in the dayside cusp region were associated with stronger 100 m to km scale irregularities than the surrounding cusp ionosphere, including two polar cap patches. The strong phase scintillation we observed was highly localized to the PMAFs, even though several polar cap patches were observed nearby. This suggests that particle precipitation in a bright PMAF is an important source of plasma irregularities in the cusp ionosphere. In Paper II we also further developed the method of the phase spectrograms by intro-

ducing wavelets. This allows increased resolution at smaller scales and does not require detrending of the raw data.

Paper III: Severe and localized GNSS scintillation at the poleward edge of the nightside auroral oval during intense substorm aurora

In Paper III we study irregularity development as patches enter the auroral oval during a substorm onset, in order to establish which features produce the strongest scintillation in the auroral and polar ionosphere. The observations showed that the most severe scintillation occurred when intense auroral precipitation coincided with patches, even though the patches were not structured before entry into the auroral oval. The study was also the first to show that GPS, GLONASS, and Galileo are similarly affected by severe scintillation in a highly localized region of the sky.

Paper IV: Scintillation and irregularities from the nightside part of a sun-aligned polar cap arc

In Paper IV, we study irregularities during northward IMF and quiet geomagnetic conditions. Such conditions are much less studied than southward, active conditions, even though northward IMF conditions occur half the time. A recent study by *Moen et al.* [2013] reviewed space weather challenges for the polar cap ionosphere, and suggested that polar cap arcs during northward IMF conditions might create irregularities of concern from a space weather perspective. In Paper IV, we address this by performing a detailed multi-instrument study of irregularities in relation to the nightside part of a polar cap arc. The arc showed significant red and green emissions, and was associated with HF backscatter indicating decameter-scale irregularities. However, GNSS data showed almost no scintillation.

Chapter 5

Discussion of results

Each of the papers address several subtopics related to the overarching question of how different high-latitude ionospheric phenomena are related to plasma structuring and scintillation on GNSS signals. We will now break the question down into separate subtopics and combine results from all papers. Section 5.1 summarizes and discusses various aspects of scintillation, such as the occurrence in relation to various phenomena in the polar regions. In Section 5.2 we discuss different aspects of the underlying irregularities.

5.1 Scintillation occurrence and characteristics

5.1.1 Storm-time tongue of ionization

The TOI [e.g., *Sato*, 1959; *Knudsen*, 1974; *Foster et al.*, 2005] is a dominant feature of the high-density storm-time polar cap. Before Paper I was published in 2014, not much research had been done on scintillation and irregularities in TOIs specifically. A case study performed by *Prikryl et al.* [2013] looked at the whole northern hemisphere, and identified a TOI in global TEC data. Such large spatial scales makes it difficult to discern between a continuous TOI and segmented patches [e.g., *Clausen et al.*, 2016], and the paper makes no distinction between the two phenomena. Another study by *Thomas et al.* [2013] found HF backscatter co-located with the TOI, which implied the presence of decameter-scale irregularities.

Paper I presents the first direct observations of scintillation along the leading edge of a TOI. The phase spectrograms were similar (showing no structuring) in the low-density plasma in front of the TOI and in the high-density plasma inside the TOI. The scintillation was localized to the leading edge. Furthermore, three different locations along the edge were structured differently, from no structuring to structuring down to decameter scale. Figure 5.1 shows the geometry of the ionospheric piercing points in relation to the TOI front.

The scintillation observed in Paper I is not particularly strong. However, while po-

Figure 5.1: ASI data showing the propagation of the TOI front. The pink circles and squares indicate the ionospheric piercing points (IPPs) of the signals from the GPS receivers in Ny-Ålesund and Longyearbyen, respectively. The arrows indicate the location and direction of travel of the IPPs 30 min before and after 19:41 UT. [From Paper I, *van der Meeren et al.*, 2014]

lar cap patches are known to cause scintillation on UHF signals [*Buchau et al.*, 1985; *Basu et al.*, 1988a, 1994; *Kersley et al.*, 1995; *Dandekar and Bullett*, 1999; *Coker et al.*, 2004], research that is published after Paper I indicate that scintillation on *L* band frequencies from patches inside the polar cap is not particularly severe, and that patches do not cause significant scintillation before entering the nightside auroral oval [*Jin et al.*, 2014, 2016; *Clausen et al.*, 2016]. This means that it is likely that the TOI scintillation seen in Paper I is comparable to patch scintillation inside the polar cap. Indeed, our observations of phase scintillation in the range 0.2–0.3 rad is not much weaker than the patch-only phase scintillation reported by *Jin et al.* [2014, 2016].

There has not been significant new research on scintillation from TOIs in the time after Paper I was published. *Prikryl et al.* [2015a] performed a statistical study and found an IMF B_y-controlled asymmetry of scintillation occurrence inside the polar cap that was consistent with the B_y asymmetry of TOI and patches for southward IMF and sun-aligned arcs for northward IMF. However, no clear distinction was made between TOI and patches, and no direct observations were presented. *Cherniak et al.* [2015] and *Cherniak and Zakharenkova* [2015] performed case studies of high-latitude irregularities during a geomagnetic storm, but studied the event at large (hemispheric) scales. They too made no significant distinction between patches and TOI.

In summary, we have shown in Paper I that continuous TOIs can be associated with weak to moderate amounts of scintillation, specifically along the leading edge, even when the high-density plasma just behind the leading edge contains no scintillation. Furthermore, the study showed that the scintillation and structuring can vary significantly along the leading edge. Future studies should be carried out to determine whether the results of Paper I are representative by investigating structuring in relation to several TOI events. Such studies should ideally study TOIs on a case by case basis, since the localization of scintillation could easily be averaged out in statistical studies. Furthermore, it should be investigated whether or not there is a significant difference between scintillation from polar cap patches and continuous TOIs, in light of recent studies which imply that patches in the polar cap might be relatively harmless from an *L* band scintillation perspective [*Clausen et al.*, 2016]. Finally, the mechanism for irregularity development in continuous TOIs should be determined. This could be aided by e.g. sounding rocket measurements, in situ satellites in the ionosphere as well as the regions of the magnetosphere mapping to the relevant ionospheric regions, solar wind data, ionospheric convection measurements, and optical data.

5.1.2 Dayside aurora

The dayside aurora, in particular the cusp region, is known to be associated with scintillation on *L* band frequencies [e.g., *Moen et al.*, 2013; *Prikryl et al.*, 2015a] and irregularities down to decameter scale [*Moen et al.*, 2012; *Oksavik et al.*, 2012]. Prior to Paper II, literature on scintillation in the dayside aurora and the cusp ionosphere was

predominantly statistical in nature [e.g., *Spogli et al.*, 2009; *Li et al.*, 2010; *Alfonsi et al.*, 2011; *Prikryl et al.*, 2011b; *Tiwari et al.*, 2012; *Jin et al.*, 2015]. Some case studies had been conducted [*Basu et al.*, 1998; *Prikryl et al.*, 2011c], focusing on the larger spatial scales and the stable cusp aurora.

PMAFs are a fundamental characteristic of the dayside aurora wherein auroral features become detached from the dayside auroral oval and drift into the polar cap [e.g., *Feldstein and Starkov*, 1967; *Vorobjev et al.*, 1975; *Sandholt et al.*, 1998]. No previous studies have specifically looked at scintillation in relation to PMAFs. *Kinrade et al.* [2012] investigated scintillation over Antarctica during disturbed conditions and found bursts of phase scintillation in the dayside cusp region, which they attributed to "cusp precipitation of some kind". The study did not provide optical data or mention PMAFs. A study by *Jin et al.* [2015], published in the same journal issue as Paper II, investigated cusp aurora and scintillation in a statistical manner. Based on the sign of IMF B_y they found that the asymmetry of scintillation around magnetic noon corresponded to that of PMAFs. However, patches are influenced by B_y in a similar manner as PMAFs, and their study did not differentiate between patches and PMAFs in the cusp region.

Paper II is the first direct observation of scintillation in relation to PMAFs. The study focuses on PMAFs and not the general dayside aurora, which could be a relevant consideration for future studies. Co-location of GNSS receivers and all-sky imagers provides reliable line of sight intensities for each signal path. The study showed that the signals that intersected the PMAFs experienced strong scintillation and in one case also a loss of signal lock, whereas the satellites not intersecting the PMAFs did not experience significant scintillation. This is illustrated in Figure 5.2. Irregularity scale sizes down to 100 m were detected. Furthermore, high-resolution TEC data were employed to detect patches in the vicinity of the PMAFs. The observations showed that the scintillation was localized to the PMAFs, and not the patches.

No studies on scintillation from PMAFs or dayside aurora have been published after Paper II. Future studies should be carried out to determine if the results are representative. Ideally these should study PMAFs on a case by case basis, since statistical studies might average out important results due to the correspondence between PMAFs and patches, the speed with which they move, and the strict localization of scintillation to PMAFs demonstrated in Paper II. A direct comparison with polar cap patches would also be beneficial, to determine which of the two features is most likely to cause scintillation in the dayside ionosphere. Furthermore, the mechanism for irregularity production in relation to PMAFs should be determined. This may be aided by the same types of instruments proposed earlier when discussing the similar question for TOIs. Finally, case studies should be carried out to investigate scintillation impact from other auroral features in the dayside aurora.

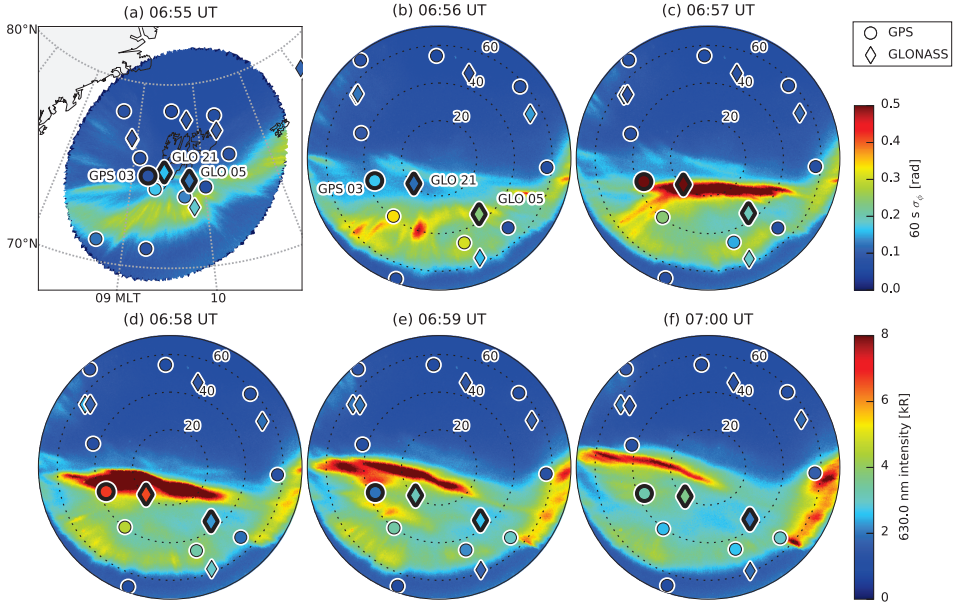

Figure 5.2: Six all-sky images from Longyearbyen show the creation and poleward motion of a PMAF, together with scintillation data from the Longyearbyen GNSS receiver. Panel (a) is mapped to a geographic grid for context. Panels (b–f) show line of sight data on a polar elevation/azimuth grid. GPS 03 and GLONASS 21 experience strong scintillation when the PMAF intersects the signals, and no scintillation is seen when there is no PMAF in the signal path. GLONASS 05 does not intersect the PMAF at all and never experiences strong scintillation. [From Paper II, *Oksavik et al.*, 2015]

5.1.3 Nightside aurora

Several studies have investigated irregularities and scintillation in relation to the nightside aurora. *Aarons et al.* [2000] was first in establishing a correlation between *L* band phase scintillations and auroral emissions. Since then, statistical studies [*Spogli et al.*, 2009; *Tiwari et al.*, 2012; *Jiao et al.*, 2013; *Kinrade et al.*, 2013] and case studies [*Prikryl et al.*, 2010; *Ngwira et al.*, 2010; *Hosokawa et al.*, 2014] have confirmed a correlation between auroral disturbances and GNSS scintillation.

An outstanding question has long been what causes the most severe scintillation in the nightside auroral ionosphere. *Jin et al.* [2014] were the first to compare scintillation from patches, aurora, and auroral blobs. Blobs caused the most severe scintillation in their events. Paper III follows up on the results of *Jin et al.* [2014] by performing a more detailed study of scintillation and irregularities in relation to a substorm onset and a later intensification when patches entered the auroral oval and became auroral blobs.

Paper III shows that during the substorm expansion, severe scintillation ($\sigma_\phi > 1$) was seen following the intense poleward edge of the auroral oval. During both the expansion and the later intensification, the scintillation in the aurora coincided with patches entering the auroral oval, and was strongly localized to signals with intense emissions in the line of sight. This supports the results of *Jin et al.* [2014]. However, in their results the patches were structured before entering the oval, whereas Paper III shows that the scintillation occurs even when the patches are not structured before entering the auroral oval, as shown in Figure 5.3. This indicates that the existing structure in the patch may not be important for the blob scintillation.

Recent studies support these results. *Jin et al.* [2016] performed a statistical study of scintillation from patches, aurora, and the combination of the two, which was based on over 40 hours of data. The study clearly showed that scintillation levels were higher when patches entered the auroral oval than it was in aurora or patches on their own. Furthermore, the study found no clear relationship between structuring of patches prior to entering the auroral oval, and the scintillation levels observed when they entered the auroral oval. This was explained by the existing irregularities being quickly dampened due to the highly conductive auroral *E* region. The aurora then continually produces intense irregularities in the patch. These results are also supported by *Clausen et al.* [2016], who studied TEC and phase scintillation during 490 events in the active polar cap and found the strongest scintillation when polar cap patches entered the auroral oval.

In summary, we have shown in Paper III that auroral precipitation and polar cap patches combined (i.e., blobs) is a highly potent combination for creating irregularities causing severe scintillation on *L* band frequencies, and that the scintillation is firmly localized to regions of intense auroral emissions. While recent studies support this, further research is needed to establish the physical mechanism by which blobs contribute

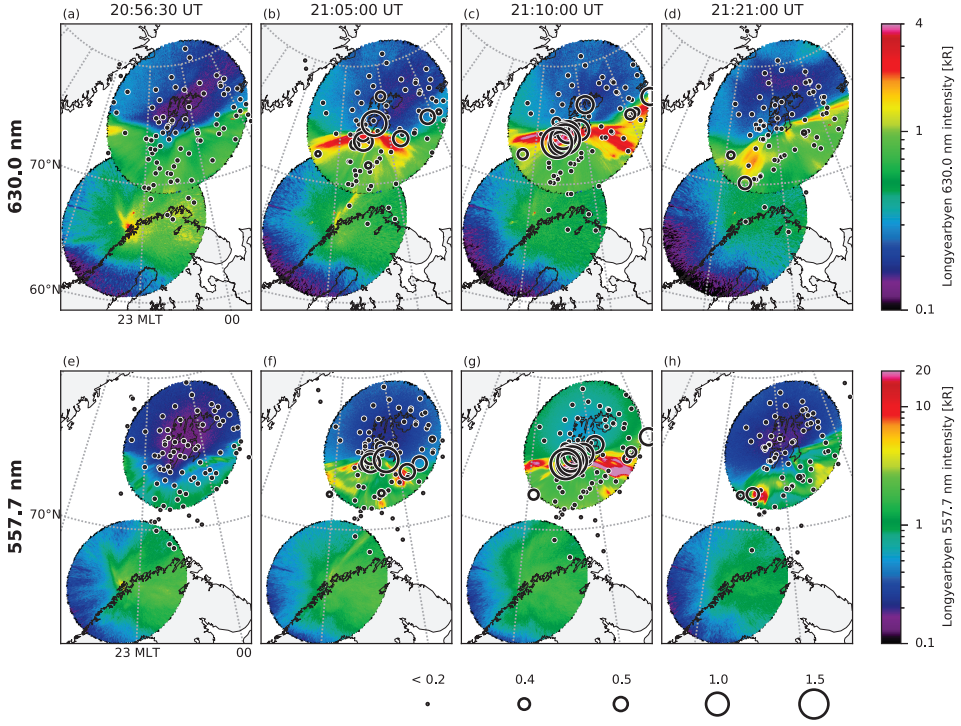

Figure 5.3: A series of all-sky imager and scintillation measurements shows that the patch (the light blue area on the top left in panel (a)) is not associated with scintillation before entering the auroral oval. The ionospheric piercing points are shown as black dots and circles, and the scintillation scale is shown at the bottom. The patch entry into the auroral oval coincides with a strong intensification of the aurora, causing severe phase scintillation in excess of 1.5 rad for signals intersecting the intense emissions. [From Paper III, *van der Meeren et al.*, 2015]

to irregularity and scintillation intensity.

5.1.4 Quiet-time polar cap

The quiet-time polar cap is much less studied than the storm-time polar cap. A predominant feature of the quiet-time polar cap is polar cap arcs [e.g., *Carlson*, 1994, and references therein], which is the focus of Paper IV. *Moen et al.* [2013] suggested that polar cap arcs might be regions of GNSS scintillation in the quiet-time polar cap. Before Paper IV, the only direct observations of *L* band scintillation in relation to polar cap arcs was an example of high-latitude scintillation in a study by *Prikryl et al.* [2015b], who classified it as "moderate to strong" scintillation without providing any numbers. *Prikryl et al.* [2015a] observed a B_y dependent asymmetry in polar cap scintillation for northward IMF consistent with the expected polar cap arc asymmetry, but provided no direct observations of scintillation from polar cap arcs.

Paper IV provides the first detailed observations of irregularities and scintillation in relation to a polar cap arc. A series of SuperDARN scans shows that the arc is associated with HF backscatter, enhanced spectral width, and a velocity shear. The presence of backscatter implies the presence of decameter scale irregularities, and the enhanced spectral width might suggest ongoing irregularity processes [*André et al.*, 2000]. The velocity shear might drive the Kelvin-Helmholtz instability (KHI) and create irregularities. Based on these observations, one might expect some scintillation. Additionally, the observed optical arc intensities are significant, and are statistically associated with some amount of scintillation [*Kinrade et al.*, 2013]. However, phase scintillation is almost always below 0.2 rad, indicating no or only very weak scintillation from the arc. This is shown in Figure 5.4.

When looking at high-resolution GNSS data as well as line of sight optical intensities from individual satellites, there is evidence of weak irregularities. Though the σ_ϕ index almost never exceeds 0.2 rad, slight enhancements are often visible when the arc crosses the signal path. The phase spectrograms also reflect this, with the spectral power being enhanced above background level, extending down to 1 s variations for some satellites. The enhancements are not particularly severe, as reflected in the σ_ϕ data.

When combined, the results indicate the presence of irregularities. HF backscatter means that there are decameter scale irregularities present, and the slight enhancements in σ_ϕ in relation to the arc indicate irregularities at larger scale sizes too. However, the irregularities appear to be weak, as evidenced by the low σ_ϕ.

TEC data have also been studied. The density was low throughout the event and stayed around 5 TECU. This number is also supported by ionosonde data and global TEC data. The low density naturally limits the severity of irregularities that can be formed. The arc itself showed an increase of around 5 TECU above this level, i.e., an increase by a factor of two. *Carlson* [1994] argues that scintillation levels scale with

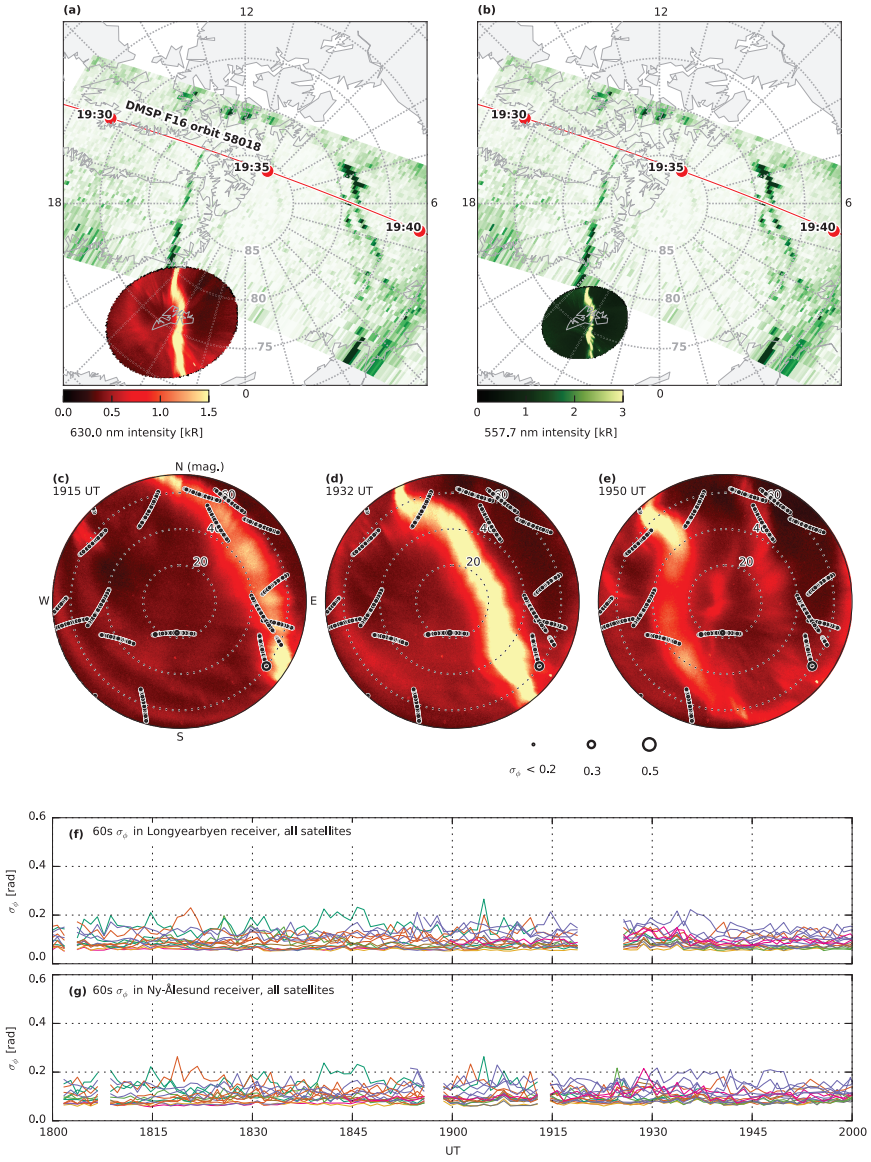

Figure 5.4: Panels (a) and (b) show the polar cap arc in ground- and satellite-based optical data. Panels (c), (d), and (e) show the arc as seen in the all-sky imager in Longyearbyen together with scintillation data from the GNSS receiver in Longyearbyen. The dots and circles show scintillation data between 19:12 and 19:52 UT (identical for the three panels). There is no significant scintillation when the arc intersects the signals. This is also seen in panels (f) and (g), which show scintillation data from all signals in Longyearbyen and Ny-Ålesund. The arc crosses almost all satellites at some point during the interval, but phase scintillation almost never exceeds 0.2 rad. [From Paper IV, *van der Meeren et al.*, 2016]

absolute fluctuation, not relative fluctuation. It is thus plausible that polar cap arcs may be associated with stronger irregularities causing more severe scintillation when the plasma density is higher. This may occur on the dayside part of the arcs, or during transition states from IMF south to IMF north, when patches and arcs may coexist in the polar cap. During such conditions, the flow shears associated with polar cap arcs might structure the high-density plasma in the polar cap.

No studies of scintillation from polar cap arcs or the quiet-time polar cap have been published after Paper IV. Future studies should be carried out to obtain a representative view of irregularities and scintillation in relation to the quiet-time polar cap in general and polar cap arcs in particular. It would also be beneficial to compare polar cap arcs and auroral arcs of similar intensities to determine whether there is a difference between irregularities created by auroral precipitation and those created by polar cap precipitation. Finally, polar cap arcs should be studied during high-density conditions, to determine if this leads to stronger irregularities near polar cap arcs. This can be done in summertime, in the dayside portion of polar cap arcs, or during transition states from IMF south to IMF north when polar cap patches and polar cap arcs may co-exist. This should be done on a case basis to determine exactly where and how such structuring occurs in relation to the arc.

5.1.5 Spatial variability at mesoscale

Papers I, II, and III show that scintillation is clearly localized from both ionospheric and geographical perspectives.

In Paper I, the scintillation was strictly localized to the front edge of the TOI. The spectrograms were essentially similar (showing no structuring) in the parts before the TOI and the parts inside the TOI. Furthermore, the structuring varied significantly between the three piercing points along the front edge, with one of the satellites not showing any structuring at all.

In Paper II, the scintillation is strongly localized to the PMAFs (as shown in Figure 5.2), even in the presence of polar cap patches. The fact that scintillation is localized to features that drift with speeds of $\sim 2\,\mathrm{km\,s^{-1}}$ implies that accurately predicting when and where scintillation may occur can be challenging.

The same implications can also be drawn from the results of Paper III. After sudden substorm onset, strong phase scintillation exceeding 1.0 rad can be seen localized to the intense poleward edge of the auroral oval, which rapidly expands poleward. Later, phase scintillation in excess of 1.5 rad is observed during a sudden intensification (as shown in Figure 5.3). The scintillation is strongly localized to signals with intense emissions in the line of sight.

The line of sight aspect of the spatial variability in Paper III also manifests itself when viewing the scintillation from a geographical perspective. There is a remarkable variability of the scintillation between two receivers located only $\sim 120\,\mathrm{km}$ apart. In

the receiver in Longyerabyen, there is severe scintillation simultaneously on 6 of 16 satellites. At the same time in Ny-Ålesund, there is no significant scintillation on any of the satellites. Such spatial variabilities can easily be averaged out in statistical studies, where binning may take place on the order of 100–1000 km [e.g., *Spogli et al.*, 2009; *Tiwari et al.*, 2012].

Much of the scintillation research is of a statistical nature. The strong localization and spatial variability evident in Papers I, II, and III makes it clear that in order to fully understand the nature of scintillations, it is crucial to also perform detailed case studies such as these.

5.1.6 Comparison of GPS, GLONASS, and Galileo

No previous studies have directly compared GPS, GLONASS, and Galileo at high latitudes. Paper III showed scintillation on satellites from all three constellations simultaneously in a highly localized region of the sky (shown in Figure 5.5). This allowed us to briefly compare the scintillation across the different constellations. It was found that all constellations experienced severe scintillation in this region. This result was expected, since all three constellations use similar frequencies in the *L* band and thus should be similarly influenced by ionospheric irregularities. The observed differences in scintillation levels may be due to differences in e.g. auroral precipitation that are too small-scale to be visible in the data. It would be of benefit to the GNSS community if careful statistical studies could be carried out to compare the climatology of scintillation across the different constellations, to determine if differences between constellations (such as orbital inclination) make some of the constellations more or less prone to high-latitude scintillation.

5.1.7 Comparison with HF backscatter

HF signals scatter off decameter-scale irregularities. A previous study by *Milan et al.* [2005] found that HF backscatter was co-located with 250 MHz amplitude scintillation. *L* band amplitude scintillation comes from irregularities below ~ 100 m scale. One may therefore expect HF backscatter and amplitude scintillations to be co-located. However, Papers I, III, and IV consistently show strong HF backscatter (~ 30 dB) in the presence of low or no amplitude scintillation. An example of strong HF backscatter from Paper IV is shown in Figure 5.6. HF backscatter without amplitude scintillation implies that HF radars can scatter off irregularities that are not of concern to GNSS users, and that HF backscatter is not a good proxy for irregularities causing *L* band scintillation. Future studies should look more carefully into the relationship between HF backscatter and *L* band scintillations.

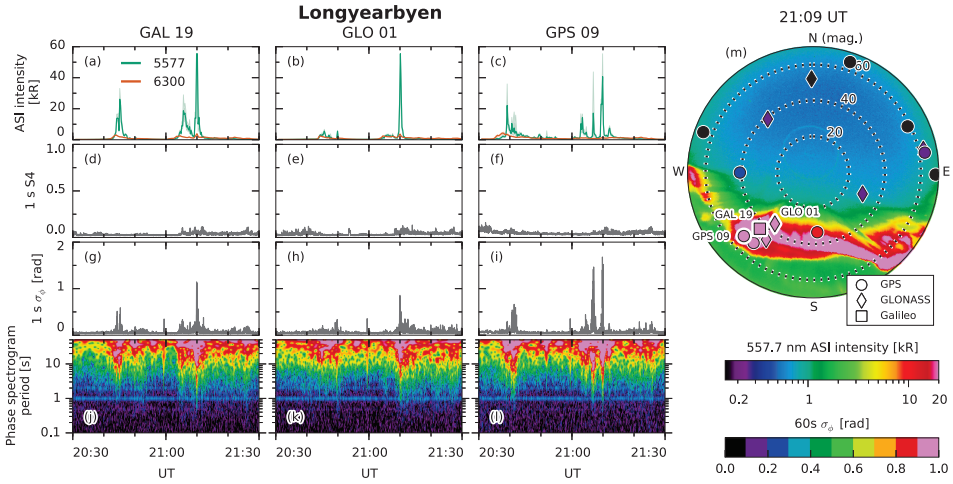

Figure 5.5: During the auroral intensification, five satellites from all three constellations were situated in a localized region of the sky (lower left of panel (m)) and experienced severe scintillation. Panels (g), (h), and (i) show that the phase scintillation index for three of these satellites reach values of 1.0–1.5 rad at 21:09 UT. [From Paper III, *van der Meeren et al.*, 2015]

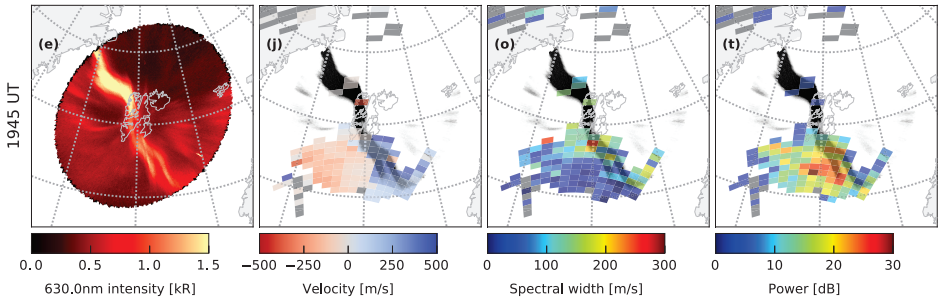

Figure 5.6: Even though SuperDARN data shows strong backscatter from the polar cap arc (panel (t)), no amplitude scintillation was observed from the arc. [Adapted from Paper IV, *van der Meeren et al.*, 2016]

5.2 Ionospheric irregularities

5.2.1 New approach: Phase spectrograms of raw GNSS data

The phase scintillation index is an aggregate number indicating the degree of phase variation across a wide range of scales. Furthermore, as detailed in Section 3.9.2, the σ_ϕ index is highly sensitive to the cutoff frequency of the detrending filter. An example of this is given in Paper I, where the σ_ϕ index with 0.1 Hz cutoff frequency is enhanced whereas the enhancement almost vanishes when detrended using 0.3 Hz.

To alleviate this, we have made use of a novel technique in studying phase variations. All four papers in this thesis have used spectrograms of high-resolution GNSS data to study ionospheric irregularities, as exemplified by Figure 5.5. *Mushini et al.* [2012] showed similar spectrograms, which in their case were used to invent a new type of scintillation index. The spectrograms in this thesis provide a more complete view of the irregularity scale sizes present in the plasma. Furthermore, the spectrograms are based on the raw, non-detrended data (except in the case of Paper I, where the spectrogram is based on detrended data but is insensitive to the data detrending). In the specific case of Paper I, this showed that even though the σ_ϕ enhancement almost vanished when using a cutoff frequency of 0.3 Hz, the structuring was in fact real and not a product of erroneous data detrending.

The phase variations are originally in the temporal domain (frequency or period). In Papers I and II, the drift speed of the observed ionospheric features (TOI and PMAFs, respectively) relative to the ionospheric piercing points of the signals was used to convert the variations into the spatial domain. This allowed us to estimate the spatial scales of the variations, and by extension, the spatial scales of the ionospheric structures causing the variations.

In Papers III and IV, such a conversion from temporal to spatial scale was unfortunately not possible. Converting the temporal variations in the signal to spatial scale requires the assumption of a temporally stable structure drifting across the signal path. The TOI observed in Paper I was just such a stable structure, drifting across the polar cap in the F region ionosphere. In Papers III and IV, due to the intense green auroral emissions, the ionization is likely significant in the E region, where the recombination rate is much higher than in the F region. There is thus a significantly more active process of ionization and recombination, and we cannot assume that the ionization produced by the aurora is a stable, drifting structure. The spectrograms do however show that there are phase variations across a wide range of scales.

We propose that future case studies using high-resolution GNSS signals could benefit from using phase spectrograms of the raw GNSS phase as a more reliable indicator of ionospheric structuring.

5.2.2 Spatial scale sizes

In-situ measurements are needed in order to accurately measure the smallest irregularity scale sizes [e.g., *Moen et al.*, 2012; *Oksavik et al.*, 2012]. However, indications of irregularity scale sizes can be determined from remote sensing techniques such as those used in this thesis. Specifically:

- Phase and amplitude scintillations at *L* band frequencies indicate the presence of irregularities with scale sizes above and below $\sim 350\,\mathrm{m}$ scale, respectively [e.g., *Basu et al.*, 1998; *Kintner et al.*, 2007].
- Regions of HF backscatter indicates the presence of decameter-scale irregularities [e.g., *Greenwald et al.*, 1995; *Moen et al.*, 2012].
- The phase spectrograms in Papers I and II are converted to spatial scale and indicate the scales of structuring in the plasma.

In general, most of the studied features show enhanced structuring at a variety of scale sizes, from decameter to kilometer scale. Specifics of each feature are provided below.

Tongue of ionization In Paper I, the TOI is structured on scale sizes from several kilometers down to tens of meters, as evidenced by elevated σ_ϕ levels, HF backscatter, and the range of scales with enhanced variations seen in the spectrograms.

Poleward-moving auroral forms In Paper II, the PMAFs show structuring from several kilometers down to hundreds of meters. This is seen in the spectrograms, and supported by elevated σ_ϕ levels.

Nightside aurora and blobs In Paper III, the results indicate that the auroral blobs are structured on a variety of different scale sizes. The severe phase scintillation indicates strong structuring above a few hundred meters. Any structuring that exists below a few hundred meters is evidently not sufficient to produce amplitude scintillation, though the presence of (sporadic) HF backscatter indicates structuring at decameter scale. The spectrograms, while not possible to convert from temporal to spatial scale, show structuring across a wide range of scales.

Polar cap arc Paper IV does not show scintillation in relation to the arc, but there is strong HF backscatter, indicating that the arc is associated with decameter-scale irregularities. From the power law spectrum of irregularities in the ionosphere, it can be inferred that larger scale sizes must exist too. However, these larger-scale irregularities are evidently not sufficiently strong to produce scintillation at GNSS frequencies. The spectrograms occasionally show enhanced structuring at larger scales when the arc

intersects the signal path, but compared to the other studies (Paper IV uses the same spectrogram color scale as Papers II and III) the enhancement is much weaker and covers a narrower range of scales.

5.2.3 Potential production mechanisms

Several irregularity production mechanisms have been proposed in literature. While it is not possible to determine accurately which mechanisms cause the structuring in the observed features, some cursory evaluations can be performed.

Tongue of ionization

The gradient drift instability (GDI) is believed to be the dominant structuring mechanism in the polar cap, and is most effective on the trailing edge of plasma structures. When the GDI is working on polar cap patches, it often structures the whole patch starting from the trailing edge [e.g., *Gondarenko and Guzdar*, 2004b, 2006; *Hosokawa et al.*, 2016]. It is therefore interesting that only the front edge of the TOI was structured. The spectrograms and scintillation indices showed no structuring inside the TOI (at least the first 700 km inside the leading edge). It is unclear why the front of the TOI is structured. It may be the case that there are smaller-scale flows not visible in the data, or that the time history of the shape of the TOI edge impacts the development of irregularities (Figure 5.1 shows that the leading edge which is perpendicular to the TOI drift in Figure 5.1c was significantly curved just minutes before, which theoretically allows for more effective structuring through the GDI).

To the discussion in Paper I we would like to add that there may be a continuum of states between fully segmented patches and a fully homogeneous TOI. This implies that even apparent TOIs could become structured by the same mechanisms as patches if there is sufficient internal structure.

Poleward-moving auroral forms

The mechanism for irregularity development in PMAFs also remain an outstanding question. It is possible that the flow shears associated with PMAFs can develop irregularities through the KHI. It is also possible that structured particle precipitation can generate weak “seed” irregularities which the GDI breaks down to smaller scales, as suggested by *Oksavik et al.* [2012]. The co-location of strong phase scintillation and bright PMAFs suggest that structured particle precipitation may also be an important source of plasma irregularities. The available data are not sufficient to point out the most likely or dominant mechanism.

Polar cap arc

The polar cap arc observed in Paper IV was associated with weak irregularities. It is difficult to determine what could be structuring the plasma and creating these irregularities. The paper covers three candidates. First, the KHI growth rate can be estimated by knowing the velocity difference and the scale length of a flow shear. Based on the SuperDARN data this can be estimated to ~ 70 min, which indicates that the KHI is not effective. However, this estimate may be severely off due to the one-dimensionality and low spatial resolution of the SuperDARN data. Unfortunately, a more accurate estimate is not possible based on the available data.

The second candidate is the GDI. This works on the trailing edges of drifting plasma structures. The precipitating nature of the arc means that the ionization will not drift since it is continually lost due the high recombination rate in the E region [e.g., *Hunsucker and Hargreaves*, 2002]. It is therefore assumed that there will be no structuring by the GDI.

Finally, irregularities may be created directly by structured precipitation. Optical auroral emissions have previously been correlated with scintillation [*Kinrade et al.*, 2013], and auroral precipitation is known to be structured on scale sizes down to tens of meters [e.g., *Sandahl et al.*, 2008, and references therein]. It is thus conceivable that the observed irregularities may be directly created by precipitation, but unfortunately the available data provides no way of determining this.

5.2.4 Potential energy sources for growth

In addition to irregularity production mechanisms, an interesting question is what the energy source for the irregularity growth is. Similar to the previous section, a complete and accurate determination is outside our scope, but the data indicate some potential energy sources.

In particular, particle precipitation is seen as an important driver for irregularities. This is most clear in Paper III, and is supported by three observations: 1) There is a remarkable correspondence between line of sight auroral intensity and phase scintillation. This is seen both during the auroral expansion, where the severe scintillation follows the intense poleward edge of the auroral oval, and during the intensification (Figures 5.3 and 5.5), where only the signals intersecting auroral emissions experienced strong scintillation. 2) There is no scintillation in relation to the patches before entering the auroral oval, as seen in Figure 5.3a. Thus, they cannot be the main cause of the scintillation-causing irregularities. 3) After the patches become blobs and the aurora fades, the region containing the blobs (but no significant emissions) do not show any scintillation, as seen in Figure 5.3d. In other words, as soon as the assumed energy input provided by the auroral precipitation is "turned off", the irregularities abate. Paper II also supports this view, where the scintillation is strongly localized to the PMAFs. The results

of *Clausen et al.* [2016] and *Jin et al.* [2016] supports the interpretation that auroral precipitation is important in creating scintillation-producing irregularities.

However, other possibilities exist as well. The irregularity growth in PMAFs may be driven by magnetic reconnection taking place at the magnetopause. As covered in the Introduction section of Paper II, PMAFs are often interpreted as the ionospheric signatures of flux transfer events. The fact that PMAFs are co-located with scintillation implies a close relationship between the irregularities and the anticipated PMAF energy source, i.e., transient reconnection at the magnetopause. A statistical study by *Prikryl et al.* [2015a] suggested that enhanced phase scintillation is highly co-located with ionospheric signatures of solar wind–magnetosphere coupling, supporting this view.

The role of the solar wind-ionosphere coupling is also seen in a study by *Thomas et al.* [2013]. They found HF backscatter co-located with a TOI, implying the presence of decameter-scale irregularities. The backscatter disappeared when the convection electric field disappeared (due to a vanishing of B_z), even though the TOI remained. This indicates that magnetic reconnection, causing transpolar circulation and drift of plasma, could provide the energy input for the decameter-scale irregularities in their study.

Future studies should be carried out in order to determine the origin of the free energy for driving irregularity growth through the various production mechanisms.

Chapter 6

Conclusions and future prospects

This thesis has investigated how dynamic phenomena in the polar cap and auroral ionosphere are causing scintillation on transionospheric radio signals at GNSS frequencies. The studies have been carried out in the Svalbard region, using the wide range of instrumentation available in this area. High-resolution GNSS receivers, all-sky imagers, coherent and incoherent scatter radars, ionosondes, and in-situ satellite measurements have been employed in multi-instrument case studies to obtain detailed information on the nature of scintillation-causing ionospheric irregularities in relation to features such as PMAFs, TOIs, polar cap patches, auroral blobs, auroral emissions, and polar cap arcs. The main conclusions of this thesis are:

- Scintillation and irregularities in TOIs:
  - Irregularities can exist on the leading edge of the TOI with scale sizes ranging from tens of meters to several kilometers.
  - The irregularities on the TOI leading edge can produce weak to moderate scintillation.
  - The leading edge of the TOI may be structured differently at different locations.
  - No structuring or scintillation was found inside the TOI for at least 700 km behind the leading edge.
- Scintillation and irregularities in the dayside aurora:
  - PMAFs are associated with irregularities at scale sizes from hundreds of meters to a few kilometers causing strong phase scintillation and loss of signal lock.
  - The scintillation is highly localized to the PMAFs, even in the presence of polar cap patches.

- Scintillation and irregularities in the nightside aurora:
  - During substorm expansion, the intense poleward edge of the auroral oval contains plasma density structuring causing severe scintillation.
  - The most severe scintillation is observed when auroral emissions and patches coincide, even when the patches were not structured before entry into the auroral oval. These findings are supported by other studies [*Jin et al.*, 2016; *Clausen et al.*, 2016] that have been published after Paper III [*van der Meeren et al.*, 2015].
  - The severe scintillation is localized to signals intersecting intense auroral emissions.
- Scintillation and irregularities in the quiet-time polar cap:
  - Weak irregularities are observed in relation to the nightside part of a long-lived polar cap arc during northward IMF conditions.
  - The irregularities cause no significant scintillation in polar cap arcs.
- Scintillation is found to be highly localized and varies significantly across distances of $\sim 100\,\mathrm{km}$, both from an ionospheric perspective and a ground-based perspective, clearly indicating that statistical studies must be complemented by detailed case studies to resolve all aspects of irregularities and scintillation.
- Strong HF backscatter frequently occurs without *L* band amplitude scintillations. This indicates that HF backscatter is not a good proxy for GNSS scintillations.
- Spectrograms of raw GNSS phase may be used to get a more complete view of irregularities than scintillation indices like σ_ϕ.
- A wide range of spatial scale sizes are observed. Specifically:
  - The TOI show structuring from decameters to several kilometers.
  - The PMAFs show structuring from hundreds of meters to several kilometers.
  - The auroral blobs, during intense precipitation, are associated with structuring from decameters up to at least several hundred meters.
  - The polar cap arc is associated with decameter-scale irregularities, though not sufficiently strong to cause amplitude scintillation. There is evidence of weak structuring at a wide range of spatial scales.

Future prospects

Some questions still remain unanswered, and we refer to the discussion in Chapter 5 for details. Here we summarize by providing a list of some open questions:

- How do irregularities develop as the plasma is convecting across the polar cap? The spatial and temporal variability evident in our results indicates the need for a dense network of instruments such as GNSS receivers to resolve the details of polar cap irregularity development.
- What are the sources of free energy driving the irregularity growth in different phenomena in the polar ionosphere (e.g., TOIs, PMAFs, auroral blobs, and polar cap arcs)?
- Are there other dayside auroral phenomena besides PMAFs that can cause strong scintillation?
- Do polar cap arcs cause stronger scintillation if they occur when there is a reservoir of high-density plasma in the polar cap, such as in the sunlit (dayside or summer) ionosphere or following rapid south-to-north IMF transitions?
- Do differences between GNSS constellations, such as orbital inclination, influence how prone the different constellations are to high-latitude scintillation?

These questions will require a combination of multi-instrument case and statistical studies. The results will improve prediction capabilities of the occurrence of radio wave scintillation in the polar areas. Answering these questions will allow us to move beyond the large-scale, static picture of the polar ionosphere as “a region where scintillations are likely to occur” to a better understanding of exactly when, where, and under which conditions transionospheric radio signals may be compromised.

Bibliography

Aarons, J., B. Lin, M. Mendillo, K. Liou, and M. Codrescu, Global Positioning System phase fluctuations and ultraviolet images from the Polar satellite, *Journal of Geophysical Research: Space Physics*, *105*(A3), 5201–5213, doi:10.1029/1999JA900409, 2000.

Akasofu, S.-I., The development of the auroral substorm, *Planetary and Space Science*, *12*(4), 273–282, doi:10.1016/0032-0633(64)90151-5, 1964.

Alcaydé, D. (Ed.), *Incoherent Scatter Theory, Practice and Science*, collection of lectures given in Cargese, Corsica, 1995.

Alfonsi, L., L. Spogli, G. De Franceschi, V. Romano, M. Aquino, A. Dodson, and C. N. Mitchell, Bipolar climatology of GPS ionospheric scintillation at solar minimum, *Radio Science*, *46*(3), doi:10.1029/2010RS004571, 2011.

Anderson, D. N., J. Buchau, and R. A. Heelis, Origin of density enhancements in the winter polar cap ionosphere, *Radio Science*, *23*(4), 513–519, doi:10.1029/RS023i004p00513, 1988.

André, R., M. Pinnock, J.-P. Villain, and C. Hanuise, On the factor conditioning the Doppler spectral width determined from SuperDARN HF radars, *International Journal of Geomagnetism and Aeronomy*, *2*(1), 77, 2000.

Axford, W. I., The solar wind, *Solar Physics*, *100*(1-2), 575–586, doi:10.1007/BF00158446, 1985.

Balogh, A., et al., The Solar Origin of Corotating Interaction Regions and their Formation in the Inner Heliosphere, in *Corotating Interaction Regions*, edited by A. Balogh, J. T. Gosling, J. R. Jokipii, R. Kallenbach, and H. Kunow, no. 7 in Space Sciences Series of ISSI, pp. 141–178, Springer Netherlands, 1999.

Barth, V. L., Identification and tracking of extreme electron densities by EISCAT Svalbard radar and SuperDARN, Ph.D. thesis, University of Oslo, 2009.

Basu, S., E. MacKenzie, and S. Basu, Ionospheric constraints on VHF/UHF communications links during solar maximum and minimum periods, *Radio Science*, *23*(3), 363–378, doi:10.1029/RS023i003p00363, 1988a.

Basu, S., S. Basu, E. MacKenzie, W. R. Coley, J. R. Sharber, and W. R. Hoegy, Plasma structuring by the gradient drift instability at high latitudes and comparison with velocity shear driven processes, *Journal of Geophysical Research: Space Physics*, *95*(A6), 7799–7818, doi:10.1029/JA095iA06p07799, 1990.

Basu, S., S. Basu, E. Costa, C. Bryant, C. E. Valladares, and R. C. Livingston, Interplanetary magnetic field control of drifts and anisotropy of high-latitude irregularities, *Radio Science*, *26*(4), 1079–1103, doi:10.1029/91RS00586, 1991.

Basu, S., S. Basu, P. K. Chaturvedi, and C. M. Bryant, Irregularity structures in the cusp/cleft and polar cap regions, *Radio Science*, *29*(1), 195–207, doi:10.1029/93RS01515, 1994.

Basu, S., et al., Simultaneous density and electric field fluctuation spectra associated with velocity shears in the auroral oval, *Journal of Geophysical Research: Space Physics*, *93*(A1), 115–136, doi:10.1029/JA093iA01p00115, 1988b.

Basu, S., et al., Characteristics of plasma structuring in the cusp/cleft region at Svalbard, *Radio Science*, *33*(6), 1885–1899, doi:10.1029/98RS01597, 1998.

Baumjohann, W., and R. A. Treumann, *Basic space plasma physics*, Imperial College Press ; Distributed by World Scientific Pub., London; River Edge, N.J., 1996.

Beach, T. L., Global Positioning System studies of equatorial scintillations, Ph.D. thesis, Cornell University, Ithaca, N. Y., 1998.

Béniguel, Y., et al., Ionospheric scintillation monitoring and modelling, *Annals of Geophysics*, *52*(3-4), 391–416, doi:10.4401/ag-4595, 2009.

Berkey, F. T., L. L. Cogger, S. Ismail, and Y. Kamide, Evidence for a correlation between Sun-aligned arcs and the interplanetary magnetic field direction, *Geophysical Research Letters*, *3*(3), 145–147, doi:10.1029/GL003i003p00145, 1976.

Bhattacharyya, A., K. C. Yeh, and S. J. Franke, Deducing turbulence parameters from transionospheric scintillation measurements, *Space Science Reviews*, *61*(3-4), 335–386, doi:10.1007/BF00222311, 1992.

Booker, H. G., J. A. Ratcliffe, and D. H. Shinn, Diffraction from an Irregular Screen with Applications to Ionospheric Problems, *Philosophical Transactions of the Royal Society of London. Series A, Mathematical and Physical Sciences*, *242*(856), 579–607, doi:10.1098/rsta.1950.0011, 1950.

Breen, A., W. Coles, R. Grall, M. Klinglesmith, J. Markkanen, P. Moran, C. Varley, and P. Williams, EISCAT measurements of interaction regions in the solar wind, *Advances in Space Research*, *20*(1), 27–30, doi:10.1016/S0273-1177(97)00475-4, 1997.

Briggs, B., and I. Parkin, On the variation of radio star and satellite scintillations with zenith angle, *Journal of Atmospheric and Terrestrial Physics*, *25*(6), 339–366, doi:10.1016/0021-9169(63)90150-8, 1963.

Buchau, J., B. W. Reinisch, E. J. Weber, and J. G. Moore, Structure and dynamics of the winter polar cap F region, *Radio Science*, *18*(6), 995–1010, doi:10.1029/RS018i006p00995, 1983.

Buchau, J., E. J. Weber, D. N. Anderson, H. C. Carlson, J. G. Moore, B. W. Reinisch, and R. C. Livingston, Ionospheric structures in the polar cap: Their origin and relation to 250-MHz scintillation, *Radio Science*, *20*(3), 325–338, doi:10.1029/RS020i003p00325, 1985.

Carlson, H. C., The dark polar ionosphere: Progress and future challenges, *Radio Science*, *29*(1), 157–165, doi:10.1029/93RS02125, 1994.

Carlson, H. C., Sharpening our thinking about polar cap ionospheric patch morphology, research, and mitigation techniques, *Radio Science*, *47*(4), doi:10.1029/2011RS004946, 2012.

Carlson, H. C., and S. W. H. Cowley, Accelerated polar rain electrons as the source of Sun-aligned arcs in the polar cap during northward interplanetary magnetic field conditions, *Journal of Geophysical Research: Space Physics*, *110*(A5), A05,302, doi:10.1029/2004JA010669, 2005.

Carlson, H. C., K. Oksavik, J. Moen, A. P. van Eyken, and P. Guio, ESR mapping of polar-cap patches in the dark cusp, *Geophysical Research Letters*, *29*(10), 24–1–24–4, doi:10.1029/2001GL014087, 2002.

Carlson, H. C., K. Oksavik, J. Moen, and T. Pedersen, Ionospheric patch formation: Direct measurements of the origin of a polar cap patch, *Geophysical Research Letters*, *31*(8), doi:10.1029/2003GL018166, 2004.

Carlson, H. C., J. Moen, K. Oksavik, C. P. Nielsen, I. W. McCrea, T. R. Pedersen, and P. Gallop, Direct observations of injection events of subauroral plasma into the polar cap, *Geophysical Research Letters*, *33*(5), doi:10.1029/2005GL025230, 2006.

Carlson, H. C., T. Pedersen, S. Basu, M. Keskinen, and J. Moen, Case for a new process, not mechanism, for cusp irregularity production, *Journal of Geophysical Research: Space Physics*, *112*(A11), doi:10.1029/2007JA012384, 2007.

Carlson, H. C., K. Oksavik, and J. Moen, On a new process for cusp irregularity production, *Annales Geophysicae*, *26*(9), 2871–2885, doi:10.5194/angeo-26-2871-2008, 2008.

Chapman, S., The absorption and dissociative or ionizing effect of monochromatic radiation in an atmosphere on a rotating earth part II. Grazing incidence, *Proceedings of the Physical Society*, *43*(5), 483, doi:10.1088/0959-5309/43/5/302, 1931.

Cherniak, I., and I. Zakharenkova, Dependence of the high-latitude plasma irregularities on the auroral activity indices: a case study of 17 March 2015 geomagnetic storm, *Earth, Planets and Space*, *67*(1), doi:10.1186/s40623-015-0316-x, 2015.

Cherniak, I., I. Zakharenkova, and R. J. Redmon, Dynamics of the high-latitude ionospheric irregularities during the 17 March 2015 St. Patrick's Day storm: Ground-based GPS measurements, *Space Weather*, *13*(9), 2015SW001,237, doi:10.1002/2015SW001237, 2015.

Chisham, G., and M. Pinnock, Assessing the contamination of SuperDARN global convection maps by non-F-region backscatter, *Annales Geophysicae*, *20*(1), 13–28, doi:10.5194/angeo-20-13-2002, 2002.

Chisham, G., T. K. Yeoman, and G. J. Sofko, Mapping ionospheric backscatter measured by the SuperDARN HF radars – Part 1: A new empirical virtual height model, *Annales Geophysicae*, *26*(4), 823–841, doi:10.5194/angeo-26-823-2008, 2008.

Chisham, G., et al., A decade of the Super Dual Auroral Radar Network (SuperDARN): scientific achievements, new techniques and future directions, *Surveys in Geophysics*, *28*(1), 33–109, doi:10.1007/s10712-007-9017-8, 2007.

Clausen, L. B. N., J. I. Moen, K. Hosokawa, and J. M. Holmes, GPS scintillations in the high latitudes during periods of dayside and nightside reconnection, *Journal of Geophysical Research: Space Physics*, doi:10.1002/2015JA022199, 2016.

Coker, C., G. S. Bust, R. A. Doe, and T. L. Gaussiran, High-latitude plasma structure and scintillation, *Radio Science*, *39*(1), doi:10.1029/2002RS002833, 2004.

Coster, A., J. Williams, A. Weatherwax, W. Rideout, and D. Herne, Accuracy of GPS total electron content: GPS receiver bias temperature dependence, *Radio Science*, *48*(2), 190–196, doi:10.1002/rds.20011, 2013.

Cousins, E. D. P., and S. G. Shepherd, A dynamical model of high-latitude convection derived from SuperDARN plasma drift measurements, *Journal of Geophysical Research: Space Physics*, *115*(A12), doi:10.1029/2010JA016017, 2010.

Crowley, G., et al., Transformation of high-latitude ionospheric F region patches into blobs during the March 21, 1990, storm, *Journal of Geophysical Research: Space Physics*, *105*(A3), 5215–5230, doi:10.1029/1999JA900357, 2000.

Cumnock, J. A., and L. G. Blomberg, Transpolar arc evolution and associated potential patterns, *Annales Geophysicae*, *22*(4), 1213–1231, doi:10.5194/angeo-22-1213-2004, 2004.

Cumnock, J. A., R. A. Heelis, M. R. Hairston, and P. T. Newell, High-latitude ionospheric convection pattern during steady northward interplanetary magnetic field, *Journal of Geophysical Research: Space Physics*, *100*(A8), 14,537–14,555, doi:10.1029/94JA03318, 1995.

Cumnock, J. A., J. R. Sharber, R. A. Heelis, M. R. Hairston, and J. D. Craven, Evolution of the global aurora during positive IMF Bz and varying IMF By conditions, *Journal of Geophysical Research: Space Physics*, *102*(A8), 17,489–17,497, doi:10.1029/97JA01182, 1997.

Cumnock, J. A., J. R. Sharber, R. A. Heelis, L. G. Blomberg, G. A. Germany, J. F. Spann, and W. R. Coley, Interplanetary magnetic field control of theta aurora development, *Journal of Geophysical Research: Space Physics*, *107*(A7), SIA 4–1, doi:10.1029/2001JA009126, 2002.

Dandekar, B. S., and T. W. Bullett, Morphology of polar cap patch activity, *Radio Science*, *34*(5), 1187–1205, doi:10.1029/1999RS900056, 1999.

David, M., J. J. Sojka, R. W. Schunk, and A. J. Coster, Polar cap patches and the tongue of ionization: A survey of GPS TEC maps from 2009 to 2015, *Geophysical Research Letters*, *43*(6), 2016GL068,136, doi:10.1002/2016GL068136, 2016.

Davis, T. N., Negative correlation between polar-cap visual aurora and magnetic activity, *Journal of Geophysical Research*, *68*(15), 4447–4453, doi:10.1029/JZ068i015p04447, 1963.

De Franceschi, G., L. Alfonsi, V. Romano, M. Aquino, A. Dodson, C. N. Mitchell, P. Spencer, and A. W. Wernik, Dynamics of high-latitude patches and associated small-scale irregularities during the October and November 2003 storms, *Journal of Atmospheric and Solar-Terrestrial Physics*, *70*(6), 879–888, doi:10.1016/j.jastp.2007.05.018, 2008.

Dungey, J. W., Interplanetary Magnetic Field and the Auroral Zones, *Physical Review Letters*, *6*(2), 47–48, doi:10.1103/PhysRevLett.6.47, 1961.

Ebert, R. W., D. J. McComas, H. A. Elliott, R. J. Forsyth, and J. T. Gosling, Bulk properties of the slow and fast solar wind and interplanetary coronal mass ejections measured by Ulysses: Three polar orbits of observations, *Journal of Geophysical Research: Space Physics*, *114*(A1), doi:10.1029/2008JA013631, 2009.

Elphinstone, R. D., J. S. Murphree, and L. L. Cogger, What is a global auroral substorm?, *Reviews of Geophysics*, *34*(2), 169–232, doi:10.1029/96RG00483, 1996.

Eriksson, S., G. Provan, F. J. Rich, M. Lester, S. E. Milan, S. Massetti, J. T. Gosling, M. W. Dunlop, and H. Rème, Electrodynamics of a split-transpolar aurora, *Journal of Geophysical Research: Space Physics*, *111*(A11), A11,319, doi:10.1029/2006JA011976, 2006.

Fasel, G. J., Dayside poleward moving auroral forms: A statistical study, *Journal of Geophysical Research: Space Physics*, *100*(A7), 11,891–11,905, doi:10.1029/95JA00854, 1995.

Fasel, G. J., L. C. Lee, and R. W. Smith, A mechanism for the multiple brightenings of dayside poleward-moving auroral forms, *Geophysical Research Letters*, *20*(20), 2247–2250, doi:10.1029/93GL02487, 1993.

Fear, R. C., and S. E. Milan, The IMF dependence of the local time of transpolar arcs: Implications for formation mechanism, *Journal of Geophysical Research: Space Physics*, *117*(A3), A03,213, doi:10.1029/2011JA017209, 2012a.

Fear, R. C., and S. E. Milan, Ionospheric flows relating to transpolar arc formation, *Journal of Geophysical Research: Space Physics*, *117*(A9), A09,230, doi:10.1029/2012JA017830, 2012b.

Feldstein, Y. I., and G. V. Starkov, Dynamics of auroral belt and polar geomagnetic disturbances, *Planetary and Space Science*, *15*(2), 209–229, doi:10.1016/0032-0633(67)90190-0, 1967.

Forte, B., Optimum detrending of raw GPS data for scintillation measurements at auroral latitudes, *Journal of Atmospheric and Solar-Terrestrial Physics*, *67*(12), 1100–1109, doi:10.1016/j.jastp.2005.01.011, 2005.

Forte, B., and S. M. Radicella, Problems in data treatment for ionospheric scintillation measurements, *Radio Science*, *37*(6), 8–1–8–5, doi:10.1029/2001RS002508, 2002.

Forte, B., and S. M. Radicella, Geometrical control of scintillation indices: What happens for GPS satellites, *Radio Science*, *39*(5), doi:10.1029/2002RS002852, 2004.

Forte, B., M. Materassi, L. Alfonsi, V. Romano, G. De Franceschi, and P. Spalla, Optimum parameter for estimating phase fluctuations on transionospheric signals at high latitudes, *Advances in Space Research*, *47*(12), 2188–2193, doi:10.1016/j.asr.2010.04.033, 2011.

Foster, J. C., Storm time plasma transport at middle and high latitudes, *Journal of Geophysical Research: Space Physics*, *98*(A2), 1675–1689, doi:10.1029/92JA02032, 1993.

Foster, J. C., and J. R. Doupnik, Plasma convection in the vicinity of the dayside cleft, *Journal of Geophysical Research: Space Physics*, *89*(A10), 9107–9113, doi:10.1029/JA089iA10p09107, 1984.

Foster, J. C., et al., Multiradar observations of the polar tongue of ionization, *Journal of Geophysical Research: Space Physics*, *110*(A9), doi:10.1029/2004JA010928, 2005.

Garner, T. W., R. B. Harris, J. A. York, C. S. Herbster, C. F. Minter, and D. L. Hampton, An auroral scintillation observation using precise, collocated GPS receivers, *Radio Science*, *46*(1), RS1018, doi:10.1029/2010RS004412, 2011.

Gondarenko, N. A., and P. N. Guzdar, Density and electric field fluctuations associated with the gradient drift instability in the high-latitude ionosphere, *Geophysical Research Letters*, *31*(11), L11,802, doi:10.1029/2004GL019703, 2004a.

Gondarenko, N. A., and P. N. Guzdar, Plasma patch structuring by the nonlinear evolution of the gradient drift instability in the high-latitude ionosphere, *Journal of Geophysical Research: Space Physics*, *109*(A9), doi:10.1029/2004JA010504, 2004b.

Gondarenko, N. A., and P. N. Guzdar, Simulations of the scintillation-producing irregularities in high-latitude plasma patches, *Geophysical Research Letters*, *33*(22), doi:10.1029/2006GL028033, 2006.

Greenwald, R. A., et al., DARN/SuperDARN, *Space Science Reviews*, *71*(1-4), 761–796, doi:10.1007/BF00751350, 1995.

Gussenhoven, M. S., Extremely high latitude auroras, *Journal of Geophysical Research: Space Physics*, *87*(A4), 2401–2412, doi:10.1029/JA087iA04p02401, 1982.

Gwal, A. K., and A. Jain, GPS scintillation studies in the arctic region during the first winter-phase 2008 Indian Arctic Expedition, *Polar Science*, *4*(4), 574–587, doi:10.1016/j.polar.2010.08.001, 2011.

Hardy, D. A., L. K. Schmitt, M. S. Gussenhoven, F. J. Marshall, and H. C. Yeh, Precipitating electron and ion detectors (SSJ/4) for the block 5D/Flights 6-10 DMSP (Defense Meteorological Satellite Program) satellites: Calibration and data presentation, *Tech. rep.*, 1984.

Hewish, A., The Diffraction of Radio Waves in Passing through a Phase-Changing Ionosphere, *Proceedings of the Royal Society of London. Series A. Mathematical and Physical Sciences*, *209*(1096), 81–96, doi:10.1098/rspa.1951.0189, 1951.

Hey, J. S., S. J. Parsons, and J. W. Phillips, Fluctuations in cosmic radiation at radio-frequencies, *Nature*, *158*(4007), 234, doi:10.1038/158234a0, 1946.

Hones, E. W. (Ed.), *Magnetic Reconnection in Space and Laboratory Plasmas*, American Geophysical Union, Washington, 1984.

Hosokawa, K., J. I. Moen, K. Shiokawa, and Y. Otsuka, Decay of polar cap patch, *Journal of Geophysical Research: Space Physics*, *116*(A5), doi:10.1029/2010JA016297, 2011.

Hosokawa, K., Y. Otsuka, Y. Ogawa, and T. Tsugawa, Observations of GPS scintillation during an isolated auroral substorm, *Progress in Earth and Planetary Science*, *1*(1), 1–9, doi:10.1186/2197-4284-1-16, 2014.

Hosokawa, K., S. Taguchi, and Y. Ogawa, Edge of polar cap patches, *Journal of Geophysical Research: Space Physics*, *121*(4), doi:10.1002/2015JA021960, 2016.

Huba, J. D., S. L. Ossakow, P. Satyanarayana, and P. N. Guzdar, Linear theory of the E×B instability with an inhomogeneous electric field, *Journal of Geophysical Research: Space Physics*, *88*(A1), 425–434, doi:10.1029/JA088iA01p00425, 1983.

Hunsucker, R. D., and J. K. Hargreaves, *The High-Latitude Ionosphere and its Effects on Radio Propagation*, Cambridge Atmospheric and Space Science Series, 1st ed., Cambridge University Press, UK, 2002.

Jiao, Y., Y. T. Morton, S. Taylor, and W. Pelgrum, Characterization of high-latitude ionospheric scintillation of GPS signals, *Radio Science*, *48*(6), 698–708, doi:10.1002/2013RS005259, 2013.

Jin, Y., J. I. Moen, and W. J. Miloch, GPS scintillation effects associated with polar cap patches and substorm auroral activity: direct comparison, *Journal of Space Weather and Space Climate*, *4*, doi:10.1051/swsc/2014019, 2014.

Jin, Y., J. I. Moen, and W. J. Miloch, On the collocation of the cusp aurora and the GPS phase scintillation: A statistical study, *Journal of Geophysical Research: Space Physics*, *120*(10), doi:10.1002/2015JA021449, 2015.

Jin, Y., J. I. Moen, W. J. Miloch, L. B. N. Clausen, and K. Oksavik, Statistical study of the GNSS phase scintillation associated with two types of auroral blobs, *Journal of Geophysical Research: Space Physics*, doi:10.1002/2016JA022613, 2016.

Johnson, C. Y., Ion and neutral composition of the ionosphere, in *Solar-Terrestrial Physics: Terrestrial aspects, Annals of the IQSY*, vol. 5, pp. 197–213, 1969.

Kelley, M. C., *The Earth's ionosphere: Plasma physics and electrodynamics*, 2nd ed., Academic Press, USA, 2009.

Kersley, L., S. E. Pryse, and N. S. Wheadon, Amplitude and phase scintillation at high latitudes over northern Europe, *Radio Science*, *23*(3), 320–330, doi:10.1029/RS023i003p00320, 1988.

Kersley, L., C. D. Russell, and D. L. Rice, Phase scintillation and irregularities in the northern polar ionosphere, *Radio Science*, *30*(3), 619–629, doi:10.1029/94RS03175, 1995.

Keskinen, M. J., Nonlinear theory of the E × B instability with an inhomogeneous electric field, *Journal of Geophysical Research: Space Physics*, *89*(A6), 3913–3920, doi:10.1029/JA089iA06p03913, 1984.

Keskinen, M. J., and S. L. Ossakow, Theories of high-latitude ionospheric irregularities: A review, *Radio Science*, *18*(6), 1077–1091, doi:10.1029/RS018i006p01077, 1983.

Keskinen, M. J., H. G. Mitchell, J. A. Fedder, P. Satyanarayana, S. T. Zalesak, and J. D. Huba, Nonlinear evolution of the Kelvin-Helmholtz instability in the high-latitude ionosphere, *Journal of Geophysical Research: Space Physics*, *93*(A1), 137–152, doi:10.1029/JA093iA01p00137, 1988.

Kinrade, J., C. N. Mitchell, P. Yin, N. Smith, M. J. Jarvis, D. J. Maxfield, M. C. Rose, G. S. Bust, and A. T. Weatherwax, Ionospheric scintillation over Antarctica during the storm of 5–6 April 2010, *Journal of Geophysical Research: Space Physics*, *117*(A5), A05,304, doi:10.1029/2011JA017073, 2012.

Kinrade, J., C. N. Mitchell, N. D. Smith, Y. Ebihara, A. T. Weatherwax, and G. S. Bust, GPS phase scintillation associated with optical auroral emissions: First statistical results from the geographic South Pole, *Journal of Geophysical Research: Space Physics*, *118*(5), 2490–2502, doi:10.1002/jgra.50214, 2013.

Kintner, P. M., and B. M. Ledvina, The ionosphere, radio navigation, and global navigation satellite systems, *Advances in Space Research*, *35*(5), 788–811, doi:10.1016/j.asr.2004.12.076, 2005.

Kintner, P. M., B. M. Ledvina, and E. R. de Paula, GPS and ionospheric scintillations, *Space Weather*, *5*(9), doi:10.1029/2006SW000260, 2007.

Knudsen, W. C., Magnetospheric convection and the high-latitude F2 ionosphere, *Journal of Geophysical Research*, *79*(7), 1046–1055, doi:10.1029/JA079i007p01046, 1974.

Kullen, A., Transpolar Arcs: Summary and Recent Results, in *Auroral Phenomenology and Magnetospheric Processes: Earth And Other Planets*, edited by A. Keiling, E. Donovan, F. Bagenal, and T. Karlsson, pp. 69–80, American Geophysical Union, 2012.

Lehtinen, M. S., and A. Huuskonen, General incoherent scatter analysis and GUISDAP, *Journal of Atmospheric and Terrestrial Physics*, *58*(1–4), 435–452, doi:10.1016/0021-9169(95)00047-X, 1996.

Lepping, R. P., et al., The WIND magnetic field investigation, *Space Science Reviews*, *71*(1-4), 207–229, doi:10.1007/BF00751330, 1995.

Li, G., B. Ning, Z. Ren, and L. Hu, Statistics of GPS ionospheric scintillation and irregularities over polar regions at solar minimum, *GPS Solutions*, *14*(4), 331–341, doi:10.1007/s10291-009-0156-x, 2010.

Linson, L. M., and J. B. Workman, Formation of striations in ionospheric plasma clouds, *Journal of Geophysical Research*, *75*(16), 3211–3219, doi:10.1029/JA075i016p03211, 1970.

Lockwood, M., and H. C. Carlson, Production of polar cap electron density patches by transient magnetopause reconnection, *Geophysical Research Letters*, *19*(17), 1731–1734, doi:10.1029/92GL01993, 1992.

Lockwood, M., J. A. Davies, J. Moen, A. P. van Eyken, K. Oksavik, I. W. McCrea, and M. Lester, Motion of the dayside polar cap boundary during substorm cycles: II. Generation of poleward-moving events and polar cap patches by pulses in the magnetopause reconnection rate, *Annales Geophysicae*, *23*(11), 3513–3532, doi:10.5194/angeo-23-3513-2005, 2005.

Lorentzen, D. A., N. Shumilov, and J. Moen, Drifting airglow patches in relation to tail reconnection, *Geophysical Research Letters*, *31*(2), doi:10.1029/2003GL017785, 2004.

Lorentzen, D. A., J. Moen, K. Oksavik, F. Sigernes, Y. Saito, and M. G. Johnsen, In situ measurement of a newly created polar cap patch, *Journal of Geophysical Research: Space Physics*, *115*(A12), doi:10.1029/2010JA015710, 2010.

Mawson, D., Auroral observations at the Cape Royds station, Antarctica, *Transactions of the Royal Society of South Australia*, *40*, 151–212, 1916.

McPherron, R. L., Growth phase of magnetospheric substorms, *Journal of Geophysical Research*, *75*(28), 5592–5599, doi:10.1029/JA075i028p05592, 1970.

McPherron, R. L., Magnetospheric substorms, *Reviews of Geophysics*, *17*(4), 657–681, doi:10.1029/RG017i004p00657, 1979.

Milan, S. E., M. Lester, and T. K. Yeoman, HF radar polar patch formation revisited: summer and winter variations in dayside plasma structuring, *Annales Geophysicae*, *20*(4), 487–499, doi:10.5194/angeo-20-487-2002, 1999.

Milan, S. E., S. Basu, T. K. Yeoman, and R. E. Sheehan, A comparison of satellite scintillation measurements with HF radar backscatter characteristics, *Annales Geophysicae*, *23*(11), 3451–3455, doi:10.5194/angeo-23-3451-2005, 2005.

Mitchell, C. N., L. Alfonsi, G. De Franceschi, M. Lester, V. Romano, and A. W. Wernik, GPS TEC and scintillation measurements from the polar ionosphere during the October 2003 storm, *Geophysical Research Letters*, *32*(12), doi:10.1029/2004GL021644, 2005.

Moen, J., I. K. Walker, L. Kersley, and S. E. Milan, On the generation of cusp HF backscatter irregularities, *Journal of Geophysical Research: Space Physics*, *107*(A4), SIA 3–1–SIA 3–5, doi:10.1029/2001JA000111, 2002.

Moen, J., H. C. Carlson, K. Oksavik, C. P. Nielsen, S. E. Pryse, H. R. Middleton, I. W. McCrea, and P. Gallop, EISCAT observations of plasma patches at sub-auroral cusp latitudes, *Annales Geophysicae*, *24*(9), 2363–2374, doi:10.5194/angeo-24-2363-2006, 2006.

Moen, J., N. Gulbrandsen, D. A. Lorentzen, and H. C. Carlson, On the MLT distribution of F region polar cap patches at night, *Geophysical Research Letters*, *34*(14), doi:10.1029/2007GL029632, 2007.

Moen, J., K. Oksavik, T. Abe, M. Lester, Y. Saito, T. A. Bekkeng, and K. S. Jacobsen, First in-situ measurements of HF radar echoing targets, *Geophysical Research Letters*, *39*(7), doi:10.1029/2012GL051407, 2012.

Moen, J., K. Oksavik, L. Alfonsi, Y. Daabakk, V. Romano, and L. Spogli, Space weather challenges of the polar cap ionosphere, *Journal of Space Weather and Space Climate*, *3*, A02, doi:10.1051/swsc/2013025, 2013.

Montenbruck, O., A. Hauschild, and P. Steigenberger, Differential Code Bias Estimation using Multi-GNSS Observations and Global Ionosphere Maps, *Navigation*, *61*(3), 191–201, doi:10.1002/navi.64, 2014.

Morley, S. K., J. P. Sullivan, M. G. Henderson, J. B. Blake, and D. N. Baker, The Global Positioning System constellation as a space weather monitor: Comparison of electron measurements with Van Allen Probes data, *Space Weather*, *14*(2), 2015SW001,339, doi:10.1002/2015SW001339, 2016.

Mushini, S. C., P. T. Jayachandran, R. B. Langley, J. W. MacDougall, and D. Pokhotelov, Improved amplitude- and phase-scintillation indices derived from wavelet detrended high-latitude GPS data, *GPS Solutions*, *16*(3), 363–373, doi:10.1007/s10291-011-0238-4, 2012.

Newell, P. T., K. Liou, and G. R. Wilson, Polar cap particle precipitation and aurora: Review and commentary, *Journal of Atmospheric and Solar-Terrestrial Physics*, *71*(2), 199–215, doi:10.1016/j.jastp.2008.11.004, 2009.

Ngwira, C. M., L.-A. McKinnell, and P. J. Cilliers, GPS phase scintillation observed over a high-latitude Antarctic station during solar minimum, *Journal of Atmospheric and Solar-Terrestrial Physics*, *72*(9–10), 718–725, doi:10.1016/j.jastp.2010.03.014, 2010.

Nicholson, D. R., *Introduction to Plasma Theory*, Wiley & Sons Inc., New York, 1983.

Nygrén, T., *Introduction to Incoherent Scatter Measurements*, Invers Oy, Sodankylä, Finland, 1996.

Ogilvie, K. W., et al., SWE, a comprehensive plasma instrument for the WIND spacecraft, *Space Science Reviews*, *71*(1-4), 55–77, doi:10.1007/BF00751326, 1995.

Oksavik, K., V. L. Barth, J. Moen, and M. Lester, On the entry and transit of high-density plasma across the polar cap, *Journal of Geophysical Research: Space Physics*, *115*(A12), doi:10.1029/2010JA015817, 2010.

Oksavik, K., J. I. Moen, E. H. Rekaa, H. C. Carlson, and M. Lester, Reversed flow events in the cusp ionosphere detected by SuperDARN HF radars, *Journal of Geophysical Research: Space Physics*, *116*(A12), doi:10.1029/2011JA016788, 2011.

Oksavik, K., J. Moen, M. Lester, T. A. Bekkeng, and J. K. Bekkeng, In situ measurements of plasma irregularity growth in the cusp ionosphere, *Journal of Geophysical Research: Space Physics*, *117*(A11), doi:10.1029/2012JA017835, 2012.

Oksavik, K., C. van der Meeren, D. A. Lorentzen, L. J. Baddeley, and J. Moen, Scintillation and loss of signal lock from poleward moving auroral forms in the cusp ionosphere, *Journal of Geophysical Research: Space Physics*, *120*(10), doi:10.1002/2015JA021528, 2015.

Ossakow, S. L., and P. K. Chaturvedi, Current convective instability in the diffuse aurora, *Geophysical Research Letters*, *6*(4), 332–334, doi:10.1029/GL006i004p00332, 1979.

Paxton, L. J., et al., Special sensor ultraviolet spectrographic imager: an instrument description, pp. 2–15, doi:10.1117/12.60595, 1992.

Prikryl, P., P. T. Jayachandran, S. C. Mushini, D. Pokhotelov, J. W. MacDougall, E. Donovan, E. Spanswick, and J.-P. St.-Maurice, GPS TEC, scintillation and cycle slips observed at high latitudes during solar minimum, *Annales Geophysicae*, *28*(6), 1307–1316, doi:10.5194/angeo-28-1307-2010, 2010.

Prikryl, P., P. T. Jayachandran, S. C. Mushini, and R. Chadwick, Climatology of GPS phase scintillation and HF radar backscatter for the high-latitude ionosphere under solar minimum conditions, *Annales Geophysicae*, *29*(2), 377–392, doi:10.5194/angeo-29-377-2011, 2011a.

Prikryl, P., P. T. Jayachandran, S. C. Mushini, and R. Chadwick, GPS phase scintillation and HF radar backscatter occurrence in the high-latitude ionosphere, in *General Assembly and Scientific Symposium, 2011 XXXth URSI*, pp. 1–4, doi:10.1109/URSIGASS.2011.6123722, 2011b.

Prikryl, P., R. Ghoddousi-Fard, B. S. R. Kunduri, E. G. Thomas, A. J. Coster, P. T. Jayachandran, E. Spanswick, and D. W. Danskin, GPS phase scintillation and proxy index at high latitudes during a moderate geomagnetic storm, *Annales Geophysicae*, *31*(5), 805–816, doi:10.5194/angeo-31-805-2013, 2013.

Prikryl, P., P. T. Jayachandran, R. Chadwick, and T. D. Kelly, Climatology of GPS phase scintillation at northern high latitudes for the period from 2008 to 2013, *Annales Geophysicae*, *33*(5), 531–545, doi:10.5194/angeo-33-531-2015, 2015a.

Prikryl, P., et al., Interhemispheric comparison of GPS phase scintillation at high latitudes during the magnetic-cloud-induced geomagnetic storm of 5–7 April 2010, *Annales Geophysicae*, *29*(12), 2287–2304, doi:10.5194/angeo-29-2287-2011, 2011c.

Prikryl, P., et al., GPS phase scintillation at high latitudes during geomagnetic storms of 7–17 March 2012 – Part 1: The North American sector, *Annales Geophysicae*, *33*(6), 637–656, doi:10.5194/angeo-33-637-2015, 2015b.

Pryse, S. E., A. G. Wood, H. R. Middleton, I. W. McCrea, and M. Lester, Reconfiguration of polar-cap plasma in the magnetic midnight sector, *Annales Geophysicae*, *24*(8), 2201–2208, doi:10.5194/angeo-24-2201-2006, 2006.

Rietveld, M. T., J. W. Wright, N. Zabotin, and M. L. V. Pitteway, The Tromsø dynasonde, *Polar Science*, *2*(1), 55–71, doi:10.1016/j.polar.2008.02.001, 2008.

Robinson, R. M., R. T. Tsunoda, J. F. Vickrey, and L. Guerin, Sources of F region ionization enhancements in the nighttime auroral zone, *Journal of Geophysical Research: Space Physics*, *90*(A8), 7533–7546, doi:10.1029/JA090iA08p07533, 1985.

Rostoker, G., S.-I. Akasofu, J. Foster, R. Greenwald, Y. Kamide, K. Kawasaki, A. Lui, R. McPherron, and C. Russell, Magnetospheric substorms—definition and signatures, *Journal of Geophysical Research: Space Physics*, *85*(A4), 1663–1668, doi:10.1029/JA085iA04p01663, 1980.

Sandahl, I., T. Sergienko, and U. Brändström, Fine structure of optical aurora, *Journal of Atmospheric and Solar-Terrestrial Physics*, *70*(18), 2275–2292, doi:10.1016/j.jastp.2008.08.016, 2008.

Sandholt, P. E., M. Lockwood, T. Oguti, S. W. H. Cowley, K. S. C. Freeman, B. Lybekk, A. Egeland, and D. M. Willis, Midday auroral breakup events and related energy and momentum transfer from the magnetosheath, *Journal of Geophysical Research: Space Physics*, *95*(A2), 1039–1060, doi:10.1029/JA095iA02p01039, 1990.

Sandholt, P. E., J. Moen, D. Opsvik, W. F. Denig, and W. J. Burke, Auroral event sequence at the dayside polar cap boundary: Signature of time-varying solar wind-magnetosphere-ionosphere coupling, *Advances in Space Research*, *13*(4), 7–15, doi:10.1016/0273-1177(93)90305-U, 1993.

Sandholt, P. E., C. J. Farrugia, J. Moen, Ø. Noraberg, B. Lybekk, T. Sten, and T. Hansen, A classification of dayside auroral forms and activities as a function of interplanetary magnetic field orientation, *Journal of Geophysical Research: Space Physics*, *103*(A10), 23,325–23,345, doi:10.1029/98JA02156, 1998.

Sato, T., Morphology of the ionospheric F2 disturbances in the polar region, *Report of Ionosphere and Space Research in Japan*, *131*, 91, 1959.

Semeter, J., M. Hirsch, F. Lind, A. Coster, P. Erickson, and V. Pankratius, GNSS-ISR data fusion: General framework with application to the high-latitude ionosphere, *Radio Science*, *51*(3), 2015RS005,794, doi:10.1002/2015RS005794, 2016.

Solomon, S. C., P. B. Hays, and V. J. Abreu, The auroral 6300 Å emission: Observations and modeling, *Journal of Geophysical Research: Space Physics*, *93*(A9), 9867–9882, doi:10.1029/JA093iA09p09867, 1988.

Spogli, L., L. Alfonsi, G. De Franceschi, V. Romano, M. H. O. Aquino, and A. Dodson, Climatology of GPS ionospheric scintillations over high and mid-latitude European regions, *Annales Geophysicae*, *27*(9), 3429–3437, doi:10.5194/angeo-27-3429-2009, 2009.

Strangeways, H. J., N. N. Zernov, and V. E. Gherm, Comparison of four methods for transionospheric scintillation evaluation, *Radio Science*, *49*(10), 2014RS005,408, doi:10.1002/2014RS005408, 2014.

Themens, D. R., P. T. Jayachandran, and R. B. Langley, The nature of GPS differential receiver bias variability: An examination in the polar cap region, *Journal of Geophysical Research: Space Physics*, *120*(9), doi:10.1002/2015JA021639, 2015.

Thomas, E. G., J. B. H. Baker, J. M. Ruohoniemi, L. B. N. Clausen, A. J. Coster, J. C. Foster, and P. J. Erickson, Direct observations of the role of convection electric field in the formation of a polar tongue of ionization from storm enhanced density, *Journal of Geophysical Research: Space Physics*, *118*(3), 1180–1189, doi:10.1002/jgra.50116, 2013.

Thorolfsson, A., J.-C. Cerisier, M. Lockwood, P. E. Sandholt, C. Senior, and M. Lester, Simultaneous optical and radar signatures of poleward-moving auroral forms, *Annales Geophysicae*, *18*(9), 1054–1066, doi:10.1007/s00585-000-1054-2, 2000.

Tiwari, S., A. Jain, S. Sarkar, S. Jain, and A. K. Gwal, Ionospheric irregularities at Antarctic using GPS measurements, *Journal of Earth System Science*, *121*(2), 345–353, doi:10.1007/s12040-012-0168-8, 2012.

Tsunoda, R. T., High-latitude F region irregularities: A review and synthesis, *Reviews of Geophysics*, *26*(4), 719–760, doi:10.1029/RG026i004p00719, 1988.

Tsurutani, B. T., et al., Corotating solar wind streams and recurrent geomagnetic activity: A review, *Journal of Geophysical Research: Space Physics*, *111*(A7), doi:10.1029/2005JA011273, 2006.

van der Meeren, C., K. Oksavik, D. Lorentzen, J. I. Moen, and V. Romano, GPS scintillation and irregularities at the front of an ionization tongue in the nightside polar ionosphere, *Journal of Geophysical Research: Space Physics*, *119*(10), 8624–8636, doi:10.1002/2014JA020114, 2014.

van der Meeren, C., K. Oksavik, D. A. Lorentzen, M. T. Rietveld, and L. B. N. Clausen, Severe and localized GNSS scintillation at the poleward edge of the nightside auroral oval during intense substorm aurora, *Journal of Geophysical Research: Space Physics*, *120*(12), doi:10.1002/2015JA021819, 2015.

van der Meeren, C., K. Oksavik, D. A. Lorentzen, L. J. Paxton, and L. B. N. Clausen, Scintillation and irregularities from the nightside part of a sun-aligned polar cap arc, *Journal of Geophysical Research: Space Physics*, *121*, doi:10.1002/2016JA022708, 2016.

Vorobjev, V. G., G. Gustafsson, G. V. Starkov, Y. I. Feldstein, and N. F. Shevnina, Dynamics of day and night aurora during substorms, *Planetary and Space Science*, *23*(2), 269–278, doi:10.1016/0032-0633(75)90132-4, 1975.

Wannberg, G., et al., The EISCAT Svalbard radar: A case study in modern incoherent scatter radar system design, *Radio Science*, *32*(6), 2283–2307, doi:10.1029/97RS01803, 1997.

Weber, E. J., J. A. Klobuchar, J. Buchau, H. C. Carlson, R. C. Livingston, O. de la Beaujardiere, M. McCready, J. G. Moore, and G. J. Bishop, Polar cap F layer patches: Structure and dynamics, *Journal of Geophysical Research: Space Physics*, *91*(A11), 12,121–12,129, doi:10.1029/JA091iA11p12121, 1986.

Wernik, A., J. Secan, and E. Fremouw, Ionospheric irregularities and scintillation, *Advances in Space Research*, *31*(4), 971–981, doi:10.1016/S0273-1177(02)00795-0, 2003.

Xue, J., S. Song, X. Liao, and W. Zhu, Estimating and assessing Galileo navigation system satellite and receiver differential code biases using the ionospheric parameter and differential code bias joint estimation approach with multi-GNSS observations, *Radio Science*, p. 2015RS005797, doi:10.1002/2015RS005797, 2016.

Zhang, Q.-H., et al., Polar cap patch segmentation of the tongue of ionization in the morning convection cell, *Geophysical Research Letters*, *40*(12), 2918–2922, doi:10.1002/grl.50616, 2013.

Zhang, Y., and L. J. Paxton, An empirical Kp-dependent global auroral model based on TIMED/GUVI FUV data, *Journal of Atmospheric and Solar-Terrestrial Physics*, *70*(8–9), 1231–1242, doi:10.1016/j.jastp.2008.03.008, 2008.

Zou, Y., Y. Nishimura, L. R. Lyons, E. F. Donovan, K. Shiokawa, J. M. Ruohoniemi, K. A. McWilliams, and N. Nishitani, Polar cap precursor of nightside auroral oval intensifications using polar cap arcs, *Journal of Geophysical Research: Space Physics*, *120*(12), doi:10.1002/2015JA021816, 2015.

I

Paper I

GPS scintillation and irregularities at the front of an ionization tongue in the nightside polar ionosphere

C. van der Meeren, K. Oksavik, D. A. Lorentzen, J. I. Moen, and V. Romano

Journal of Geophysical Research: Space Physics, Vol. 119, doi:10.1002/2014JA020114 (2014)

AGU PUBLICATIONS

JGR

Journal of Geophysical Research: Space Physics

RESEARCH ARTICLE
10.1002/2014JA020114

Key Points:
- A TOI front is locally structured on scale sizes from decameters to kilometers
- The structuring is localized to and varies along the leading gradient
- Phase spectra are similar inside and in front of the TOI

Correspondence to:
C. van der Meeren,
christer.meeren@ift.uib.no

Citation:
van der Meeren, C., K. Oksavik, D. Lorentzen, J. I. Moen, and V. Romano (2014), GPS scintillation and irregularities at the front of an ionization tongue in the nightside polar ionosphere, *J. Geophys. Res. Space Physics*, *119*, 8624–8636, doi:10.1002/2014JA020114.

Received 22 APR 2014
Accepted 23 SEP 2014
Accepted article online 28 SEP 2014
Published online 16 OCT 2014

The copyright line for this article was changed on 13 DEC 2014 after original online publication.

GPS scintillation and irregularities at the front of an ionization tongue in the nightside polar ionosphere

Christer van der Meeren[1], Kjellmar Oksavik[1,2], Dag Lorentzen[2,3], Jøran Idar Moen[2,4], and Vincenzo Romano[5]

[1]Birkeland Centre for Space Science, Department of Physics and Technology, University of Bergen, Bergen, Norway, [2]University Centre in Svalbard, Longyearbyen, Norway, [3]Birkeland Centre for Space Science, University Centre in Svalbard, Longyearbyen, Norway, [4]Department of Physics, University of Oslo, Oslo, Norway, [5]Istituto Nazionale di Geofisica e Vulcanologia, Rome, Italy

Abstract In this paper we study a tongue of ionization (TOI) on 31 October 2011 which stretched across the polar cap from the Canadian dayside sector to Svalbard in the nightside ionosphere. The TOI front arrived over Svalbard around 1930 UT. We have investigated GPS scintillation and irregularities in relation to this TOI front. This is the first study presenting such detailed multi-instrument data of scintillation and irregularities in relation to a TOI front. Combining data from an all-sky imager, the European Incoherent Scatter Svalbard Radar, the Super Dual Auroral Radar Network Hankasalmi radar, and three GPS scintillation and total electron content (TEC) monitors in Longyearbyen and Ny-Ålesund, we observe bursts of phase scintillation and no amplitude scintillation in relation to the leading gradient of the TOI. Spectrograms of 50 Hz phase measurements show highly localized and variable structuring of the TOI leading gradient, with no structuring or scintillation within the TOI or ahead of the TOI.

1. Introduction

During active geomagnetic conditions, especially southward oriented interplanetary magnetic field (IMF), high-density plasma may be convected from a solar-ionized high-density plasma reservoir in the dayside ionosphere, through the cusp region, and across the polar cap to the nightside auroral oval [*Dungey*, 1961; *Weber et al.*, 1984; *Foster and Doupnik*, 1984; *Buchau et al.*, 1985; *Foster*, 1993; *Foster et al.*, 2005; *Moen et al.*, 2008; *Cousins and Shepherd*, 2010; *Oksavik et al.*, 2010; *Zhang et al.*, 2013a; *Nishimura et al.*, 2014]. This plasma may be segmented in the cusp region into discrete 100–1000 km islands of high-density plasma called *F* region polar cap patches. Several possible patch creation mechanisms have been suggested [e.g., *Carlson*, 2012, and references therein], among them is transient magnetopause reconnection, which has been proposed as the dominant segmentation mechanism [*Lockwood and Carlson*, 1992; *Carlson et al.*, 2002, 2004, 2006; *Lockwood et al.*, 2005; *Moen et al.*, 2006; *Lorentzen et al.*, 2010; *Zhang et al.*, 2013b]. In the absence of segmentation, the plasma may instead form a continuous tongue of ionization (TOI) convecting and extending across the polar cap [*Sato*, 1959; *Knudsen*, 1974; *Foster et al.*, 2005]. Areas of enhanced electron densities such as patches and TOIs show up as regions of 630.0 nm airglow emissions from dissociative recombination of O^{2+} with *F* region electrons creating $O(^1D)$ [*Wickwar et al.*, 1974; *Hosokawa et al.*, 2011]. These emissions are detectable from ground-based optical instruments [e.g., *Buchau et al.*, 1983; *Weber et al.*, 1984; *Lorentzen et al.*, 2004; *Hosokawa et al.*, 2006; *Moen et al.*, 2007; *Nishimura et al.*, 2014].

Large-scale ionospheric plasma structures such as polar cap patches often contain decameter- to kilometer-scale irregularities, particularly on the edges [*Weber et al.*, 1986; *Basu et al.*, 1990, 1991, 1994, 1998; *Moen et al.*, 2012; *Oksavik et al.*, 2012; *Carlson*, 2012, and references therein]. It has been suggested that the Lockwood-Carlson patch segmentation mechanism may initially structure patches through the Kelvin-Helmholtz instability (KHI), creating seed irregularities which allows the gradient drift instability (GDI) to effectively further structure the patch through its transit across the polar cap [*Carlson et al.*, 2007, 2008]. The GDI works on all gradients except where the gradient is exactly antiparallel to the plasma flow, but it is effective primarily at the trailing edges of density enhancements, and it is considered the dominant instability mode in the polar cap [e.g., *Ossakow and Chaturvedi*, 1979; *Keskinen and Ossakow*, 1983; *Buchau et al.*, 1985; *Tsunoda*, 1988; *Basu et al.*, 1990, 1998; *Coker et al.*, 2004; *Prikryl et al.*, 2011a; *Basu et al.*, 1994; *Gondarenko and Guzdar*, 2004a]. Simulations show that these irregularities may propagate from the trailing

AGU Journal of Geophysical Research: Space Physics 10.1002/2014JA020114

edge into the interior of the patch, possibly structuring the whole patch at these scale sizes [*Gondarenko and Guzdar*, 2004b]. Observations have indeed shown that patches may be structured throughout [e.g., *Hosokawa et al.*, 2009].

Irregularities with scale sizes of decameters to kilometers may cause rapid phase and/or amplitude variations in transionospheric signals, such as global navigation satellite system (GNSS) signals [e.g., *Hey et al.*, 1946; *Basu et al.*, 1990, 1998; *Kintner et al.*, 2007]. If the irregularities have sufficiently small scale sizes, the phase and amplitude variations are diffractive in nature and are termed scintillations [e.g., *Mushini et al.*, 2012]. Intense scintillation may cause failure of signal reception due to loss of signal lock [e.g., *Kintner et al.*, 2007], even during solar minimum [*Prikryl et al.*, 2010]. Scintillation is present in both hemispheres [*Prikryl et al.*, 2011b].

Ionospheric scintillations are categorized into amplitude scintillations and phase scintillations. Amplitude scintillations are caused by irregularities with scale sizes of tens of meters to hundreds of meters [e.g., *Kintner et al.*, 2007], more precisely at and below the Fresnel radius, which is approximately 360 m for GPS L1 frequency (1575.42 MHz) and a phase screen altitude of 350 km [e.g., *Forte and Radicella*, 2002]. Amplitude scintillations are normally quantified by the S_4 index, which is the standard deviation of the received power normalized by its mean value [*Briggs and Parkin*, 1963]:

$$S_4^2 = \frac{\langle I^2 \rangle - \langle I \rangle^2}{\langle I \rangle^2}$$

Here I is the power, and the brackets indicate the expected value, in practice replaced by temporal averaging [e.g., *Beach*, 2006]. Phase scintillations are caused by irregularities of scale sizes from hundreds of meters to some kilometers [e.g., *Kintner et al.*, 2007] and are normally quantified by the σ_ϕ index, which is the standard deviation of the detrended carrier phase ϕ [*Fremouw et al.*, 1978]:

$$\sigma_\phi^2 = \langle \phi^2 \rangle - \langle \phi \rangle^2$$

The σ_ϕ index is highly sensitive to refractive larger-scale (lower-frequency) phase variations not pertaining to scintillations [e.g., *Basu et al.*, 1991; *Mushini et al.*, 2012], and careful detrending of the raw phase is needed. Specifically, σ_ϕ is highly sensitive to the detrending filter cutoff frequency. This will be further detailed in section 5.

Performance of GNSS services at high latitudes is of increasing importance in, e.g., offshore and aviation; and understanding scintillation-inducing irregularities is critical for scintillation modeling, forecasting, and mitigation [e.g., *Moen et al.*, 2013]. Much of the research on scintillation is using a statistical approach [e.g., *Spogli et al.*, 2009; *Alfonsi et al.*, 2011a; *Li et al.*, 2010; *Prikryl et al.*, 2010, 2011a; *Tiwari et al.*, 2012]. Some case studies in the Svalbard region have been performed [*De Franceschi et al.*, 2008; *Coker et al.*, 2004; *Mitchell et al.*, 2005]. These studies focus mainly on patches. While patches are known to be structured, it is less known how the TOI is structured. It is readily conceivable that the irregularity processes may differ: Patches may be initially structured by the KHI, and these irregularities are further developed by the GDI. Continuous tongues will not experience this initial KHI structuring. Furthermore, depending on the degree of large-scale structuring within the tongue, there may not be any clear gradients on which the GDI can work. On the other hand, TOIs are regions of steep density gradients where we might expect strong irregularities to be present.

In order to better understand irregularities in relation to TOIs, we present findings of GPS scintillation in relation to the arriving front of a tongue of ionization in the nightside polar cap over Svalbard, using GPS scintillation and total electron content (TEC) monitors, the European Incoherent Scatter (EISCAT) Svalbard Radar (ESR), an optical all-sky airglow imager, and backscatter from Super Dual Auroral Radar Network (SuperDARN) high-frequency (HF) radars. To our knowledge, this is the first paper presenting such a detailed multi-instrument observation of scintillation in the Svalbard region in relation to a TOI.

2. Instrumentation

2.1. GPS Receivers

The GPS data in this study come from three NovAtel GSV4004B GPS Ionospheric Scintillation and TEC Monitors. Two receivers are located in Ny-Ålesund (78.9° GLAT, 11.9° GLON, 76.6° Altitude Adjusted Corrected

AGU Journal of Geophysical Research: Space Physics 10.1002/2014JA020114

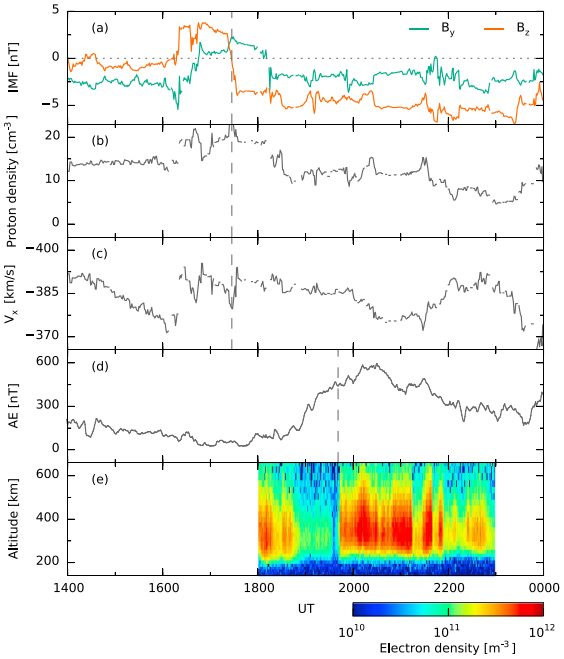

Figure 1. Overview of solar wind parameters, substorm activity, and vertical electron density profiles from the EISCAT Svalbard Radar (ESR) on 31 October 2011: (a) IMF B_y in green and B_z in red, (b) solar wind proton density, (c) solar wind speed, (d) the *AE* index, and (e) ESR vertical electron density profiles over Longyearbyen. The vertical line in Figures 1a–1c marks the time of southward turning of the IMF. The vertical line in Figure 1d corresponds to the sharp gradient in Figure 1e and the time shown in Figure 3c (1941 UT).

Geomagnetic Coordinates (AACGM) latitude [*Baker and Wing*, 1989]) and one in Longyearbyen (78.1° GLAT, 16.0° GLON, 75.5° AACGM latitude).

One of the Ny-Ålesund receivers (hereafter NYA) is operated by the University of Oslo (UiO), Norway. Only 60 s data were available from this receiver. The software produces calibrated TEC mapped to vertical TEC (VTEC) and the S_4 amplitude scintillation index. The software does not produce the phase scintillation index σ_ϕ or the rate of TEC (ROT). The real-time software is developed by *Carrano and Groves* [2006], and the data have been postprocessed using WinTEC-P [*Carrano et al.*, 2009], an extension of WinTEC [*Anghel et al.*, 2008].

The other receiver in Ny-Ålesund (hereafter NYA1) and the receiver in Longyearbyen (hereafter LYB0) are operated by the Istituto Nazionale di Geosica e Vulcanologia (INGV, Italy), as part of the Ionospheric Scintillations Arctic Campaign Coordinated Observations (ISACCO) project [*Franceschi et al.*, 2006]. Data are available online by means of the electronic Space Weather upper atmosphere system [*Romano et al.*, 2008, 2013]. These receivers use NovAtel software [*NovAtel*, 2007]. Raw high-resolution data were available from these two receivers. Uncalibrated slant TEC was available at a 1 Hz cadence. The TEC has been tuned to correspond better to the TEC data of the UiO-operated NYA receiver. This is sufficient for our purposes since we do not require absolute TEC measurements. Furthermore, the slant TEC has been mapped to vertical TEC as done by *Alfonsi et al.* [2011b]. ROT was also available at a 0.1 Hz cadence, but due to noisy data in the LYB0

AGU Journal of Geophysical Research: Space Physics 10.1002/2014JA020114

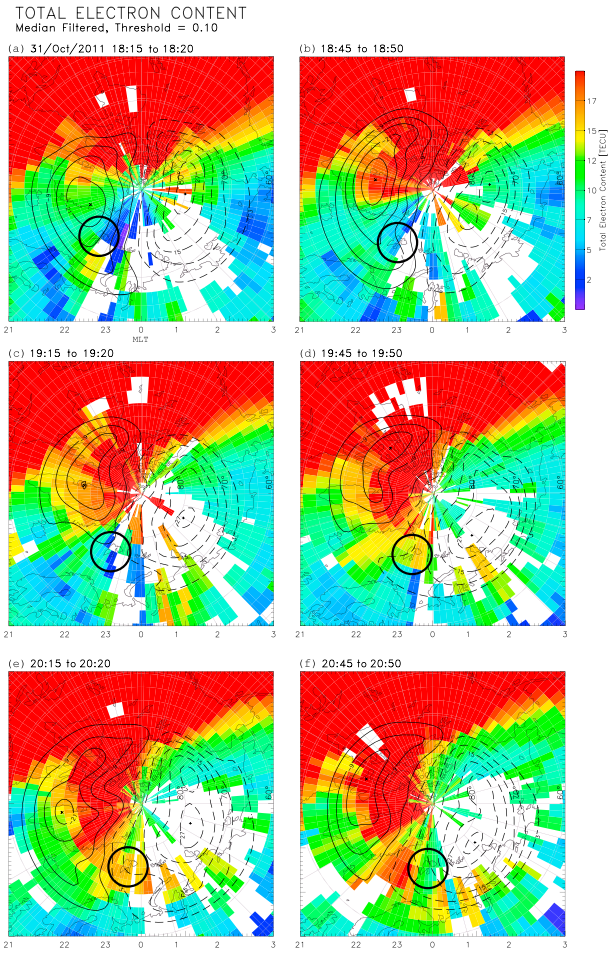

Figure 2. (a–f) The progression of the ionization tongue as it follows the dusk cell of the convection pattern across the polar cap. Svalbard is marked by a black circle. Magnetic local time (MLT) is shown on the horizontal axis.

1 Hz ROT, only 60 s ROT is presented for this receiver. ROT is not influenced by satellite-receiver biases. The S_4 amplitude scintillation index has been calculated by subtracting the S_4 due to ambient noise from the total S_4 in a root-sum-square sense according to the user manual [*NovAtel*, 2007]. The 60 s σ_ϕ phase scintillation index in this study is presented using both a 0.1 Hz and 0.3 Hz detrending filter cutoff frequency. The 0.1 Hz version is calculated by the receiver software in real time, while the 0.3 Hz version is calculated from the 50 Hz raw phase data by us.

AGU Journal of Geophysical Research: Space Physics 10.1002/2014JA020114

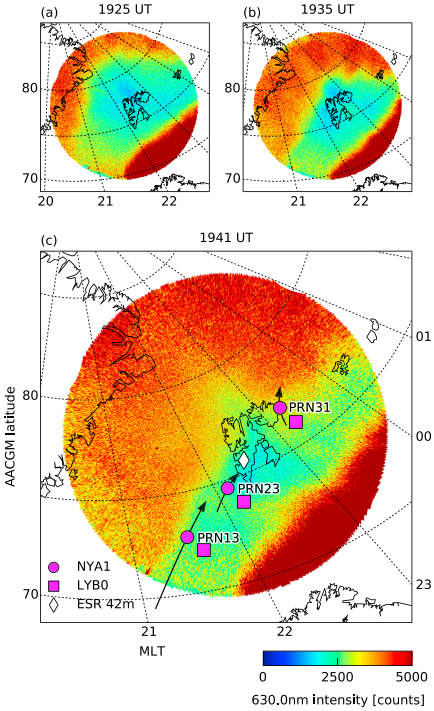

Figure 3. All-sky imager (ASI) data showing the propagation of the (a and b) ionization front leading up to its arrival over Longyearbyen at (c) 1941 UT. A geomagnetic grid is shown using Altitude Adjusted Corrected Geomagnetic Coordinates (AACGM) latitude and magnetic local time (MLT). GPS and ESR ionospheric piercing points (IPPs) are shown in Figure 3c. IPPs are shown for both receiver locations (Ny-Ålesund and Longyearbyen) for three different satellites (PRN13, PRN23, and PRN31). Arrows on the GPS IPPs indicate direction and orbit (IPP location) at 1941 UT ±30 min. The saturation in the lower right of the ASI data is due to auroral emissions. At 300 km projection altitude, the diameter of the all-sky projection is ~1700 km.

For all receivers, some limits were imposed on data validity according to *NovAtel* [2007]. For TEC, ROT, and S_4 data, a lock time of at least 60 s has been required. For σ_ϕ data, a lock time of at least 240 s has been required. In addition to this, we require the elevation to be at least 20° for all data in order to remove clutter associated with multipath signals near the horizon.

2.2. Radars

The EISCAT Svalbard Radar (ESR) is a 500 MHz incoherent scatter radar located in Longyearbyen (78.2° GLAT, 16.0° GLON, 75.5° AACGM latitude). The radar consists of two antennae: One 42 m antenna of fixed, field-aligned orientation (81.6° elevation, 182.1° azimuth), and one fully steerable 32 m antenna. In this study, data from the 42 m antenna are presented. We also use data from the 32 m antenna, pointing toward magnetic south at 30° elevation, in the estimation of the plasma drift velocity and for determining the optimal projection altitude. The data have been analyzed using GUISDAP (Grand Unified Incoherent Scatter Design and Analysis Package) [*Lehtinen and Huuskonen*, 1996].

The Super Dual Auroral Radar Network (SuperDARN) is a network of coherent HF scatter radars in both hemispheres measuring backscatter from field-aligned decameter-scale ionospheric irregularities [*Greenwald et al.*, 1995; *Chisham et al.*, 2007]. In this study we present data from the Hankasalmi SuperDARN radar, which has a field of view covering Svalbard.

2.3. Optics

The all-sky imager (ASI) used in this study is operated by the University of Oslo and located at Ny-Ålesund. We will present data from the 630.0 nm (red) interference filter in order to study airglow from the recombination of *F* region electrons with molecular oxygen. The intensity of the airglow is proportional to the plasma density at *F* region altitudes [e.g., *Hosokawa et al.*, 2011]. The camera is not calibrated and thus the intensity readings will be given in raw counts.

2.4. Solar Wind

Solar wind data are provided by the NASA OMNIWeb service. The data come from the Wind spacecraft, specifically the two instruments Magnetic Field Investigation [*Lepping et al.*, 1995] and Solar Wind Experiment [*Ogilvie et al.*, 1995]. Wind was located at $X = 257\,R_E$, $Y = 32\,R_E$, and $Z = 22\,R_E$ (geomagnetic solar ecliptic coordinates). The data are time shifted to the bow shock by the OMNIWeb service.

AGU Journal of Geophysical Research: Space Physics 10.1002/2014JA020114

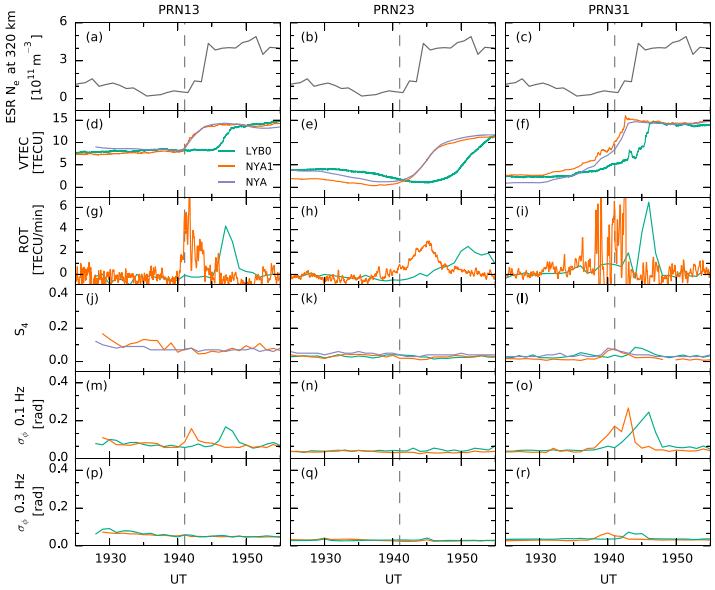

Figure 4. GPS data from three satellites (one per column). (a–c) The panels are identical and show the ESR electron density at 320 km altitude. The GPS parameters are (d–f) vertical total electron content (VTEC), (g–i) rate of TEC (ROT), (j–l) the S_4 amplitude scintillation index (not available for PRN13 in the LYB0 receiver), and the σ_ϕ phase scintillation index calculated using a (m–o) 0.1 Hz cutoff frequency and (p–r) a 0.3 Hz cutoff frequency. The vertical dashed lines mark the time shown in Figure 3c. The 0.3 Hz-detrended σ_ϕ has been calculated by first subtracting a fourth-order polynomial fit from the raw phase, and then filtering the result using a high-pass Butterworth filter with a cutoff frequency of 0.3 Hz. The standard deviation was then computed for each minute of data.

3. Geographic Projection of Data

The optimal altitude for the geographic projection of the GPS data was determined by two separate methods. The first method was correlating the TEC values of GPS PRN20 and the electron density (n_e) values from the ESR 32 m antenna at a time when the GPS ionospheric piercing point (IPP) closely followed the ESR 32 m beam. The second method was the determination of the altitude of the maximum *F* region density around the time of interest, based on the assumption that most of the effects on the GPS signal are located in this region. Both methods yielded a result of 320 km for the projection altitude. In order to further test the phase screen model we also verified, using the ESR, that the vertical electron density profile was in fact dominated by *F* region plasma.

The geographic projection of the ASI data were done using an altitude of 300 km, as recommended by literature [*Hosokawa et al.*, 2011; *Lorentzen et al.*, 2004; *Millward et al.*, 1999]. This projection is sufficient for our purposes because the ASI data are only used as an indicator of enhanced plasma densities in the *F* region.

4. Observations

4.1. Overview

A campaign was run at the ESR on 31 October 2011, 18–23 UT. Figure 1 shows an overview of solar wind parameters, substorm activity, and the ESR vertical electron density profiles on this day. The vertical line in Figures 1a–1c marks the time of a southward turning of the IMF, which causes high-density plasma from the dayside to be convected into the polar cap. Figure 1d shows the *AE* index, whose positive bay signature is

AGU Journal of Geophysical Research: Space Physics 10.1002/2014JA020114

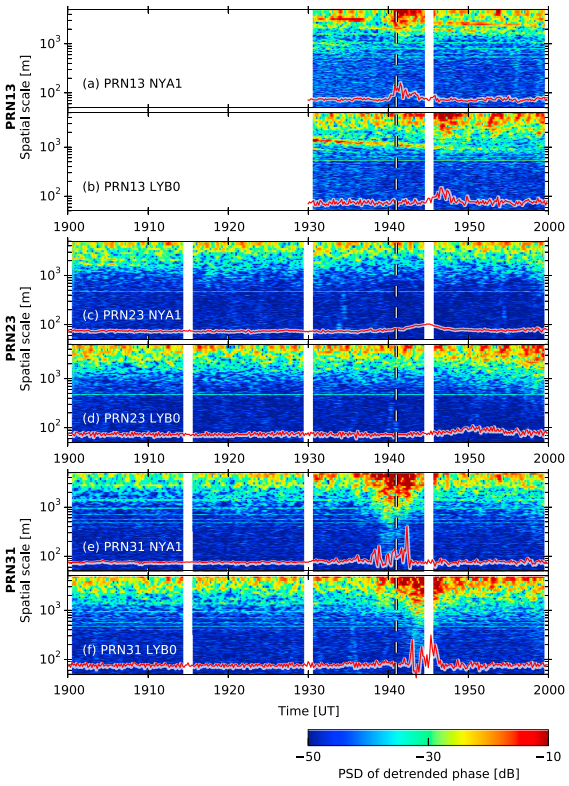

Figure 5. Power spectral densities (PSD) of detrended raw 50 Hz phase data for each satellite-receiver pair. The dashed line indicates 1941 UT. The red line shows the 10 s average of 1 Hz ROT (arbitrary units) as an indicator of the TOI leading edge. The white areas in the spectrogram are due to data gaps.

indicative of a substorm. Figure 1e shows electron density from the ESR 42 m field-aligned antenna. When the front of the TOI passes overhead at 1941 UT, the ESR data show a sudden enhancement of *F* region electron density. This is further enhanced, though not as suddenly, until 2000 UT. The enhanced densities seem to persist until a sudden drop around 2115 UT. Figure 2 shows the progression of the TOI across the polar cap in the antisunward portion of the dusk convection cell. The TOI begins to form on the dayside around 1815 UT (Figure 2a). The front of the TOI arrives over Svalbard around 1930 UT.

4.2. GPS Parameters

Figure 3 presents ASI data showing the propagation of the TOI front and the ionospheric piercing points (IPPs) of the ESR and the GPS satellites at 320 km altitude. The IPP drift speeds at 1941 UT are 167 m/s, 66 m/s, and 60 m/s for PRN13, PRN23, and PRN31, respectively. The drift speed of the plasma is estimated to be 430–480 m/s, based on calculations of the delay between the appearance of the TOI front in the two ESR antennae. Combined with a visual estimation of the plasma drift direction (135–139° geographic east) this yields relative drift velocities of 500–560 m/s, 450–500 m/s, and 460–520 m/s for PRN13, PRN23, and PRN31, respectively.

AGU Journal of Geophysical Research: Space Physics 10.1002/2014JA020114

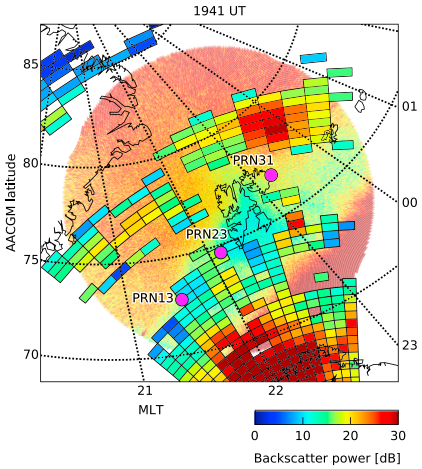

Figure 6. SuperDARN backscatter power overlaid on top of all-sky imager data (for reference). GPS ionospheric piercing points are shown together with an Altitude Adjusted Corrected Geomagnetic Coordinates (AACGM) latitude and magnetic local time (MLT) grid.

Figure 4 shows data from the three GPS satellites and the ESR electron density at 320 km altitude. The ESR data (Figures 4a–4c are all identical) show a sudden increase of the electron density to around 4 times the background level as the TOI front passes overhead. In the PRN13 data, we can see an abrupt increase in the VTEC (Figure 4d), also clearly visible in the ROT (Figure 4g), just as the TOI front hits. This is seen first in the two Ny-Ålesund receivers and some minutes later in the Longyearbyen receiver, as one would expect with the current geometry of receivers and drifting plasma structures. Coincident with this TEC gradient at both receiver locations is a burst of weak phase scintillation (Figure 4m), reaching values of $\sigma_\phi = 0.15$ radians before returning to quiet levels just after the TOI front passes and the VTEC stabilizes (and the ROT returns to zero). The S_4 amplitude scintillation index (Figure 4j) is practically flat. There are no clear changes in S_4 as the TOI front intersects the signal paths.

In the PRN23 data, the VTEC increase (Figure 4e) is softer than in the PRN13 data. This is also seen in the weaker and more gentle ROT increases. There is no indication of any phase or amplitude scintillation (Figures 4k and 4n).

In the PRN31 data, even though the TEC increase (Figure 4f) seems softer than in the PRN13 data, the ROT indicates a structured and steep TEC gradient. Fine structure is also visible in the 1 Hz TEC data from LYB0 and NYA1. There are clear and moderate spikes in σ_ϕ (Figure 4o) coinciding with the arrival of the TOI front, reaching values of $\sigma_\phi = 0.25$ radians. S_4 is very small ($S_4 < 0.1$), though very slight enhancements can be seen colocated with the gradient.

For all satellite-receiver pairs, Figures 4p–4r clearly demonstrates the sensitivity of σ_ϕ to the detrending cutoff frequency. When detrended with a cutoff frequency of 0.3 Hz, the σ_ϕ values are reduced significantly compared to detrending using 0.1 Hz.

Figure 5 shows spectrograms of phase variations calculated from detrended raw 50 Hz phase data. The phase variations have been converted to spatial scale sizes by taking into account the relative motion between the plasma and the GPS IPPs. The spectrograms provide a more complete picture of phase variations than σ_ϕ and are not distorted by the choice of detrending cutoff frequency, since the cutoff frequency only specifies the frequency limit below which (i.e., the spatial scale above which) information is suppressed. A 32,768 m wide Hamming window was used in the calculation of the spectrogram.

In the PRN13 data (Figures 5a and 5b), there is increased power in phase variations at frequencies corresponding to spatial scales of 3–5 km colocated with the gradient (the red lines show the ROT). The PRN23 spectrograms (Figures 5c and 5d) show no such increase in phase variations. The PRN31 spectrograms (Figures 5e and 5f) clearly shows increased power at a wide range of spatial scales, most strongly at ~5 km but still visible all the way down to ~100 m, where it reaches the noise level. The SuperDARN data in Figure 6 show that there is strongly enhanced backscatter power (~30 dB) in the enhanced-density region upstream of PRN31. This is a clear indication of decameter-scale irregularities and supports the wide range of scale sizes shown in the spectrogram.

AGU Journal of Geophysical Research: Space Physics 10.1002/2014JA020114

5. Discussion

We have identified the front of a TOI arriving over Svalbard around 1941 UT on 31 October 2011. Electron density data from the ESR show an increase to about 4 times the background density. The signals of three GPS satellites intersected the TOI front almost simultaneously. Phase scintillations were detected at the two satellites experiencing the steepest TEC gradient (PRN13 and PRN31), and the scintillation seemed very well colocated with the TOI leading gradient. The phase spectra showed phase variations at spatial scales of 3–5 km for PRN13 and 100 m–5 km for PRN31.

5.1. Cutoff Frequency and σ_ϕ

The increases in σ_ϕ alone might indicate a structured TOI gradient, but the σ_ϕ index as it is normally computed is not necessarily a reliable indicator of diffractive structuring at high latitudes [*Forte and Radicella*, 2002; *Forte*, 2005; *Beach*, 2006]. While the S_4 amplitude scintillation index is mainly sensitive to irregularity scale sizes at and below the first Fresnel radius, the σ_ϕ phase scintillation index is highly sensitive to irregularity scale sizes above the Fresnel radius [e.g., *Basu et al.*, 1991]. Such larger-scale sizes correspond to lower-frequency phase fluctuations not pertaining properly to scintillations [e.g., *Forte and Radicella*, 2002]. Thus, the σ_ϕ index is highly sensitive to the cutoff frequency of the detrending filter, whose function is to remove low-frequency phase variations. The present study clearly exemplifies the dependency of σ_ϕ on the cutoff frequency (Figures 4m–4r). Examples of the different sensitivity of S_4 and σ_ϕ to the cutoff frequency can be seen in *Forte* [2005].

Several past studies have shown that a detrending cutoff frequency of 0.1 Hz is too low to properly remove refractive phase shifts at high latitudes, which can lead to TEC gradients themselves significantly influencing σ_ϕ [*Forte and Radicella*, 2002; *Béniguel et al.*, 2004; *Forte*, 2005; *Beach*, 2006]. A cutoff frequency of 0.1 Hz is prevalent in the GNSS community and was originally used in the Wideband satellite experiment of *Fremouw et al.* [1978]. A higher cutoff frequency can mitigate the refractive effects [*Béniguel et al.*, 2009; *Mushini et al.*, 2012]. Other phase scintillation indices based on entirely different calculations or detrending methods have been proposed and may be more suited for high-latitude scintillation studies [*Forte*, 2005; *Mushini et al.*, 2012], but these have not yet been widely used in literature and may have problems of their own [*Mushini et al.*, 2012].

We suggest that spectrograms of detrended phase like Figure 5 may provide a potentially better way to study ionospheric irregularities than phase scintillation indices. First, this avoids the problematic sensitivity of σ_ϕ to the detrending filter cutoff frequency. Second, spectrograms like Figure 5 provide a more complete view of the irregularity scale sizes present in the plasma, instead of presenting an aggregate number indicating the degree of structuring across a wide range of scale sizes.

5.2. Geometrical Effects on Scintillation

Figure 4 showed significant differences in scintillation levels at three different locations (cf. Figure 3). Can geometrical effects cause these differences? While satellites in polar orbits may experience enhanced scintillation from field-aligned irregularities when the signal path aligns with the magnetic field, this has been found not to be a concern for GPS satellites [*Forte and Radicella*, 2004]. GPS scintillation values may however be overestimated at low elevation angles, and while S_4 and σ_ϕ can be projected to the vertical, this is not trivial and depends on, e.g., the anisotropy of the irregularities [*Spogli et al.*, 2009; *Alfonsi et al.*, 2011a]. When the TOI gradient intersected the signal paths, the elevation angles were 25–30°, 46–53°, and 41–42° for PRN13, PRN23, and PRN31, respectively. While PRN23 has the highest elevation angle and the lowest scintillation levels, PRN31 shows higher scintillation levels than PRN13 even though the elevation angle is greater for PRN31 than for PRN13. Thus, the different elevation angles cannot be solely responsible for the observed differences in scintillation levels. Figure 5 indicates that there is in fact structuring at various scales, and we conclude that even though the σ_ϕ may be overestimated due to detrending or geometrical effects, the variability in σ_ϕ along the leading edge of the TOI must be real.

5.3. Localized Structuring and Plasma Instabilities

The generally low scintillation values (both σ_ϕ and S_4) indicate that the leading TOI gradient is not severely structured. It is however clear from Figure 5 that the front of the TOI is structured at a variety of scale sizes. It is interesting to note the spatial variation of the structuring: First, only the TOI gradient itself seem structured, with no structuring inside the TOI (at least 630–720 km from the front based on PRN31 at 2000 UT,

AGU Journal of Geophysical Research: Space Physics 10.1002/2014JA020114

Figure 5e). Second, the structuring varies significantly along the TOI gradient at distances of several hundred kilometers (the IPP distances are 360 km for PRN13–PRN23 and 550 km for PRN23–PRN31).

It is clear from Figure 5 that the structuring is highly localized to the gradient itself (as indicated by the red line), and that the spectra in the high-density region after the TOI gradient has passed are similar to that of the low-density region before the arrival of the TOI front. While the GDI works on all density gradients, except where the gradient is antiparallel to the plasma flow, it is most effective at trailing edges where the gradient is parallel with the flow. In the case of patches, the GDI may structure the whole patch starting at the trailing edge and working its way toward the leading edge [*Gondarenko and Guzdar*, 2004b]. The present observations indicate that the GDI has not yet developed irregularities from a trailing edge or a structured area through the leading edge of the TOI. Instead, the GDI may be working to some degree along the leading edge of the TOI. Since the GDI is not very effective at leading edges of drifting plasma structures, this means that the GDI may be enhanced by mesoscale flows not visible in our data [e.g., *Grocott et al.*, 2004; *Lyons et al.*, 2011; *Zou et al.*, 2009; *Nishimura et al.*, 2014]. Another possibility is that the leading TOI gradient may not always or everywhere be entirely antiparallel to the plasma flow. Figure 3 shows this: While the leading TOI edge seems straight and perpendicular to the flow in Figure 3c, it is clear from Figures 3a and 3b that this was not the case some minutes earlier. This has implications for the effectiveness of the GDI and could provide an explanation for the differences seen at three different locations along the TOI front. In other words, it may be important to look at the history of the TOI edge morphology.

It is also possible that other instability processes may cause the observed irregularities. *Nishimura et al.* [2014] found flow shears along the edges of a polar cap patch, which persisted as the patch drifted across the polar cap. Such flow shears may be a source of energy for the KHI. *Oksavik et al.* [2011, 2012] have suggested that the KHI may be efficient at spatial scales greater than a few kilometers, so this process may not be important for the structuring we observe at the smallest scales (hundreds of meters). However, our data set cannot exclude the KHI mechanism. In situ measurements [e.g., *Moen et al.*, 2012] of the TOI would be desirable.

5.4. HF Backscatter Versus Amplitude Scintillation

Figure 6 shows HF backscatter in the region close to PRN31. HF signals backscatter from field-aligned decameter-scale irregularities [*Greenwald et al.*, 1995]. Figure 6 then indicates decameter-scale irregularities in the region of the TOI intersecting the PRN31 IPP. Amplitude scintillations arise from irregularities of scale sizes between decameters and hundreds of meters. The PRN31 data (Figure 4l) show no significant amplitude scintillations inside the TOI and only very weak amplitude scintillations at the TOI gradient. This may suggest that the decameter-scale irregularities in this case are not strong enough to cause significant amplitude scintillation of the GPS signal. In situ measurements would be required to quantify the irregularities at these scale sizes.

6. Conclusions

We have studied the occurrence and nature of GPS ionospheric scintillation at the leading edge of a tongue of ionization (TOI) on 31 October 2011 over Svalbard. Our results indicate the following:

1. The front of the TOI is structured on scale sizes from tens of meters to several kilometers, and the structuring varies significantly along the leading TOI edge at distances of several hundred kilometers.
2. The scintillation and structuring are highly localized to the TOI density gradient. There is no scintillation and no structuring of impact to GPS signals seen well inside the high-density TOI (hundreds of kilometers from the TOI leading edge) as it traverses the nightside polar cap.
3. The phase spectra are similar in the low-density and high-density regions inside and in front of the TOI. It is only at the TOI edge that the spectra differ.
4. We also suggest that spectrograms of detrended phase may be a better way to characterize ionospheric irregularities than is the σ_ϕ index, which is sensitive to the detrending filter cutoff frequency.

In situ measurements of the TOI, such as sounding rocket measurements, would be needed to determine which mechanism (GDI and/or KHI) dominates the production of irregularities at the leading gradient of the TOI.

AGU Journal of Geophysical Research: Space Physics 10.1002/2014JA020114

Acknowledgments

The EISCAT data are available from http://eiscat.se. The UiO ASI data are available at http://tid.uio.no/plasma/aurora. The IMF and solar wind data were provided by the NASA OMNIWeb service (http://omniweb.gsfc.nasa.gov). The *AE* index was retrieved from the World Data Center for Geomagnetism, Kyoto (http://wdc.kugi.kyoto-u.ac.jp). Figure 2 was made using the tools at the Virginia Tech SuperDARN website (http://vt.superdarn.org/tiki-index.php). The website also provides information for SuperDARN data access. The GPS data can be made available upon request from the author. This study was supported by the Research Council of Norway under contracts 223252/F50, 212014/F50, 208006/F50, 230935/F50, and 230996/F50. EISCAT is an international association supported by research organizations in China (CRIRP), Finland (SA), Japan (NIPR and STEL), Norway (NFR), Sweden (VR), and the United Kingdom (NERC). The Hankasalmi SuperDARN radar is operated by the Radio and Space Physics Plasma Group at the University of Leicester in conjunction with the Finnish Meteorological Institute, Helsinki. We thank PNRA (Italian National Program for Antarctic Researches) and POLARNET-CNR for supporting the ISACCO GNSS network. We would especially like to thank Kshitija Deshpande at Virginia Tech for fruitful discussions at the 2014 CEDAR workshop and Bjørn Lybekk at the University of Oslo for providing the UiO GPS data.

Alan Rodger thanks Knut Jacobsen and another reviewer for their assistance in evaluating this paper.

References

Alfonsi, L., L. Spogli, G. De Franceschi, V. Romano, M. Aquino, A. Dodson, and C. N. Mitchell (2011a), Bipolar climatology of GPS ionospheric scintillation at solar minimum, *Radio Sci.*, *46*, RS0D05, doi:10.1029/2010RS004571.

Alfonsi, L., L. Spogli, J. Tong, G. De Franceschi, V. Romano, A. Bourdillon, M. Le Huy, and C. Mitchell (2011b), GPS scintillation and TEC gradients at equatorial latitudes in April 2006, *Adv. Space Res.*, *47*(10), 1750–1757, doi:10.1016/j.asr.2010.04.020.

Anghel, A., A. Astilean, T. Letia, and A. Komjathy (2008), Near real-time monitoring of the ionosphere using dual frequency GPS data in a Kalman filter approach, in *IEEE International Conference on Automation, Quality and Testing, Robotics, 2008. AQTR 2008*, 54–58, doi:10.1109/AQTR.2008.4588793.

Baker, K. B., and S. Wing (1989), A new magnetic coordinate system for conjugate studies at high latitudes, *J. Geophys. Res.*, *94*(A7), 9139–9143, doi:10.1029/JA094iA07p09139.

Basu, S., S. Basu, E. MacKenzie, W. R. Coley, J. R. Sharber, and W. R. Hoegy (1990), Plasma structuring by the gradient drift instability at high latitudes and comparison with velocity shear driven processes, *J. Geophys. Res.*, *95*(A6), 7799–7818, doi:10.1029/JA095iA06p07799.

Basu, S., S. Basu, E. Costa, C. Bryant, C. E. Valladares, and R. C. Livingston (1991), Interplanetary magnetic field control of drifts and anisotropy of high-latitude irregularities, *Radio Sci.*, *26*(4), 1079–1103, doi:10.1029/91RS00586.

Basu, S., S. Basu, P. K. Chaturvedi, and C. M. Bryant (1994), Irregularity structures in the cusp/cleft and polar cap regions, *Radio Sci.*, *29*(1), 195–207, doi:10.1029/93RS01515.

Basu, S., E. J. Weber, T. W. Bullett, M. J. Keskinen, E. MacKenzie, P. Doherty, R. Sheehan, H. Kuenzler, P. Ning, and J. Bongiolatti (1998), Characteristics of plasma structuring in the cusp/cleft region at Svalbard, *Radio Sci.*, *33*(6), 1885–1899, doi:10.1029/98RS01597.

Beach, T. L. (2006), Perils of the GPS phase scintillation index (σ_ϕ), *Radio Sci.*, *41*, RS5S31, doi:10.1029/2005RS003356.

Béniguel, Y., B. Forte, S. M. Radicella, H. J. Strangeways, V. E. Gherm, and N. N. Zernov (2004), Scintillations effects on satellite to earth links for telecommunication and navigation purposes, *Ann. Geophys.*, *47*(2-3), 1179–1199, doi:10.4401/ag-3293.

Béniguel, Y., et al. (2009), Ionospheric scintillation monitoring and modelling, *Ann. Geophys.*, *52*(3-4), 391–416, doi:10.4401/ag-4595.

Briggs, B., and I. Parkin (1963), On the variation of radio star and satellite scintillations with zenith angle, *J. Atmos. Terr. Phys.*, *25*(6), 339–366, doi:10.1016/0021-9169(63)90150-8.

Buchau, J., B. W. Reinisch, E. J. Weber, and J. G. Moore (1983), Structure and dynamics of the winter polar cap f region, *Radio Sci.*, *18*(6), 995–1010, doi:10.1029/RS018i006p00995.

Buchau, J., E. J. Weber, D. N. Anderson, H. C. Carlson, J. G. Moore, B. W. Reinisch, and R. C. Livingston (1985), Ionospheric structures in the polar cap: Their origin and relation to 250-MHz scintillation, *Radio Sci.*, *20*(3), 325–338, doi:10.1029/RS020i003p00325.

Carlson, H. C. (2012), Sharpening our thinking about polar cap ionospheric patch morphology, research, and mitigation techniques, *Radio Sci.*, *47*, RS0L21, doi:10.1029/2011RS004946.

Carlson, H. C., K. Oksavik, J. Moen, A. P. van Eyken, and P. Guio (2002), ESR mapping of polar-cap patches in the dark cusp, *Geophys. Res. Lett.*, *29*(10), 24–1–24–4, doi:10.1029/2001GL014087.

Carlson, H. C., K. Oksavik, J. Moen, and T. Pedersen (2004), Ionospheric patch formation: Direct measurements of the origin of a polar cap patch, *Geophys. Res. Lett.*, *31*, L08806, doi:10.1029/2003GL018166.

Carlson, H. C., J. Moen, K. Oksavik, C. P. Nielsen, I. W. McCrea, T. R. Pedersen, and P. Gallop (2006), Direct observations of injection events of subauroral plasma into the polar cap, *Geophys. Res. Lett.*, *33*, L05103, doi:10.1029/2005GL025230.

Carlson, H. C., T. Pedersen, S. Basu, M. Keskinen, and J. Moen (2007), Case for a new process, not mechanism, for cusp irregularity production, *J. Geophys. Res.*, *112*, A11304, doi:10.1029/2007JA012384.

Carlson, H. C., K. Oksavik, and J. Moen (2008), On a new process for cusp irregularity production, *Ann. Geophys.*, *26*(9), 2871–2885, doi:10.5194/angeo-26-2871-2008.

Carrano, C. S., and K. Groves (2006), The GPS segment of the AFRL-SCINDA global network and the challenges of real-time TEC estimation in the equatorial ionosphere, *Proceedings of the 2006 National Technical Meeting of The Institute of Navigation*, pp. 1036–1047, Monterey, Calif.

Carrano, C. S., A. Anghel, R. A. Quinn, and K. M. Groves (2009), Kalman filter estimation of plasmaspheric total electron content using GPS, *Radio Sci.*, *44*, RS0A10, doi:10.1029/2008RS004070.

Chisham, G., et al. (2007), A decade of the super dual auroral radar network (SuperDARN): Scientific achievements, new techniques and future directions, *Surv. Geophys.*, *28*(1), 33–109, doi:10.1007/s10712-007-9017-8.

Coker, C., G. S. Bust, R. A. Doe, and T. L. Gaussiran (2004), High-latitude plasma structure and scintillation, *Radio Sci.*, *39*, RS1S15, doi:10.1029/2002RS002833.

Cousins, E. D. P., and S. G. Shepherd (2010), A dynamical model of high-latitude convection derived from SuperDARN plasma drift measurements, *J. Geophys. Res.*, *115*, A12329, doi:10.1029/2010JA016017.

De Franceschi, G., L. Alfonsi, V. Romano, M. Aquino, A. Dodson, C. N. Mitchell, P. Spencer, and A. W. Wernik (2008), Dynamics of high-latitude patches and associated small-scale irregularities during the October and November 2003 storms, *J. Atmos. Sol. Terr. Phys.*, *70*(6), 879–888, doi:10.1016/j.jastp.2007.05.018.

Dungey, J. W. (1961), Interplanetary magnetic field and the auroral zones, *Phys. Rev. Lett.*, *6*(2), 47–48, doi:10.1103/PhysRevLett.6.47.

Forte, B. (2005), Optimum detrending of raw GPS data for scintillation measurements at auroral latitudes, *J. Atmos. Sol. Terr. Phys.*, *67*(12), 1100–1109, doi:10.1016/j.jastp.2005.01.011.

Forte, B., and S. M. Radicella (2002), Problems in data treatment for ionospheric scintillation measurements, *Radio Sci.*, *37*(6), 1096, doi:10.1029/2001RS002508.

Forte, B., and S. M. Radicella (2004), Geometrical control of scintillation indices: What happens for GPS satellites, *Radio Sci.*, *39*, RS5014, doi:10.1029/2002RS002852.

Foster, J. C. (1993), Storm time plasma transport at middle and high latitudes, *J. Geophys. Res.*, *98*(A2), 1675–1689, doi:10.1029/92JA02032.

Foster, J. C., and J. R. Doupnik (1984), Plasma convection in the vicinity of the dayside cleft, *J. Geophys. Res.*, *89*(A10), 9107–9113, doi:10.1029/JA089iA10p09107.

Foster, J. C., et al. (2005), Multiradar observations of the polar tongue of ionization, *J. Geophys. Res.*, *110*, A09S31, doi:10.1029/2004JA010928.

Franceschi, G. D., L. Alfonsi, and V. Romano (2006), ISACCO: An Italian project to monitor the high latitudes ionosphere by means of GPS receivers, *GPS Solutions*, *10*(4), 263–267, doi:10.1007/s10291-006-0036-6.

Fremouw, E. J., R. L. Leadabrand, R. C. Livingston, M. D. Cousins, C. L. Rino, B. C. Fair, and R. A. Long (1978), Early results from the DNA wideband satellite experiment-Complex-signal scintillation, *Radio Sci.*, *13*(1), 167–187, doi:10.1029/RS013i001p00167.

Gondarenko, N. A., and P. N. Guzdar (2004a), Density and electric field fluctuations associated with the gradient drift instability in the high-latitude ionosphere, *Geophys. Res. Lett.*, *31*, L11802, doi:10.1029/2004GL019703.

AGU Journal of Geophysical Research: Space Physics 10.1002/2014JA020114

Gondarenko, N. A., and P. N. Guzdar (2004b), Plasma patch structuring by the nonlinear evolution of the gradient drift instability in the high-latitude ionosphere, *J. Geophys. Res.*, *109*, A09301, doi:10.1029/2004JA010504.
Greenwald, R. A., et al. (1995), DARN/SuperDARN, *Space Sci. Rev.*, *71*(1-4), 761–796, doi:10.1007/BF00751350.
Grocott, A., T. K. Yeoman, R. Nakamura, S. W. H. Cowley, H. U. Frey, H. Rème, and B. Klecker (2004), Multi-instrument observations of the ionospheric counterpart of a bursty bulk flow in the near-earth plasma sheet, *Ann. Geophys.*, *22*(4), 1061–1075, doi:10.5194/angeo-22-1061-2004.
Hey, J. S., S. J. Parsons, and J. W. Phillips (1946), Fluctuations in cosmic radiation at radio-frequencies, *Nature*, *158*(4007), 234–234, doi:10.1038/158234a0.
Hosokawa, K., K. Shiokawa, Y. Otsuka, A. Nakajima, T. Ogawa, and J. D. Kelly (2006), Estimating drift velocity of polar cap patches with all-sky airglow imager at Resolute Bay, Canada, *Geophys. Res. Lett.*, *33*, L15111, doi:10.1029/2006GL026916.
Hosokawa, K., K. Shiokawa, Y. Otsuka, T. Ogawa, J.-P. St-Maurice, G. J. Sofko, and D. A. Andre (2009), Relationship between polar cap patches and field-aligned irregularities as observed with an all-sky airglow imager at Resolute Bay and the PolarDARN radar at Rankin inlet, *J. Geophys. Res.*, *114*, A03306, doi:10.1029/2008JA013707.
Hosokawa, K., J. I. Moen, K. Shiokawa, and Y. Otsuka (2011), Decay of polar cap patch, *J. Geophys. Res.*, *116*, A05306, doi:10.1029/2010JA016297.
Keskinen, M. J., and S. L. Ossakow (1983), Theories of high-latitude ionospheric irregularities: A review, *Radio Sci.*, *18*(6), 1077–1091, doi:10.1029/RS018i006p01077.
Kintner, P. M., B. M. Ledvina, and E. R. de Paula (2007), GPS and ionospheric scintillations, *Space Weather*, *5*, S09003, doi:10.1029/2006SW000260.
Knudsen, W. C. (1974), Magnetospheric convection and the high-latitude F2 ionosphere, *J. Geophys. Res.*, *79*(7), 1046–1055, doi:10.1029/JA079i007p01046.
Lehtinen, M. S., and A. Huuskonen (1996), General incoherent scatter analysis and GUISDAP, *J. Atmos. Terr. Phys.*, *58*(1-4), 435–452, doi:10.1016/0021-9169(95)00047-X.
Lepping, R. P., et al. (1995), The WIND magnetic field investigation, *Space Sci. Rev.*, *71*(1-4), 207–229, doi:10.1007/BF00751330.
Li, G., B. Ning, Z. Ren, and L. Hu (2010), Statistics of GPS ionospheric scintillation and irregularities over polar regions at solar minimum, *GPS Solutions*, *14*(4), 331–341, doi:10.1007/s10291-009-0156-x.
Lockwood, M., and H. C. Carlson (1992), Production of polar cap electron density patches by transient magnetopause reconnection, *Geophys. Res. Lett.*, *19*(17), 1731–1734, doi:10.1029/92GL01993.
Lockwood, M., J. A. Davies, J. Moen, A. P. van Eyken, K. Oksavik, I. W. McCrea, and M. Lester (2005), Motion of the dayside polar cap boundary during substorm cycles: II. Generation of poleward-moving events and polar cap patches by pulses in the magnetopause reconnection rate, *Ann. Geophys.*, *23*(11), 3513–3532, doi:10.5194/angeo-23-3513-2005.
Lorentzen, D. A., N. Shumilov, and J. Moen (2004), Drifting airglow patches in relation to tail reconnection, *Geophys. Res. Lett.*, *31*, L02806, doi:10.1029/2003GL017785.
Lorentzen, D. A., J. Moen, K. Oksavik, F. Sigernes, Y. Saito, and M. G. Johnsen (2010), In situ measurement of a newly created polar cap patch, *J. Geophys. Res.*, *115*, A12323, doi:10.1029/2010JA015710.
Lyons, L. R., Y. Nishimura, H.-J. Kim, E. Donovan, V. Angelopoulos, G. Sofko, M. Nicolls, C. Heinselman, J. M. Ruohoniemi, and N. Nishitani (2011), Possible connection of polar cap flows to pre- and post-substorm onset PBIs and streamers, *J. Geophys. Res.*, *116*, A12225, doi:10.1029/2011JA016850.
Millward, G. H., R. J. Moffett, H. F. Balmforth, and A. S. Rodger (1999), Modeling the ionospheric effects of ion and electron precipitation in the cusp, *J. Geophys. Res.*, *104*(A11), 24,603–24,612, doi:10.1029/1999JA900249.
Mitchell, C. N., L. Alfonsi, G. De Franceschi, M. Lester, V. Romano, and A. W. Wernik (2005), GPS TEC and scintillation measurements from the polar ionosphere during the October 2003 storm, *Geophys. Res. Lett.*, *32*, L12S03, doi:10.1029/2004GL021644.
Moen, J., H. C. Carlson, K. Oksavik, C. P. Nielsen, S. E. Pryse, H. R. Middleton, I. W. McCrea, and P. Gallop (2006), EISCAT observations of plasma patches at sub-auroral cusp latitudes, *Ann. Geophys.*, *24*(9), 2363–2374, doi:10.5194/angeo-24-2363-2006.
Moen, J., N. Gulbrandsen, D. A. Lorentzen, and H. C. Carlson (2007), On the MLT distribution of f region polar cap patches at night, *Geophys. Res. Lett.*, *34*, L14113, doi:10.1029/2007GL029632.
Moen, J., X. C. Qiu, H. C. Carlson, R. Fujii, and I. W. McCrea (2008), On the diurnal variability in F2-region plasma density above the EISCAT Svalbard radar, *Ann. Geophys.*, *26*(8), 2427–2433, doi:10.5194/angeo-26-2427-2008.
Moen, J., K. Oksavik, T. Abe, M. Lester, Y. Saito, T. A. Bekkeng, and K. S. Jacobsen (2012), First in-situ measurements of HF radar echoing targets, *Geophys. Res. Lett.*, *39*, L07104, doi:10.1029/2012GL051407.
Moen, J., K. Oksavik, L. Alfonsi, Y. Daabakk, V. Romano, and L. Spogli (2013), Space weather challenges of the polar cap ionosphere, *J. Space Weather Space Clim.*, *3*, A02, doi:10.1051/swsc/2013025.
Mushini, S. C., P. T. Jayachandran, R. B. Langley, J. W. MacDougall, and D. Pokhotelov (2012), Improved amplitude- and phase-scintillation indices derived from wavelet detrended high-latitude GPS data, *GPS Solutions*, *16*(3), 363–373, doi:10.1007/s10291-011-0238-4.
Nishimura, Y., et al. (2014), Day-night coupling by a localized flow channel visualized by polar cap patch propagation, *Geophys. Res. Lett.*, *41*, 3701–3709, doi:10.1002/2014GL060301.
NovAtel (2007), *GSV4004B GPS Ionospheric Scintillation & TEC Monitor User's Manual*.
Ogilvie, K. W., et al. (1995), SWE, a comprehensive plasma instrument for the WIND spacecraft, *Space Sci. Rev.*, *71*(1-4), 55–77, doi:10.1007/BF00751326.
Oksavik, K., V. L. Barth, J. Moen, and M. Lester (2010), On the entry and transit of high-density plasma across the polar cap, *J. Geophys. Res.*, *115*, A12308, doi:10.1029/2010JA015817.
Oksavik, K., J. I. Moen, E. H. Rekaa, H. C. Carlson, and M. Lester (2011), Reversed flow events in the cusp ionosphere detected by SuperDARN HF radars, *J. Geophys. Res.*, *116*, A12303, doi:10.1029/2011JA016788.
Oksavik, K., J. Moen, M. Lester, T. A. Bekkeng, and J. K. Bekkeng (2012), In situ measurements of plasma irregularity growth in the cusp ionosphere, *J. Geophys. Res.*, *117*, A11301, doi:10.1029/2012JA017835.
Ossakow, S. L., and P. K. Chaturvedi (1979), Current convective instability in the diffuse aurora, *Geophys. Res. Lett.*, *6*(4), 332–334, doi:10.1029/GL006i004p00332.
Prikryl, P., P. T. Jayachandran, S. C. Mushini, D. Pokhotelov, J. W. MacDougall, E. Donovan, E. Spanswick, and J.-P. St.-Maurice (2010), GPS TEC, scintillation and cycle slips observed at high latitudes during solar minimum, *Ann. Geophys.*, *28*(6), 1307–1316, doi:10.5194/angeo-28-1307-2010.
Prikryl, P., P. T. Jayachandran, S. C. Mushini, and R. Chadwick (2011a), Climatology of GPS phase scintillation and HF radar backscatter for the high-latitude ionosphere under solar minimum conditions, *Ann. Geophys.*, *29*(2), 377–392, doi:10.5194/angeo-29-377-2011.

AGU Journal of Geophysical Research: Space Physics 10.1002/2014JA020114

Prikryl, P., et al. (2011b), Interhemispheric comparison of GPS phase scintillation at high latitudes during the magnetic-cloud-induced geomagnetic storm of 5-7 April 2010, *Ann. Geophys.*, *29*(12), 2287–2304, doi:10.5194/angeo-29-2287-2011.

Romano, V., S. Pau, M. Pezzopane, E. Zuccheretti, B. Zolesi, G. De Franceschi, and S. Locatelli (2008), The electronic space weather upper atmosphere (eSWua) project at INGV: Advancements and state of the art, *Ann. Geophys.*, *26*(2), 345–351, doi:10.5194/angeo-26-345-2008.

Romano, V., S. Pau, M. Pezzopane, L. Spogli, E. Zuccheretti, M. Aquino, and C. M. Hancock (2013), eSWua: A tool to manage and access GNSS ionospheric data from mid-to-high latitudes, *Ann. Geophys.*, *56*(2), R0223, doi:10.4401/ag-6244.

Sato, T. (1959), Morphology of the ionospheric f2 disturbances in the polar region, *Rep. Ionos. Space Res. Jpn.*, *13*, 91–95.

Spogli, L., L. Alfonsi, G. De Franceschi, V. Romano, M. H. O. Aquino, and A. Dodson (2009), Climatology of GPS ionospheric scintillations over high and mid-latitude European regions, *Ann. Geophys.*, *27*(9), 3429–3437, doi:10.5194/angeo-27-3429-2009.

Tiwari, S., A. Jain, S. Sarkar, S. Jain, and A. K. Gwal (2012), Ionospheric irregularities at antarctic using GPS measurements, *J. Earth Syst. Sci.*, *121*(2), 345–353, doi:10.1007/s12040-012-0168-8.

Tsunoda, R. T. (1988), High-latitude F region irregularities: A review and synthesis, *Rev. Geophys.*, *26*(4), 719–760, doi:10.1029/RG026i004p00719.

Weber, E. J., J. Buchau, J. G. Moore, J. R. Sharber, R. C. Livingston, J. D. Winningham, and B. W. Reinisch (1984), F layer ionization patches in the polar cap, *J. Geophys. Res.*, *89*(A3), 1683–1694, doi:10.1029/JA089iA03p01683.

Weber, E. J., J. A. Klobuchar, J. Buchau, H. C. Carlson, R. C. Livingston, O. de la Beaujardiere, M. McCready, J. G. Moore, and G. J. Bishop (1986), Polar cap f layer patches: Structure and dynamics, *J. Geophys. Res.*, *91*(A11), 12,121–12,129, doi:10.1029/JA091iA11p12121.

Wickwar, V. B., L. L. Cogger, and H. C. Carlson (1974), The 6300 å O1D airglow and dissociative recombination, *Planet. Space Sci.*, *22*(5), 709–724, doi:10.1016/0032-0633(74)90141-X.

Zhang, Q.-H., et al. (2013a), Direct observations of the evolution of polar cap ionization patches, *Science*, *339*(6127), 1597–1600, doi:10.1126/science.1231487, PMID: 23539601.

Zhang, Q.-H., B.-C. Zhang, J. Moen, M. Lockwood, I. W. McCrea, H.-G. Yang, H.-Q. Hu, R.-Y. Liu, S.-R. Zhang, and M. Lester (2013b), Polar cap patch segmentation of the tongue of ionization in the morning convection cell, *Geophys. Res. Lett.*, *40*, 2918–2922, doi:10.1002/grl.50616.

Zou, S., L. R. Lyons, M. J. Nicolls, and C. J. Heinselman (2009), PFISR observations of strong azimuthal flow bursts in the ionosphere and their relation to nightside aurora, *J. Atmos. Sol. Terr. Phys.*, *71*(6-7), 729–737, doi:10.1016/j.jastp.2008.06.015.

Paper II

Scintillation and loss of signal lock from poleward moving auroral forms in the cusp ionosphere

K. Oksavik, C. van der Meeren, D. A. Lorentzen, L. J. Baddeley, J. I. Moen

Journal of Geophysical Research: Space Physics, Vol. 120, doi:10.1002/2015JA021819 (2015)

II

AGU PUBLICATIONS

JGR

Journal of Geophysical Research: Space Physics

RESEARCH ARTICLE
10.1002/2015JA021528

Key Points:
- Intense phase scintillation from dayside poleward moving auroral forms (PMAFs)
- PMAFs can have stronger ionospheric irregularities than polar cap patches
- PMAFs can cause loss of signal lock

Correspondence to:
K. Oksavik,
kjellmar.oksavik@uib.no

Citation:
Oksavik, K., C. van der Meeren, D. A. Lorentzen, L. J. Baddeley, and J. Moen (2015), Scintillation and loss of signal lock from poleward moving auroral forms in the cusp ionosphere, *J. Geophys. Res. Space Physics*, *120*, doi:10.1002/2015JA021528.

Received 2 JUN 2015
Accepted 30 SEP 2015
Accepted article online 2 OCT 2015

Scintillation and loss of signal lock from poleward moving auroral forms in the cusp ionosphere

K. Oksavik[1,2], C. van der Meeren[1], D. A. Lorentzen[1,2], L. J. Baddeley[1,2], and J. Moen[2,3]

[1]Birkeland Centre for Space Science, Department of Physics and Technology, University of Bergen, Bergen, Norway, [2]University Centre in Svalbard, Longyearbyen, Norway, [3]Department of Physics, University of Oslo, Oslo, Norway

Abstract We present two examples from the cusp ionosphere over Svalbard, where poleward moving auroral forms (PMAFs) are causing significant phase scintillation in signals from navigation satellites. The data were obtained using a combination of ground-based optical instruments and a newly installed multiconstellation navigation signal receiver at Longyearbyen. Both events affected signals from GPS and Global Navigation Satellite System (GLONASS). When one intense PMAF appeared, the signal from one GPS spacecraft also experienced a temporary loss of signal lock. Although several polar cap patches were also observed in the area as enhancements in total electron content, the most severe scintillation and loss of signal lock appear to be attributed to very intense PMAF activity. This shows that PMAFs are locations of strong ionospheric irregularities, which at times may cause more severe disturbances in the cusp ionosphere for navigation signals than polar cap patches.

1. Introduction

A fundamental characteristic of the dayside aurora is transients and poleward moving auroral forms (PMAFs). Early studies [e.g., *Feldstein and Starkov*, 1967; *Vorobjev et al*., 1975] identified poleward moving events that detached from the dayside auroral oval and drifted into the polar cap. The motion of PMAFs is controlled by the polarity of the interplanetary magnetic field (IMF) B_y component [*Sandholt et al*., 1986, 1993; *Moen et al*., 1999]. The PMAFs move northwest when B_y is positive, and northeast when B_y is negative [*Sandholt et al*., 1998], and PMAFs are most frequent when $|B_y| > |B_z|$ [*Sandholt et al*., 2004], corresponding to IMF clock angles between 45° and 135°.

PMAFs have often been interpreted as ionospheric signatures of flux transfer events (FTEs) [*Sandholt et al*., 1990, 1993; *Denig et al*., 1993; *Milan et al*., 1999, 2000; *Thorolfsson et al*., 2000], where dayside transients often show repetition rates [*Milan et al*., 1999] comparable to FTEs at the magnetopause [*Russell and Elphic*, 1978, 1979; *Haerendel et al*., 1978]. Transient reconnection is believed to be the primary transfer mechanism of flux from the solar wind to the magnetosphere [*Cowley and Lockwood*, 1992; *Lockwood et al*., 1995]. A burst of reconnection propagates from the magnetopause to the ionosphere as an Alfvénic disturbance with an associated system of field-aligned Birkeland currents [*Glassmeier and Stellmacher*, 1996]. In the cusp ionosphere it sets up a mesoscale twin-cell flow pattern [*Southwood*, 1985, 1987]. The same process may also create isolated polar cap patches of increased electron density in the *F* region ionosphere [*Lockwood and Carlson*, 1992; *Carlson et al*., 2002, 2004, 2006; *Lockwood et al*., 2005a, 2005b; *Lorentzen et al*., 2010], which are often closely associated with PMAFs and an optical flash at the foot of the newly opened flux [*Carlson et al*., 2006].

A series of publications have used fast scan modes at the European Incoherent Scatter Svalbard Radar to investigate the time evolution of mesoscale flow channels in relation to PMAFs [*Carlson et al*., 2004; *Oksavik et al*., 2004, 2005, 2011; *Rinne et al*., 2007, 2010; *Moen et al*., 2008]. *Oksavik et al*. [2004, 2005] found that the clockwise vorticity on one side of a flow channel is consistent with an upward Birkeland current (i.e., intense PMAF aurora), while the counterclockwise vorticity on the other side of the flow channel is consistent with a downward Birkeland current (i.e., weak or no aurora). *Rinne et al*. [2007] identified a new type of flow channel (reversed flow events) that gives enhanced flow in the reverse direction of the large-scale background convection. *Moen et al*. [2008] point out that this phenomenon is related to a Birkeland Current Arc and provide two possible explanations: (1) coupling through a poorly conducting ionosphere of two MI current loops forced by independent voltage generators or (2) that the flow channel is driven by an inverted V.

The Super Dual Auroral Radar Network (SuperDARN) community has shown that the dayside aurora is often co-located with coherent HF radar echoes [*Rodger et al*., 1995; *Yeoman et al*., 1997; *Moen et al*., 2001]. A wide

AGU Journal of Geophysical Research: Space Physics 10.1002/2015JA021528

range of poleward moving transients are observed: flow channel events [*Pinnock et al.*, 1993, 1995; *Chisham et al.*, 2000; *Neudegg et al.*, 1999, 2000], pulsed ionospheric flows (PIFs) [*Provan et al.*, 1998, 2002; *Provan and Yeoman*, 1999; *McWilliams et al.*, 2000] and poleward moving radar auroral forms [*Milan et al.*, 2000, 2002; *Wild et al.*, 2001; *Davies et al.*, 2002; *Rae et al.*, 2004]. SuperDARN obtains echoes from decametre-scale field-aligned plasma irregularities that track the background convection in the ionosphere [*Greenwald et al.*, 1995; *Chisham et al.*, 2007]. The close association between PMAFs and transient features in HF radar backscatter [*Milan et al.*, 1999] therefore suggests that PMAFs are associated with plasma irregularities, which may cause severe scintillation and disturbance of ground-to-satellite links and communication and navigation systems [*Buchau et al.*, 1985; *Basu et al.*, 1988, 1990, 1994, 1998].

Several studies have looked at scintillation of spacecraft signals in a statistical manner [*Kersley et al.*, 1995; *Spogli et al.*, 2009; *Li et al.*, 2010; *Alfonsi et al.*, 2011; *Tiwari et al.*, 2012]. Both 250 MHz satellite beacon scintillation measurements [*Aarons et al.*, 1981] and GPS scintillation measurements have found the highest occurrence of scintillation during the local winter months [*Li et al.*, 2010] or in the autumn-winter season [*Prikryl et al.*, 2011, 2015]. *Kersley et al.* [1995] pointed out that the occurrence of scintillation in winter often maximizes near magnetic noon and extends in a latitudinal belt into the afternoon/evening sector. Another study [*Prikryl et al.*, 2011] found maximum scintillation in the prenoon hours of the perturbed cusp ionosphere, in addition to nightside auroral arc brightening and substorms. Cusp region dynamics is proposed as a potentially strong source for phase scintillation and potential cycle slips [*Prikryl et al.*, 2010]. They defined a cycle slip as a jump in differential phase total electron content (TEC) of more than 1.5 TECU in 1 s (1 TECU corresponds to 10^{16} el/m^2). Scintillation and cycle slips have been found to peak when high-speed streams or interplanetary coronal mass ejections impact the Earth's magnetosphere [*Prikryl et al.*, 2014]. Intense auroral arcs have produced loss of signal lock during strong substorms in the nightside ionosphere [*Smith et al.*, 2008]; however, we have not yet found any reports in literature on loss of lock in the traditionally weaker dayside cusp aurora.

In a pioneering piece of work *Basu et al.* [1998] studied plasma structuring and scintillation over Svalbard for three active days in January 1997, but their work mostly focused on much larger spatial scales and the stable cusp aurora near magnetic noon. Later, *Milan et al.* [2005] found a close correspondence between the occurrence of amplitude scintillations of 250 MHz satellite beacon signals and SuperDARN backscatter power at 10 MHz. *Prikryl et al.* [2010, 2011] have also shown that GPS phase scintillation to coexist with SuperDARN backscatter. However, *Milan et al.* [2005] and *Prikryl et al.* [2010, 2011] have not related it to PMAF activity and moving auroral forms. Other case studies [*De Franceschi et al.*, 2008; *Coker et al.*, 2004; *Mitchell et al.*, 2005; *van der Meeren et al.*, 2014; *Jin et al.*, 2014; *Hosokawa et al.*, 2014] have mostly focused on nightside events in the context of magnetic storms or auroral substorms.

Kinrade et al. [2012] investigated ionospheric scintillation over Antarctica during a large geomagnetic storm following a coronal mass ejection. Significant phase scintillation was seen in the plasma depletion region both in the dayside noon sector and in the dayside cusp. Near 13:00 magnetic local time they observed ~30 s bursts of phase scintillation. Within each burst there were ~5–6 s pseudo-periodic oscillations. They suspected that this was due to "cusp precipitation of some kind," but no optical data or mentioning of PMAFs was presented.

Kinrade et al. [2013] compared auroral images with scintillation measurements from the South Pole Station by tracking up to 11 satellites simultaneously. At magnetic noon they found phase scintillation to be associated with 630.0 nm rather than 557.7 nm emissions. Summing over all local times (both day and night) they found that phase scintillations are generally more correlated with 557.7 nm than 630.0 nm emissions (correlation levels of up to 74% versus up to 63%). Their explanation was that 557.7 nm emissions have shorter lifetime and are generally more intense than 630.0 nm emission, which is usually not the case in the cusp region where 630.0 nm is expected to dominate [e.g., *Sandholt et al.*, 1986]. *Kinrade et al.* [2013] did not mention PMAFs or relate their dayside scintillation events to pulsed reconnection events at the magnetopause.

In the current paper we will follow up on the hypothesis of *Kinrade et al.* [2012] that the significant phase scintillation near magnetic noon is due to cusp precipitation of some kind. We will present data from a new receiver which is tracking data at Svalbard from GPS, Global Navigation Satellite System (GLONASS) and Galileo. In 2013, our receiver was on average tracking 20–24 satellites simultaneously. Using data from two intense PMAF events on 14 January 2013 we will document that PMAF activity is producing transient and highly localized areas of severe phase scintillation that move through the cusp region ionosphere and into the polar cap.

Journal of Geophysical Research: Space Physics 10.1002/2015JA021528

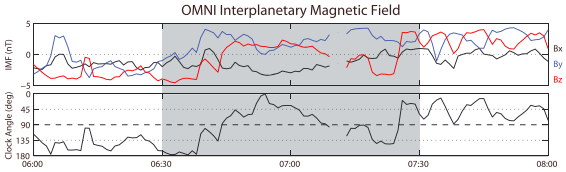

Figure 1. (top) Components of the interplanetary magnetic field (IMF): B_x (black line), B_y (blue line), B_z (red line). (bottom) The IMF clock angle is also shown. Grey shading is used to indicate the time interval shown in Figure 2.

2. Instrumentation

For this study we use a newly installed NovAtel GPStation-6 receiver at the Kjell Henriksen Observatory (KHO) in Longyearbyen (78.1°N, 16.0°E). It is a multiconstellation and multifrequency receiver, which is currently tracking signals from GPS (L1/L2/L2C/L5), GLONASS (L1/L2), and Galileo (E1/E5a/E5b/Alt-BOC). The receiver outputs the phase scintillation σ_ϕ index [*Fremouw et al.*, 1978; *Rino*, 1979]. A sixth-order Butterworth high-pass filter with a cutoff frequency of 0.1 Hz is used to find the detrended raw carrier phase ϕ, and the σ_ϕ index is computed over 60 s intervals [*van Dierendonck et al.*, 1993, 1996]:

$$\sigma_\phi^2 = \langle \phi^2 \rangle - \langle \phi^2 \rangle$$

The phase scintillation index is generally influenced by the observation geometry, but *Forte and Radicella* [2004] have shown that geometrical factors are not important for scintillation indices at high latitudes for satellites flying in GPS-like orbits. The receiver also outputs the 60 s amplitude scintillation S_4 index, which is the standard deviation of the received power I normalized by its mean value [*Briggs and Parkin*, 1963]:

$$S_4^2 = \frac{\langle I^2 \rangle - \langle I \rangle^2}{\langle I \rangle^2}$$

The receiver also provides the total electron content (TEC) and rate of TEC (ROT), both at 1 s and 60 s resolution. Raw data of the amplitude and phase are available at 50 Hz resolution.

For optical monitoring of the PMAF activity we use a meridian scanning photometer (MSP) and an all-sky imager (ASI) both located at KHO. The geographic location of KHO relative to the magnetic pole allows for detailed observations of the dayside aurora in the midst of winter. The MSP is operated by the University Centre in Svalbard, and it was recording auroral emissions at 557.7 and 630.0 nm. The ASI is operated by the University of Oslo, and it was recording auroral emissions at 630.0 nm. We will also use solar wind data from the NASA OMNIWeb service, which provides data that are already time-shifted to the bow shock.

3. Data Presentation

Around 07:00 UT on 14 January 2013 the solar wind speed was 520–560 km/s and the solar wind density was 2–3 cm^{-3} (data not shown). The Earth's geomagnetic field was weakly disturbed ($Kp = 3$). Figure 1 presents interplanetary magnetic field (IMF) data that have been extracted from the NASA/ Goddard Space Flight Center's OMNI data set. Figure 1 (top) shows the components B_x (black line), B_y (blue line), and B_z (red line). Although there is a brief data gap around 07:10 UT, the figure shows that B_x is negative and both B_y and B_z are weakly positive around 07:00 UT. Figure 1 (bottom) shows the IMF clock angle in the GSM y-z plane [see, e.g., *Oksavik et al.*, 2000]. It is defined as $\theta = \tan^{-1}(|B_y/B_z|)$ for $B_z > 0$ and $180^\circ - \tan^{-1}(|B_y/B_z|)$ for $B_z < 0$. In the interval 06:45–07:10 UT the IMF clock angle is between 0° and 90°. The positive B_y is favorable for PMAF activity over Svalbard with motion from southeast to northwest [*Sandholt et al.*, 1998, 2004].

Figure 2 gives an overview of optical and scintillation data from the Kjell Henriksen Observatory (KHO) in Longyearbyen. Figures 2a and 2b show the intensity of the meridian scanning photometer (MSP) 630.0 nm and 557.7 nm channels, respectively. The MSP scans the sky from north (0° elevation) to south (180° elevation) with a time resolution of 16 s. The background has been subtracted, and the color scale gives the intensity in Rayleigh (R). Up until 06:55 UT there was a bright arc in the southern part of the sky (around 120–150° elevation),

AGU Journal of Geophysical Research: Space Physics 10.1002/2015JA021528

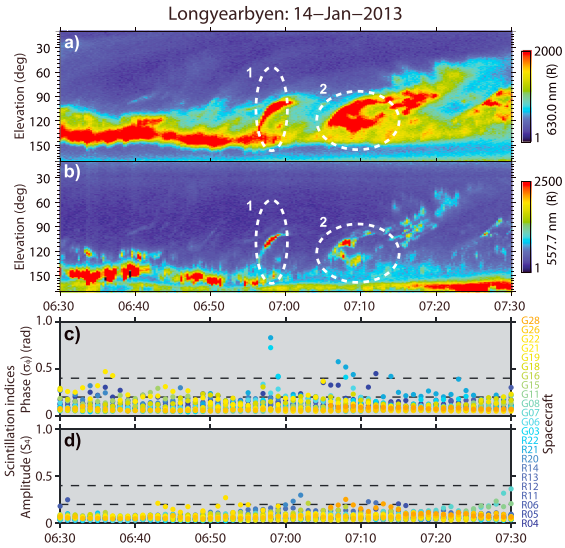

Figure 2. Optical and scintillation data from the Kjell Henriksen Observatory (KHO) in Longyearbyen: (a) the 630.0 nm meridian scanning photometer (MSP) intensity, (b) the 557.7 nm MSP intensity, (c) the 60 s phase scintillation σ_Φ index, and (d) 60 s amplitude scintillation S_4 index. Colors are used in Figures 2c and 2d to separate the different spacecraft. The dashed lines in Figures 2a and 2b indicate the PMAF events 1 and 2. See text for more details.

which is characteristic for the strongly southward IMF dayside cusp aurora [*Sandholt et al.*, 1998, 2004]. At 06:55–07:00 UT and 07:05–07:15 UT there were two PMAFs that formed and drifted into the polar cap. These events are indicated with dashed lines and numbers 1 and 2 and occurred for positive IMF B_y, which is favorable for PMAF activity [*Sandholt et al.*, 1998, 2004].

Figures 2c and 2d show the corresponding scintillation data from our new multiconstellation navigation signal receiver at KHO in Longyearbyen, and colors are used to separate the different spacecraft. Figure 2c shows the 60 s phase scintillation σ_Φ index. Phase scintillations are caused by irregularities of scale size from hundreds of meters to several kilometers [*Kintner et al.*, 2007]. In Figure 2c we notice that both PMAF events coincide in time with two intervals of enhanced phase scintillation ($\sigma_\Phi = 0.2$ to 0.8 radians). The first event had enhanced phase scintillation lasting for 3 min (06:57–06:59 UT). The second event had enhanced phase scintillation lasting for 5 min (07:05–07:09 UT) and an additional 3 min (07:11–07:14 UT). Figure 2d shows the 60 s amplitude scintillation S_4 index. In the weak scattering regime [*Rino*, 1979] of these observations, amplitude scintillations at L band are caused by irregularities of scale size from tens of meters to hundreds of meters, which is at and below the Fresnel radius [*Kintner et al.*, 2007]. In Figure 2d we notice that the amplitude scintillation S_4 index is generally less than 0.2, which is typical for high latitudes where amplitude scintillations are weak and phase scintillations dominate [*Kintner et al.*, 2007].

Figure 3 presents six images (06:55–07:00 UT) from the University of Oslo all-sky imager at KHO in Longyearbyen. In Figure 3a the image has been projected onto a magnetic grid, assuming auroral emissions at 250 km altitude, which is a typical altitude for 630.0 nm emissions in the cusp ionosphere [*Lockwood et al.*, 1993; *Johnsen et al.*, 2012], while the other panels show unprojected all-sky images (north up, east right). The color scale indicates the auroral intensity at 630.0 nm (lower color bar). Overlaid onto each panel we also show scintillation data, where shapes indicate the type of constellation: GLONASS (diamonds) and GPS

AGU Journal of Geophysical Research: Space Physics 10.1002/2015JA021528

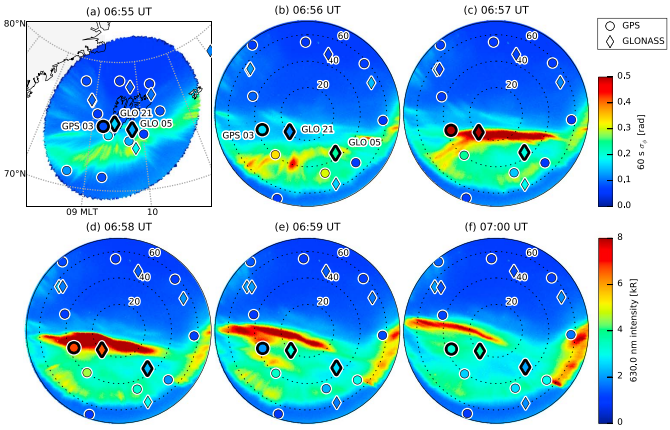

Figure 3. Six 630.0 nm all-sky images from the Kjell Henriksen Observatory (KHO) in Longyearbyen on 14 January 2013 with ionospheric piercing points (IPPs) overlaid for all available GPS and GLONASS spacecraft. In the first panel (a) the image is projected to a magnetic grid, while the other panels show unprojected all-sky images (magnetic north is up, east is right). The marker color is the phase scintillation index (upper color bar). Intense phase scintillation occurred when the GPS 03 and GLONASS 21 signals intersected a bright PMAF between 06:57 and 06:58 UT.

(circles). The marker color is the phase scintillation index (upper color bar). Both the auroral and phase scintillation activity is low in the first two panels (06:55–06:56 UT). At 06:57 UT a bright PMAF appeared, and the phase scintillation immediately began to rise in its vicinity (GLONASS 21 and GPS 03). At 06:58 UT the PMAF had intensified further and began drifting northwest. GPS 03 and GLONASS 21 showed strong phase scintillation right in the middle of the PMAF. At 07:00 UT the PMAF had left the area covered by GPS and GLONASS, and the phase scintillation returned back to low levels. It should also be pointed out that throughout the entire time interval 06:55–07:00 UT the phase scintillation only changed in the vicinity of the PMAF. The phase scintillation was weak in the rest of the field of view. Consequently, the area of strong phase scintillation and PMAF activity appears to be related.

Figure 4 presents another example in the same format. The first image frame (07:03 UT) shows a bright PMAF east of Svalbard. At 07:04 UT the PMAF begins to intersect GLONASS 05, which shows elevated phase scintillation. The PMAF moves northwest. At 07:06 UT GLONASS 05 continues to show enhanced phase scintillation, while GLONASS 21 starts to show strong phase scintillation. At 07:07 UT the PMAF has intensified and moved further northwest, and both GPS 03 and GLONASS 21 show strong phase scintillation. At 07:08 UT the PMAF is located more to the northwest. GPS 03 is no longer affected, while GLONASS 21 continues to show strong phase scintillation. Consequently, the area of strong phase scintillation again overlaps with the PMAF.

Figures 5, 6, and 7 provide a closer look at the phase scintillation and TEC variations in relation to line-of-sight auroral emissions for the three spacecraft that were highlighted in Figures 3 and 4 (GLONASS 05, GLONASS 21, and GPS 03). The grey shading indicates the intervals covered by Figures 3 and 4 for easier comparison.

Figures 5a, 6a, and 7a present the line-of-sight auroral intensity at 557.7 and 630.0 nm in an area that is 7×7 pixels wide and centered at the elevation and azimuth of each spacecraft. The width of each line represents the range of observed auroral intensities in the 7×7 pixel area (from minimum to maximum intensity). For both events the GLONASS 05 (Figure 5a) signal was experiencing significantly lower auroral intensities than GLONASS 21 (Figure 6a) and GPS 03 (Figure 7a), which is consistent with GLONASS 05 being slightly equatorward of the two PMAF events. For GLONASS 05 (Figure 5a) the intensity ratio 630.0 nm versus 557.7 nm stayed around 2:1, which is typical for the dayside aurora, where 630.0 nm usually dominates [e.g., *Sandholt et al.*, 1986]. For GLONASS 21 (Figure 6a) and GPS 03 (Figure 7a) the intensity ratio stayed

AGU Journal of Geophysical Research: Space Physics 10.1002/2015JA021528

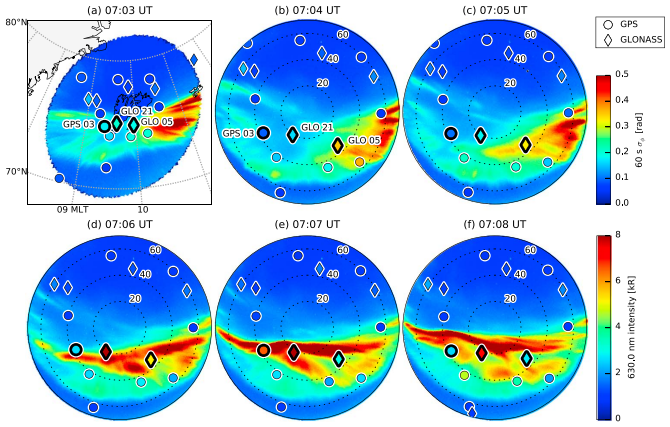

Figure 4. Same as Figure 3 but for 07:03–07:08 UT on 14 January 2013. Intense phase scintillation occurred when the GPS 03 and GLONASS 21 signals intersected a bright PMAF between 07:06 and 07:08 UT.

around 2:1 before/after the two PMAF events. In the middle of each PMAF event the auroral intensity spiked for both 630.0 and 557.7 nm, and the intensity ratio approached 1:1. For GPS 03 (Figure 7a) the 557.7 nm intensity also exceeded the 630.0 nm intensity for a few seconds around 06:57:30 UT.

Figures 5b and 5c, 6b and 6c, and 7b and 7c present the TEC and the absolute value of the rate of TEC (ROT), respectively. All spacecraft were at high elevations, so there is generally little difference between the slant TEC (solid lines) and the vertical TEC (dashed lines). All TEC data have been calibrated (corrected for bias). In the TEC data (Figures 5b, 6b, and 7b) there were several polar cap patches (indicated with the letter P), which can be identified as transient TEC enhancements lasting just a few minutes. For GLONASS 05 (Figures 5a and 5b) the PMAFs at 06:56 and 07:06 UT were co-located with local TEC minima, that were followed by polar cap patches (i.e., the PMAFs were on the poleward side of the polar cap patch, given that the drift speed was in the poleward direction in Figures 3 and 4). For GLONASS 21 (Figures 6a and 6b) the first PMAF at 06:57 UT was co-located with a TEC minimum, while the second PMAF at 07:07 UT was inside a polar cap patch.

For GPS 03 (Figures 7a and 7b) the PMAF at 07:07 UT was co-located with a TEC minimum, while the PMAF at 06:57 UT coincided with a dramatic TEC enhancement. From 06:57:13 to 06:57:20 UT the TEC jumped from 2.8 to 18.9 TECU, corresponding to a gradient of 2.3 TECU/s, which according to *Prikryl et al.* [2010] would be classified as a cycle slip (change of more than 1.5 TECU/s). A careful examination of the raw data also reveals that the receiver lost lock for the L2Y signal (center frequency at 1227.60 MHz) between 06:56:44 and 06:57:36 UT (indicated with cyan shading in Figure 7b). There was no loss of lock for L1CA, which corresponds to a higher center frequency (1575.42 MHz). Unfortunately, the receiver was only recording 50 Hz data of L1CA at the time, but 1 s resolution TEC data, which were recorded in real-time and were based on L1CA and L2Y signals, reveal two 5 and 3 s data gaps (06:57:13 to 06:57:18 UT and 06:57:33 to 06:57:36 UT). It suggests that the L2Y loss of lock occurred at those particular times. It should be noticed that 06:57:13 to 06:57:18 UT coincides both with the extremely bright 557.7 and 630.0 nm PMAF (Figure 7a) and the steep TEC gradient (Figure 7b) that *Prikryl et al*. [2010] would classify as a cycle slip.

For GLONASS 05 the ROT (Figure 5c) was generally lower than for the other two spacecraft (see Figures 6c and 7c). GLONASS 05 observed the highest ROT of around 0.25 TECU/s in the vicinity of local TEC minima (e.g., 06:56, 06:59, 07:06, and 07:11 UT), often in connection with a positive TEC gradient. Given the poleward drift seen in Figures 3 and 4, it suggests the highest ROT was for the most part detected at the poleward side (leading edge) of polar cap patches. Only two of the ROT enhancements appear to be related to small enhancements of auroral emissions (06:56 and 07:06 UT). Both GLONASS 21 and GPS 03 had their highest ROT in connection

AGU Journal of Geophysical Research: Space Physics 10.1002/2015JA021528

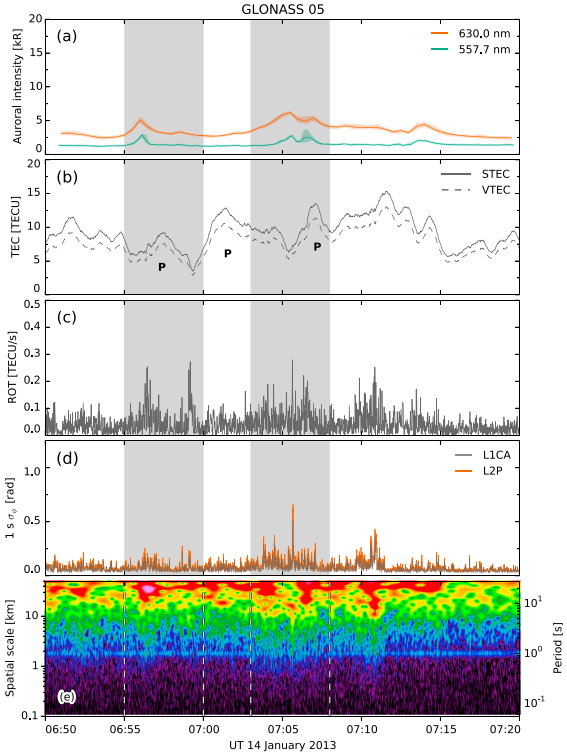

Figure 5. GLONASS 05 data on 14 January 2013. (a) The 557.7 and 630.0 nm auroral intensity in the vicinity of the satellite IPPs. (b): Slant and vertical total electron content (TEC) in units of TECU (1 TECU = 10^{16} el m^{-2}). Three polar cap patches are indicated using the letter P. (c) Rate of TEC (ROT). (d) The phase scintillation index computed from raw 50 Hz phase data over periods of 1 s for the signals L1CA and L2P. (e): Wavelet power spectra of raw 50 Hz phase data versus the corresponding period (right axis) and spatial scale (left axis). Grey shading indicates the duration of Figures 3 and 4. The fluctuations are generally lower than for the other two spacecraft (see Figures 6 and 7).

with the two PMAFs at 06:57 and 07:07 UT. For GLONASS 21 the ROT exceeded 0.5 TECU/s (Figure 6c), and for GPS 03 the ROT exceeded 0.2–0.3 TECU/s (Figure 7c).

Figures 5d, 6d, and 7d present a high-resolution σ_ϕ scintillation index that we have calculated to provide a more detailed view of the phase scintillation during the events. The raw 50 Hz phase data were detrended using a sixth-order Butterworth high-pass filter with a cutoff frequency of 0.1 Hz, and the σ_ϕ index was computed over 1 s intervals. We have carefully examined that this high-resolution σ_ϕ index matches the overall features of the lower-resolution 60 s data, which is output by the receiver in real time. For GLONASS 05 (Figure 5d) and GLONASS 21 (Figure 6d) the 1 s σ_ϕ index was computed for both L1CA and L2P. For GPS 03 (Figure 7d) we could only calculate it for L1CA, because L2Y was not recorded.

For GLONASS 05 (Figure 5d) the phase scintillation was relatively low, except for a brief enhancement of $\sigma_\phi > 0.5$ rad around 07:06 UT in connection with the second PMAF event. The otherwise weak scintillation

AGU Journal of Geophysical Research: Space Physics 10.1002/2015JA021528

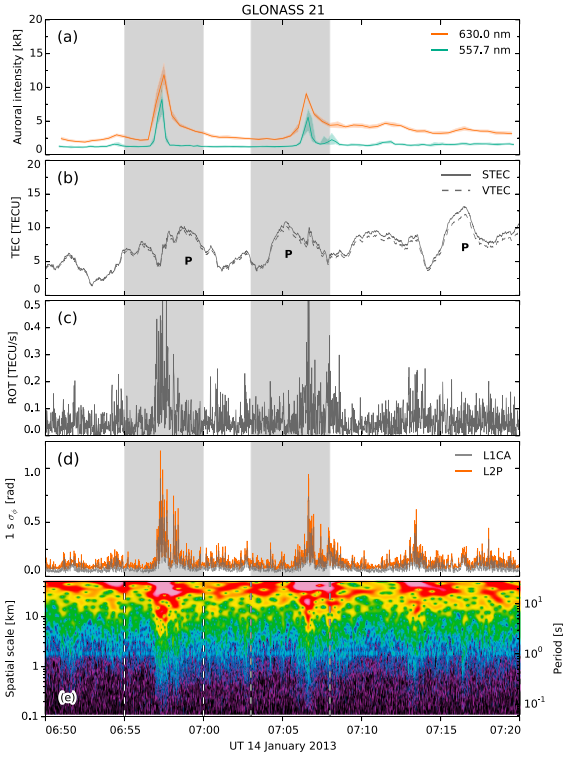

Figure 6. Same as Figure 5 but for GLONASS 21. Notice the high auroral intensities, enhanced fluctuations of phase and TEC, and the spectrum extending down to spatial scales of a few hundreds of meters during the two intervals highlighted with grey shading.

is consistent with GLONASS 05 being slightly equatorward of the PMAF activity. For GLONASS 21 (Figure 6d) and GPS 05 (Figure 7d) the phase scintillation peaked in connection with the two PMAF events at 06:57 and 07:07 UT, reaching σ_ϕ~1.0 rad for GLONASS 21, and σ_ϕ~0.5 rad for GPS 03. Both are indicative of severe phase scintillation in connection with the bright PMAFs. We should also point out that for GLONASS 05 and 21 (Figures 5d and 6d) the phase scintillation was generally higher at L2P (center frequency at 1242–1248 MHz) than at L1CA (center frequency at 1598–1605 MHz), which is indicative of irregularities being stronger at longer spatial scales (lower frequency corresponds to longer wavelength). We will investigate this next.

Figures 5e, 6e, and 7e present spectrograms of the raw phase in order to obtain more detailed information on the phase variations in relation to spatial scale size, using a similar approach to *van der Meeren et al*. [2014]. The axes on the right side show the period of the phase variations. The spectrograms were made using a wavelet analysis, based on software provided by *Torrence and Compo* [1998]. The Morlet wavelet was chosen as the mother wavelet. This method has previously been used by other GNSS studies [e.g., *Mushini et al*., 2012]. Some key advantages of the wavelet technique are that (1) no detrending of the GNSS data is required

AGU Journal of Geophysical Research: Space Physics 10.1002/2015JA021528

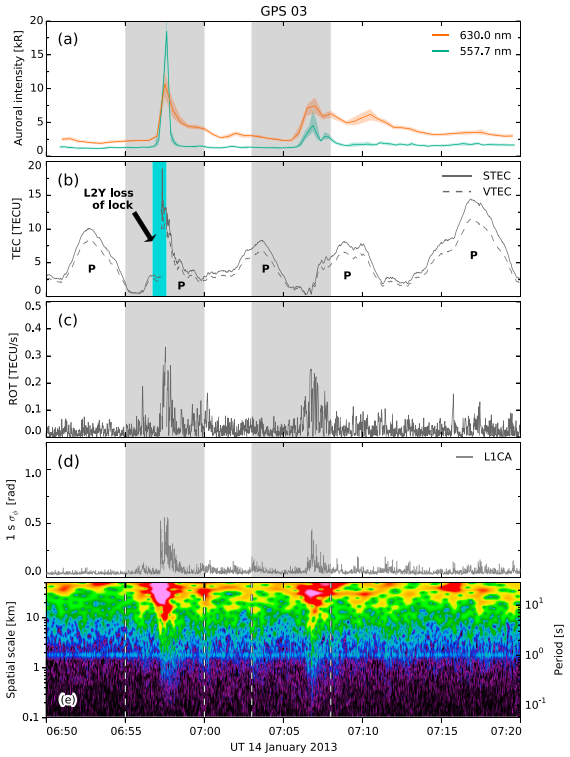

Figure 7. Same as Figure 5 but for GPS 03. The phase scintillation index in Figure 7d is computed using the L1CA signal. Notice the high auroral intensities, enhanced fluctuations of phase and TEC, and the spectrum extending down to spatial scales of a few hundreds of meters during the two intervals highlighted with grey shading. A loss of lock was observed for the first PMAF event (cyan shading in Figure 7b).

to produce a wavelet spectrogram and (2) wavelet spectrograms provide better resolution at smaller scales. The spectrograms have been carefully examined and compared to Fourier spectrograms of detrended data to verify that the two techniques give similar results. For further details on the wavelet technique we refer to *Torrence and Compo* [1998] and *Mushini et al.* [2012].

The wavelet spectrograms were converted to spatial scale (see left axes), using information on the drift speed of the PMAFs. From an analysis of all-sky images we found that two PMAFs had drift speeds of around 1600 and 2300 m/s, respectively. At the same time the ionospheric piercing points of the satellites moved at 40–50 m/s, which is insignificant in this regard. An average value of 1800 m/s was chosen for the conversion of temporal features to a spatial scale. Note that the spatial scale is only used in an order-of-magnitude sense (i.e., an adjustment to the assumed drift velocity by a factor 2 will only cause a corresponding linear adjustment to the spatial scale in the spectrogram, which will not change the order of magnitude).

For GLONASS 05 (Figure 5e) the strongest spectral power enhancements (red and yellow colors) were seen at spatial scales greater than 10 km, and some spectral power enhancements (green and bright blue colors)

AGU Journal of Geophysical Research: Space Physics 10.1002/2015JA021528

extended all the way down to ~2 km spatial scale. This picture was quite uniform throughout the whole time interval, which is consistent with GLONASS 05 being less affected by PMAF activity. For the most intense PMAF activity around 06:57 and 07:07 UT, GLONASS 21 (Figure 6e) and GPS 03 (Figure 7e) showed strong spectral power enhancements (red and yellow colors) at spatial scales greater than 4–5 km, and some spectral power enhancements (green and bright blue colors) extended all the way down to just a few hundreds of meters. Consequently, the finest structuring appears to be highly localized and attributed to PMAFs. It suggests that PMAFs are locations of stronger irregularities than the surrounding cusp ionosphere, which also included several polar cap patches (Figures 5b, 6b, and 7b), in particular at spatial scales of a few hundreds of meters to a few kilometers.

4. Discussion

Our results show that both GPS and GLONASS signals were affected by PMAF activity. The enhanced scintillation in the cusp ionosphere was observed to be highly localized and highly transient in nature. This is contrary to the results of *Prikryl et al.* [2011], who reported that scintillation often covers a large geographic area of the cusp/cleft region and with duration of several hours. While most of the field of view was unaffected, the phase scintillation was enhanced in the close vicinity of the two PMAF events. It therefore appears that the cusp precipitation of some kind, which *Kinrade et al.* [2012] were referring to as the cause of significant phase scintillation near magnetic noon, must be the well-known phenomenon in the dayside aurora called PMAFs. The area of enhanced phase scintillation drifted poleward into the polar cap together with the PMAF. The motion of the two PMAF events is consistent with reports on PMAFs in literature [e.g., *Sandholt et al.*, 1998].

The introduction section pointed out that PMAFs are often closely associated with polar cap patches [*Carlson et al.*, 2006], which also are known to follow the antisunward convective flow across the polar cap. Polar cap patches are known to have densities 2–20 times higher than the surrounding background electron density [*Buchau et al.*, 1983; *Weber et al.*, 1984; *Crowley et al.*, 2000]. They form near the dayside polar cap boundary and drift across the polar cap to the nightside [*Lorentzen et al.*, 2004; *Oksavik et al.*, 2010; *Moen et al.*, 2013; *Nishimura et al.*, 2014; *Zhang et al.*, 2015]. Polar cap patches are known to cause field-aligned plasma irregularities [e.g., *Hosokawa et al.*, 2009], and several mechanisms have been proposed in literature.

One example is plasma density gradients that by themselves can grow unstable due to the gradient drift (GD) plasma instability [*Ossakow and Chaturvedi*, 1979; *Keskinen and Ossakow*, 1983; *Tsunoda*, 1988; *Basu et al.*, 1988, 1990, 1994, 1998; *Gondarenko and Guzdar*, 2004], which is often regarded as the dominant mode for production of electron density irregularities in the *F* region cusp. The GD plasma instability mechanism occurs for plasma drift, of the correct sign, across a steep plasma density gradient perpendicular to the Earth's magnetic field at high latitudes [*Keskinen and Ossakow*, 1983]. Plasma drift in the opposite direction will set up polarization fields that stabilize the plasma against formation of irregularities. Recent sounding rocket data have shown that decametre-scale irregularities are located on kilometre-scale electron density gradients in the cusp ionosphere produced by electron precipitation, with estimated growth times of 10–50 s for the GD process [*Moen et al.*, 2012].

Another example is shears and vorticity in the plasma flow that are associated with PMAFs [*Oksavik et al.*, 2004, 2005, 2011; *Rinne et al.*, 2007, 2010; *Moen et al.*, 2008]. Flow shears are known to trigger the Kelvin-Helmholtz (KH) plasma instability [*Basu et al.*, 1988, 1990; *Keskinen et al.*, 1988]. The KH theory has been further developed by *Keskinen et al.* [1988], who also included a refinement of ionosphere-magnetosphere electrical coupling. Using SuperDARN observations of flow shears, *Oksavik et al.* [2011] found KH irregularity growth times of 1–5 min. Several of their events were associated with wide Doppler spectra and enhanced backscatter power, consistent with the growth of plasma irregularities.

There have also been attempts to merge the GD and KH plasma instability mechanisms in a two-step process. *Carlson et al.* [2007, 2008] proposed initial structuring driven by the KH instabilities, followed by additional structuring down to much finer scales driven by the GD instabilities. *Oksavik et al.* [2012] studied sounding rocket data from the cusp ionosphere, revealing plasma irregularities extending from hundreds of meters down to a few tens of meters. However, the KH mechanism could not explain the finest-scale irregularities. *Oksavik et al.* [2012] noticed that the strongest plasma irregularities were observed 2 min after a significant enhancement in the aurora and proposed an alternative two-step process: (1) structured particle precipitation

AGU Journal of Geophysical Research: Space Physics 10.1002/2015JA021528

first generates weak "seed" irregularities and (2) the GD instability then breaks these seed irregularities down to smaller scales.

The cases we presented have several polar cap patches (indicated with the character P in Figures 5b, 6b, and 7b). However, it is surprising to notice that most patches did not produce enhanced scintillation. One would normally expect the plasma inside a polar cap patch to become fully structured soon after initiation and with irregularities extending throughout the whole patch [*Hosokawa et al.*, 2009]. Alternatively, one would at least expect irregularities at the steep gradients near the trailing edge of polar cap patches, which is unstable to irregularity growth via the GD mechanism [e.g., *Milan et al.*, 2002]. However, our observations do not support any of these two options. Both Figures 6 and 7 show the strongest phase scintillation to be co-located with extremely bright PMAFs, suggesting that structured particle precipitation is a very important source for plasma irregularities, at least at kilometer to hundred meter scale [*Oksavik et al.*, 2012]. PMAFs are also associated with severe flow shears [*Oksavik et al.*, 2004, 2005, 2011; *Rinne et al.*, 2007, 2010; *Moen et al.*, 2008], which may contribute to irregularities via the KH mechanism [*Oksavik et al.*, 2011].

The observed phase scintillations are believed to be due to irregularities of scale size from hundreds of meters to several kilometers [*Kintner et al.*, 2007]. Our observations in Figures 6e and 7e show that irregularities at these spatial scales are present when PMAFs intersect the signal path. Sounding rocket data [*Moen et al.*, 2012; *Oksavik et al.*, 2012] also document that irregularities can exist all the way down to decameter scale, which is consistent with the frequent observation of transient features in HF radar backscatter in the cusp ionosphere [*Milan et al.*, 1999]. *Milan et al.* [2005] also showed a close correspondence between amplitude scintillations of 250 MHz satellite beacon signals and SuperDARN backscatter power at 10 MHz. It should be pointed out that 250 MHz satellite beacon signals are more severely affected by scintillation than the 1575.42 MHz (GPS L1) band. We can also see this effect in Figures 5d and 6d, where scintillation is stronger at 1242–1248 MHz (GLONASS L2P) than at 1598–1605 MHz (GLONAS L1CA). It is due to the typical nature of irregularity spectra which show a rapid decay toward shorter wavelengths (higher frequencies), see, e.g., Figures 5e, 6e, and 7e.

The production of irregularities requires energy. PMAFs are believed to be caused by transient reconnection at the dayside magnetopause. Magnetic reconnection transfers flux from the solar wind to the magnetosphere and initiates plasma motion in the polar ionosphere [*Cowley and Lockwood*, 1992; *Lockwood et al.*, 1995]. PMAFs have often been interpreted as ionospheric signatures of FTEs [*Sandholt et al.*, 1990, 1993; *Denig et al.*, 1993; *Milan et al.*, 1999, 2000; *Thorolfsson et al.*, 2000]. At the magnetopause FTEs typically have a scale size of one Earth radius in the boundary normal direction [*Saunders et al.*, 1984]. In the ionosphere the FTE flux tube maps to around 100–200 km along the meridian [*Southwood*, 1985, 1987]. The FTE footprint sets up a PMAF and associated flow shears [*Oksavik et al.*, 2004, 2005], and plasma instabilities continue to structure the plasma down to smaller and smaller spatial scales. The structuring can only continue if energy is input into the system. As we have shown in Figures 3 and 4, the scintillation is co-located with the PMAF, indicating a close relation to their anticipated energy source, transient reconnection at the magnetosphere. A statistical study by *Prikryl et al.* [2015] also suggests that enhanced phase scintillation is highly collocated with regions that are known as ionospheric signatures of the coupling between the solar wind and magnetosphere.

Once formed, the irregularities may cause problems for radio communication and navigation signals, like the severe phase scintillation, loss of signal lock, and cycle slips. It is therefore interesting to note that a process initially starting at the Earth's magnetopause tens of thousands of kilometres away may have impact at much smaller scales in the ionosphere (down to a few hundreds of meters, possibly also smaller) and cause problems of potential importance for society. A particular challenge with PMAF events and their associated plasma irregularities is that they often move with high speeds exceeding 1 km/s. With newly installed multiconstellation receivers offering wide and dense coverage we can now track the scintillation from these disturbances, which would otherwise be smeared out in statistical data sets.

5. Concluding Remarks

In this paper we have presented two examples from the cusp ionosphere over Svalbard where bright poleward moving auroral forms (PMAFs) are observed to be associated with severe phase scintillation and strong plasma irregularities at spatial scales of a few hundred meters to a few kilometers. Using a combination of ground-based optical instruments and a newly installed multiconstellation navigation signal receiver we

AGU Journal of Geophysical Research: Space Physics 10.1002/2015JA021528

tracked an area of enhanced phase scintillation that was co-located with two PMAFs and moved into the polar cap. Both events affected signals from GPS and GLONASS. One bright PMAF, where the 557.7 nm exceeded the 630.0 nm intensity, also coincided with the steep TEC gradient on the leading edge (poleward side) of a polar cap patch causing a cycle slip; i.e., a change of more than 1.5 TECU per second [*Prikryl et al.*, 2010]. At the same time the receiver also experienced a temporary loss of lock which compromised the GPS L2Y signal (1227.60 MHz) of one spacecraft. The loss of lock appears to have occurred twice in less than one minute, each loss of lock lasting 3–5 s. It shows that PMAF events can cause important space weather effects in the polar ionosphere. Although several polar cap patches were also observed in the TEC data, the scintillation was much stronger from the PMAF events, which also appear to be associated with stronger irregularities than the surrounding cusp ionosphere. It suggests that the structured particle precipitation of a bright PMAF event is an important source for plasma irregularities in the cusp ionosphere, at least at kilometer to hectometer scale [*Oksavik et al.*, 2012].

Acknowledgments
The interplanetary magnetic field and solar wind data were provided by the NASA OMNIWeb service (http://omniweb.gsfc.nasa.gov). The UiO ASI data are available at http://tid.uio.no/plasma/aurora. The scintillation data may be obtained from Kjellmar Oksavik (e-mail: kjellmar.oksavik@uib.no). This project has been supported by the Research Council of Norway under contracts 212014, 223252, and 230935.

References

Aarons, J., J. P. Mullen, H. E. Whitney, A. L. Johnson, and E. J. Weber (1981), UHF scintillation activity over polar latitudes, *Geophys. Res. Lett.*, *8*(3), 277–280, doi:10.1029/GL008i003p00277.

Alfonsi, L., L. Spogli, G. De Franceschi, V. Romano, M. Aquino, A. Dodson, and C. N. Mitchell (2011), Bipolar climatology of GPS ionospheric scintillation at solar minimum, *Radio Sci.*, *46*, RS0D05, doi:10.1029/2010RS004571.

Basu, S., S. Basu, E. MacKenzie, P. F. Fougere, W. R. Coley, N. C. Maynard, J. D. Winningham, M. Sugiura, W. B. Hanson, and W. R. Hoegy (1988), Simultaneous density and electric field fluctuation spectra associated with velocity shears in the auroral oval, *J. Geophys. Res.*, *93*(A1), 115–136, doi:10.1029/JA093iA01p00115.

Basu, S., S. Basu, E. MacKenzie, W. R. Coley, J. R. Sharber, and W. R. Hoegy (1990), Plasma structuring by the gradient drift instability at high latitudes and comparison with velocity shear driven processes, *J. Geophys. Res.*, *95*(A6), 7799–7818, doi:10.1029/JA095iA06p07799.

Basu, S., S. Basu, P. K. Chaturvedi, and C. M. Bryant Jr. (1994), Irregularity structures in the cusp/cleft and polar cap regions, *Radio Sci.*, *29*(1), 195–207, doi:10.1029/93RS01515.

Basu, S., E. J. Weber, T. W. Bullett, M. J. Keskinen, E. MacKenzie, P. Doherty, R. Sheehan, H. Kuenzler, P. Ning, and J. Bongiolatti (1998), Characteristics of plasma structuring in the cusp/cleft region at Svalbard, *Radio Sci.*, *33*(6), 1885–1899, doi:10.1029/98RS01597.

Briggs, B. H., and I. A. Parkin (1963), On the variation of radio star and satellite scintillations with zenith angle, *J. Atmos. Sol. Terr. Phys.*, *25*(6), 339–366.

Buchau, J., B. W. Reinisch, E. J. Weber, and J. G. Moore (1983), Structure and dynamics of the winter polar cap F region, *Radio Sci.*, *18*(6), 995–1010, doi:10.1029/RS018i006p00995.

Buchau, J., E. J. Weber, D. N. Anderson, H. C. Carlson Jr., J. G. Moore, B. W. Reinisch, and R. C. Livingston (1985), Ionospheric structures in the polar cap: Their origin and relation to 250-MHz scintillation, *Radio Sci.*, *20*(3), 325–338, doi:10.1029/RS020i003p00325.

Carlson, H. C., K. Oksavik, J. Moen, A. P. van Eyken, and P. Guio (2002), ESR mapping of polar-cap patches in the dark cusp, *Geophys. Res. Lett.*, *29*(10), 1386, doi:10.1029/2001GL014087.

Carlson, H. C., Jr., K. Oksavik, J. Moen, and T. Pedersen (2004), Ionospheric patch formation: Direct measurements of the origin of a polar cap patch, *Geophys. Res. Lett.*, *31*, L08806, doi:10.1029/2003GL018166.

Carlson, H. C., J. Moen, K. Oksavik, C. P. Nielsen, I. W. McCrea, T. R. Pedersen, and P. Gallop (2006), Direct observations of injection events of subauroral plasma into the polar cap, *Geophys. Res. Lett.*, *33*, L05103, doi:10.1029/2005GL025230.

Carlson, H. C., T. Pedersen, S. Basu, M. Keskinen, and J. Moen (2007), Case for a new process, not mechanism, for cusp irregularity production, *J. Geophys. Res.*, *112*, A11304, doi:10.1029/2007JA012384.

Carlson, H. C., K. Oksavik, and J. Moen (2008), On a new process for cusp irregularity production, *Ann. Geophys.*, *26*, 2871–2885.

Chisham, G., M. Pinnock, and A. S. Rodger (2000), Poleward-moving HF radar flow bursts in the cusp: Transient changes in flow speed or direction?, *Geophys. Res. Lett.*, *27*(7), 919–922, doi:10.1029/1999GL010760.

Chisham, G., et al. (2007), A decade of the Super Dual Auroral Radar Network (SuperDARN): Scientific achievements, new techniques and future directions, *Surv. Geophys.*, *28*(1), 33–109, doi:10.1007/s10712-007-9017-8.

Coker, C., G. S. Bust, R. A. Doe, and T. L. Gaussiran II (2004), High-latitude plasma structure and scintillation, *Radio Sci.*, *39*, RS1S15, doi:10.1029/2002RS002833.

Cowley, S. W. H., and M. Lockwood (1992), Excitation and decay of solar wind-driven flows in the magnetosphere-ionosphere system, *Ann. Geophys.*, *10*, 103–115.

Crowley, G., A. J. Ridley, D. Deist, S. Wing, D. J. Knipp, B. A. Emery, J. Foster, R. Heelis, M. Hairston, and B. W. Reinisch (2000), Transformation of high-latitude ionospheric F region patches into blobs during the March 21, 1990, storm, *J. Geophys. Res.*, *105*(A3), 5215–5230, doi:10.1029/1999JA900357.

Davies, J. A., T. K. Yeoman, I. J. Rae, S. E. Milan, M. Lester, M. Lockwood, and A. McWilliams (2002), Ground-based observations of the auroral zone and polar cap ionospheric responses to dayside transient reconnection, *Ann. Geophys.*, *20*, 781–794.

De Franceschi, G., L. Alfonsi, V. Romano, M. Aquino, A. Dodson, C. N. Mitchell, P. Spencer, and A. W. Wernik (2008), Dynamics of high-latitude patches and associated small-scale irregularities during the October and November 2003 storms, *J. Atmos. Sol. Terr. Phys.*, *70*, 879–888.

Denig, W. F., W. J. Burke, N. C. Maynard, F. J. Rich, B. Jacobsen, P. E. Sandholt, A. Egeland, S. Leontjev, and V. G. Vorobjev (1993), Ionospheric signatures of dayside magnetopause transients: A case study using satellite and ground measurements, *J. Geophys. Res.*, *98*(A4), 5969–5980, doi:10.1029/92JA01541.

Feldstein, Y. I., and G. V. Starkov (1967), Dynamics of auroral belt and polar geomagnetic disturbances, *Planet. Space Sci.*, *15*, 209–229.

Forte, B., and S. M. Radicella (2004), Geometrical control of scintillation indices: What happens for GPS satellites, *Radio Sci.*, *39*, RS5014, doi:10.1029/2002RS002852.

Fremouw, E. J., R. L. Leadabrand, R. C. Livingston, M. D. Cousins, C. L. Rino, B. C. Fair, and R. A. Long (1978), Early results from the DNA wideband satellite experiment – Complex-signal scintillation, *Radio Sci.*, *13*(1), 167–187, doi:10.1029/RS013i001p00167.

AGU Journal of Geophysical Research: Space Physics 10.1002/2015JA021528

Glassmeier, K.-H., and M. Stellmacher (1996), Mapping flux transfer events to the ionosphere, *Adv. Space Res.*, *18*(8), 151–160.
Gondarenko, N. A., and P. N. Guzdar (2004), Plasma patch structuring by the nonlinear evolution of the gradient drift instability in the high-latitude ionosphere, *J. Geophys. Res.*, *109*, A09301, doi:10.1029/2004JA010504.
Greenwald, R. A., et al. (1995), DARN/SuperDARN: A global view of the dynamics of high-latitude convection, *Space Sci. Rev.*, *71*, 761–796.
Haerendel, G., G. Paschmann, N. Sckopke, H. Rosenbauer, and P. C. Hedgecock (1978), The frontside boundary layer of the magnetosphere and the problem of reconnection, *J. Geophys. Res.*, *83*(A7), 3195–3216, doi:10.1029/JA083iA07p03195.
Hosokawa, K., K. Shiokawa, Y. Otsuka, T. Ogawa, J.-P. St-Maurice, G. J. Sofko, and D. A. Andre (2009), Relationship between polar cap patches and field-aligned irregularities as observed with an all-sky airglow imager at Resolute Bay and the PolarDARN radar at Rankin Inlet, *J. Geophys. Res.*, *114*, A03306, doi:10.1029/2008JA013707.
Hosokawa, K., Y. Otsuka, Y. Ogawa, and T. Tsugawa (2014), Observations of GPS scintillation during an isolated auroral substorm, *Prog. Earth Planet. Sci.*, *1*(1), 16, doi:10.1186/2197-4284-1-16.
Jin, Y., J. I. Moen, and W. J. Miloch (2014), GPS scintillation effects associated with polar cap patches and substorm auroral activity: Direct comparison, *J. Space Weather Space Clim.*, *4*, doi:10.1051/swsc/2014019.
Johnsen, M. G., D. A. Lorentzen, J. M. Holmes, and U. P. Løvhaug (2012), A model based method for obtaining the open/closed field line boundary from the cusp auroral 6300 Å[OI] red line, *J. Geophys. Res.*, *117*, A03319, doi:10.1029/2011JA016980.
Kersley, L., C. D. Russell, and D. L. Rice (1995), Phase scintillation and irregularities in the northern polar ionosphere, *Radio Sci.*, *30*(3), 619–629, doi:10.1029/94RS03175.
Keskinen, M. J., and S. L. Ossakow (1983), Theories of high-latitude ionospheric irregularities: A review, *Radio Sci.*, *18*(6), 1077–1091, doi:10.1029/RS018i006p01077.
Keskinen, M. J., H. G. Mitchell, J. A. Fedder, P. Satyanarayana, S. T. Zalesak, and J. D. Huba (1988), Nonlinear evolution of the Kelvin-Helmholtz instability in the high-latitude ionosphere, *J. Geophys. Res.*, *93*(A1), 137–152, doi:10.1029/JA093iA01p00137.
Kinrade, J., C. N. Mitchell, P. Yin, N. Smith, M. J. Jarvis, D. J. Maxfield, M. C. Rose, G. S. Bust, and A. T. Weatherwax (2012), Ionospheric scintillation over Antarctica during the storm of 5–6 April 2010, *J. Geophys. Res.*, *117*, A05304, doi:10.1029/2011JA017073.
Kinrade, J., C. N. Mitchell, N. D. Smith, Y. Ebihara, A. T. Weatherwax, and G. S. Bust (2013), GPS phase scintillation associated with optical auroral emissions: First statistical results from the geographic South Pole, *J. Geophys. Res. Space Physics*, *118*, 2490–2502, doi:10.1002/jgra.50214.
Kintner, P. M., B. M. Ledvina, and E. R. de Paula (2007), GPS and ionospheric scintillations, *Space Weather*, *5*, S09003, doi:10.1029/2006SW000260.
Li, G., B. Ning, Z. Ren, and L. Hu (2010), Statistics of GPS ionospheric scintillation and irregularities over polar regions at solar minimum, *GPS Solutions*, *14*, 331–341, doi:10.1007/s10291-009-0156-x.
Lockwood, M., and H. C. Carlson Jr. (1992), Production of polar cap electron density patches by transient magnetopause reconnection, *Geophys. Res. Lett.*, *19*, 1731–1734, doi:10.1029/92GL01993.
Lockwood, M., H. C. Carlson Jr., and P. E. Sandholt (1993), Implications of the altitude of transient 630-nm dayside auroral emissions, *J. Geophys. Res.*, *98*(A9), 15,571–15,587, doi:10.1029/93JA00811.
Lockwood, M., S. W. H. Cowley, M. F. Smith, R. P. Rijnbeek, and R. C. Elphic (1995), The contribution of flux transfer events to convection, *Geophys. Res. Lett.*, *22*(10), 1185–1188, doi:10.1029/95GL01008.
Lockwood, M., J. Moen, A. P. van Eyken, J. A. Davies, K. Oksavik, and I. W. McCrea (2005a), Motion of the dayside polar cap boundary during substorm cycles: I. Observations of pulses in the magnetopause reconnection rate, *Ann. Geophys.*, *23*, 3495–3511.
Lockwood, M., J. A. Davies, J. Moen, A. P. van Eyken, K. Oksavik, I. W. McCrea, and M. Lester (2005b), Motion of the dayside polar cap boundary during substorm cycles: II. Generation of poleward-moving events and polar cap patches by pulses in the magnetopause reconnection rate, *Ann. Geophys.*, *23*, 3513–3532.
Lorentzen, D. A., N. Shumilov, and J. Moen (2004), Drifting airglow patches in relation to tail reconnection, *Geophys. Res. Lett.*, *31*, L02806, doi:10.1029/2003GL017785.
Lorentzen, D. A., J. Moen, K. Oksavik, F. Sigernes, Y. Saito, and M. G. Johnsen (2010), In situ measurement of a newly created polar cap patch, *J. Geophys. Res.*, *115*, A12323, doi:10.1029/2010JA015710.
McWilliams, K. A., T. K. Yeoman, and G. Provan (2000), A statistical survey of dayside pulsed ionospheric flows as seen by the CUTLASS Finland HF radar, *Ann. Geophys.*, *18*, 445–453.
Milan, S. E., M. Lester, S. W. H. Cowley, J. Moen, P. E. Sandholt, and C. J. Owen (1999), Meridian-scanning photometer, coherent HF radar, and magnetometer observations of the cusp: A case study, *Ann. Geophys.*, *17*, 159–172.
Milan, S. E., M. Lester, S. W. H. Cowley, and M. Brittnacher (2000), Convection and auroral response to a southward turning of the IMF: Polar UVI, CUTLASS, and IMAGE signatures of transient magnetic flux transfer at the magnetopause, *J. Geophys. Res.*, *105*(A7), 15,741–15,755, doi:10.1029/2000JA900022.
Milan, S. E., M. Lester, and T. K. Yeoman (2002), HF radar polar patch formation revisited: Summer and winter variations in dayside plasma structuring, *Ann. Geophys.*, *20*, 487–499, doi:10.5194/angeo-20-487-2002.
Milan, S. E., S. Basu, T. K. Yeoman, and R. E. Sheehan (2005), A comparison of satellite scintillation measurements with HF radar backscatter characteristics, *Ann. Geophys.*, *23*, 3451–3455, doi:10.5194/angeo-23-3451-2005.
Mitchell, C. N., L. Alfonsi, G. De Franceschi, M. Lester, V. Romano, and A. W. Wernik (2005), GPS TEC and scintillation measurements from the polar ionosphere during the October 2003 storm, *Geophys. Res. Lett.*, *32*, L12S03, doi:10.1029/2004GL021644.
Moen, J., H. C. Carlson, and P. E. Sandholt (1999), Continuous observations of cusp auroral dynamics in response to an IMF BY polarity change, *Geophys. Res. Lett.*, *26*, 1243–1246, doi:10.1029/1999GL900224.
Moen, J., H. C. Carlson, S. E. Milan, N. Shumilov, B. Lybekk, P. E. Sandholt, and M. Lester (2001), On the collocation between dayside auroral activity and coherent HF radar backscatter, *Ann. Geophys.*, *18*, 1531–1549.
Moen, J., Y. Rinne, H. C. Carlson, K. Oksavik, R. Fujii, and H. Opgenoorth (2008), On the relationship between thin Birkeland current arcs and reversed flow channels in the winter cusp/cleft ionosphere, *J. Geophys. Res.*, *113*, A09220, doi:10.1029/2008JA013061.
Moen, J., K. Oksavik, T. Abe, M. Lester, Y. Saito, T. A. Bekkeng, and K. S. Jacobsen (2012), First in-situ measurements of HF radar echoing targets, *Geophys. Res. Lett.*, *39*, L07104, doi:10.1029/2012GL051407.
Moen, J., K. Oksavik, L. Alfonsi, Y. Daabakk, V. Romano, and L. Spogli (2013), Space weather challenges of the polar cap ionosphere, *J. Space Weather Space Clim.*, *3*, doi:10.1051/swsc/2013025.
Mushini, S. C., P. T. Jayachandran, R. B. Langley, J. W. MacDougall, and D. Pokhotelov (2012), Improved amplitude- and phase-scintillation indices derived from wavelet detrended high-latitude GPS data, *GPS Solutions*, *16*(3), 363–373, doi:10.1007/s10291-011-0238-4.
Neudegg, D. A., T. K. Yeoman, S. W. H. Cowley, G. Provan, G. Haerendel, W. Baumjohann, U. Auster, K.-H. Fornacon, E. Georgescu, and C. J. Owen (1999), A flux transfer event observed at the magnetopause by the Equator-S spacecraft and in the ionosphere by the CUTLASS HF radar, *Ann. Geophys.*, *17*, 707–711.

AGU Journal of Geophysical Research: Space Physics 10.1002/2015JA021528

Neudegg, D. A., et al. (2000), A survey of magnetopause FTEs and associated flow bursts in the polar ionosphere, *Ann. Geophys.*, *18*, 416–435.
Nishimura, Y., et al. (2014), Day-night coupling by a localized flow channel visualized by polar cap patch propagation, *Geophys. Res. Lett.*, *41*, 3701–3709, doi:10.1002/2014GL060301.
Oksavik, K., F. Søraas, J. Moen, and W. J. Burke (2000), Optical and particle signatures of magnetospheric boundary layers near magnetic noon: Satellite and ground-based observations, *J. Geophys. Res.*, *105*(A12), 27,555–27,568, doi:10.1029/1999JA000237.
Oksavik, K., J. Moen, and H. C. Carlson (2004), High-resolution observations of the small-scale flow pattern associated with a poleward moving auroral form in the cusp, *Geophys. Res. Lett.*, *31*, L11807, doi:10.1029/2004GL019838.
Oksavik, K., J. Moen, H. C. Carlson, R. A. Greenwald, S. E. Milan, M. Lester, W. F. Denig, and R. J. Barnes (2005), Multi-instrument mapping of the small-scale flow dynamics related to a cusp auroral transient, *Ann. Geophys.*, *23*, 2657–2670.
Oksavik, K., V. L. Barth, J. Moen, and M. Lester (2010), On the entry and transit of high-density plasma across the polar cap, *J. Geophys. Res.*, *115*, A12308, doi:10.1029/2010JA015817.
Oksavik, K., J. I. Moen, E. H. Rekaa, H. C. Carlson, and M. Lester (2011), Reversed flow events in the cusp ionosphere detected by SuperDARN HF radars, *J. Geophys. Res.*, *116*, A12303, doi:10.1029/2011JA016788.
Oksavik, K., J. Moen, M. Lester, T. A. Bekkeng, and J. K. Bekkeng (2012), In situ measurements of plasma irregularity growth in the cusp ionosphere, *J. Geophys. Res.*, *117*, A11301, doi:10.1029/2012JA017835.
Ossakow, S. L., and P. K. Chaturvedi (1979), Current convective instability in the diffuse aurora, *Geophys. Res. Lett.*, *6*(4), 332–334, doi:10.1029/GL006i004p00332.
Pinnock, M., A. S. Rodger, J. R. Dudeney, K. B. Baker, P. T. Newell, R. A. Greenwald, and M. E. Greenspan (1993), Observations of an enhanced convection channel in the cusp ionosphere, *J. Geophys. Res.*, *98*(A3), 3767–3776, doi:10.1029/92JA01382.
Pinnock, M., A. S. Rodger, J. R. Dudeney, F. Rich, and K. B. Baker (1995), High spatial and temporal resolution observations of the ionospheric cusp, *Ann. Geophys.*, *13*, 919–925.
Prikryl, P., P. T. Jayachandran, S. C. Mushini, D. Pokhotelov, J. W. MacDougall, E. Donovan, E. Spanswick, and J.-P. St.-Maurice (2010), GPS TEC, scintillation and cycle slips observed at high latitudes during solar minimum, *Ann. Geophys.*, *28*, 1307–1316, doi:10.5194/angeo-28-1307-2010.
Prikryl, P., P. T. Jayachandran, S. C. Mushini, and R. Chadwick (2011), Climatology of GPS phase scintillation and HF radar backscatter for the high-latitude ionosphere under solar minimum conditions, *Ann. Geophys.*, *29*, 377–392, doi:10.5194/angeo-29-377-2011.
Prikryl, P., P. T. Jayachandran, S. C. Mushini, and I. G. Richardson (2014), High-latitude GPS phase scintillation and cycle slips during high-speed solar wind streams and interplanetary coronal mass ejections: A superposed epoch analysis, *Earth Planets Space*, *66*, 62, doi:10.1186/1880-5981-66-62.
Prikryl, P., P. T. Jayachandran, R. Chadwick, and T. D. Kelly (2015), Climatology of GPS phase scintillation at northern high latitudes for the period from 2008 to 2013, *Ann. Geophys.*, *33*, 531–545, doi:10.5194/angeo-33-531-2015.
Provan, G., and T. K. Yeoman (1999), Statistical observations of the MLT, latitude and size of pulsed ionospheric flows with the CUTLASS Finland radar, *Ann. Geophys.*, *17*, 855–867.
Provan, G., T. K. Yeoman, and S. E. Milan (1998), CUTLASS Finland radar observations of the ionospheric signatures of flux transfer events and the resulting plasma flows, *Ann. Geophys.*, *16*, 1411–1422.
Provan, G., S. E. Milan, M. Lester, T. K. Yeoman, and H. Khan (2002), Simultaneous observations of the ionospheric footprint of flux transfer events and dispersed ion signatures, *Ann. Geophys.*, *20*, 281–287.
Rae, I. J., F. R. Fenrich, M. Lester, K. A. McWilliams, and J. D. Scudder (2004), Solar wind modulation of cusp particle signatures and their associated ionospheric flows, *J. Geophys. Res.*, *109*, A03223, doi:10.1029/2003JA010188.
Rinne, Y., J. Moen, K. Oksavik, and H. C. Carlson (2007), Reversed flow events in the winter cusp ionosphere observed by the European Incoherent Scatter (EISCAT) Svalbard radar, *J. Geophys. Res.*, *112*, A10313, doi:10.1029/2007JA012366.
Rinne, Y., J. Moen, H. C. Carlson, and M. R. Hairston (2010), Stratification of east–west plasma flow channels observed in the ionospheric cusp in response to IMF BY polarity changes, *Geophys. Res. Lett.*, *37*, L13102, doi:10.1029/2010GL043307.
Rino, C. L. (1979), A power law phase screen model for ionospheric scintillation: 1. Weak scatter, *Radio Sci.*, *14*(6), 1135–1145, doi:10.1029/RS014i006p01135.
Rodger, A. S., S. B. Mende, T. J. Rosenberg, and K. B. Baker (1995), Simultaneous optical and HF radar observations of the ionospheric cusp, *Geophys. Res. Lett.*, *22*(15), 2045–2048, doi:10.1029/95GL01797.
Russell, C. T., and R. C. Elphic (1978), Initial ISEE magnetometer results: Magnetopause observations, *Space Sci. Rev.*, *22*, 681–715.
Russell, C. T., and R. C. Elphic (1979), ISEE observations of flux transfer events at the dayside magnetopause, *Geophys. Res. Lett.*, *6*(1), 33–36, doi:10.1029/GL006i001p00033.
Sandholt, P. E., C. S. Deehr, A. Egeland, B. Lybekk, R. Viereck, and G. J. Romick (1986), Signatures in the dayside aurora of plasma transfer from the magnetosheath, *J. Geophys. Res.*, *91*(A9), 10,063–10,079, doi:10.1029/JA091iA09p10063.
Sandholt, P. E., M. Lockwood, T. Oguti, S. W. H. Cowley, K. S. C. Freeman, B. Lybekk, A. Egeland, and D. M. Willis (1990), Midday auroral breakup events and related energy and momentum transfer from the magnetosheath, *J. Geophys. Res.*, *95*(A2), 1039–1060, doi:10.1029/JA095iA02p01039.
Sandholt, P. E., J. Moen, D. Opsvik, W. F. Denig, and W. J. Burke (1993), Auroral event sequence at the dayside polar cap boundary: Signature of time-varying solar wind-magnetosphere-ionosphere coupling, *Adv. Space Res.*, *13*(4), 7–15.
Sandholt, P. E., C. J. Farrugia, J. Moen, Ø. Noraberg, B. Lybekk, T. Sten, and T. Hansen (1998), A classification of dayside auroral forms and activities as a function of interplanetary magnetic field orientation, *J. Geophys. Res.*, *103*(A10), 23,325–23,345, doi:10.1029/98JA02156.
Sandholt, P. E., C. J. Farrugia, and W. F. Denig (2004), Dayside aurora and the role of IMF |By|/|Bz|: Detailed morphology and response to magnetopause reconnection, *Ann. Geophys.*, *22*, 613–628.
Saunders, M. A., C. T. Russell, and N. Sckopke (1984), Flux transfer events: Scale size and interior structure, *Geophys. Res. Lett.*, *11*(2), 131–134, doi:10.1029/GL011i002p00131.
Smith, A. M., C. N. Mitchell, R. J. Watson, R. W. Meggs, P. M. Kintner, K. Kauristie, and F. Honary (2008), GPS scintillation in the high arctic associated with an auroral arc, *Space Weather*, *6*, S03D01, doi:10.1029/2007SW000349.
Southwood, D. J. (1985), Theoretical aspects of ionosphere-magnetosphere-solar wind coupling, *Adv. Space Res.*, *5*(4), 7–14.
Southwood, D. J. (1987), The ionospheric signature of flux transfer events, *J. Geophys. Res.*, *92*(A4), 3207–3213, doi:10.1029/JA092iA04p03207.
Spogli, L., L. Alfonsi, G. De Franceschi, V. Romano, M. H. O. Aquino, and A. Dodson (2009), Climatology of GPS ionospheric scintillations over high and mid-latitude European regions, *Ann. Geophys.*, *27*, 3429–3437, doi:10.5194/angeo-27-3429-2009.
Thorolfsson, A., J.-C. Cerisier, M. Lockwood, P. E. Sandholt, C. Senior, and M. Lester (2000), Simultaneous optical and radar signatures of poleward-moving auroral forms, *Ann. Geophys.*, *18*, 1054–1066.
Tiwari, S., A. Jain, S. Sarkar, S. Jain, and A. K. Gwal (2012), Ionospheric irregularities at Antarctic using GPS measurements, *J. Earth Syst. Sci.*, *121*(2), 345–353, doi:10.1007/s12040-012-0168-8.

AGU Journal of Geophysical Research: Space Physics 10.1002/2015JA021528

Torrence, C., and G. P. Compo (1998), A practical guide to wavelet analysis, *Bull. Am. Meteorol. Soc.*, *79*, 61–78, doi:10.1175/1520-0477(1998)079<0061:APGTWA>2.0.CO;2.

Tsunoda, R. T. (1988), High-latitude F region irregularities: A review and synthesis, *Rev. Geophys.*, *26*(4), 719–760, doi:10.1029/RG026i004p00719.

van der Meeren, C., K. Oksavik, D. Lorentzen, J. I. Moen, and V. Romano (2014), GPS scintillation and irregularities at the front of an ionization tongue in the nightside polar ionosphere, *J. Geophys. Res. Space Physics*, *119*, 8624–8636, doi:10.1002/2014JA020114.

van Dierendonck, A. J., J. Klobuchar, and Q. Hua (1993), Ionospheric scintillation monitoring using commercial single frequency C/A code receivers Proceedings of the 6th International Technical Meeting of the Satellite Division of The Institute of Navigation (ION GPS 1993), Salt Lake City, Utah, September 1993, pp. 1333–1342.

van Dierendonck, A. J., Q. Hua, P. Fenton, and J. Klobuchar (1996), Commercial ionospheric scintillation monitoring receiver development and test results in 52nd Annual Meeting Proceedings: Navigational Technology for the Third Millennium, Inst. of Navig., Fairfax, Va., pp. 573–582.

Vorobjev, V. G., G. Gustafsson, G. V. Starkov, Y. I. Feldstein, and N. F. Shevnina (1975), Dynamics of day and night aurora during substorms, *Planet. Space Sci.*, *23*, 269–278.

Weber, E. J., J. Buchau, J. G. Moore, J. R. Sharber, R. C. Livingston, J. D. Winningham, and B. W. Reinisch (1984), F layer ionization patches in the polar cap, *J. Geophys. Res.*, *89*(A3), 1683–1694, doi:10.1029/JA089iA03p01683.

Wild, J. A., et al. (2001), First simultaneous observations of flux transfer events at the high-latitude magnetopause by the Cluster spacecraft and pulsed radar signatures in the conjugate ionosphere by the CUTLASS and EISCAT radars, *Ann. Geophys.*, *19*, 1491–1508.

Yeoman, T. K., M. Lester, S. W. H. Cowley, S. E. Milan, J. Moen, and P. E. Sandholt (1997), Simultaneous observations of the cusp in optical, DMSP and HF radar data, *Geophys. Res. Lett.*, *24*(17), 2251–2254, doi:10.1029/97GL02072.

Zhang, Q.-H., M. Lockwood, J. C. Foster, S.-R. Zhang, B.-C. Zhang, I. W. McCrea, J. Moen, M. Lester, and J. M. Ruohoniemi (2015), Direct observations of the full Dungey convection cycle in the polar ionosphere for southward interplanetary magnetic field conditions, *J. Geophys. Res. Space Physics*, *120*, 4519–4530, doi:10.1002/2015JA021172.

Paper III

Severe and localized GNSS scintillation at the poleward edge of the nightside auroral oval during intense substorm aurora

C. van der Meeren, K. Oksavik, D. A. Lorentzen, M. T. Rietveld, and L. B. N. Clausen

Journal of Geophysical Research: Space Physics, Vol. 120, doi:10.1002/2015JA021819 (2015)

III

AGU PUBLICATIONS

JGR

Journal of Geophysical Research: Space Physics

RESEARCH ARTICLE
10.1002/2015JA021819

Key Points:
- Strongest phase scintillation from the poleward edge of the nightside substorm auroral oval
- No scintillation is observed from polar cap patches prior to entry into the auroral oval
- Two receivers spaced 120 km apart report completely different scintillation levels

Supporting Information:
- Movie S1
- Movie S1 caption

Correspondence to:
C. van der Meeren,
christer.meeren@uib.no

Citation:
van der Meeren, C., K. Oksavik, D. A. Lorentzen, M. T. Rietveld, and L. B. N.Clausen (2015), Severe and localized GNSS scintillation at the poleward edge of the nightside auroral oval during intense substorm aurora, *J. Geophys. Res. Space Physics*, *120*, doi:10.1002/2015JA021819.

Received 18 AUG 2015
Accepted 7 NOV 2015
Accepted article online 11 NOV 2015

Severe and localized GNSS scintillation at the poleward edge of the nightside auroral oval during intense substorm aurora

Christer van der Meeren[1], Kjellmar Oksavik[1,2], Dag A. Lorentzen[3,4], Michael T. Rietveld[5], and Lasse B. N. Clausen[6]

[1]Birkeland Centre for Space Science, Department of Physics and Technology, University of Bergen, Bergen, Norway, [2]University Centre in Svalbard, Longyearbyen, Norway, [3]Birkeland Centre for Space Science, University Centre in Svalbard, Longyearbyen, Norway, [4]Now at British Antarctic Survey, Cambridge, UK, [5]European Incoherent Scatter Association, Ramfjordbotn, Norway, [6]Department of Physics, University of Oslo, Oslo, Norway

Abstract In this paper we study how GPS, GLONASS, and Galileo navigation signals are compromised by strong irregularities causing severe phase scintillation ($\sigma_\phi > 1$) in the nightside high-latitude ionosphere during a substorm on 3 November 2013. Substorm onset and a later intensification coincided with polar cap patches entering the auroral oval to become auroral blobs. Using Global Navigation Satellite Systems (GNSS) receivers and optical data, we show severe scintillation driven by intense auroral emissions in the line of sight between the receiver and the satellites. During substorm expansion, the area of scintillation followed the intense poleward edge of the auroral oval. The intense auroral emissions were colocated with polar cap patches (blobs). The patches did not contain strong irregularities, neither before entering the auroral oval nor after the aurora had faded. Signals from all three GNSS constellations were similarly affected by the irregularities. Furthermore, two receivers spaced around 120km apart reported highly different scintillation impacts, with strong scintillation on half of the satellites in one receiver and no scintillation in the other. This shows that areas of severe irregularities in the nightside ionosphere can be highly localized. Amplitude scintillations were low throughout the entire interval.

1. Introduction

Ionospheric scintillations are disturbances on transionospheric communication links such as Global Navigation Satellite Systems (GNSS) signals. Scintillations are caused by irregularities in the plasma density. In the high-latitude ionosphere, such irregularities are known to be associated with auroral particle precipitation, polar cap patches, and auroral blobs [e.g., *Moen et al.*, 2013; *Jakowski et al.*, 2012; *Aarons et al.*, 2000; *Hosokawa et al.*, 2014; *Buchau et al.*, 1985; *Weber et al.*, 1986; *Jin et al.*, 2014]. The current paper provides a multiinstrument case study of an event with severe scintillation in the nightside ionosphere involving auroral precipitation, patches, and blobs. It will be shown that the scintillation can be highly localized and colocated with substorm auroral precipitation. Since the nightside polar cap and auroral ionosphere is a highly dynamic and complicated environment, a brief overview of auroral precipitation, patches, and blobs and their relation to GNSS scintillation is provided next as a background for the case study.

1.1. Auroral Emissions and Substorm Activity

An important and well-known feature of the active magnetosphere-ionosphere system is the magnetospheric substorm. A magnetospheric substorm is a transient process initiated on the nightside of the Earth, in which a significant amount of energy derived from the solar wind-magnetosphere interaction is deposited in the auroral ionosphere and magnetosphere [*Rostoker et al.*, 1980]. This is manifested most visibly as auroral emissions, primarily 557.7nm emissions from O(^1S) at ~120 km altitude and 630.0nm emissions from O(^1D) at ~200–250km altitude [e.g., *Solomon et al.*, 1988]. The substorm is normally divided into three phases called growth, expansion, and recovery [e.g., *McPherron*, 1979, 1970; *Akasofu*, 1964]. A review of the substorm and its phases is provided by *Elphinstone et al.* [1996]. We will highlight points relevant to our study: In the growth phase, energy is loaded into the magnetosphere by a southward oriented interplanetary magnetic field (IMF) and dayside reconnection. The polar cap expands due to the added open flux, and the auroral oval migrates

AGU Journal of Geophysical Research: Space Physics 10.1002/2015JA021819

equatorward. In the expansion phase, energy stored in the magnetotail is explosively released into the ionosphere. The aurora suddenly brightens and expands poleward as the magnetotail performs a dipolarization. The energetic particle precipitation enhances the conductivity in the ionosphere, which causes a sudden enhancement of the eastward and westward auroral electrojets. This enhancement is detectable in ground magnetometers due to the westward/eastward electrojet causing a negative/positive deviation in the horizontal component of the magnetic field above the station. The third phase of the substorm is the recovery phase, during which the intensity of the auroral emissions are reduced. The duration of the entire substorm cycle is on the order of a few hours, though during periods of continuous southward IMF the recovery phase may coincide with the growth phase of the next substorm.

1.2. Polar Cap Patch Activity

Another well-known high-latitude feature during active geomagnetic conditions is polar cap patches [e.g., *Carlson*, 2012, and references therein]. During periods of southward IMF, a two-cell convection pattern is set up in the ionosphere which can convect plasma from the solar-ionized high-density plasma reservoir in the dayside ionosphere, through the cusp region, and across the polar cap to the nightside auroral oval [*Dungey*, 1961; *Weber et al.*, 1984; *Foster and Doupnik*, 1984; *Buchau et al.*, 1985; *Foster*, 1993; *Foster et al.*, 2005; *Moen et al.*, 2008; *Cousins and Shepherd*, 2010; *Oksavik et al.*, 2010; *Zhang et al.*, 2013a; *Nishimura et al.*, 2014; *van der Meeren et al.*, 2014]. This plasma is frequently segmented upon entry to the polar cap, with magnetopause reconnection proposed as the dominant segmentation mechanism [*Lockwood and Carlson*, 1992; *Carlson et al.*, 2002, 2004, 2006; *Lockwood et al.*, 2005; *Moen et al.*, 2006; *Lorentzen et al.*, 2010; *Zhang et al.*, 2013b]. The resulting islands of enhanced plasma density are called *F* region polar cap patches. These are typically 100–1000km across and show up as regions of 630.0nm emissions from dissociative recombination of O_2^+ with *F* region electrons creating $O(^1D)$ [e.g., *Wickwar et al.*, 1974; *Hosokawa et al.*, 2011]. These airglow emissions are frequently detectable from ground-based optical instruments [e.g., *Buchau et al.*, 1983; *Weber et al.*, 1984; *Lorentzen et al.*, 2004; *Hosokawa et al.*, 2006; *Moen et al.*, 2007; *Nishimura et al.*, 2014; *van der Meeren et al.*, 2014]. In the nightside ionosphere, patches convect into the nightside auroral oval under the influence of tail reconnection. Patches convecting into the auroral oval have been shown to be associated with substorm onset [*Lyons et al.*, 2011; *Nishimura et al.*, 2013, 2014; *Shi and Zesta*, 2014]. In the auroral oval, they are termed auroral blobs [*Tsunoda*, 1988; *Crowley et al.*, 2000; *Lorentzen et al.*, 2004; *Pryse et al.*, 2006]. Several types of auroral blobs are referred to in literature, namely, boundary blobs, subauroral blobs, and auroral blobs [e.g., *Crowley et al.*, 2000]. In this study, following the example of *Jin et al.* [2014], we use the term to describe patches inside the active auroral oval.

1.3. Ionospheric Scintillations

Both patches and auroral emissions are known to be associated with disturbances of transionospheric signals, also termed scintillations (these relationships will be detailed shortly). Scintillations are rapid variations in the amplitude or phase of radio signals, such as global navigation satellite system (GNSS) signals, and are associated with decameter- to kilometer-scale irregularities in the ionosphere [e.g., *Hey et al.*, 1946; *Basu et al.*, 1990, 1998; *Kintner et al.*, 2007]. Scintillations are categorized into amplitude and phase scintillations. Amplitude scintillations are caused by irregularities with scale sizes of tens of meters to hundreds of meters, more precisely at and below the Fresnel radius, which is approximately 360m for GPS L1 frequency (1575.42MHz) and an irregularity altitude of 350km [e.g., *Forte and Radicella*, 2002]. Amplitude scintillations are normally quantified by the dimensionless S_4 index, which is the standard deviation of the received power I normalized by its mean value over some period of time [*Briggs and Parkin*, 1963]:

$$S_4^2 = \frac{\langle I^2 \rangle - \langle I \rangle^2}{\langle I \rangle^2}$$

Phase scintillations are caused by irregularities with scale sizes from a few hundred meters up to several kilometers [e.g., *Kintner et al.*, 2007] and are normally quantified by the σ_ϕ index, which is the standard deviation of the detrended carrier phase ϕ in radians over some period of time [*Fremouw et al.*, 1978]:

$$\sigma_\phi^2 = \langle \phi^2 \rangle - \langle \phi \rangle^2$$

The period is normally 60s, and the detrending is usually done using a sixth-order Butterworth filter with a cutoff frequency of 0.1Hz [e.g., *Mitchell et al.*, 2005; *Béniguel et al.*, 2009; *Li et al.*, 2010; *Alfonsi et al.*, 2011;

AGU Journal of Geophysical Research: Space Physics 10.1002/2015JA021819

Forte et al., 2011; *Garner et al.*, 2011; *Gwal and Jain*, 2011; *Kinrade et al.*, 2012; *Jiao et al.*, 2013; *Jin et al.*, 2014]. This is not without problems, as the σ_ϕ index is highly sensitive to the cutoff frequency, and 0.1Hz has been shown to be problematic at high latitudes [e.g., *Forte*, 2005]. However, it is possible to get a better overview of the phase variations at different scales by looking at a spectrogram of the raw phase, as was done by *van der Meeren et al.* [2014]. While phase scintillation from satellites in polar orbits are heavily influenced by geometrical factors (specifically, scintillation levels are significantly enhanced when the signal path is *L* shell aligned), this has been shown not to be important at high latitudes for satellites in GPS-like orbits [*Forte and Radicella*, 2004].

Scintillations are found where ionospheric irregularities occur, predominantly in the equatorial and auroral/polar regions [*Basu et al.*, 1988]. High-latitude scintillation is correlated with solar cycle [*Basu et al.*, 1988; *Skone*, 2001] and magnetic activity [*Tiwari et al.*, 2012] and occurs primarily in the cusp and nightside auroral oval [*Kersley et al.*, 1995; *Prikryl et al.*, 2011; *Jin et al.*, 2015]. Phase scintillation is more prominent than amplitude scintillation in the polar ionosphere [*Spogli et al.*, 2009; *Prikryl et al.*, 2010; *Gwal and Jain*, 2011].

1.4. Scintillation From Auroral Activity

Aarons et al. [2000] was the first to show a correlation between fluctuations in GPS phase and substorm-related auroral disturbances. Statistical studies have found that the auroral region is more sensitive to phase than amplitude scintillation and that the phase scintillation occurs at lower latitudes during perturbed conditions, implying a close relationship with the auroral oval [*Spogli et al.*, 2009; *Tiwari et al.*, 2012; *Jiao et al.*, 2013]. Indeed, *Spogli et al.* [2009] found an enhancement of scintillation associated with the boundaries of the statistical auroral oval. It has also been found that auroral scintillation occurs most frequently near midnight magnetic local time (MLT) and that the occurrence and magnitude is strongly correlated with the disturbance of the local magnetic field [*Jiao et al.*, 2013]. *Kinrade et al.* [2013] correlated auroral emissions (557.7nm and 630.0nm) with phase scintillation on a geographical grid and found a proxy relationship between optical emissions and σ_ϕ in the presence of strong auroral activity.

Case studies support the statistical findings. Phase scintillation has been associated with auroral arc brightening and substorms [*Prikryl et al.*, 2010; *Ngwira et al.*, 2010]. *Hosokawa et al.* [2014] found that phase scintillation was enhanced in relation to substorm onset and decreased as the aurora became more diffuse. They suggested that discrete aurora in the GPS signal path is necessary for the occurrence of phase scintillation during substorm intervals. In addition to scintillation, other adverse effects such as loss of lock [*Smith et al.*, 2008] and cycle slips [*Prikryl et al.*, 2010] have been directly observed in relation to auroral emissions.

1.5. Scintillation From Polar Cap Patches

It has long been known that polar cap patches are source regions for decameter- to kilometer-scale irregularities causing scintillation [*Buchau et al.*, 1985; *Weber et al.*, 1986; *Basu et al.*, 1990, 1991, 1994, 1998; *Coker et al.*, 2004; *Carlson*, 2012, and references therein]. It has been suggested that the patches may be initially structured through the Kelvin-Helmholtz instability in the dayside patch segmentation region, creating seed irregularities which allow the gradient drift instability to effectively structure the patch at smaller scale sizes during its transit across the polar cap [*Carlson et al.*, 2007, 2008]. While the gradient drift instability is most effective on the trailing edge of density structures, simulations have shown that the irregularities may propagate from the trailing edge into the interior of the patch, structuring the whole patch at a variety of scale sizes [*Gondarenko and Guzdar*, 2004]. This is supported by observations [e.g., *Hosokawa et al.*, 2009]. Case studies have found an agreement between scintillation and optical airglow from patches [*Jin et al.*, 2014; *Coker et al.*, 2004].

Statistically, an agreement has been found between scintillations at polar latitudes and the asymmetric distribution of patches around magnetic midnight [*Spogli et al.*, 2009], as well as with the IMF dependence of polar cap patches [*Li et al.*, 2010]. Patches are linked to both phase and amplitude scintillation [*Alfonsi et al.*, 2011].

1.6. Motivation for This Study

It is not yet clearly established which ionospheric phenomena produce the strongest irregularities associated with problematic scintillation. *Jin et al.* [2014] studied scintillation from polar cap patches, auroral arcs, and auroral blobs (patches in the auroral oval). They concluded that the most severe scintillation in the European Arctic sector are due to blobs, i.e., when patches are structured by substorm auroral arc dynamics. Specifically, they found that auroral blobs were associated with the strongest scintillation, followed by polar cap patches on their own, with auroral arcs alone showing the least scintillation. That was, however, a case study of only a single night, and further studies are needed to ascertain whether their observations are representative.

AGU Journal of Geophysical Research: Space Physics 10.1002/2015JA021819

Furthermore, while there have been many statistical studies of scintillation-producing irregularities, the temporal and spatial averaging inherent to these studies means it is difficult to clearly establish a direct link between scintillations and highly transient phenomena such as polar cap patches and auroral arc dynamics.

A notable space weather impact of intense scintillation is loss of signal lock on GNSS signals, potentially resulting in the receiver being unable to compute a navigation solution if sufficiently many signals are affected [e.g., *Kintner et al.*, 2007]. The propensity for losing lock is receiver-dependent and may be influenced by the internal state of the receiver [*Garner et al.*, 2011]. Several GNSS constellations exist, e.g., GPS, GLONASS, and Galileo. For multiconstellation GNSS receivers, this increases the likelihood that a sufficient number of signals will remain trackable during scintillation events. However, the signals of all three constellations use similar frequencies in the L band, and one should therefore expect that all constellations are prone to similar scintillation effects.

This case study uses three all-sky imagers and 50Hz raw data from four multiconstellation GNSS receivers in the Svalbard region to provide a detailed look at when and where scintillation occurs during substorm activity in the nightside polar cap. The study shows that severe scintillation is observed when auroral precipitation coincides with patches. Our observations further indicate that the irregularities are driven by auroral precipitation and that the scintillation is highly localized. This is also the first study to show directly that GPS, GLONASS, and Galileo are similarly affected by severe scintillation in relation to intense line-of-sight auroral emissions in a highly localized region of the sky.

2. Instrumentation

2.1. GNSS Receivers

The GNSS data used in this study come from four NovAtel GPStation-6 GNSS Ionospheric Scintillation and TEC Monitors installed in Svalbard in 2013 and operated by the University of Bergen. The receiver locations, geographic latitudes (GLAT), geographic longitudes (GLON), and magnetic latitudes (MLAT, Altitude Adjusted Corrected Geomagnetic Coordinates (AACGM) [*Baker and Wing*, 1989]) are Ny-Ålesund (78.9° GLAT, 11.9° GLON, 76.4° MLAT), Longyearbyen (78.1° GLAT, 16.0° GLON, 75.4° MLAT), Hopen (76.5° GLAT, 25.0° GLON, 73.3° MLAT), and Bjørnøya (74.5° GLAT, 19.0° GLON, 71.6° MLAT).

Magnetic midnight is around 2100–2130 UT. All receivers track GPS, GLONASS, and Galileo at several frequencies. For the period of study, all constellations were tracked at L1 (1575.42MHz). Additionally, GLONASS was tracked at L2 (1227.60MHz) and Galileo was tracked at E5 (1191.795MHz). There was no significant difference in scintillation levels in the different signals (the lower frequencies showed marginally higher levels), so L1 will be used in this study.

The receivers output both 60s reduced data and 50Hz raw data (phase and power). In this paper, both are used. Specifically, 50Hz raw data are used to compute the σ_ϕ index with 1s resolution. When calculating the phase scintillation index, the raw phase is detrended by subtracting a polynomial fit and filtered using a sixth-order Butterworth high-pass filter with a cutoff frequency of 0.1Hz. The S_4 index is calculated by subtracting S_4 due to ambient noise from the total S_4 in a root-sum-square sense according to the user manual [*NovAtel*, 2012]. A minimum lock time of 60s was required for S_4 data, and 240s for σ_ϕ. The elevation was required to be at least 20° to limit multipath effects.

The GNSS ionospheric piercing points (IPPs) have been projected to 150km altitude when shown together with green 557.7nm aurora and 250km when shown together with red 630.0nm emissions.

In the same manner as *van der Meeren et al.* [2014] and *Oksavik et al.* [2015], spectrograms of the raw phase are used in order to obtain more detailed information on the phase variations. The spectrograms were made using wavelet analysis, based on software provided by *Torrence and Compo* [1998]. The Morlet wavelet was chosen as the mother wavelet. This method has been used previously by other GNSS studies [e.g., *Mushini et al.*, 2012]. No detrending of the raw phase is required to produce the wavelet spectrograms. For the reader's information, the wavelet spectrograms were compared to spectrograms made using Fourier analysis of detrended data and showed exactly the same features. The wavelet spectrograms provided much better resolution at smaller scales and were thus chosen for this study. For further details on wavelet analysis we refer to the literature [e.g., *Torrence and Compo*, 1998; *Mushini et al.*, 2012].

2.2. Optics

We use data from three all-sky imagers (ASI) and a meridian-scanning photometer (MSP). The fields of view at 250km altitude are indicated in red in Figure 1.

AGU Journal of Geophysical Research: Space Physics 10.1002/2015JA021819

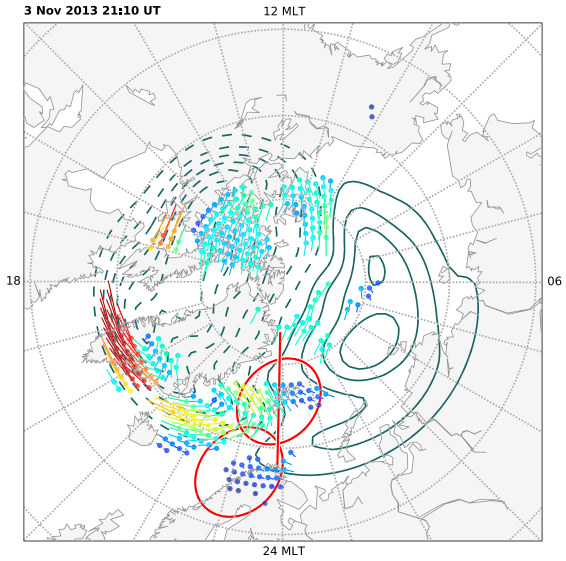

Figure 1. SuperDARN drift vectors and polar cap potential data at 2110 UT showing a two-cell convection pattern (representative of the whole period). The data are displayed in an MLAT/MLT grid. The red line and circles indicate the fields of view of the meridian-scanning photometer in Longyearbyen and the all-sky imagers in Longyearbyen and at Andøya projected to 250km altitude.

The ASIs are operated by the University of Oslo and are located in Ny-Ålesund and Longyearbyen (colocated with the GNSS receivers) and at Andøya (69.2° GLAT, 16.0° GLON, 66.3° MLAT). All three imagers have filters for green line (557.7nm) and red line (630.0nm) emissions. The imager in Longyearbyen is calibrated. Emissions at 557.7nm are projected to 150km altitude, while emissions at 630.0nm are projected to 250km.

The MSP is located in Longyearbyen and is operated by the University Centre in Svalbard. It scans along the magnetic meridian and records a full scan at a 16s cadence of green (557.7nm) and red (630.0nm) emissions. The intensity is calibrated.

2.3. Solar Wind and the *AE* Index

Data from the IMF and solar wind, as well as the auroral electrojet (*AE*) index, are provided by the NASA OMNIWeb service. Both the IMF and plasma data are provided by the Wind spacecraft [*Lepping et al.*, 1995; *Ogilvie et al.*, 1995]. The spacecraft was located at $(X, Y, Z) = (254, 48, 20)\,R_E$ (geocentric solar ecliptic coordinates). The data are time shifted to the bow shock by the OMNIWeb service.

2.4. Magnetometer Data

We make use of the horizontal component of the magnetic field measured at Bjørnøya (BJN). The magnetometer is a fluxgate magnetometer colocated with the GNSS receiver at Bjørnøya.

2.5. SuperDARN and Convection Data

The Super Dual Auroral Radar Network (SuperDARN) is a network of coherent high-frequency (HF) scatter radars measuring backscatter from field-aligned decameter-scale irregularities [*Greenwald et al.*, 1995; *Chisham et al.*, 2007]. HF backscatter is therefore an indicator of the presence of decameter-scale irregularities. Drift velocity data are used to calculate the polar cap potential and convection pattern. The SuperDARN data is retrieved from Virginia Tech using the DaViTpy software package.

AGU Journal of Geophysical Research: Space Physics 10.1002/2015JA021819

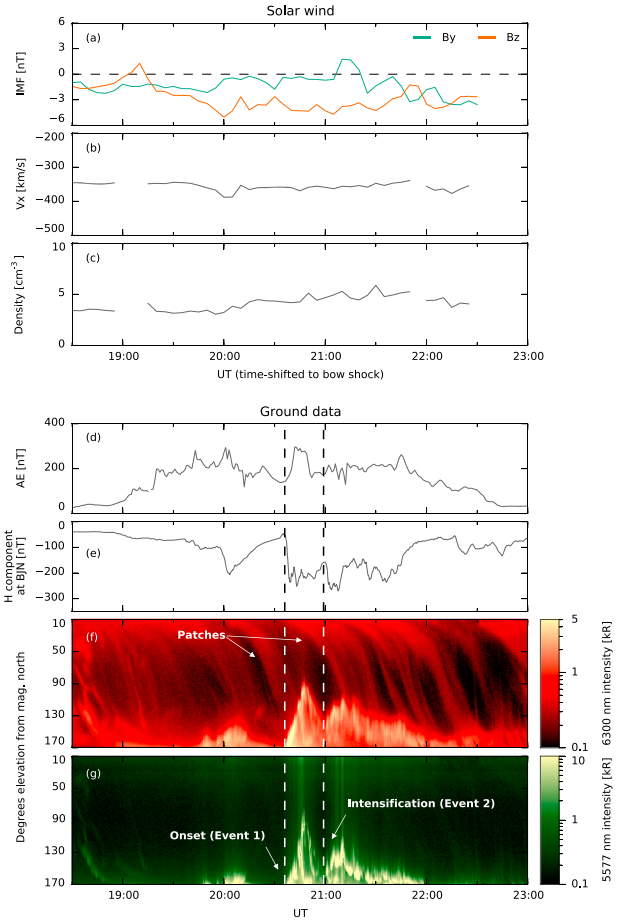

Figure 2. Overview of the geomagnetic conditions. (a) The B_y and B_z GSM (geocentric solar magnetic) components of the interplanetary magnetic field, (b) the radial solar wind speed, and (c) the solar wind density. The data are from the Wind satellite at $(X, Y, Z) = (254, 48, 20)\, R_E$ and have been time shifted to the bow shock by OMNIWeb. (d) The *AE* (auroral electrojet) index. (e) The deviation in the horizontal *H* component of the geomagnetic field at Bjørnøya (BJN). The (f) 630.0nm and (g) 557.7nm emissions as observed by the meridian-scanning photometer in Longyearbyen between elevation angles of 10° (magnetic north) and 170° (magnetic south). The vertical lines mark the substorm onset and intensification.

AGU Journal of Geophysical Research: Space Physics 10.1002/2015JA021819

3. Observations

Figure 2 shows an overview of the solar wind and geomagnetic conditions on 3 November 2013 between 1830 and 2300 UT. Figure 2a shows the B_y and B_z components of the IMF. The IMF was southward oriented, which is known to be associated with a two-cell convection pattern across the polar cap. This is exemplified by Figure 1, which shows the polar cap potential from the SuperDARN radars at 2110 UT. Figures 2b and 2c indicate stable conditions in the solar wind speed and density, respectively.

The *AE* index (Figure 2d) shows increased magnetic activity during a period of around 4 h. The *Kp* index was around 2 (not shown), which indicates weakly disturbed geomagnetic conditions. Figure 2e shows the deviation of the horizontal (*H*) component of the magnetic field at Bjørnøya (BJN). The *H* component drops sharply around 2035 UT, which indicates a sudden enhancement of the westward electrojet over this station consistent with ongoing substorm activity. Another sharp drop is seen around 2100 UT, coinciding with a new intensification of the aurora.

The MSP data (Figures 2f and 2g) clearly show the poleward expansion of the aurora after onset, as well as an intensification and a slight expansion around 2100 UT. In this study, we will refer to the onset and expansion as Event 1, and the intensification as Event 2. The red line emissions show several patches drifting southward from the polar cap and into the auroral oval. Two of these patches (indicated in the figure) coincide with the substorm onset and the intensification, respectively. The MSP data also show a brightening around 2000 UT, which may be a pseudo-onset. While this was accompanied by fairly strong scintillation (σ_ϕ up to 0.7–0.8, not shown), the observation geometry was not favorable for this event due to the aurora being too low on the horizon. In this study we will only consider the aforementioned onset and intensification events.

Figure 3 gives a detailed view of auroral intensity and phase scintillation at four different times during Event 1 (onset/expansion). Figures 3a–3d and 3e–3h show red line and green line emissions, respectively. Figures 3a and 3e are before onset and shows that $\sigma_\phi < 0.2$ for all satellites and all four receivers. This includes the patch, which can be seen in the red line emissions (Figure 2a) as a light blue area stretching from west to northeast of Svalbard. According to ionosonde data from Longyearbyen (not shown), the patch has a critical frequency of 6.2MHz (corresponding to an electron density of 4.8×10^{11} m^{-3}), which is 1.5 times the background density. (For the reader's information, total electron content (TEC) data were studied but were inconclusive both in the patch and auroral regions and were not found to be helpful to the current study.) Figures 3b–3c and 3f–3g show scintillation during the poleward expansion of the aurora. The patch drifts southward, and as the southwestern edge of the patch reaches the auroral oval, onset and poleward expansion of the aurora occurs. This can be seen in Figure 2b but is more easily seen in the supporting information Movie S1. The phase scintillation follows the intense poleward edge of the aurora as it expands northward (across the patch) and reaches values of $\sigma_\phi > 1$ during the expansion. There are only minor scintillations in the more diffuse emissions further equatorward of the edge. Finally, the rightmost column shows scintillation after the expansion has subsided and the aurora has faded. Due to the auroral emissions, it is not possible to see the patch in the optical data. There is no significant scintillation ($\sigma_\phi < 0.2$ for almost all satellites).

Figure 4 is in the same format as Figure 3 and shows the auroral intensity and phase scintillation during Event 2 (the intensification). Figures 4a and 4e show the conditions before the intensification. A patch is seen as a light blue area to the northwest of Svalbard. The peak density of the patch is difficult to determine due to only a small part of it drifting over the ionosonde in Longyearbyen, but a later part of the patch drifting over Longyearbyen at 2122 UT was studied and showed a critical frequency of 6.0MHz (electron density 4.5×10^{11} m^{-3}) over a background of 4.0MHz (2.0×10^{11} m^{-3}), which is a relative density of 2.3. There is no scintillation ($\sigma_\phi < 0.2$) in relation to the patch or the dim aurora. The exact time of arrival of the patch at the poleward edge of the aurora is difficult to ascertain due to the patch entering the aurora at an oblique angle, but the arrival roughly coincides with an auroral intensification and strong scintillations. The brightest aurora and strongest scintillation occurs around 2110 UT (column 3). Here the aurora peaks at 55kR, and $\sigma_\phi > 1.5$ in the most intense aurora for satellites from all three constellations. As in the previous event, the patch is colocated with the strong aurora and the scintillations. Figures 4d and 4h show that there are no strong scintillations after the aurora has faded and the patch has entered the auroral zone.

Data from a GPS receiver at Hornsund (not shown) have also been studied and support these findings. For the reader's reference, an animation in the style of Figures 3 and 4 for the period 2000–2130 UT is provided in the supporting information Movie S1.

AGU Journal of Geophysical Research: Space Physics 10.1002/2015JA021819

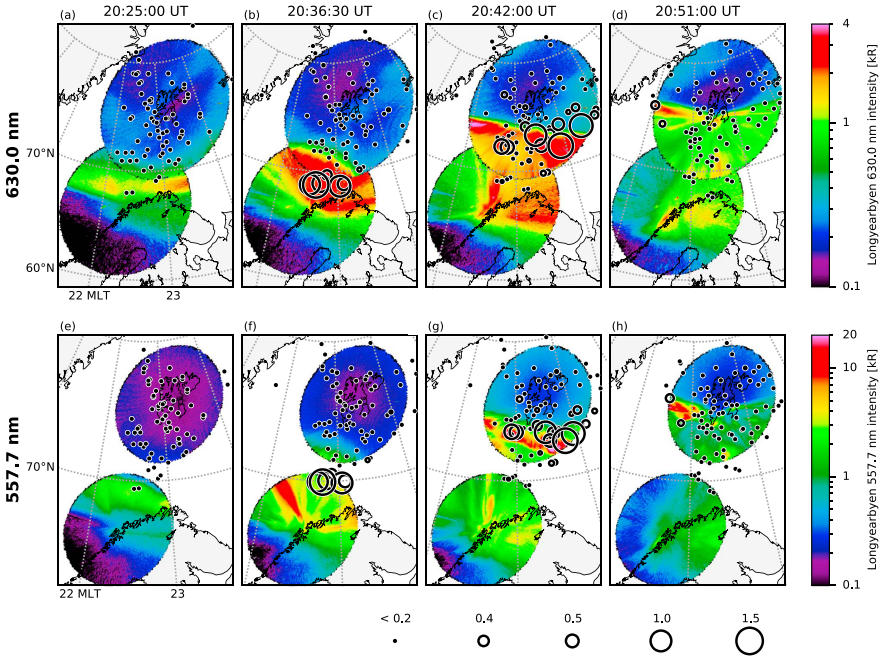

Figure 3. Auroral emissions and phase scintillation (a, e) before, (b–c and f–g) during, and (d, h) after Event 1 (the substorm expansion). Panels (a–d) and (e–h) show red line (630.0nm) and green line (557.7nm) emissions, respectively. The GNSS ionospheric piercing points are shown as circles, with the size representing the intensity of the phase scintillation. The arriving patch can be seen in Figure 3a as a light blue area stretching from west to northeast of Svalbard.

Figures 5 and 6 provide a closer look at scintillation and phase variations in relation to line-of-sight auroral emissions for three selected satellites at two receiver locations. In these figures we have computed high-resolution scintillation indices over periods of 1s from the 50Hz raw data. These high-resolution data match closely the corresponding lower resolution 60s data (not shown) and provide a more fine-grained view of the observations. In Longyearbyen (Figure 5), there is little or no amplitude scintillation. However, strong phase scintillation is observed in relation to Event 1, and severe phase scintillation ($\sigma_\phi > 1.5$) is observed in relation to Event 2. The most intense line-of-sight emissions are seen in Event 2. The intensity in Figures 5a–5c (and Figures 6a–6c) is based on a 7-by-7 pixel window centered at the elevation and azimuth of the satellite, and the panels show the median of the pixels as lines and the minimum and maximum of the window as shaded regions. The data show a close correspondence between intense 557.7nm emissions and phase scintillation. In Figure 5m, the severe scintillation is observed for a cluster of five satellites including GPS, GLONASS, and Galileo, three of which are shown in Figures 5a–5l. These signals are intersecting a region of intense 557.7nm emissions (up to 55kR). Strong scintillations are also seen in another satellite in the aurora further east. The phase spectra show enhanced phase variations at a variety of temporal scales (1–50s) during the two events, with short bursts of highly localized variations at smaller scales concurrent with the most intense phase scintillation and auroral emissions.

Figure 6 shows the same type of data from Ny-Ålesund. Since Ny-Ålesund is north of Longyearbyen, the aurora in the south is observed at a lower elevation. Again, there is no amplitude scintillation. The southernmost of the three satellites (GPS 09) show severe phase scintillation (σ_ϕ ~1) in relation to Event 1, when the aurora is

AGU Journal of Geophysical Research: Space Physics 10.1002/2015JA021819

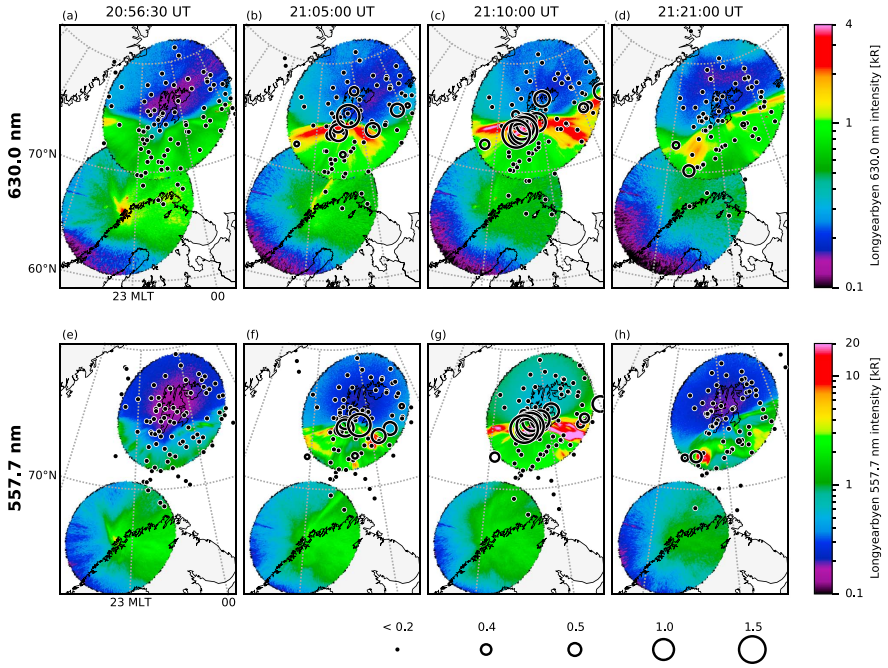

Figure 4. Auroral emissions and phase scintillation before, during, and after Event 2 (the intensification). See Figure 3 for description.

at its most poleward point during the whole period under study (cf. the MSP data in Figures 2f and 2g). Around this time, the auroral emissions saturate the ASI (Figure 6c). However, unlike in Longyearbyen, only very weak phase scintillation is produced during Event 2. From Figure 6m we observe that the intense 557.7nm emissions during the intensification do not cross the line of sight between the receiver and the satellites. The spectra show enhanced variations at a range of frequencies, but the variations are less severe (lower spectral power), less temporally localized, and less spectrally wide than in the Longyearbyen data.

None of the four receivers experienced loss of lock above 25° elevation during the whole period (2030–2130 UT).

4. Discussion

4.1. Comparison of Aurora, Patches, and Auroral Blobs

The severe scintillation in this study appears to be driven by intense auroral emissions. For both events, Figures 5a–5i shows a remarkable correspondence between phase scintillations and the intensity of line-of-sight auroral 557.7nm emissions, as suggested by *Hosokawa et al.* [2014]. For Event 1, Figure 3 shows clearly that the severe phase scintillation follows the intense poleward edge of the auroral oval. This implies a close relation between the scintillations and the poleward expanding arc of auroral emissions. This is in line with previous statistical studies, which have shown a relationship between scintillation and the auroral oval in general [*Tiwari et al.*, 2012; *Jiao et al.*, 2013; *Kinrade et al.*, 2013] and the auroral oval walls in particular [*Spogli et al.*, 2009]. Case studies have also indicated a relationship between auroral emissions and GNSS scintillations [*Prikryl et al.*, 2010; *Ngwira et al.*, 2010; *Kinrade et al.*, 2013]. For our events, Figures 3 and 4 show that there is no scintillation in relation to the patches. Together with Figures 5m and 6m they support the conclusion

AGU Journal of Geophysical Research: Space Physics 10.1002/2015JA021819

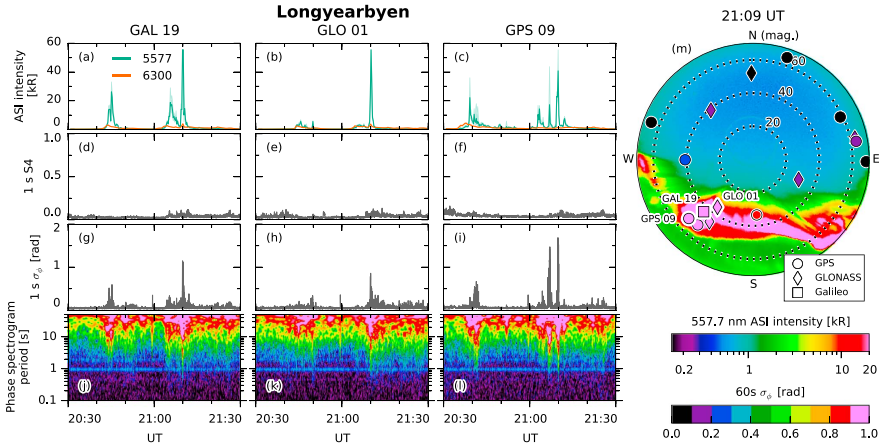

Figure 5. GNSS scintillations and phase variations for three selected satellites in relation to line-of-sight auroral intensity at Longyearbyen. (a–c) The auroral intensity in the vicinity of the satellite IPPs. (d–f) The S_4 amplitude scintillation index computed from 50Hz raw data over periods of 1s. (g–i) The σ_ϕ phase scintillation index computed from 50Hz raw data over periods of 1s. (j–l) Wavelet power spectra of 50Hz raw phase on a decibel (logarithmic) color scale (not shown). (m) GNSS satellites and a selected 557.7nm all-sky image on a polar axis (zenith angle versus azimuth; magnetic north is up, magnetic east is right). The three satellites shown in Figures 5a–5l are highlighted.

that the scintillation is driven by the aurora and not the patches: In Ny-Ålesund (Figure 6m), the cluster of five satellites to the southwest do not intersect the aurora, and there is no scintillation. In Longyearbyen (Figure 5m), the signals do intersect the aurora and there is severe scintillation. The patch (not visible in these 557.7nm images) is intersected by the signals at both locations (it arrives first at Ny-Ålesund and then in Longyearbyen). It is thus clear from our observations in the nightside polar cap that the observed patches on their own are not sufficient for creating scintillation-inducing irregularities. This suggests that the auroral precipitation is providing the energy input for the irregularities.

While the presence of the scintillation can be mainly attributed to the precipitation, the magnitude of the scintillation is still an outstanding question in these events. Specifically, is the auroral precipitation sufficient to produce the observed severe scintillation, or do the blobs (patches in the auroral region) contribute to the strength of the irregularities and scintillation? Fully answering this question requires further studies and more events with both aurora-only and aurora/blob events. To address this issue in a cursory manner, we can compare our results with those of *Jin et al.* [2014]. One of the events they studied was a period of scintillation from aurora without patches. Calibrated ASI data were not available when that study was performed, but the ASI in Longyearbyen has since been calibrated. A brief analysis of line-of-sight intensities and corresponding scintillation (using the Longyearbyen GNSS receiver in the current study) in the manner of Figure 5 indicated values up to 50 kR with corresponding σ_ϕ levels around 0.2–0.3 (not shown). The intensity values are similar to those of our events, but the scintillation levels are significantly lower. This may indicate that intense aurora alone is not sufficient to produce the severe scintillation we observe in the current study and that the patches/blobs in our events have contributed to the severe scintillation levels observed in the auroral region. If this is the case, we do not have the data to infer the process behind this contribution. Our data do, however, show that the scintillation quickly disappears when the aurora fades. This suggests that if there is such a process, it appears to be directly driven by the auroral precipitation, and the irregularities created by it quickly dissipate when the aurora fades. Further studies are needed to ascertain whether blobs in the auroral region really do contribute to scintillation levels and, if they do, find a physical process behind such a contribution.

AGU Journal of Geophysical Research: Space Physics 10.1002/2015JA021819

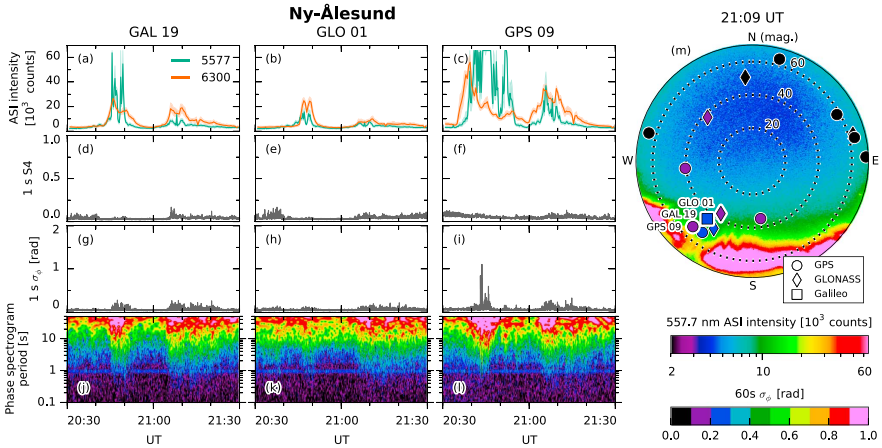

Figure 6. Same as Figure 5 but for the Ny-Ålesund receiver and all-sky imager. Note that the emission intensity (Figures 6a–6c) is uncalibrated for both color channels.

The critical reader may be interested to know that while our patches are not associated with scintillation before entering the auroral oval, and the patches studied by *Jin et al.* [2014] are, the patches in the two studies are otherwise similar: Ionosonde data from the period studied by *Jin et al.* [2014] (not shown) are not entirely conclusive due to many *E* region echoes but suggest patch critical frequencies of 6.0–7.2MHz (corresponding to peak densities of $4.4–6.4 \times 10^{11}$ m^{-3}), which is 1.5–2.7 times the respective background densities. This is similar to the absolute and relative densities in our study and was not reported in their paper.

4.2. Irregularity Scales

van der Meeren et al. [2014] studied a drifting *F* region plasma structure which, due to the low recombination rate in the *F* region, could be viewed as a stable structure (not changing in time) compared to its drift speed across the signal line of sight. Based on the relative drift speed between the plasma and the IPPs, it was therefore possible to convert the temporal scale size of the phase variations to spatial scale and get valuable quantitative information on the scale sizes of the irregularities. Unfortunately, this is not straightforward in this study. The scintillations probably have a strong contribution from energetic particle precipitation in the *E* region. In this region the recombination rate is much higher than in the *F* region, and the plasma cannot be assumed to be a stable, drifting structure. Additionally, there are temporal variations in the auroral precipitation which causes variation in the irregularities. However, since amplitude scintillation is most sensitive to irregularities with scale sizes at and below the Fresnel radius, which does not depend on the drift speed and is on the order of ~300 m [e.g., *Forte and Radicella*, 2002], the lack of amplitude scintillation implies weaker irregularities at 10–100m scale. Decameter-scale irregularities may also be studied using HF backscatter data. SuperDARN backscatter from the polar cap was sporadic, and we were not able to see the patches in the radar data. However, the Hankasalmi SuperDARN radar generally show strong backscatter (> 30 dB) from the region of auroral emissions (not shown), which implies the presence of decameter-scale irregularities in the aurora. HF backscatter from visible aurora and precipitation regions have been extensively documented [*Chisham et al.*, 2007, and references therein]. However, since GNSS amplitude scintillation remains low even in the presence of intense auroral emissions and strong HF backscatter, this suggests that in our event the irregularities detected by SuperDARN are not strong enough to cause amplitude scintillation. This was also found in a previous study [*van der Meeren et al.*, 2014] (note, however, that some correspondence between HF backscatter and 250MHz amplitude scintillation has been found [*Milan et al.*, 2005]).

AGU Journal of Geophysical Research: Space Physics 10.1002/2015JA021819

4.3. Spatial Variability of Scintillation Between Two Sites

Another salient point of our observations is the spatial variability of the scintillation. There is a remarkable difference between Longyearbyen and Ny-Ålesund, which are located only ~120 km apart. During Event 2, Longyearbyen (the southernmost of the two locations) reports severe scintillation ($\sigma_\phi > 0.8$) on 6 of 16 visible satellites (Figure 5m). At the same time in Ny-Ålesund (Figure 6m), there is no or only weak scintillation ($\sigma_\phi < 0.3$). The difference between the two locations suggests that intense aurora in the line of sight between the receiver and the satellite is required to produce severe scintillation, as suggested by *Hosokawa et al.* [2014]. Furthermore, it shows that scintillation events and severe ionospheric irregularities can be highly localized and demonstrates the need for a dense network of receivers to properly capture the spatial variability of irregularities. Such localization differences are easily averaged out in statistical studies, where binning may take place on the order of 100–1000km [e.g., *Spogli et al.*, 2009; *Tiwari et al.*, 2012].

4.4. Comparison of GNSS Constellations

The arrangement of the GNSS satellites during this event presents a unique opportunity to compare directly scintillation levels across GPS, GLONASS, and Galileo. Figures 5 and 6 show high-resolution 1s scintillation data from all three constellations. As expected due to all constellations using similar frequencies, GPS, GLONASS, and Galileo are similarly affected. Galileo 19 show a maximum phase scintillation of σ_ϕ ~1.2, GLONASS 01 show σ_ϕ~1.0, and GPS 09 experience the most severe scintillation at σ_ϕ~1.7. The differences in scintillation levels may be due to (for example) the observational geometry or small-scale differences in line-of-sight emissions, but we cannot make any further conclusions on this based on our data set. It is, however, clear that all constellations experience severe scintillation in a highly localized region of the sky where there are intense auroral emissions causing strong ionospheric irregularities at a wide range of spatial scales.

The level of amplitude scintillation is low across all constellations. There are some very slight enhancements at times seen in Figures 5 and 6, but S_4 is always less than 0.2, even in the presence of the intense auroral emissions. The low amplitude scintillation level is in accordance with previous statistical and case studies [*Spogli et al.*, 2009; *Hosokawa et al.*, 2014]. Furthermore, there was no amplitude scintillation ($S_4 < 0.2$) in relation to the patches (data not shown).

5. Conclusions

This study has demonstrated where scintillation-producing irregularities may occur in the nighttime polar ionosphere when patches enter the auroral oval during a substorm. The main findings of this study can be summarized as follows:

1. During substorm expansion, severe phase scintillation ($\sigma_\phi > 1$) is observed following the intense poleward edge of the auroral oval as it expands poleward.
2. No phase scintillation ($\sigma_\phi < 0.2$) is observed in relation to two relatively low-density patches exiting the polar cap into the auroral region.
3. No phase scintillation ($\sigma_\phi < 0.2$) is observed in relation to the same patches after having been colocated with intense auroral emissions.
4. Signals may experience strong scintillation when they intersect auroral emissions.
5. In our events the irregularities are most probably driven by intense auroral precipitation. Further studies are needed to ascertain whether patches (blobs) in the region of auroral emissions contribute to the severe scintillation levels.
6. The combination of HF backscatter and low amplitude scintillation suggests that the decameter-scale irregularities causing backscatter are not strong enough to cause amplitude scintillation.
7. Two receivers located ~120 km apart report highly different scintillation impacts, with almost half of the signals scintillating heavily in one receiver and none in the other.
8. GPS, GLONASS, and Galileo were similarly affected by severe phase scintillation in relation to intense line-of-sight auroral emissions in a highly localized region of the sky.

Acknowledgments
The University of Oslo ASI data are available at http://tid.uio.no/plasma/aurora. The IMF, solar wind, and *AE* data were provided by the NASA OMNIWeb service (http://omniweb.gsfc.nasa.gov). The Bjørnøya (BJN) magnetometer data were provided by Tromsø Geophysical Observatory, UiT The Arctic University of Norway, and are available from http://flux.phys.uit.no/ascii. The convection data are retrieved from Virginia Tech servers using the DaViTpy software package. GPS data from Hornsund were provided by Marcin Grzesiak and Mariusz Pozoga the Space Research Centre of Polish Academy of Sciences. The GNSS data can be made available upon request from the author. This study was supported by the Research Council of Norway under contracts 212014, 223252, and 230935. We wish to thank Yaqi Jin and Jøran Moen at the University of Oslo for helpful discussions.

References

Aarons, J., B. Lin, M. Mendillo, K. Liou, and M. Codrescu (2000), Global positioning system phase fluctuations and ultraviolet images from the polar satellite, *J. Geophys. Res.*, *105*(A3), 5201–5213, doi:10.1029/1999JA900409.

Akasofu, S.-I. (1964), The development of the auroral substorm, *Planet. Space Sci.*, *12*(4), 273–282, doi:10.1016/0032-0633(64)90151-5.

Alfonsi, L., L. Spogli, G. De Franceschi, V. Romano, M. Aquino, A. Dodson, and C. N. Mitchell (2011), Bipolar climatology of GPS ionospheric scintillation at solar minimum, *Radio Sci.*, *46*, RS0D05, doi:10.1029/2010RS004571.

AGU Journal of Geophysical Research: Space Physics 10.1002/2015JA021819

Baker, K. B., and S. Wing (1989), A new magnetic coordinate system for conjugate studies at high latitudes, *J. Geophys. Res.*, *94*(A7), 9139–9143, doi:10.1029/JA094iA07p09139.
Basu, S., E. MacKenzie, and S. Basu (1988), Ionospheric constraints on VHF/UHF communications links during solar maximum and minimum periods, *Radio Sci.*, *23*(3), 363–378, doi:10.1029/RS023i003p00363.
Basu, S., S. Basu, E. MacKenzie, W. R. Coley, J. R. Sharber, and W. R. Hoegy (1990), Plasma structuring by the gradient drift instability at high latitudes and comparison with velocity shear driven processes, *J. Geophys. Res.*, *95*(A6), 7799–7818, doi:10.1029/JA095iA06p07799.
Basu, S., S. Basu, E. Costa, C. Bryant, C. E. Valladares, and R. C. Livingston (1991), Interplanetary magnetic field control of drifts and anisotropy of high-latitude irregularities, *Radio Sci.*, *26*(4), 1079–1103, doi:10.1029/91RS00586.
Basu, S., S. Basu, P. K. Chaturvedi, and C. M. Bryant (1994), Irregularity structures in the cusp/cleft and polar cap regions, *Radio Sci.*, *29*(1), 195–207, doi:10.1029/93RS01515.
Basu, S., E. J. Weber, T. W. Bullett, M. J. Keskinen, E. MacKenzie, P. Doherty, R. Sheehan, H. Kuenzler, P. Ning, and J. Bongiolatti (1998), Characteristics of plasma structuring in the cusp/cleft region at Svalbard, *Radio Sci.*, *33*(6), 1885–1899, doi:10.1029/98RS01597.
Béniguel, Y., et al. (2009), Ionospheric scintillation monitoring and modelling, *Ann. Geophys.*, *52*(3–4), 391–416, doi:10.4401/ag-4595.
Briggs, B., and I. Parkin (1963), On the variation of radio star and satellite scintillations with zenith angle, *J. Atmos. Terr. Phys.*, *25*(6), 339–366, doi:10.1016/0021-9169(63)90150-8.
Buchau, J., B. W. Reinisch, E. J. Weber, and J. G. Moore (1983), Structure and dynamics of the winter polar cap F region, *Radio Sci.*, *18*(6), 995–1010, doi:10.1029/RS018i006p00995.
Buchau, J., E. J. Weber, D. N. Anderson, H. C. Carlson, J. G. Moore, B. W. Reinisch, and R. C. Livingston (1985), Ionospheric structures in the polar cap: Their origin and relation to 250-MHz scintillation, *Radio Sci.*, *20*(3), 325–338, doi:10.1029/RS020i003p00325.
Carlson, H. C. (2012), Sharpening our thinking about polar cap ionospheric patch morphology, research, and mitigation techniques, *Radio Sci.*, *47*, RS0L21, doi:10.1029/2011RS004946.
Carlson, H. C., K. Oksavik, J. Moen, A. P. van Eyken, and P. Guio (2002), ESR mapping of polar-cap patches in the dark cusp, *Geophys. Res. Lett.*, *29*(10), 1386, doi:10.1029/2001GL014087.
Carlson, H. C., K. Oksavik, J. Moen, and T. Pedersen (2004), Ionospheric patch formation: Direct measurements of the origin of a polar cap patch, *Geophys. Res. Lett.*, *31*(8), 1386, doi:10.1029/2003GL018166.
Carlson, H. C., J. Moen, K. Oksavik, C. P. Nielsen, I. W. McCrea, T. R. Pedersen, and P. Gallop (2006), Direct observations of injection events of subauroral plasma into the polar cap, *Geophys. Res. Lett.*, *33*, L05103, doi:10.1029/2005GL025230.
Carlson, H. C., T. Pedersen, S. Basu, M. Keskinen, and J. Moen (2007), Case for a new process, not mechanism, for cusp irregularity production, *J. Geophys. Res.*, *112*, A11304, doi:10.1029/2007JA012384.
Carlson, H. C., K. Oksavik, and J. Moen (2008), On a new process for cusp irregularity production, *Ann. Geophys.*, *26*(9), 2871–2885, doi:10.5194/angeo-26-2871-2008.
Chisham, G., et al. (2007), A decade of the Super Dual Auroral Radar Network (SuperDARN): Scientific achievements, new techniques and future directions, *Surv. Geophys.*, *28*(1), 33–109, doi:10.1007/s10712-007-9017-8.
Coker, C., G. S. Bust, R. A. Doe, and T. L. Gaussiran (2004), High-latitude plasma structure and scintillation, *Radio Sci.*, *39*, RS1S15, doi:10.1029/2002RS002833.
Cousins, E. D. P., and S. G. Shepherd (2010), A dynamical model of high-latitude convection derived from SuperDARN plasma drift measurements, *J. Geophys. Res.*, *115*, A12329, doi:10.1029/2010JA016017.
Crowley, G., A. J. Ridley, D. Deist, S. Wing, D. J. Knipp, B. A. Emery, J. Foster, R. Heelis, M. Hairston, and B. W. Reinisch (2000), Transformation of high-latitude ionospheric F region patches into blobs during the March 21, 1990, storm, *J. Geophys. Res.*, *105*(A3), 5215–5230, doi:10.1029/1999JA900357.
Dungey, J. W. (1961), Interplanetary magnetic field and the auroral zones, *Phys. Rev. Lett.*, *6*(2), 47–48, doi:10.1103/PhysRevLett.6.47.
Elphinstone, R. D., J. S. Murphree, and L. L. Cogger (1996), What is a global auroral substorm?, *Rev. Geophys.*, *34*(2), 169–232, doi:10.1029/96RG00483.
Forte, B. (2005), Optimum detrending of raw GPS data for scintillation measurements at auroral latitudes, *J. Atmos. Sol. Terr. Phys.*, *67*(12), 1100–1109, doi:10.1016/j.jastp.2005.01.011.
Forte, B., and S. M. Radicella (2002), Problems in data treatment for ionospheric scintillation measurements, *Radio Sci.*, *37*(6), 1096, doi:10.1029/2001RS002508.
Forte, B., and S. M. Radicella (2004), Geometrical control of scintillation indices: What happens for GPS satellites, *Radio Sci.*, *39*, RS5014, doi:10.1029/2002RS002852.
Forte, B., M. Materassi, L. Alfonsi, V. Romano, G. De Franceschi, and P. Spalla (2011), Optimum parameter for estimating phase fluctuations on transionospheric signals at high latitudes, *Adv. Space Res.*, *47*(12), 2188–2193, doi:10.1016/j.asr.2010.04.033.
Foster, J. C. (1993), Storm time plasma transport at middle and high latitudes, *J. Geophys. Res.*, *98*(A2), 1675–1689, doi:10.1029/92JA02032.
Foster, J. C., and J. R. Doupnik (1984), Plasma convection in the vicinity of the dayside cleft, *J. Geophys. Res.*, *89*(A10), 9107–9113, doi:10.1029/JA089iA10p09107.
Foster, J. C., A. J. Coster, P. J. Erickson, J. M. Holt, F. D. Lind, W. Rideout, M. McCready, A. van Eyken, R. J. Barnes, R. A. Greenwald, and F. J. Rich (2005), Multiradar observations of the polar tongue of ionization, *J. Geophys. Res.*, *110*, A09S31, doi:10.1029/2004JA010928.
Fremouw, E. J., R. L. Leadabrand, R. C. Livingston, M. D. Cousins, C. L. Rino, B. C. Fair, and R. A. Long (1978), Early results from the DNA wideband satellite experiment—Complex-signal scintillation, *Radio Sci.*, *13*(1), 167–187, doi:10.1029/RS013i001p00167.
Garner, T. W., R. B. Harris, J. A. York, C. S. Herbster, C. F. Minter, and D. L. Hampton (2011), An auroral scintillation observation using precise, collocated GPS receivers, *Radio Sci.*, *46*, RS1018, doi:10.1029/2010RS004412.
Gondarenko, N. A., and P. N. Guzdar (2004), Density and electric field fluctuations associated with the gradient drift instability in the high-latitude ionosphere, *Geophys. Res. Lett.*, *31*, L11802, doi:10.1029/2004GL019703.
Greenwald, R. A., et al. (1995), DARN/SuperDARN, *Space Sci. Rev.*, *71*(1–4), 761–796, doi:10.1007/BF00751350.
Gwal, A. K., and A. Jain (2011), GPS scintillation studies in the Arctic region during the first winter-phase 2008 Indian Arctic Expedition, *Pol. Sci.*, *4*(4), 574–587, doi:10.1016/j.polar.2010.08.001.
Hey, J. S., S. J. Parsons, and J. W. Phillips (1946), Fluctuations in cosmic radiation at radio-frequencies, *Nature*, *158*(4007), 234, doi:10.1038/158234a0.
Hosokawa, K., K. Shiokawa, Y. Otsuka, A. Nakajima, T. Ogawa, and J. D. Kelly (2006), Estimating drift velocity of polar cap patches with all-sky airglow imager at Resolute Bay, Canada, *Geophys. Res. Lett.*, *33*, L15111, doi:10.1029/2006GL026916.
Hosokawa, K., K. Shiokawa, Y. Otsuka, T. Ogawa, J.-P. St-Maurice, G. J. Sofko, and D. A. Andre (2009), Relationship between polar cap patches and field-aligned irregularities as observed with an all-sky airglow imager at resolute bay and the PolarDARN radar at Rankin inlet, *J. Geophys. Res.*, *114*, A03306, doi:10.1029/2008JA013707.

AGU Journal of Geophysical Research: Space Physics 10.1002/2015JA021819

Hosokawa, K., J. I. Moen, K. Shiokawa, and Y. Otsuka (2011), Decay of polar cap patch, *J. Geophys. Res.*, *116*, A05306, doi:10.1029/2010JA016297.

Hosokawa, K., Y. Otsuka, Y. Ogawa, and T. Tsugawa (2014), Observations of GPS scintillation during an isolated auroral substorm, *Prog. Earth Planet. Sci.*, *1*(1), 1–9, doi:10.1186/2197-4284-1-16.

Jakowski, N., Y. Béniguel, G. De Franceschi, M. H. Pajares, K. S. Jacobsen, I. Stanislawska, L. Tomasik, R. Warnant, and G. Wautelet (2012), Monitoring, tracking and forecasting ionospheric perturbations using GNSS techniques, *J. Space Weather Space Clim.*, *2*, A22, doi:10.1051/swsc/2012022.

Jiao, Y., Y. T. Morton, S. Taylor, and W. Pelgrum (2013), Characterization of high-latitude ionospheric scintillation of GPS signals, *Radio Sci.*, *48*, 698–708, doi:10.1002/2013RS005259.

Jin, Y., J. I. Moen, and W. J. Miloch (2014), GPS scintillation effects associated with polar cap patches and substorm auroral activity: Direct comparison, *J. Space Weather Space Clim.*, *4*, A23, doi:10.1051/swsc/2014019.

Jin, Y., J. I. Moen, and W. J. Miloch (2015), On the collocation of the cusp aurora and the GPS phase scintillation: A statistical study, *J. Geophys. Res. Space Physics*, *120*, 9176–9191, doi:10.1002/2015JA021449.

Kersley, L., C. D. Russell, and D. L. Rice (1995), Phase scintillation and irregularities in the northern polar ionosphere, *Radio Sci.*, *30*(3), 619–629, doi:10.1029/94RS03175.

Kinrade, J., C. N. Mitchell, P. Yin, N. Smith, M. J. Jarvis, D. J. Maxfield, M. C. Rose, G. S. Bust, and A. T. Weatherwax (2012), Ionospheric scintillation over antarctica during the storm of 5–6 April 2010, *J. Geophys. Res.*, *117*, A05304, doi:10.1029/2011JA017073.

Kinrade, J., C. N. Mitchell, N. D. Smith, Y. Ebihara, A. T. Weatherwax, and G. S. Bust (2013), GPS phase scintillation associated with optical auroral emissions: First statistical results from the geographic South Pole, *J. Geophys. Res. Space Physics*, *118*, 2490–2502, doi:10.1002/jgra.50214.

Kintner, P. M., B. M. Ledvina, and E. R. de Paula (2007), GPS and ionospheric scintillations, *Space Weather*, *5*, S09003, doi:10.1029/2006SW000260.

Lepping, R. P., et al. (1995), The WIND magnetic field investigation, *Space Sci. Rev.*, *71*(1–4), 207–229, doi:10.1007/BF00751330.

Li, G., B. Ning, Z. Ren, and L. Hu (2010), Statistics of GPS ionospheric scintillation and irregularities over polar regions at solar minimum, *GPS Solut.*, *14*(4), 331–341, doi:10.1007/s10291-009-0156-x.

Lockwood, M., and H. C. Carlson (1992), Production of polar cap electron density patches by transient magnetopause reconnection, *Geophys. Res. Lett.*, *19*(17), 1731–1734, doi:10.1029/92GL01993.

Lockwood, M., J. A. Davies, J. Moen, A. P. van Eyken, K. Oksavik, I. W. McCrea, and M. Lester (2005), Motion of the dayside polar cap boundary during substorm cycles: II. Generation of poleward-moving events and polar cap patches by pulses in the magnetopause reconnection rate, *Ann. Geophys.*, *23*(11), 3513–3532, doi:10.5194/angeo-23-3513-2005.

Lorentzen, D. A., N. Shumilov, and J. Moen (2004), Drifting airglow patches in relation to tail reconnection, *Geophys. Res. Lett.*, *31*, L02806, doi:10.1029/2003GL017785.

Lorentzen, D. A., J. Moen, K. Oksavik, F. Sigernes, Y. Saito, and M. G. Johnsen (2010), In situ measurement of a newly created polar cap patch, *J. Geophys. Res.*, *115*, A12323, doi:10.1029/2010JA015710.

Lyons, L. R., Y. Nishimura, H.-J. Kim, E. Donovan, V. Angelopoulos, G. Sofko, M. Nicolls, C. Heinselman, J. M. Ruohoniemi, and N. Nishitani (2011), Possible connection of polar cap flows to pre- and post-substorm onset PBIs and streamers, *J. Geophys. Res.*, *116*, A12225, doi:10.1029/2011JA016850.

McPherron, R. L. (1970), Growth phase of magnetospheric substorms, *J. Geophys. Res.*, *75*(28), 5592–5599, doi:10.1029/JA075i028p05592.

McPherron, R. L. (1979), Magnetospheric substorms, *Rev. Geophys.*, *17*(4), 657–681, doi:10.1029/RG017i004p00657.

Milan, S. E., S. Basu, T. K. Yeoman, and R. E. Sheehan (2005), A comparison of satellite scintillation measurements with HF radar backscatter characteristics, *Ann. Geophys.*, *23*(11), 3451–3455, doi:10.5194/angeo-23-3451-2005.

Mitchell, C. N., L. Alfonsi, G. De Franceschi, M. Lester, V. Romano, and A. W. Wernik (2005), GPS TEC and scintillation measurements from the polar ionosphere during the October 2003 storm, *Geophys. Res. Lett.*, *32*, L12S03, doi:10.1029/2004GL021644.

Moen, J., H. C. Carlson, K. Oksavik, C. P. Nielsen, S. E. Pryse, H. R. Middleton, I. W. McCrea, and P. Gallop (2006), EISCAT observations of plasma patches at sub-auroral cusp latitudes, *Ann. Geophys.*, *24*(9), 2363–2374, doi:10.5194/angeo-24-2363-2006.

Moen, J., N. Gulbrandsen, D. A. Lorentzen, and H. C. Carlson (2007), On the MLT distribution of F region polar cap patches at night, *Geophys. Res. Lett.*, *34*, L14113, doi:10.1029/2007GL029632.

Moen, J., X. C. Qiu, H. C. Carlson, R. Fujii, and I. W. McCrea (2008), On the diurnal variability in F2-region plasma density above the EISCAT Svalbard radar, *Ann. Geophys.*, *26*(8), 2427–2433, doi:10.5194/angeo-26-2427-2008.

Moen, J., K. Oksavik, L. Alfonsi, Y. Daabakk, V. Romano, and L. Spogli (2013), Space weather challenges of the polar cap ionosphere, *J. Space Weather Space Clim.*, *3*, A02, doi:10.1051/swsc/2013025.

Mushini, S. C., P. T. Jayachandran, R. B. Langley, J. W. MacDougall, and D. Pokhotelov (2012), Improved amplitude- and phase-scintillation indices derived from wavelet detrended high-latitude GPS data, *GPS Solut.*, *16*(3), 363–373, doi:10.1007/s10291-011-0238-4.

Ngwira, C. M., L.-A. McKinnell, and P. J. Cilliers (2010), GPS phase scintillation observed over a high-latitude antarctic station during solar minimum, *J. Atmos. Sol. Terr. Phys.*, *72*(9–10), 718–725, doi:10.1016/j.jastp.2010.03.014.

Nishimura, Y., L. R. Lyons, K. Shiokawa, V. Angelopoulos, E. F. Donovan, and S. B. Mende (2013), Substorm onset and expansion phase intensification precursors seen in polar cap patches and arcs, *J. Geophys. Res. Space Physics*, *118*, 2034–2042, doi:10.1002/jgra.50279.

Nishimura, Y., et al. (2014), Day-night coupling by a localized flow channel visualized by polar cap patch propagation, *Geophys. Res. Lett.*, *41*, 3701–3709, doi:10.1002/2014GL060301.

NovAtel (2012), GPStation-6 GNSS Ionospheric Scintillation and TEC Monitor (GISTM) Receiver User Manual, NovAtel Inc., Calgary, Alberta. [Available at http://www.novatel.com/assets/Documents/Manuals/om-20000132.pdf, Accessed date 1 Dec. 2012.]

Ogilvie, K. W., et al. (1995), SWE, a comprehensive plasma instrument for the WIND spacecraft, *Space Sci. Rev.*, *71*(1–4), 55–77, doi:10.1007/BF00751326.

Oksavik, K., V. L. Barth, J. Moen, and M. Lester (2010), On the entry and transit of high-density plasma across the polar cap, *J. Geophys. Res.*, *115*, A12308, doi:10.1029/2010JA015817.

Oksavik, K., C. van der Meeren, D. A. Lorentzen, L. J. Baddeley, and J. Moen (2015), Scintillation and loss of signal lock from poleward moving auroral forms in the cusp ionosphere, *J. Geophys. Res. Space Physics*, *120*, 9161–9175, doi:10.1002/2015JA021528.

Prikryl, P., P. T. Jayachandran, S. C. Mushini, D. Pokhotelov, J. W. MacDougall, E. Donovan, E. Spanswick, and J.-P. St-Maurice (2010), GPS TEC, scintillation and cycle slips observed at high latitudes during solar minimum, *Ann. Geophys.*, *28*(6), 1307–1316, doi:10.5194/angeo-28-1307-2010.

Prikryl, P., P. T. Jayachandran, S. C. Mushini, and R. Chadwick (2011), Climatology of GPS phase scintillation and HF radar backscatter for the high-latitude ionosphere under solar minimum conditions, *Ann. Geophys.*, *29*(2), 377–392, doi:10.5194/angeo-29-377-2011.

Pryse, S. E., A. G. Wood, H. R. Middleton, I. W. McCrea, and M. Lester (2006), Reconfiguration of polar-cap plasma in the magnetic midnight sector, *Ann. Geophys.*, *24*(8), 2201–2208, doi:10.5194/angeo-24-2201-2006.

Rostoker, G., S.-I. Akasofu, J. Foster, R. Greenwald, Y. Kamide, K. Kawasaki, A. Lui, R. McPherron, and C. Russell (1980), Magnetospheric substorms-definition and signatures, *J. Geophys. Res.*, *85*(A4), 1663–1668, doi:10.1029/JA085iA04p01663.

Shi, Y., and E. Zesta (2014), Global-scale ionospheric flow and aurora precursors of auroral substorms: Coordinated SuperDARN and IMAGE/WIC observations, *J. Geophys. Res. Space Physics*, *119*, 4860–4871, doi:10.1002/2013JA019175.

Skone, S. H. (2001), The impact of magnetic storms on GPS receiver performance, *J. Geod.*, *75*(9–10), 457–468, doi:10.1007/s001900100198.

Smith, A. M., C. N. Mitchell, R. J. Watson, R. W. Meggs, P. M. Kintner, K. Kauristie, and F. Honary (2008), GPS scintillation in the high arctic associated with an auroral arc, *Space Weather*, *6*, S03D01, doi:10.1029/2007SW000349.

Solomon, S. C., P. B. Hays, and V. J. Abreu (1988), The auroral 6300 Å emission: Observations and modeling, *J. Geophys. Res.*, *93*(A9), 9867–9882, doi:10.1029/JA093iA09p09867.

Spogli, L., L. Alfonsi, G. De Franceschi, V. Romano, M. H. O. Aquino, and A. Dodson (2009), Climatology of GPS ionospheric scintillations over high and mid-latitude european regions, *Ann. Geophys.*, *27*(9), 3429–3437, doi:10.5194/angeo-27-3429-2009.

Tiwari, S., A. Jain, S. Sarkar, S. Jain, and A. K. Gwal (2012), Ionospheric irregularities at antarctic using GPS measurements, *J. Earth Syst. Sci.*, *121*(2), 345–353, doi:10.1007/s12040-012-0168-8.

Torrence, C., and G. P. Compo (1998), A practical guide to wavelet analysis, *Bull. Am. Meteorol. Soc.*, *79*(1), 61–78, doi:10.1175/1520-0477(1998)079.

Tsunoda, R. T. (1988), High-latitude F region irregularities: A review and synthesis, *Rev. Geophys.*, *26*(4), 719–760, doi:10.1029/RG026i004p00719.

van der Meeren, C., K. Oksavik, D. Lorentzen, J. I. Moen, and V. Romano (2014), GPS scintillation and irregularities at the front of an ionization tongue in the nightside polar ionosphere, *J. Geophys. Res. Space Physics*, *119*, 8624–8636, doi:10.1002/2014JA020114.

Weber, E. J., J. Buchau, J. G. Moore, J. R. Sharber, R. C. Livingston, J. D. Winningham, and B. W. Reinisch (1984), F layer ionization patches in the polar cap, *J. Geophys. Res.*, *89*(A3), 1683–1694, doi:10.1029/JA089iA03p01683.

Weber, E. J., J. A. Klobuchar, J. Buchau, H. C. Carlson, R. C. Livingston, O. de la Beaujardiere, M. McCready, J. G. Moore, and G. J. Bishop (1986), Polar cap F layer patches: Structure and dynamics, *J. Geophys. Res.*, *91*(A11), 12,121–12,129, doi:10.1029/JA091iA11p12121.

Wickwar, V. B., L. L. Cogger, and H. C. Carlson (1974), The 6300 Å O1D airglow and dissociative recombination, *Planet. Space Sci.*, *22*(5), 709–724, doi:10.1016/0032-0633(74)90141-X.

Zhang, Q.-H., et al. (2013a), Direct observations of the evolution of polar cap ionization patches, *Science*, *339*(6127), 1597–1600, doi:10.1126/science.1231487.

Zhang, Q.-H., B.-C. Zhang, J. Moen, M. Lockwood, I. W. McCrea, H.-G. Yang, H.-Q. Hu, R.-Y. Liu, S.-R. Zhang, and M. Lester (2013b), Polar cap patch segmentation of the tongue of ionization in the morning convection cell, *Geophys. Res. Lett.*, *40*, 2918–2922, doi:10.1002/grl.50616.

Paper IV

Scintillation and irregularities from the nightside part of a sun-aligned polar cap arc

C. van der Meeren, K. Oksavik, D. A. Lorentzen, L. J. Paxton, and L. B. N. Clausen

Journal of Geophysical Research: Space Physics, Vol. 121, doi:10.1002/2016JA022708 (2016)

IV

AGU PUBLICATIONS

JGR

Journal of Geophysical Research: Space Physics

RESEARCH ARTICLE
10.1002/2016JA022708

Key Points:
- Sun-aligned polar cap arcs in the nightside northward IMF ionosphere have weak irregularities
- No significant amplitude or phase scintillation is seen, although there is enhanced HF backscatter
- Even with intense precipitation within the arc, the low background plasma density may prevent strong irregularities from forming

Correspondence to:
C. van der Meeren,
christer.meeren@uib.no

Citation:
van der Meeren, C., K. Oksavik, D. A. Lorentzen, L. J. Paxton, and L. B. N.Clausen (2016), Scintillation and irregularities from the nightside part of a Sun-aligned polar cap arc, *J. Geophys. Res. Space Physics*, *121*, doi:10.1002/2016JA022708.

Received 16 MAR 2016
Accepted 27 MAY 2016
Accepted article online 1 JUN 2016

Scintillation and irregularities from the nightside part of a Sun-aligned polar cap arc

Christer van der Meeren[1], Kjellmar Oksavik[1,2], Dag A. Lorentzen[3,4], Larry J. Paxton[5], and Lasse B. N. Clausen[6]

[1]Birkeland Centre for Space Science, Department of Physics and Technology, University of Bergen, Bergen, Norway, [2]University Centre in Svalbard, Longyearbyen, Norway, [3]Birkeland Centre for Space Science, University Centre in Svalbard, Longyearbyen, Norway, [4]Now at British Antarctic Survey, Cambridge, UK, [5]The Johns Hopkins University Applied Physics Laboratory, Laurel, Maryland, USA, [6]Department of Physics, University of Oslo, Oslo, Norway

Abstract In this paper we study the presence of irregularities and scintillation in relation to the nightside part of a long-lived, Sun-aligned transpolar arc on 15 January 2015. The arc was observed in DMSP UV and particle data and lasted at least 3 h between 1700 and 2000 UT. The arc was more intense than the main oval during this time. From all-sky imagers on Svalbard we were able to study the evolution of the arc, which drifted slowly westward toward the dusk cell. The intensity of the arc as observed from ground was 10–17 kR in 557.7 nm and 2–3.5 kR in 630.0 nm, i.e., significant emissions in both green and red emission lines. We have used high-resolution raw data from global navigation satellite systems (GNSS) receivers and backscatter from Super Dual Auroral Radar Network (SuperDARN) radars to study irregularities and scintillation in relation to the polar cap arc. Even though the literature has suggested that polar cap arcs are potential sources for irregularities, our results indicate only very weak irregularities. This may be due to the background density in the northward IMF polar cap being too low for significant irregularities to be created.

1. Introduction

The high-latitude ionosphere is highly dynamic, forming plasma irregularities on a wide variety of scale sizes, from 1000 km scale islands of enhanced plasma density down to irregularities at decameter scale [e.g., *Weber et al.*, 1984; *Basu et al.*, 1990a, 1990b; *Oksavik et al.*, 2012; *Moen et al.*, 2012, 2013].

Southward interplanetary magnetic field (IMF) conditions are thoroughly investigated and are the focus of most irregularity studies. During southward IMF conditions one can frequently observe polar cap patches, tongues of ionization, poleward moving auroral forms, and magnetospheric substorms. Polar cap patches are 100–1000 km islands of enhanced plasma density being segmented from the dayside high-density plasma in the cusp region [e.g., *Weber et al.*, 1984; *Lockwood and Carlson*, 1992; *Oksavik et al.*, 2010; *Carlson*, 2012; *Zhang et al.*, 2013a, 2013b]. Patches may develop smaller-scale irregularities down to decameter scale through the Kelvin-Helmholtz (KH) and gradient drift instabilities [e.g., *Basu et al.*, 1990a; *Carlson et al.*, 2007, 2008; *Moen et al.*, 2012; *Oksavik et al.*, 2012; *Clausen et al.*, 2016]. During strong and stable polar cap convection, segmentation may not happen and a continuous tongue of ionization (TOI) may be formed across the polar cap [*Sato*, 1959; *Knudsen*, 1974; *Foster et al.*, 2005]. In addition to patches, transient magnetopause reconnection gives rise to poleward moving auroral forms (PMAFs) [e.g., *Feldstein and Starkov*, 1967; *Vorobjev et al.*, 1975; *Sandholt et al.*, 1990, 1993; *Thorolfsson et al.*, 2000]. Magnetospheric substorms cause an explosive release of energy into the auroral ionosphere [e.g., *Akasofu*, 1964; *McPherron*, 1970, 1979; *Rostoker et al.*, 1980; *Elphinstone et al.*, 1996]. All of these phenomena are associated with irregularities causing disturbances in transionospheric radio links: Patches [*Buchau et al.*, 1985; *Weber et al.*, 1986; *Basu et al.*, 1990a, 1991, 1994, 1998; *Coker et al.*, 2004; *Clausen et al.*, 2016], TOIs [*van der Meeren et al.*, 2014], PMAFs [*Oksavik et al.*, 2015; *Jin et al.*, 2015], and auroral activity [*Aarons et al.*, 2000; *Spogli et al.*, 2009; *Prikryl et al.*, 2010; *Ngwira et al.*, 2010; *Tiwari et al.*, 2012; *Jiao et al.*, 2013; *Kinrade et al.*, 2013; *Hosokawa et al.*, 2014; *van der Meeren et al.*, 2015; *Clausen et al.*, 2016].

However, northward IMF conditions are much less studied, although they occur half the time. During such conditions, the predominant feature of the polar ionosphere is polar cap arcs [e.g., *Carlson*, 1994, and references therein]. While reviewing space weather challenges for the polar cap ionosphere, *Moen et al.* [2013] suggested in passing that flow shears near transpolar arcs might be a space weather concern by creating irregularities

AGU Journal of Geophysical Research: Space Physics 10.1002/2016JA022708

through the KH instability. Unfortunately, there exists barely any studies at all on irregularities from polar cap arcs. In this paper, following the general methods of *van der Meeren et al.* [2014, 2015] and *Oksavik et al.* [2015], we use all-sky images, raw and reduced data from several multiconstellation global navigation satellite system (GNSS) receivers, and Super Dual Auroral Radar Network (SuperDARN) backscatter, as well as DMSP UV and particle data to study scintillation and irregularities in relation to an intense, detached polar cap arc.

First, we will give a brief overview of polar cap arcs, GNSS scintillations, and the current state of knowledge of the relation between these two phenomena.

1.1. Polar Cap Arcs

Optical arcs poleward of the auroral oval have been observed for at least a century [*Mawson*, 1916] and primarily occur during quiet geomagnetic conditions [*Davis*, 1963] and northward IMF [*Berkey et al.*, 1976; *Gussenhoven*, 1982]. The phenomenon is not yet fully understood.

The naming is not entirely consistent in literature. Usually [e.g., *Fear and Milan*, 2012a, 2012b; *Carlson*, 1994; *Newell et al.*, 2009, and references therein], the term "polar cap arcs" and "high-latitude arcs" refer to any type of aurora inside the polar cap. Such auroral features are often Sun-aligned and may stretch across a significant part of the polar cap, giving rise to the names Sun-aligned arcs and transpolar arcs, respectively. In the case that they connect the nightside and dayside auroral oval, they are often termed theta aurora. In this paper we will use the term "polar cap arc."

According to a review by *Newell et al.* [2009], three different types of polar cap arcs exist, possibly with different underlying mechanisms. The first type is intensifications of polar rain. These are common, but weak, and consist of only electron precipitation (without associated ions). The second type is Sun-aligned arcs which appear detached from the auroral oval in optical data but are adjacent to the auroral oval in particle data (though usually with a plasma regime distinct from the auroral oval). The third type occurs very rarely, and is intense, Sun-aligned arcs well detached from the auroral oval in both particle and optical data. These events can include plasma sheet ions (such as O^+) as well as electrons.

Convection has been observed to be antisunward in the nightside portion of the arc and either sunward [*Eriksson et al.*, 2006] or mixed [*Liou et al.*, 2005] in the dayside portion of the arc. In the vicinity of polar cap arcs, convection is structured, with multiple reversals, flow shears, and flow channels [e.g., *Carlson and Cowley*, 2005; *Eriksson et al.*, 2006; *Zou et al.*, 2015].

1.2. Scintillation From Polar Cap Arcs

Scintillations are rapid fluctuations in the amplitude or phase of a radio signal, such as GNSS signals, and can be caused by irregularities in the ionosphere with scale sizes of decameters to kilometers [e.g., *Hey et al.*, 1946; *Basu et al.*, 1990a, 1998; *Kintner et al.*, 2007]. The irregularity scale sizes causing scintillation are determined by the Fresnel radius, which for GPS L1 signals (1575.42 MHz) passing through irregularities at an altitude of 350 km is approximately 360 m [*Forte and Radicella*, 2002]. Amplitude scintillations are represented by the S_4 index and are due to irregularities with scale sizes at and below the Fresnel radius, from hundreds of meters down to tens of meters. Phase scintillations are represented by the σ_ϕ index and are caused by irregularities above the Fresnel radius, from a few hundred meters to several kilometers [e.g., *Kintner et al.*, 2007].

Buchau et al. [1985] and *Basu et al.* [1990b] observed 250 MHz scintillation in relation to polar cap arcs. The latter study found an increase in σ_ϕ of ~7 times the background level and attributed it to sheared plasma flow in association with the arc. Scintillation from polar cap arcs at GNSS *L* band frequencies (~1.2–1.6 GHz) is less studied. *Prikryl et al.* [2015a] included one example of moderate to strong GPS phase scintillation from the dayside part of a transpolar arc following a strong solar wind dynamic pressure pulse which resulted in large B_y oscillations. *Prikryl et al.* [2015b] performed a statistical study of high-latitude scintillation and found that for northward IMF, the B_y-dependent dayside dawn-dusk asymmetry in scintillation was consistent with the expected asymmetry of Sun-aligned arcs. The statistical scintillation in the duskside and dawnside sectors was then attributed to Sun-aligned arcs.

We have not been able to find any studies of GNSS scintillation from polar cap arcs in the nightside ionosphere.

2. Instrumentation

2.1. GNSS Receivers

The GNSS data used in this study come from two NovAtel GPStation-6 GNSS Ionospheric Scintillation and TEC Monitor. The receivers were installed in Svalbard in 2013 and are operated by the University of Bergen.

AGU Journal of Geophysical Research: Space Physics 10.1002/2016JA022708

The locations, geographic latitudes (GLAT), geographic longitudes (GLON), and magnetic latitudes (MLAT) of the receivers are Longyearbyen (78.1° GLAT, 16.0° GLON, and 75.4° MLAT) and Ny-Ålesund (78.9° GLAT, 11.9° GLON, and 76.4° MLAT). Magnetic midnight is around 2100 UT at these locations.

All receivers track the GPS, GLONASS, and Galileo constellations at several frequencies. GPS and GLONASS satellites were visible during the period of study and were tracked at L1 (1575.42 MHz). Additionally, one GPS satellite was tracked at L5 (1176.45 MHz), and GLONASS was tracked at L2 (1227.60 MHz). The different signals showed no significant difference in scintillation intensity (the levels were marginally higher in the lower frequencies), so L1 will be used in this study.

The receivers output 60 s averaged data. The σ_ϕ index is computed by detrending the carrier phase using a sixth-order Butterworth filter with a cutoff frequency of 0.1 Hz and computing the standard deviation over periods of 60 s. The S_4 index is computed by taking the standard deviation of the received power over periods of 60 s and normalizing by its mean value.

Using a 0.1 Hz cutoff frequency for the σ_ϕ index is prevalent in the literature [e.g., *Mitchell et al.*, 2005; *Béniguel et al.*, 2009; *Li et al.*, 2010; *Forte et al.*, 2011; *Gwal and Jain*, 2011; *Alfonsi et al.*, 2011; *Garner et al.*, 2011; *Kinrade et al.*, 2012; *Jiao et al.*, 2013; *Jin et al.*, 2014]. The σ_ϕ index has been shown to be highly sensitive to the detrending filter cutoff frequency, and 0.1 Hz can be problematic in the high-latitude regions [e.g., *Forte*, 2005]. However, as performed by *van der Meeren et al.* [2014, 2015] and *Oksavik et al.* [2015], it is possible to use a spectrogram of the raw phase to get a better overview of the phase variations at different scales. The spectrograms were made using wavelet analysis, based on software provided by *Torrence and Compo* [1998]. In line with previous GNSS studies, the Morlet wavelet was chosen as the mother wavelet [e.g., *Mushini et al.*, 2012]. The wavelet spectrograms require no detrending of the raw phase. For further details on wavelet analysis the reader is referred to the literature [e.g., *Torrence and Compo*, 1998; *Mushini et al.*, 2012].

The receivers also output 50 Hz raw data (phase and power). In this study, the raw data are used to compute the σ_ϕ index with 1 s resolution using the method described above with periods of 1 s instead of 60 s.

For each receiver, data from satellites were excluded in directions (elevation/azimuth) known to cause multipath problems for that receiver. No satellites were used below 20° elevation. Occasionally, the receivers glitch (most likely due to clock adjustments), causing a transient increase in scintillation for all satellites seen in that receiver. Scintillation data around these glitches have been removed in this study.

The two all-sky imagers used in this study (to be detailed below) are colocated with the GNSS receivers. Therefore, we have not performed any geographical projection of the GNSS ionospheric piercing points. We have instead shown ground-based optical data and associated GNSS data on a polar grid using elevation and azimuth.

2.2. All-Sky Imagers

We use data from two all-sky imagers (ASI). The ASIs are colocated with the GNSS receivers in Ny-Ålesund and Longyearbyen and are operated by the University of Oslo. Both imagers are calibrated and have filters for red (630.0 nm) and green (557.7 nm) emissions. Emissions at 630.0 nm are projected to 250 km, while emissions at 557.7 nm are projected to 150 km altitude. The exact projection altitude is not important for how the optical data are used in this study.

For most of the time under study, parts of the 557.7 nm data were of relatively poor quality due to technical problems (though the arc was clearly visible throughout the interval). We have, therefore, chosen to show mostly 630.0 nm images. These problems did not influence the line-of-sight data shown in Figures 5 and 6.

2.3. DMSP UV and Particle Data

The Defense Meteorological Satellite Program (DMSP) spacecraft are in polar, Sun-synchronous orbits at a nominal altitude of 840 km. The Special Sensor Ultraviolet Spectrographic Imager (SSUSI) instrument observes UV emissions at several wavelengths [*Paxton et al.*, 1992]. The channel used in the current study is 140–150 nm (Lyman-Birge-Hopfield short filter, LBHS). We use calibrated, background-corrected intensities from the Sensor Data Record (SDR) product. The data are projected to 150 km altitude. The projection is only used to show that the satellite- and ground-based optical data are consistent, and the exact choice of altitude is not critical for the purposes of this study.

The DMSP SSJ/4 particle detectors always point toward the zenith and measure precipitating electrons and ions between 30 eV and 30 keV.

AGU Journal of Geophysical Research: Space Physics 10.1002/2016JA022708

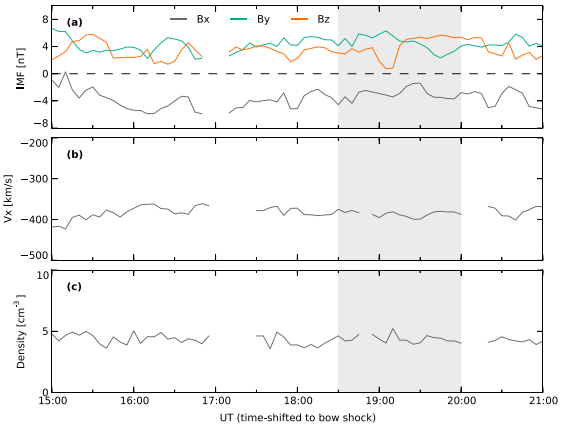

Figure 1. Solar wind conditions on 15 January 2015 several hours prior to, during, and after the event. The data show (a) northward IMF, (b) stable speed, and (c) stable density. The approximate time under study is shaded in gray.

2.4. Solar Wind

We use plasma and IMF data from the Wind spacecraft [*Lepping et al.*, 1995; *Ogilvie et al.*, 1995]. The spacecraft was located at $(X, Y, Z) = (196, 37, -15)\, R_E$ (geocentric solar ecliptic coordinates). The data are time shifted to the bow shock by the NASA OMNIWeb service.

2.5. SuperDARN Data

The Super Dual Auroral Radar Network (SuperDARN) transmits signals in the high-frequency (HF) range, which scatters coherently from field-aligned decameter-scale irregularities [*Greenwald et al.*, 1995; *Chisham et al.*, 2007]. HF backscatter is, therefore, an indicator of the presence of irregularities with scale sizes of tens of meters.

3. Observations

Figure 1 shows the solar wind conditions around the time of the event on 15 January 2015. The time under study is shaded in gray. The IMF is northward with B_y positive several hours prior to the event. The solar wind conditions, in general, are stable. Figure 2 shows a polar cap arc in both optical and particle data (the particle data are from the dayside part of the arc; unfortunately, there were no DMSP passes of the nightside part of the arc). The arc is very long-lived, lasting at least 3 h from 1700 to 2000 UT. In the spectrograms, diffuse aurora is visible at the equatorward edges, with discrete auroral structures farther poleward followed by polar rain. The arc precipitation is outlined with black borders. The arc exceeds the main oval in optical intensity (LBHS) and shows similar fluxes and higher electron energies than the discrete part of the main oval. The inverted V structures in the arc (most clear in Figure 2d but visible in Figures 2e and 2f as well) indicate field-aligned acceleration of electrons with resulting energies of up to ~3 keV. High-energy ions (~10 keV) are also visible in the arc, though the ion flux is very low. The dayside part of the arc seems to be broken up into multiple arcs in both the optical and particle data. In the nightside optical data (supported by the ground-based optical data to be shown later), the arc seems not to be broken up.

The stability and intensity of the arc makes this an ideal candidate for a detailed case study. It is also interesting to note that the arc seems well separated from the main oval in both optical and particle data, and this may thus be the rare "type 3" arc as described by *Newell et al.* [2009].

Figures 3a and 3b show a good match between ground-based (from Longyearbyen) and satellite-based optical data. The arc is clearly visible in both red (630.0 nm) and green (557.7 nm) emissions throughout the interval under study. Figures 3c–3e show how the arc moves across the ASI field of view in elevation/azimuth

AGU Journal of Geophysical Research: Space Physics 10.1002/2016JA022708

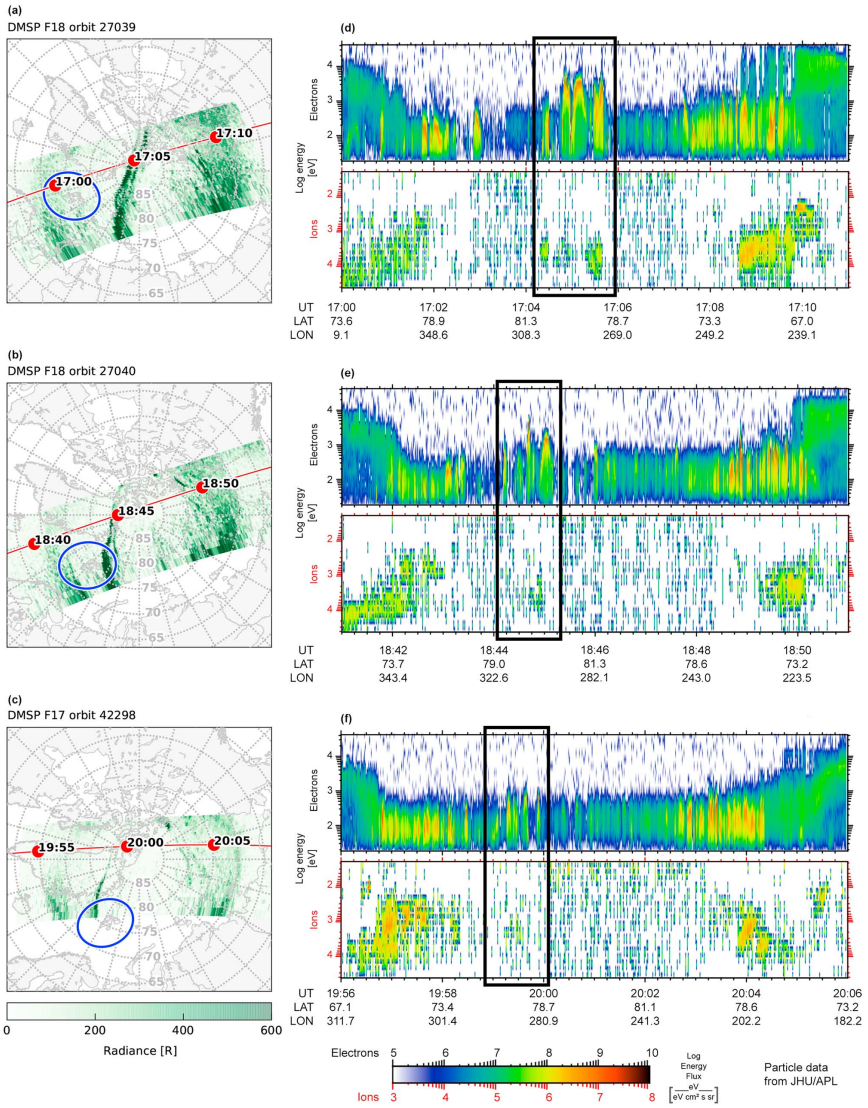

Figure 2. (a–c) Optical data and (d–f) particle spectra from three passes of DMSP satellites on 15 January 2015. The data show a stable transpolar Sun-aligned arc lasting for at least 3 h, well separated from the auroral oval in both optical and particle data. The field of view of the Longyearbyen ASI at 250 km altitude is shown as a blue circle. The optical data are projected onto a geomagnetic grid. Black boxes outline the (dayside) polar cap arc in the particle data.

AGU Journal of Geophysical Research: Space Physics 10.1002/2016JA022708

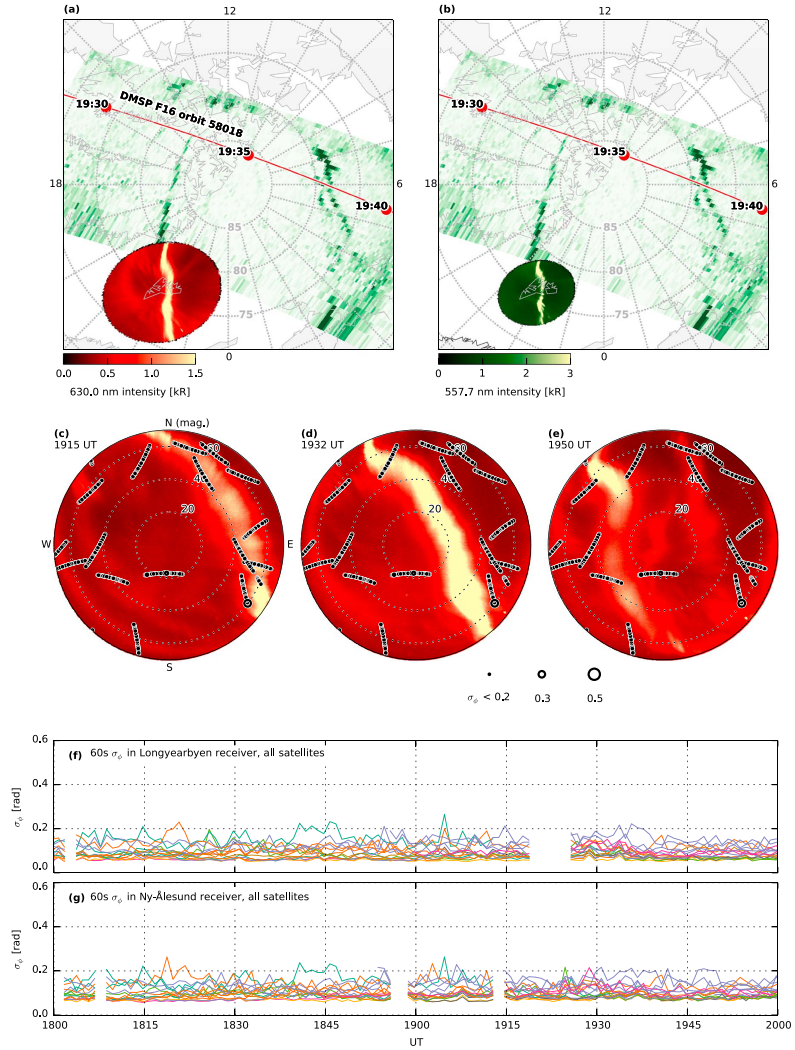

Figure 3. (a–b) Ground- and space-based optical data from the event on 15 January 2015. The arc is visible from the ground in both 630.0 nm and 557.7 nm data. (c–e) The movement of the arc across the all-sky field of view, displayed on an azimuth/zenith angle grid. Magnetic north is up, magnetic west is left. Scintillation data from all visible satellites between 1912 and 1952 UT are shown as traces of dots/circles (identical for all three images). The circles below the images indicate the scintillation scale. (f–g) Scintillation data from all visible satellites in Longyearbyen and Ny-Ålesund. Even though the arc crosses most satellites in both receivers, scintillation is very low at all times.

AGU Journal of Geophysical Research: Space Physics 10.1002/2016JA022708

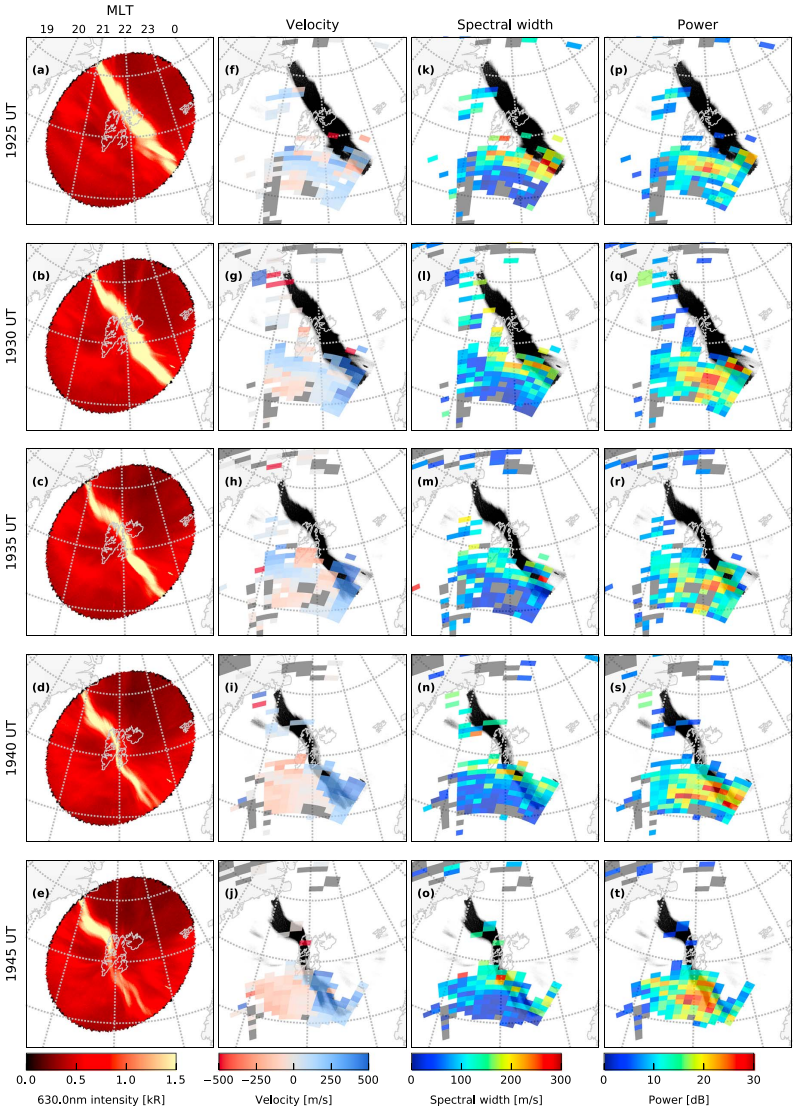

Figure 4. Backscatter data from the Hankasalmi SuperDARN radar at five different times during the event on 15 January 2015. (a–e) Optical data for reference. The arc is shown in black in the other panels. (f–j) Drift velocity. (k–o) Spectral width. (p–t) Backscatter power. Observe the flow shear in the velocity data (Figures 4i–4j), as well as the enhanced spectral width and backscatter power near the arc.

AGU Journal of Geophysical Research: Space Physics 10.1002/2016JA022708

coordinates. The movement across the ASI field of view is partly because of the rotation of the Earth and partly because the arc drifts toward dusk. The movement is irregular: It seems stationary in a magnetic local time (MLT) frame until around 1905 UT. After this it drifts westward at a speed of around 600–900 m/s until it starts to fade around 2000 UT, but with intermittent stops and slight bulges along the way which makes it difficult to pin down an exact drift speed. The correction for the rotation of the Earth is around 100 m/s and is not important in this context. The intensity of the arc varies during the event. The maximum intensity as measured by the ASI is 10–17 kR in 557.7 nm and 2–3.5 kR in 630.0 nm. These are significant emission intensities, and one should expect some scintillation [*Kinrade et al.*, 2013].

Overlaid on top of Figures 3c–3e are tracks of phase scintillation for all the visible satellites in the Longyearbyen receiver between 1912 and 1952 UT (identical for all three panels). This shows that phase scintillation is almost always below $\sigma_\phi = 0.2$. Figures 3f and 3g show phase scintillation for all satellites in both Longyearbyen and Ny-Ålesund. Phase scintillation is almost always below 0.2, only barely exceeding 0.2 for short amounts of time. This shows clearly that there is no or only very weak scintillation from the arc. A more detailed look at scintillation in relation to line-of-sight intensities for specific satellites will be given shortly.

Figure 4 shows backscatter data from the Hankasalmi SuperDARN radar. The auroral images (Figures 4a–4e) are shown for reference, and the arc itself is shown in black in the other panels. The presence of backscatter near the arc indicates field-aligned irregularities at decameter scale. There is also enhanced spectral width (∼200 m/s) and backscatter power (∼25–30 dB) in relation to the arc. The velocity data (Figures 4f–4j, especially Figures 4i–4j) show a clear velocity shear in relation to the arc. At 22 MLT (where the radar observations are made) during strongly positive IMF B_y, one would expect steady westward flow which would result in flows toward the radar in the east and away from the radar in the west [e.g., *Ruohoniemi et al.*, 1989]. However, the flow shear we observe moves with the arc and seems sufficiently abrupt (350 m/s toward versus 50 m/s away in two adjacent range gates 350 km apart) that this is likely a proper flow shear associated with the arc.

Next we will provide a more detailed look at scintillation data for six selected satellites. Figure 5 shows the first three, which are GPS 11, GLONASS 20, and GPS 28. Figures 5a–5c and 5g–5i show emission intensities in the line of sight to the satellites from the Longyearbyen and Ny-Ålesund ASIs, respectively. The intensities are based on the median of a 7-by-7 pixel window centered on the satellite. The arc moves slowly at first, which is why GPS 11 spends a long time in the emissions. The arc passes GLONASS 20 and GPS 28 much more quickly, both between 1920 and 1930 UT. The maximum emission intensities in the line of sight to the satellites vary between 4 and 16 kR for 557.7 nm and are consistently around 2 kR for 630.0 nm.

Figures 5d–5f and 5j–5l show wavelet power spectra of 50 Hz raw phase. In the satellite/receiver combinations where the passing of the arc is clearest and most intense, namely, Figures 5e, 5f, and 5l, slight enhancements of phase variations are visible over the background spectrum, extending down to 1 s variations in Figures 5f and 5l. These enhancements are not particularly severe, and the scintillation data reflect this: Figures 5m–5o show amplitude scintillation, which stays very low throughout the passing of the arc, normally around 0.1 and at all times below 0.2. Figures 5p–5r show phase scintillation, which during the crossing of the arc is slightly enhanced in GLONASS 20 and GPS 28 (Figures 5q–5r) but only up to $\sigma_\phi = 0.2$ which is still only very weak scintillation.

Figures 5s–5u show vertical total electron content (VTEC) from the three satellites. A clear enhancement is visible during the passing of the arc. It is most clear in GPS 28 (Figure 5u), where a 5 total electron content unit (TECU; 1 TECU = 10^{16} el m^{-2}) increase can be seen. This is effectively an increase in TEC by a factor of 2. It is unknown what the earlier VTEC enhancement in Ny-Ålesund is for this satellite.

Figure 6 tells much the same story for three different satellites at a later time. The passing of the arc is clearly visible in the optical line-of-sight intensities (Figures 6a–6c and 6g–6i), though very weak in GPS 24. When crossing GPS 24 the arc had faded and the intensity varied greatly along the arc (as shown in Figure 3e), with a dim part of the arc crossing the satellite. The spectrograms (Figures 6d–6f and 6j–6l) show no or only very slight enhancements during the arc crossing. Amplitude scintillation stays around $S_4 = 0.1$ at all times, and phase scintillation stays below $\sigma_\phi = 0.2$, effectively meaning there is no or only very weak scintillation at all (though some slight enhancements over the background level can still be seen at times). The VTEC data again show enhancements of 2–5 TECU in relation to the arc.

We would like to end this section by pointing out that other satellites besides these six were studied in the same manner and support these findings. Additionally, we have briefly looked at four other polar cap arc

AGU Journal of Geophysical Research: Space Physics 10.1002/2016JA022708

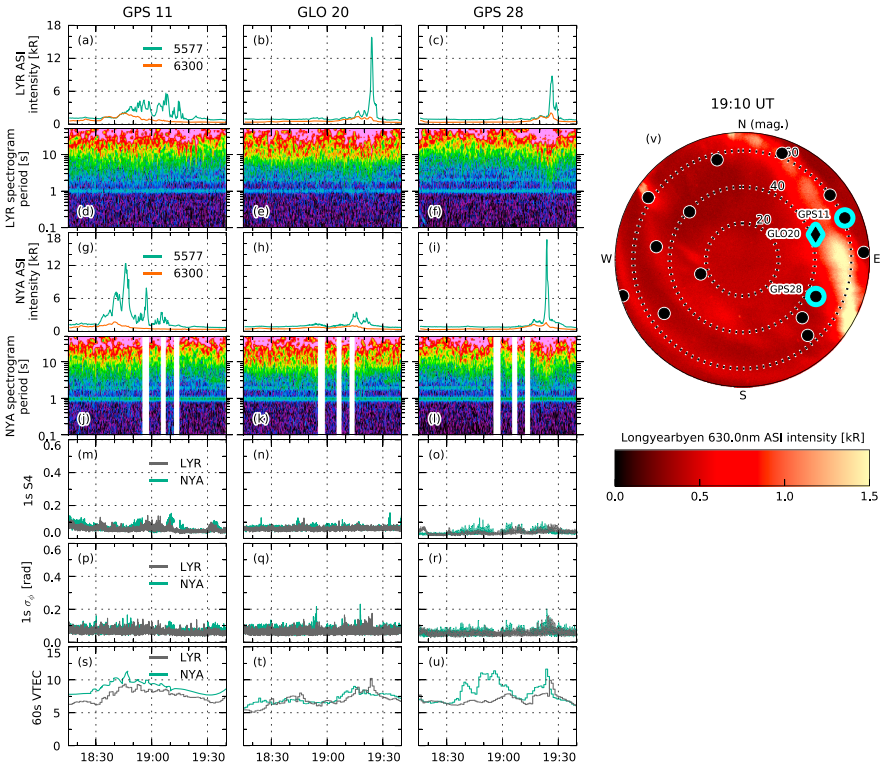

Figure 5. GNSS scintillations, vertical total electron content (VTEC), and phase variations for three selected satellites in relation to line-of-sight auroral intensity during the event on 15 January 2015. (a–c) Longyearbyen (LYR) auroral intensity in the line of sight of the three satellites. (d–f) Wavelet power spectra of 50 Hz raw phase from the Longyearbyen receiver on a decibel (logarithmic) color scale. (g–i) Ny-Ålesund (NYA) line-of-sight auroral intensity. (j–l) Wavelet power spectra from the Ny-Ålesund receiver. (m–o) 1 s S_4 amplitude scintillation index from both receivers. (p–r) 1 s σ_ϕ phase scintillation index from both receivers. (s–u) 60 s VTEC from the satellites at both receivers. (v) GNSS satellites and a selected 630.0 nm all-sky image on a polar axis (zenith angle versus azimuth; magnetic north is up, magnetic east is right).

events (22 December 2014 22:10, 15 January 2015 21:30, 16 January 2015 22:30, and 16 January 2015 23:40). These events were smaller and more transient and complex, which is why we chose to focus on a single, clear event in this study. It bears mentioning, however, that the other events seemed to support the above findings, and that we found no results in contradiction with those of the current study.

4. Discussion

4.1. Evidence of Irregularities

There is evidence of irregularities in relation to the arc. The presence of SuperDARN backscatter and the enhanced backscatter power indicates the presence of decameter field-aligned irregularities near the arc. There is also enhanced spectral width in relation to the arc. The physical reasons behind enhanced spectral width are complex, but the enhancement might suggest ongoing irregularity processes [*André et al.*, 2000].

AGU Journal of Geophysical Research: Space Physics 10.1002/2016JA022708

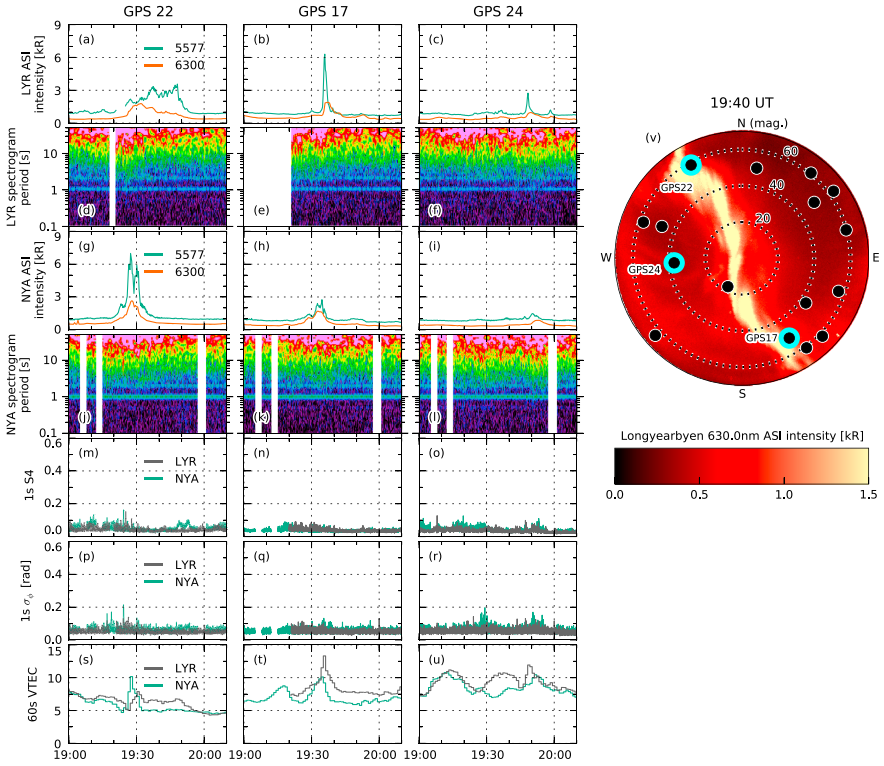

Figure 6. See Figure 5 for description. This figure highlights three different satellites.

Another evidence of increased structuring in relation to the arc is the slight enhancements in scintillation and the increase in spectral power in the phase spectrograms. Although the scintillation levels are very low, there are slight increases in phase scintillation in several satellites when the arc crosses the line of sight (as seen in Figures 5 and 6). This indicates that there are indeed some enhancement of irregularities in relation to the arc. This is naturally also visible in the phase spectrograms (since they are derived from the exact same data as the σ_ϕ index), which show slightly enhanced phase variations down to 1 s. *van der Meeren et al.* [2014] used such spectrograms to study a drifting plasma structure which could be assumed to be stable (not changing in time) compared to its drift speed. It was, therefore, possible to convert the temporal scale of the spectrum to spatial scale by using the drift speed of the plasma. In the current study (as in *van der Meeren et al.* [2015]) we are looking at ionization from particle precipitation, with a significant contribution from the *E* region (as evidenced by the much stronger 557.7 nm emissions occurring at lower altitudes than the weaker 630.0 nm emissions). The recombination rate at *E* region altitudes is much higher than in the *F* region, and the ionized plasma cannot be assumed to be a stable structure drifting westward with the arc. Therefore, we cannot convert the temporal spectrogram scale to spatial scale in this case.

In general, the observations indicate the presence of decameter-scale irregularities in relation to the polar cap arc. From the power law spectrum of irregularities in the ionosphere we can then infer that irregularities must

AGU Journal of Geophysical Research: Space Physics 10.1002/2016JA022708

exist at larger scale lengths, too. The irregularities are, however, too weak to cause scintillation effects of concern to GPS users. The presence of strong HF backscatter colocated with low levels of amplitude scintillation has been noted in previous studies [*van der Meeren et al.*, 2014, 2015].

4.2. Irregularity Mechanisms

An extensive discussion of all possible structuring mechanisms is outside the scope of this study. However, we would like to briefly discuss some important candidates.

Polar cap arcs are known to be associated with flow shears [e.g., *Carlson and Cowley*, 2005; *Eriksson et al.*, 2006]. The velocity shear seen in the SuperDARN data (Figures 4i and 4j) could drive the Kelvin-Helmholtz (KH) instability. The KH growth rate can be estimated by $\gamma_{KH} = 0.2\Delta V/L$ where ΔV is the velocity difference and L is the scale length of the velocity difference [*Carlson et al.*, 2008]. Based on the velocity data shown in Figure 4j, the KH growth time can be estimated to ~70 min, which indicates the KH instability is not effective. However, due to the one-dimensionality and low spatial resolution of the SuperDARN data, this estimate may be wildly off in either direction. Based on the available data for our event, we are unable to provide an accurate estimate of the KH growth time.

The gradient drift instability is another common instability mechanism in the polar ionosphere, which works on the trailing edge of drifting plasma structures [e.g., *Tsunoda*, 1988]. It was pointed out in the previous section that there is no single plasma structure drifting westward with the arc, but rather a continuous ionization and recombination which moves westward. Therefore, we assume there will be no structuring by the gradient drift instability.

Finally, we would like to mention the creation of irregularities directly by structured ionization. Previous studies have observed that soft electron precipitation may create *F* region irregularities [*Kelley et al.*, 1982; *Moen et al.*, 2002]. A statistical study by *Kinrade et al.* [2013] found a relationship between GPS phase scintillation and optical auroral emissions at 557.7 nm (*E* region). Auroral precipitation is known to be structured on spatial scales down to tens of meters [e.g., *Sandahl et al.*, 2008, and references therein], so it is conceivable that the irregularities are directly created by the auroral precipitation associated with the arc. Unfortunately, we have no way of investigating this further based on the available data from this event.

4.3. Electron Density Considerations

A possible explanation for the lack of strong irregularities might be the low density of the plasma. The VTEC measurements (Figures 5s–5u and 6s–6u) indicate a background density of ~5 TECU. This is supported by ionosonde data from Longyearbyen as well as global TEC data from the Madrigal database (not shown). The low density naturally limits the severity of irregularities formed by instability processes. This is in contrast to southward IMF conditions, where dayside density plasma is prominent in the polar cap and the instability processes often develop strong irregularities causing severe scintillation. It is possible that the dayside (and thus higher density) nature of the observations by *Prikryl et al.* [2015a] has contributed to the scintillation levels they observed. Studies of the equatorial ionosphere have shown that the background density can influence the severity of scintillation [*Whalen*, 2009; *Li et al.*, 2011].

Another salient point concerning the electron density is the fact that the arc shows an increase in up to 5 TECU. The total electron content thus reaches twice the background level, and ionosonde data from Longyearbyen show a similar increase (factor of 2) in the F_2 peak critical frequency. This meets the relative density requirements of polar cap patches (though the arc is of course not a patch), which are associated with strong scintillation [e.g., *Carlson*, 2012, and references therein]. A review by *Carlson* [1994] points out that scintillation intensity scales with absolute fluctuation in TEC, not relative fluctuation. Thus, even though the arc displays a factor of 2 increase in TEC, the increase is still smaller in absolute terms than high-density patches with dayside densities. It is possible that this is part of the reason why there is no strong scintillation in relation to the arc.

Previous studies have shown that during transitions from IMF south to IMF north, polar cap arcs and patches can coexist due to the sudden appearance of polar cap arcs during IMF north conditions compared to the slower response of patches exiting the polar cap [*Valladares et al.*, 1998; *Basu and Valladares*, 1999]. This could mean that during such transition states, flow shears associated with polar cap arcs may structure the existing high-density plasma (such as patches) through the KH instability. It is thus conceivable that polar cap arcs in a high-density ionosphere could pose a problem with regards to scintillation. In the current study the IMF was consistently northward oriented several hours before the event, so the transition effect is not relevant (as confirmed by the background density measurements). It would be beneficial for future studies to study

AGU Journal of Geophysical Research: Space Physics 10.1002/2016JA022708

plasma structuring associated with polar cap arcs when the background density is high, such as in summer or during transition states from IMF north to IMF south.

5. Conclusions

This study has shown a single case of scintillation and irregularities in relation to a polar cap arc in unprecedented detail. The main findings of the study can be summarized as follows.

1. During northward IMF conditions, weak irregularities are observed in relation to the nightside part of a long-lived, Sun-aligned polar cap arc.
2. The irregularities are evidenced by the presence of HF backscatter (indicating decameter-scale irregularities) as well as slight enhancements of GNSS phase variations and 1 s σ_ϕ.
3. The polar cap arc causes no amplitude scintillation and does not cause significant phase scintillation ($\sigma_\phi \leq 0.2$).
4. The lack of scintillation may be related to the low density in the polar cap after several hours of northward IMF.

Further studies should be carried out to close the gap in our knowledge of high-latitude irregularities during northward IMF conditions. Specifically,

1. further case studies and statistical studies should be carried out to get a representative view of irregularities and scintillation in relation to polar cap arcs;
2. direct comparisons should be made between auroral arcs and polar cap arcs of similar intensities, to find out if there is a difference between the effects of irregularities created by precipitation in the auroral oval and in the polar cap; and
3. polar cap arcs should be studied when there are high background densities, which could enable more severe irregularity formation and possibly a stronger impact on GNSS scintillation. This could be done by studying polar cap arcs after a south-to-north transition of the IMF, where the polar cap may be filled with high-density dayside plasma when the arc forms. Alternatively, one could study the dayside portion of a polar cap arc or arcs during summer.

Acknowledgments
The University of Oslo ASI data are available at http://tid.uio.no/plasma/aurora. The IMF and solar wind data were provided by the NASA OMNIWeb service (http://omniweb.gsfc.nasa.gov). The DMSP SSUSI data are available from http://ssusi.jhuapl.edu. The DMSP particle detectors were designed by Dave Hardy of AFRL and data obtained from JHU/APL. The SuperDARN data are retrieved from Virginia Tech using the DaViTpy software package. The ionosonde data (not shown) are available from http://dynserv.eiscat.uit.no. The GNSS data can be made available upon request from the author. This study was supported by the Research Council of Norway under contracts 212014, 223252, and 230935. We wish to thank Nikolai Østgaard at the Birkeland Centre for Space Science, University of Bergen for helpful discussions.

References

Aarons, J., B. Lin, M. Mendillo, K. Liou, and M. Codrescu (2000), Global positioning system phase fluctuations and ultraviolet images from the polar satellite, *J. Geophys. Res.*, *105*(A3), 5201–5213, doi:10.1029/1999JA900409.
Akasofu, S.-I. (1964), The development of the auroral substorm, *Planet. Space Sci.*, *12*(4), 273–282, doi:10.1016/0032-0633(64)90151-5.
Alfonsi, L., L. Spogli, G. De Franceschi, V. Romano, M. Aquino, A. Dodson, and C. N. Mitchell (2011), Bipolar climatology of GPS ionospheric scintillation at solar minimum, *Radio Sci.*, *46*, RS0D05, doi:10.1029/2010RS004571.
André, R., M. Pinnock, J.-P. Villain, and C. Hanuise (2000), On the factor conditioning the doppler spectral width determined from SuperDARN HF radars, *Int. J. Geomag. Aeron.*, *2*(1), 77–86.
Basu, S., and C. Valladares (1999), Global aspects of plasma structures, *J. Atmos. Sol. Terr. Phys.*, *61*(1–2), 127–139, doi:10.1016/S1364-6826(98)00122-9.
Basu, S., S. Basu, E. MacKenzie, W. R. Coley, J. R. Sharber, and W. R. Hoegy (1990a), Plasma structuring by the gradient drift instability at high latitudes and comparison with velocity shear driven processes, *J. Geophys. Res.*, *95*(A6), 7799–7818, doi:10.1029/JA095iA06p07799.
Basu, S., S. Basu, E. J. Weber, and G. J. Bishop (1990b), Plasma structuring in the polar cap, *J. Geomagn. Geoelectr.*, *42*(6), 763–776, doi:10.5636/jgg.42.763.
Basu, S., S. Basu, E. Costa, C. Bryant, C. E. Valladares, and R. C. Livingston (1991), Interplanetary magnetic field control of drifts and anisotropy of high-latitude irregularities, *Radio Sci.*, *26*(4), 1079–1103, doi:10.1029/91RS00586.
Basu, S., S. Basu, P. K. Chaturvedi, and C. M. Bryant (1994), Irregularity structures in the cusp/cleft and polar cap regions, *Radio Sci.*, *29*(1), 195–207, doi:10.1029/93RS01515.
Basu, S., E. J. Weber, T. W. Bullett, M. J. Keskinen, E. MacKenzie, P. Doherty, R. Sheehan, H. Kuenzler, P. Ning, and J. Bongiolatti (1998), Characteristics of plasma structuring in the cusp/cleft region at Svalbard, *Radio Sci.*, *33*(6), 1885–1899, doi:10.1029/98RS01597.
Béniguel, Y., et al. (2009), Ionospheric scintillation monitoring and modelling, *Ann. Geophys.*, *52*(3–4), 391–416, doi:10.4401/ag-4595.
Berkey, F. T., L. L. Cogger, S. Ismail, and Y. Kamide (1976), Evidence for a correlation between Sun-aligned arcs and the interplanetary magnetic field direction, *Geophys. Res. Lett.*, *3*(3), 145–147, doi:10.1029/GL003i003p00145.
Buchau, J., E. J. Weber, D. N. Anderson, H. C. Carlson, J. G. Moore, B. W. Reinisch, and R. C. Livingston (1985), Ionospheric structures in the polar cap: Their origin and relation to 250-MHz scintillation, *Radio Sci.*, *20*(3), 325–338, doi:10.1029/RS020i003p00325.
Carlson, H. C. (1994), The dark polar ionosphere: Progress and future challenges, *Radio Sci.*, *29*(1), 157–165, doi:10.1029/93RS02125.
Carlson, H. C. (2012), Sharpening our thinking about polar cap ionospheric patch morphology, research, and mitigation techniques, *Radio Sci.*, *47*, RS0L21, doi:10.1029/2011RS004946.
Carlson, H. C., and S. W. H. Cowley (2005), Accelerated polar rain electrons as the source of Sun-aligned arcs in the polar cap during northward interplanetary magnetic field conditions, *J. Geophys. Res.*, *110*, A05302, doi:10.1029/2004JA010669.
Carlson, H. C., T. Pedersen, S. Basu, M. Keskinen, and J. Moen (2007), Case for a new process, not mechanism, for cusp irregularity production, *J. Geophys. Res.*, *112*, A11304, doi:10.1029/2007JA012384.
Carlson, H. C., K. Oksavik, and J. Moen (2008), On a new process for cusp irregularity production, *Ann. Geophys.*, *26*(9), 2871–2885, doi:10.5194/angeo-26-2871-2008.

AGU Journal of Geophysical Research: Space Physics 10.1002/2016JA022708

Chisham, G., et al. (2007), A decade of the Super Dual Auroral Radar Network (SuperDARN): Scientific achievements, new techniques and future directions, *Surv. Geophys.*, *28*(1), 33–109, doi:10.1007/s10712-007-9017-8.
Clausen, L. B. N., J. I. Moen, K. Hosokawa, and J. M. Holmes (2016), GPS scintillations in the high latitudes during periods of dayside and nightside reconnection, *J. Geophys. Res. Space Physics*, *121*, 3293–3309, doi:10.1002/2015JA022199.
Coker, C., G. S. Bust, R. A. Doe, and T. L. Gaussiran (2004), High-latitude plasma structure and scintillation, *Radio Sci.*, *39*, RS1S15, doi:10.1029/2002RS002833.
Davis, T. N. (1963), Negative correlation between polar-cap visual aurora and magnetic activity, *J. Geophys. Res.*, *68*(15), 4447–4453, doi:10.1029/JZ068i015p04447.
Elphinstone, R. D., J. S. Murphree, and L. L. Cogger (1996), What is a global auroral substorm?, *Rev. Geophys.*, *34*(2), 169–232, doi:10.1029/96RG00483.
Eriksson, S., G. Provan, F. J. Rich, M. Lester, S. E. Milan, S. Massetti, J. T. Gosling, M. W. Dunlop, and H. Rème (2006), Electrodynamics of a split-transpolar aurora, *J. Geophys. Res.*, *111*, A11319, doi:10.1029/2006JA011976.
Fear, R. C., and S. E. Milan (2012a), The IMF dependence of the local time of transpolar arcs: Implications for formation mechanism, *J. Geophys. Res.*, *117*, A03213, doi:10.1029/2011JA017209.
Fear, R. C., and S. E. Milan (2012b), Ionospheric flows relating to transpolar arc formation, *J. Geophys. Res.*, *117*, A09230, doi:10.1029/2012JA017830.
Feldstein, Y. I., and G. V. Starkov (1967), Dynamics of auroral belt and polar geomagnetic disturbances, *Planet. Space Sci.*, *15*(2), 209–229, doi:10.1016/0032-0633(67)90190-0.
Forte, B. (2005), Optimum detrending of raw GPS data for scintillation measurements at auroral latitudes, *J. Atmos. Sol. Terr. Phys.*, *67*(12), 1100–1109, doi:10.1016/j.jastp.2005.01.011.
Forte, B., and S. M. Radicella (2002), Problems in data treatment for ionospheric scintillation measurements, *Radio Sci.*, *37*(6), 1096, doi:10.1029/2001RS002508.
Forte, B., M. Materassi, L. Alfonsi, V. Romano, G. De Franceschi, and P. Spalla (2011), Optimum parameter for estimating phase fluctuations on transionospheric signals at high latitudes, *Adv. Space Res.*, *47*(12), 2188–2193, doi:10.1016/j.asr.2010.04.033.
Foster, J. C., et al. (2005), Multiradar observations of the polar tongue of ionization, *J. Geophys. Res.*, *110*, A09S31, doi:10.1029/2004JA010928.
Garner, T. W., R. B. Harris, J. A. York, C. S. Herbster, C. F. Minter, and D. L. Hampton (2011), An auroral scintillation observation using precise, collocated GPS receivers, *Radio Sci.*, *46*, RS1018, doi:10.1029/2010RS004412.
Greenwald, R. A., et al. (1995), DARN/SuperDARN, *Space Sci. Rev.*, *71*(1–4), 761–796, doi:10.1007/BF00751350.
Gussenhoven, M. S. (1982), Extremely high latitude auroras, *J. Geophys. Res.*, *87*(A4), 2401–2412, doi:10.1029/JA087iA04p02401.
Gwal, A. K., and A. Jain (2011), GPS scintillation studies in the arctic region during the first winter-phase 2008 Indian Arctic Expedition, *Polar Sci.*, *4*(4), 574–587, doi:10.1016/j.polar.2010.08.001.
Hey, J. S., S. J. Parsons, and J. W. Phillips (1946), Fluctuations in cosmic radiation at radio-frequencies, *Nature*, *158*(4007), 234, doi:10.1038/158234a0.
Hosokawa, K., Y. Otsuka, Y. Ogawa, and T. Tsugawa (2014), Observations of GPS scintillation during an isolated auroral substorm, *Prog. Earth Planet. Sci.*, *1*(1), 1–9, doi:10.1186/2197-4284-1-16.
Jiao, Y., Y. T. Morton, S. Taylor, and W. Pelgrum (2013), Characterization of high-latitude ionospheric scintillation of GPS signals, *Radio Sci.*, *48*, 698–708, doi:10.1002/2013RS005259.
Jin, Y., J. I. Moen, and W. J. Miloch (2014), GPS scintillation effects associated with polar cap patches and substorm auroral activity: Direct comparison, *J. Space Weather Space Clim.*, *4*, A23, doi:10.1051/swsc/2014019.
Jin, Y., J. I. Moen, and W. J. Miloch (2015), On the collocation of the cusp aurora and the GPS phase scintillation: A statistical study, *J. Geophys. Res. Space Physics*, *120*, 9176–9191, doi:10.1002/2015JA021449.
Kelley, M. C., J. F. Vickrey, C. W. Carlson, and R. Torbert (1982), On the origin and spatial extent of high-latitude *F* region irregularities, *J. Geophys. Res.*, *87*(A6), 4469–4475, doi:10.1029/JA087iA06p04469.
Kinrade, J., C. N. Mitchell, P. Yin, N. Smith, M. J. Jarvis, D. J. Maxfield, M. C. Rose, G. S. Bust, and A. T. Weatherwax (2012), Ionospheric scintillation over Antarctica during the storm of 5–6 April 2010, *J. Geophys. Res.*, *117*, A05304, doi:10.1029/2011JA017073.
Kinrade, J., C. N. Mitchell, N. D. Smith, Y. Ebihara, A. T. Weatherwax, and G. S. Bust (2013), GPS phase scintillation associated with optical auroral emissions: First statistical results from the geographic south pole, *J. Geophys. Res. Space Physics*, *118*, 2490–2502, doi:10.1002/jgra.50214.
Kintner, P. M., B. M. Ledvina, and E. R. de Paula (2007), GPS and ionospheric scintillations, *Space Weather*, *5*, S09003, doi:10.1029/2006SW000260.
Knudsen, W. C. (1974), Magnetospheric convection and the high-latitude F_2 ionosphere, *J. Geophys. Res.*, *79*(7), 1046–1055, doi:10.1029/JA079i007p01046.
Lepping, R. P., et al. (1995), The WIND magnetic field investigation, *Space Sci. Rev.*, *71*(1–4), 207–229, doi:10.1007/BF00751330.
Li, G., B. Ning, Z. Ren, and L. Hu (2010), Statistics of GPS ionospheric scintillation and irregularities over polar regions at solar minimum, *GPS Solutions*, *14*(4), 331–341, doi:10.1007/s10291-009-0156-x.
Li, G., B. Ning, M. A. Abdu, X. Yue, L. Liu, W. Wan, and L. Hu (2011), On the occurrence of postmidnight equatorial *F* region irregularities during the June solstice, *J. Geophys. Res.*, *116*, A04318, doi:10.1029/2010JA016056.
Liou, K., J. M. Ruohoniemi, P. T. Newell, R. Greenwald, C.-I. Meng, and M. R. Hairston (2005), Observations of ionospheric plasma flows within theta auroras, *J. Geophys. Res.*, *110*, A03303, doi:10.1029/2004JA010735.
Lockwood, M., and H. C. Carlson (1992), Production of polar cap electron density patches by transient magnetopause reconnection, *Geophys. Res. Lett.*, *19*(17), 1731–1734, doi:10.1029/92GL01993.
Mawson, D. (1916), Auroral observations at the Cape Royds Station, Antarctica, *Trans. R. Soc. South Aust.*, *40*, 151–212.
McPherron, R. L. (1970), Growth phase of magnetospheric substorms, *J. Geophys. Res.*, *75*(28), 5592–5599, doi:10.1029/JA075i028p05592.
McPherron, R. L. (1979), Magnetospheric substorms, *Rev. Geophys.*, *17*(4), 657–681, doi:10.1029/RG017i004p00657.
Mitchell, C. N., L. Alfonsi, G. De Franceschi, M. Lester, V. Romano, and A. W. Wernik (2005), GPS TEC and scintillation measurements from the polar ionosphere during the October 2003 storm, *Geophys. Res. Lett.*, *32*, L12S03, doi:10.1029/2004GL021644.
Moen, J., I. K. Walker, L. Kersley, and S. E. Milan (2002), On the generation of cusp HF backscatter irregularities, *J. Geophys. Res.*, *107*(A4), 1044, doi:10.1029/2001JA000111.
Moen, J., K. Oksavik, T. Abe, M. Lester, Y. Saito, T. A. Bekkeng, and K. S. Jacobsen (2012), First in-situ measurements of HF radar echoing targets, *Geophys. Res. Lett.*, *39*, L07104, doi:10.1029/2012GL051407.
Moen, J., K. Oksavik, L. Alfonsi, Y. Daabakk, V. Romano, and L. Spogli (2013), Space weather challenges of the polar cap ionosphere, *J. Space Weather Space Clim.*, *3*, A02, doi:10.1051/swsc/2013025.

Mushini, S. C., P. T. Jayachandran, R. B. Langley, J. W. MacDougall, and D. Pokhotelov (2012), Improved amplitude- and phase-scintillation indices derived from wavelet detrended high-latitude GPS data, *GPS Solutions*, *16*(3), 363–373, doi:10.1007/s10291-011-0238-4.

Newell, P. T., K. Liou, and G. R. Wilson (2009), Polar cap particle precipitation and aurora: Review and commentary, *J. Atmos. Sol. Terr. Phys.*, *71*(2), 199–215, doi:10.1016/j.jastp.2008.11.004.

Ngwira, C. M., L.-A. McKinnell, and P. J. Cilliers (2010), GPS phase scintillation observed over a high-latitude Antarctic station during solar minimum, *J. Atmos. Sol. Terr. Phys.*, *72*(9–10), 718–725, doi:10.1016/j.jastp.2010.03.014.

Ogilvie, K. W., et al. (1995), SWE, a comprehensive plasma instrument for the Wind spacecraft, *Space Sci. Rev.*, *71*(1–4), 55–77, doi:10.1007/BF00751326.

Oksavik, K., V. L. Barth, J. Moen, and M. Lester (2010), On the entry and transit of high-density plasma across the polar cap, *J. Geophys. Res.*, *115*, A12308, doi:10.1029/2010JA015817.

Oksavik, K., J. Moen, M. Lester, T. A. Bekkeng, and J. K. Bekkeng (2012), In situ measurements of plasma irregularity growth in the cusp ionosphere, *J. Geophys. Res.*, *117*, A11301, doi:10.1029/2012JA017835.

Oksavik, K., C. van der Meeren, D. A. Lorentzen, L. J. Baddeley, and J. Moen (2015), Scintillation and loss of signal lock from poleward moving auroral forms in the cusp ionosphere, *J. Geophys. Res. Space Physics*, *120*, 9161–9175, doi:10.1002/2015JA021528.

Paxton, L. J., et al. (1992), *Special Sensor Ultraviolet Spectrographic Imager: An Instrument Description*, pp. 2–15, Int. Soc. Opt. and Photonics, San Diego, Calif., doi:10.1117/12.60595.

Prikryl, P., P. T. Jayachandran, S. C. Mushini, D. Pokhotelov, J. W. MacDougall, E. Donovan, E. Spanswick, and J.-P. St.-Maurice (2010), GPS TEC, scintillation and cycle slips observed at high latitudes during solar minimum, *Ann. Geophys.*, *28*(6), 1307–1316, doi:10.5194/angeo-28-1307-2010.

Prikryl, P., et al. (2015a), GPS phase scintillation at high latitudes during geomagnetic storms of 7–17 March 2012—Part 1: The North American sector, *Ann. Geophys.*, *33*(6), 637–656, doi:10.5194/angeo-33-637-2015.

Prikryl, P., P. T. Jayachandran, R. Chadwick, and T. D. Kelly (2015b), Climatology of GPS phase scintillation at northern high latitudes for the period from 2008 to 2013, *Ann. Geophys.*, *33*(5), 531–545, doi:10.5194/angeo-33-531-2015.

Rostoker, G., S.-I. Akasofu, J. Foster, R. Greenwald, Y. Kamide, K. Kawasaki, A. Lui, R. McPherron, and C. Russell (1980), Magnetospheric substorms—Definition and signatures, *J. Geophys. Res.*, *85*(A4), 1663–1668, doi:10.1029/JA085iA04p01663.

Ruohoniemi, J. M., R. A. Greenwald, K. B. Baker, J.-P. Villain, C. Hanuise, and J. Kelly (1989), Mapping high-latitude plasma convection with coherent HF radars, *J. Geophys. Res.*, *94*(A10), 13,463–13,477, doi:10.1029/JA094iA10p13463.

Sandahl, I., T. Sergienko, and U. Brändström (2008), Fine structure of optical aurora, *J. Atmos. Sol. Terr. Phys.*, *70*(18), 2275–2292, doi:10.1016/j.jastp.2008.08.016.

Sandholt, P. E., M. Lockwood, T. Oguti, S. W. H. Cowley, K. S. C. Freeman, B. Lybekk, A. Egeland, and D. M. Willis (1990), Midday auroral breakup events and related energy and momentum transfer from the magnetosheath, *J. Geophys. Res.*, *95*(A2), 1039–1060, doi:10.1029/JA095iA02p01039.

Sandholt, P. E., J. Moen, D. Opsvik, W. F. Denig, and W. J. Burke (1993), Auroral event sequence at the dayside polar cap boundary: Signature of time-varying solar wind-magnetosphere-ionosphere coupling, *Adv. Space Res.*, *13*(4), 7–15, doi:10.1016/0273-1177(93)90305-U.

Sato, T. (1959), Morphology of the ionospheric F_2 disturbances in the polar region, *Rep. Ionos. Space Res. Jpn.*, *131*, 91–104.

Spogli, L., L. Alfonsi, G. De Franceschi, V. Romano, M. H. O. Aquino, and A. Dodson (2009), Climatology of GPS ionospheric scintillations over high and mid-latitude European regions, *Ann. Geophys.*, *27*(9), 3429–3437, doi:10.5194/angeo-27-3429-2009.

Thorolfsson, A., J.-C. Cerisier, M. Lockwood, P. E. Sandholt, C. Senior, and M. Lester (2000), Simultaneous optical and radar signatures of poleward-moving auroral forms, *Ann. Geophys.*, *18*(9), 1054–1066, doi:10.1007/s00585-000-1054-2.

Tiwari, S., A. Jain, S. Sarkar, S. Jain, and A. K. Gwal (2012), Ionospheric irregularities at Antarctic using GPS measurements, *J. Earth Syst. Sci.*, *121*(2), 345–353, doi:10.1007/s12040-012-0168-8.

Torrence, C., and G. P. Compo (1998), A practical guide to wavelet analysis, *Bull. Am. Meteorol. Soc.*, *79*(1), 61–78, doi:10.1175/1520-0477(1998)079.

Tsunoda, R. T. (1988), High-latitude F region irregularities: A review and synthesis, *Rev. Geophys.*, *26*(4), 719–760, doi:10.1029/RG026i004p00719.

Valladares, C. E., K. Fukui, R. Sheehan, H. C. Carlson, and T. Bullett (1998), Simultaneous observations of polar cap patches and Sun-aligned arcs during transitions of the IMF, *Radio Sci.*, *33*(6), 1829–1845, doi:10.1029/98RS02187.

van der Meeren, C., K. Oksavik, D. Lorentzen, J. I. Moen, and V. Romano (2014), GPS scintillation and irregularities at the front of an ionization tongue in the nightside polar ionosphere, *J. Geophys. Res. Space Physics*, *119*, 8624–8636, doi:10.1002/2014JA020114.

van der Meeren, C., K. Oksavik, D. A. Lorentzen, M. T. Rietveld, and L. B. N. Clausen (2015), Severe and localized GNSS scintillation at the poleward edge of the nightside auroral oval during intense substorm aurora, *J. Geophys. Res. Space Physics*, *120*, 10,607–10,621, doi:10.1002/2015JA021819.

Vorobjev, V. G., G. Gustafsson, G. V. Starkov, Y. I. Feldstein, and N. F. Shevnina (1975), Dynamics of day and night aurora during substorms, *Planet. Space Sci.*, *23*(2), 269–278, doi:10.1016/0032-0633(75)90132-4.

Weber, E. J., J. Buchau, J. G. Moore, J. R. Sharber, R. C. Livingston, J. D. Winningham, and B. W. Reinisch (1984), F layer ionization patches in the polar cap, *J. Geophys. Res.*, *89*(A3), 1683–1694, doi:10.1029/JA089iA03p01683.

Weber, E. J., J. A. Klobuchar, J. Buchau, H. C. Carlson, R. C. Livingston, O. de la Beaujardiere, M. McCready, J. G. Moore, and G. J. Bishop (1986), Polar cap F layer patches: Structure and dynamics, *J. Geophys. Res.*, *91*(A11), 12,121–12,129, doi:10.1029/JA091iA11p12121.

Whalen, J. A. (2009), The linear dependence of GHz scintillation on electron density observed in the equatorial anomaly, *Ann. Geophys.*, *27*(4), 1755–1761, doi:10.5194/angeo-27-1755-2009.

Zhang, Q.-H., B.-C. Zhang, J. Moen, M. Lockwood, I. W. McCrea, H.-G. Yang, H.-Q. Hu, R.-Y. Liu, S.-R. Zhang, and M. Lester (2013a), Polar cap patch segmentation of the tongue of ionization in the morning convection cell, *Geophys. Res. Lett.*, *40*, 2918–2922, doi:10.1002/grl.50616.

Zhang, Q.-H., et al. (2013b), Direct observations of the evolution of polar cap ionization patches, *Science*, *339*(6127), 1597–1600, doi:10.1126/science.1231487.

Zou, Y., Y. Nishimura, L. R. Lyons, E. F. Donovan, K. Shiokawa, J. M. Ruohoniemi, K. A. McWilliams, and N. Nishitani (2015), Polar cap precursor of nightside auroral oval intensifications using polar cap arcs, *J. Geophys. Res. Space Physics*, *120*, 10,698–10,711, doi:10.1002/2015JA021816.